Laser Metrology in Fluid Mechanics

Laser Metrology in Fluid Mechanics

Granulometry, Temperature and Concentration Measurements

Edited by
Alain Boutier

ISTE WILEY

First published 2013 in Great Britain and the United States by ISTE Ltd and John Wiley & Sons, Inc.

ISTE Ltd
27-37 St George's Road
London SW19 4EU
UK

www.iste.co.uk

John Wiley & Sons, Inc.
111 River Street
Hoboken, NJ 07030
USA

www.wiley.com

Library of Congress Control Number: 2012950203

British Library Cataloguing-in-Publication Data
A CIP record for this book is available from the British Library
ISBN: 978-1-84821-398-2

Printed and bound in Great Britain by CPI Group (UK) Ltd., Croydon, Surrey CR0 4YY

Table of Contents

Preface

This book has been elaborated from lectures given in the framework of autumn schools organized since 1997 by AFVL – *Association Francophone de Vélocimétrie Laser* (French-speaking Association of Laser Velocimetry).

AFVL activities are especially dedicated to foster and facilitate transfer of knowledge in laser velocimetry and all techniques making use of lasers employed for metrology in fluid mechanics. Among the main objectives, a good use of laser techniques is looked at to fulfill requirements of potential applications in research and industry.

The authors of this book have thus shared their expertise within AFVL, which led them to write the various chapters within a teaching environment, which allows the reader to learn and perfect perspective both for his/her theoretical and practical knowledge.

Introduction

In fluid mechanics, non-intrusive measurements are fundamental to improve knowledge about flow behavior. Flow maps of velocity, temperature and concentration, as well as particle granulometry in two-phase flows, uniquely help in understanding the physical phenomena inside flows, which in turn enables code validation.

Different techniques are required for velocity measurements using spectroscopic principles, based on light scattering by molecules: laser-induced fluorescence, coherent anti-Stokes Raman scattering and tuneable laser diode. They are generally better suited for characterization of high-velocity flows. These devices also very often allow access to temperatures and concentrations of species present in reactive flows. Chapter 2 is especially dedicated to the determination of particle granulometry by optical means, measurement techniques being more adapted to two-phase flows studies; whereas Chapter 1 describes light scattering principles. For each technique, basic principles are described, as well as optical setups and signal processors.

The last chapter (Chapter 6) is dedicated to laser safety; it sums up the main precautions that must be taken for any device using an intense laser source.

Another book by the same authors, titled “Laser Velocimetry in Fluid Mechanics”, describes the various techniques of velocity measurement based on particle scattering. These velocity measurement techniques give access to the mean velocity field, as well as to detailed turbulence knowledge.

Introduction is written by Alain BOUTIER.

Chapter 1

Basics on Light Scattering by Particles

1.1. Introduction

This chapter introduces the basic concepts of the properties of electromagnetic waves, and the models and theories that describe the light scattering properties of small particles (droplets, bubbles, nanoaggregates, etc.) that are encountered in fluid mechanics and mechanical engineering problems. Light scattering models are fundamental to understanding the principles of optical particle characterization (OPC) techniques (see Chapter 2) and, to a lesser extent, laser velocimetry techniques[1]. Recognizing the need for an abbreviated format, this chapter covers the following topics:

– the basic properties of electromagnetic waves interacting with linear materials (propagation, polarization, absorption, phase shift, etc.);

– quantities and concepts commonly used to describe the elastic interaction of electromagnetic waves with particles (scattering matrix, cross-sections, scattering diagrams, radiation pressure, photon mean free path, etc.);

– rigorous theories describing the absorption and scattering properties of highly symmetric particles (Lorenz–Mie theory (LMT) and Debye theory);

– asymptotic models that are computationally efficient but only valid for particles that are small or large with respect to the wavelength, or for particular

---

Chapter written by Fabrice ONOFRI and Séverine BARBOSA.

1 See the book by the same authors, *Laser Velocimetry in Fluid Mechanics* [BOU 12].

refraction index ranges: Rayleigh (electrostatic dipoles), Fraunhofer (edge) diffraction, Airy (rainbow phenomena) and geometrical optics approximations;

– semi-analytical and numerical methods allowing us to model the optical properties of complex-shaped nanoparticles or nanoparticulate systems (the T-matrix method, the discrete dipole approximation and the Monte Carlo method).

Chapters 3 and 5 complement the present chapter by addressing molecular diagnostics based on inelastic and nonlinear scattering.

1.2. A brief synopsis of electromagnetic theory

1.2.1. *Maxwell's equations*

The general form of Maxwell's equations for an isotropic and linear medium may be written as follows:

$$\begin{cases} \vec{\nabla} \bullet \vec{D} = \rho_F, \\ \vec{\nabla} \times \vec{E} = -\dfrac{\partial \vec{B}}{\partial t}, \\ \vec{\nabla} \bullet \vec{B} = 0, \\ \vec{\nabla} \times \vec{H} = \vec{J}_F + \dfrac{\partial \vec{D}}{\partial t}, \end{cases} \qquad [1.1]$$

where $\vec{D}$ represents the electric displacement (i.e. a vector), $\vec{E}$ is the electric field, $\vec{B}$ is the magnetic induction, $\vec{H}$ is the magnetic field, ρ_F is the electric charge density and $\vec{J}_F$ is the electric current density [BOR 02]. Electromagnetic fields are related to excitations by the following expressions:

$$\vec{D} = \varepsilon_0 \vec{E} + \vec{P}, \quad \vec{H} = \vec{B} / \mu_0 - \vec{M}, \qquad [1.2]$$

where ε_0 and μ_0 denote the permittivity and magnetic permeability of free space, respectively, and $\vec{P}$ and $\vec{M}$ denote the polarization and magnetization in a volume of the medium, respectively. Simple constitutive laws relate the electrical and magnetic properties of a linear medium:

$$\vec{J}_F = \sigma \vec{E}, \qquad \vec{B} = \mu \vec{H}, \qquad \vec{P} = \varepsilon_0 \chi \vec{E}, \qquad [1.3]$$

where σ, μ and χ denote its electrical conductivity, magnetic permeability and electrical susceptibility, respectively.

Although particles and fluids are generally not charged and without specific magnetic properties ($\sigma_F \equiv |J_F|, \mu \approx \mu_0$), their polarizability is never zero. In fact, their material prevents the propagation of electromagnetic waves due to the constant susceptibility. For isotropic materials and media, the electrical susceptibility is simply a scalar. For anisotropic materials and media (optical fibers under mechanical constraints, saccharine droplets, crystals, etc.), the individual or averaged electrical susceptibility is a tensor of dimension two or three: $\vec{P} = \varepsilon_0 [\chi] \vec{E}$. The electrical permittivity of a material $[\varepsilon_r] = [1 + \chi]$ is often referenced to that of free space:

$$\vec{D} = \varepsilon_0 \vec{E} + \varepsilon_0 [\chi] \vec{E} = \varepsilon_0 [\varepsilon_r] \vec{E} = [\varepsilon] \vec{E}, \text{ with } [\varepsilon] = \varepsilon_0 [\varepsilon_r]. \quad [1.4]$$

When a material is illuminated by a very intense beam of light (to get us thinking, let us say when $|E|$ >100 kV/m), the amplitude of the electrical field induced within the material is no longer proportional to the amplitude of the incident field. In this case, the material polarizability is composed of a set of contributions corresponding to increasingly nonlinear responses of the material (e.g. [BOR 02] and [BAS 95a]):

$$|P| = \varepsilon_0 (\chi^{(1)} |E| + \chi^{(2)} : |EE| + \chi^{(3)} : |EEE| + ...), \quad [1.5]$$

where the superscript (n) indicates the number of photons involved in the induced response and:

– $\chi^{(1)}$ is responsible for the usual observed mechanisms: Rayleigh, Mie and spontaneous Raman scattering; spontaneous absorption and fluorescence (see Chapter 3).

– $\chi^{(2)}$ (zero for gases) induces frequency doubling phenomena (e.g. frequency doubling crystals used by most particle image velocimetry systems (PIV, i.e. Nd-YAG lasers) and stimulated Raman scattering.

– $\chi^{(3)}$ induces frequency tripling phenomena used by PIV/Nd-YAG lasers as well as by coherent anti-Stokes Raman scattering and degenerate four-wave mixing diagnostics (see Chapter 5).

The appearance of nonlinear effects may also be induced by non-optical phenomena (e.g. Brillouin scattering).

1.2.2. *Harmonic electromagnetic plane waves*

For an infinite and isotropic medium free of electrical charge and with no magnetic properties, harmonic plane waves are solutions to Maxwell's equations. The general form of these plane waves is given by:

$$\vec{E} = \vec{E}_0 e^{i(\vec{k}\bullet\vec{x}-\omega t)}, \vec{H} = \vec{H}_0 e^{i(\vec{k}\bullet\vec{x}-\omega t)}. \quad [1.6]$$

The wave vector $\vec{k}$ is *a priori* complex, that is $\vec{k} = \vec{k}' + i\vec{k}''$, so that the electrical fields can be written as follows:

$$\vec{E} = \vec{E}_0 e^{-\vec{k}''\bullet\vec{x}} e^{i(\vec{k}'\bullet\vec{x}-\omega t)}, \quad \vec{H} = \vec{H}_0 e^{-\vec{k}''\bullet\vec{x}} e^{i(\vec{k}'\bullet\vec{x}-\omega t)}, \quad [1.7]$$

where $e^{-\vec{k}''\bullet\vec{x}}$ accounts for the exponential attenuation of the amplitude of the propagating wave and $e^{i(\vec{k}'\bullet\vec{x}-\omega t)}$ accounts for a phase delay that increases with time and distance. For such a medium, Maxwell's equations are reduced to:

$$\begin{cases} \vec{\nabla}\bullet\left(\varepsilon\vec{E}_0\right) = 0, \\ \vec{\nabla}\times\vec{E}_0 = \omega\mu\vec{H}_0, \\ \vec{\nabla}\bullet\vec{H}_0 = 0, \\ \vec{\nabla}\times\vec{H}_0 = -\omega\varepsilon\vec{E}_0, \end{cases} \quad [1.8]$$

where $\omega = 2\pi\nu = 2\pi c/\lambda_0$ is the wave pulsation (or angular frequency), ν its frequency and λ_0 its wavelength in free space. $\varepsilon = \varepsilon_0(1+\chi)$ is the complex permittivity of the medium under consideration.

Plane harmonic electromagnetic waves are solutions of Maxwell's equations under the following conditions:

$$\vec{k}\bullet\vec{E}_0 = \vec{k}\bullet\vec{H}_0 = \vec{E}_0\bullet\vec{H}_0 = 0, \quad [1.9]$$

$$\vec{k}\bullet\vec{k} = \omega^2\varepsilon\mu. \quad [1.10]$$

From equation [1.9], it appears that vectors $\vec{k}, \vec{E}_0$ and $\vec{H}_0$ are perpendicular to each other. Inserting equation [1.7] into equation [1.8] yields:

$$\vec{k}_0 \wedge \vec{E}_0 = \mu\omega H_0. \quad [1.11]$$

The wavefront (i.e. an equiphase surface wave, see Figure 1.1) is defined by the set of vectors $\left(\vec{E}_0, \vec{H}_0\right)$.

Figure 1.1. *Schematic of a harmonic electromagnetic plane wave propagating within an infinite, homogenous and non-absorbing medium*

1.2.2.1. *Intensity and amplitude*

The wave vector does not necessarily indicate the direction of propagation of a wave. The direction of propagation of the wave energy is given by the Poynting vector, the value of which is averaged over a time period $1/\nu$ given by:

$$\left\langle \vec{S} \right\rangle_{1/\nu} = \frac{1}{2}\mathrm{Re}\left\{\vec{E}_0 \wedge \vec{H}_0^*\right\}, \qquad [1.12]$$

where $\vec{H}_0^*$ represents the complex conjugate of the magnetic field vector. The modulus of the Poynting vector is commonly called the beam or wave intensity. It can be seen from equations [1.11] and [1.12] that this intensity is simply proportional to the square of the modulus of the electric field amplitude:

$$\left\langle I \right\rangle_{1/\nu} = \frac{k_0}{2\mu\omega}\left|\vec{E}_0\right|^2. \qquad [1.13]$$

Let us introduce a new optical constant, $\tilde{m}$, which will later be referred to as the medium complex refractive index:

$$k = k' + ik'' \equiv \frac{\omega\tilde{m}}{c}, \qquad [1.14]$$

where the constant $c = 1/\sqrt{\varepsilon\mu}$ is the speed of light in free space and $\tilde{m} = c\sqrt{\varepsilon\mu} = m + ik_m$, where $m \geq 0$ and $k_m \geq 0$ denote the real and imaginary parts of $\tilde{m}$, respectively. Thus, the electrical field can be written as follows:

$$\vec{E} = \vec{E}_0 e^{-\frac{2\pi k_m x}{\lambda}} e^{i\left(\frac{2\pi m x}{\lambda} - \omega t\right)}, \qquad [1.15]$$

where the first term accounts for the amplitude and the state of polarization of the wave as it propagates, the second term accounts for its attenuation (which is related to the imaginary part of the refractive index) and the third term accounts for the evolution of its phase (which is related to the real part of the refractive index).

It follows from equations [1.13] and [1.15] that the intensity of a plane wave (and by extension, a collimated beam) propagating in an absorbing medium of length *L* decreases as follows:

$$I / I_0 = e^{-KL}, \qquad [1.16]$$

where $K = 4\pi k_m / \lambda$ denotes the absorption of the medium (the symbols a and α are also commonly used instead of *K*) and I_0 denotes the intensity of the incident wave (see Figure 1.2(a)). Equation [1.16] is often referred to as the Beer–Lambert law and is obtained by integrating infinitesimal absorptions over the wave trajectory:

$$\begin{aligned} &I(x+dx) - I(x) = -KI(x)\,dx\text{: homogeneous and absorbing medium,} \\ &I(x+dx) - I(x) \simeq -C_N \overline{C}_e I(x)\,dx\text{: extinction by a particle system.} \end{aligned} \qquad [1.17]$$

Figure 1.2. *Schematics of a) the attenuation of a wave propagating in a homogeneous and absorbing medium; and b) the extinction of a wave propagating in a particulate system*

The absorption of a material depends on its atomic and molecular composition, so that the measurement of the rate of attenuation of a collimated laser beam may be used, for instance, to characterize flow mixing properties (e.g. Table 1.2 and

[HOU 95]). The material absorption depends also on thermophysical conditions (see Table 1.2) and the frequency of the incident wave (i.e. the wavelength; see Table 1.1 and Figure 1.5 for the dispersion of various materials). Under certain conditions, the Beer–Lambert law may be used to estimate the rate of attenuation of a beam propagating in a particulate medium (see Figure 1.2(b) and equation [1.17]). In this case, the absorption constant is replaced by the medium turbidity, $K \equiv \tau = C_N \overline{C}_e$. The turbidity τ is related to the particle number concentration C_N of the medium and the average light extinction cross section $\overline{C}_e$ of the illuminated particles (see sections 1.2 and 1.7.1, and Chapter 2 for applications) (e.g. [ONO 12]).

Table 1.1. *Order of magnitude ranges for the wavelength, frequency and energy of electromagnetic waves (1 eV ≈ 1.602 × 10^{-19} J)*

1.2.2.2. *Polarization*

By definition, the direction of the electric field vector indicates the polarization direction of an electromagnetic wave. The polarization is said to be linear when the direction of the electric field is constant (Figure 1.3). The polarization state is said to be circular, naturally polarized or unpolarized, when the average direction of the electric field appears to be isotropic (i.e. in terms of the response time of the photodetector). Natural light sources tend to produce unpolarized light (due to the nature of spontaneous emission and the very low coherence of these sources). In nature, light is usually weakly polarized except when it reflects on a dielectric medium near the Brewster angle (section 1.7) (e.g. [BOR 02, BAS 95a]). The polarization of many lasers is said to be linear, although, in practice, their polarization is usually elliptical with an ellipticity factor $\zeta = b/a$ ranging typically from $\zeta = 1/50$ down to 1/500.

For birefringent materials, the effective refractive index depends both on the polarization state and the direction of propagation of the incident wave with respect to the optical axes of the material. The birefringence may be intrinsic to the material (i.e. crystals) or induced (by mechanical or thermal stress, or flow conditions, etc.) [FUL 95]. There exist other media, such as sucrose solutions which have the ability to preferentially rotate the direction of the polarization either to the left or to the right.

The polarization properties of particulate systems can be analyzed by ellipsometers[2] and optical rheometers [FUL 95] to determine the size or orientation of small particles. These polarization properties are also harnessed in interferometry and diffractometric techniques (see Chapter 2).

Figure 1.3. *Common polarization states of light*

1.2.2.3. *Trajectory and phase delay*

A wave propagating in a medium that is homogeneous on the scale of the wavelength, but inhomogeneous at the macroscopic scale, must satisfy the following condition to be a solution to Maxwell's equations:

$$\vec{\nabla}\phi(\vec{r}) = m(\vec{r})\vec{u}. \qquad [1.18]$$

This equation is called the eikonal equation of geometrical optics. It shows that the wave propagates locally along the gradient of the phase function $\phi(\vec{r})$ of the medium (i.e. along the refractive index gradient), $\vec{u}$ being a unit vector pointing in the direction of the gradient. Thus, the trajectory of a pencil of light propagating in such a medium may be curved (Figure 1.3). Shadowgraph, conventional Schlieren or back-oriented Schlieren techniques [BOU 12] use this property to detect (and sometimes quantify) the density and/or temperature gradients in aerodynamic, compressive or combustion flows (e.g., [MEI]).

Figure 1.4. *The trajectory of a pencil of light in a macroscopically inhomogeneous but continuous medium*

2 See [BOU 12] by the same authors.

The phase delay during wave propagation is derived from a line integral along the three-dimensional wave trajectory:

$$\Delta\phi = \int_{\vec{r}_1}^{\vec{r}_2} \vec{k}.d\vec{r}. \qquad [1.19]$$

It is usually impossible to recover the 3D properties of the medium from phase delay measurements if the medium does not possess any symmetry (see Chapter 2) [MEI 02]. The situation is simpler in a homogeneous medium, where $\vec{k}$ and $\vec{r}$ are always tangential to each other and the phase delay is directly related to the Euclidean distance, $L = \sqrt{\|\vec{r}_2 - \vec{r}_1\|}$:

$$\Delta\phi_{12} = kL = \frac{2\pi}{\lambda_0} mL. \qquad [1.20]$$

Equation [1.20] is used by most interferometric techniques to characterize, for instance, the diameter (section 2.4) or the 3D position (section 2.10) of small particles.

1.2.3. *Optical constants*

Within linear optics, the intrinsic properties of a homogeneous and isotropic material are related to its linear dispersion properties. However, because most optical techniques used in fluid mechanics use lasers emitting monochromatic radiation in the visible range, the fluid or particle optical material properties reduce to two parameters (i.e. the two complex refractive indices for the laser wavelength under consideration).

1.2.3.1. *Spectral range*

Table 1.1 provides orders of magnitude for the wavelength, frequency and energy of the different classes of electromagnetic waves. The spectrum of optical waves (i.e. waves that can be detected by the human eye and perceived as visible light) is restricted to a narrow range in which the wavelengths typically range from 0.38 to 0.78 μm.

1.2.3.2. *Complex refractive index*

The refractive index of particles in multiphase flows or suspensions[3] may vary due to chemical reactions, coalescence or drying phenomena, as well as changes in

3 An effective refractive index may also be defined for some particulate medium (e.g. [NIK 81, BOH 88, DOI 01b]).

the thermophysical conditions of the system. Table 1.2 shows the dependence of the refractive index on the temperature or mixing ratio for various materials. As an example, for an *n*-decane droplet whose absorption is negligible in the visible domain, the real part of its refractive index decreases by ≈ -0.006 (i.e. $\approx -0.4\%$) for a temperature increase of 10°C. Figure 1.5 shows the dispersion of pure water from the ultraviolet to the mid-wavelength infrared (MWIR) spectral ranges [SEG 81].

Table 1.2. *Evolution of the real or imaginary part of the refractive index of various materials versus their temperature (T °C) or mass mixing ratio (Y = 0–100%) – visible light*

Figure 1.5. *Dispersion of water at STP conditions in a) the ultraviolet range ($\lambda \approx$ 10–390 nm), the visible range (0.39–0.75 μm), the near-infrared (NIR, 0.75–1.4 μm), short-wavelength infrared (SWIR, 1.4–3 μm) and mid-wavelength infrared (MWIR, 3–8 μm) spectral ranges [SEG 81], and b) magnified illustration of the visible range*

Through the above examples, it may be understood how some OPC techniques can infer the temperature and composition of particles from a measurement of their refractive index (section 2.7).

1.2.4. *Light scattering by a single particle*

We now move on to the modeling of the scattering and absorption properties of a single particle made of a homogeneous, isotropic, linear and non-magnetic material with a complex refractive index m_1. The surrounding medium is taken to possess similar properties as the particle, except that the medium is assumed to be infinite and non-absorbing (i.e. its refractive index m_2 is purely real). The incident wave is a harmonic electromagnetic plane wave that is linearly polarized with wavelength λ. The observer is a large distance away from the particle (see Figure 1.6(a)).

Figure 1.6. *(a-b) Schematics of the electromagnetic scattering models [BOH 88]*

1.2.4.1. *Amplitude scattering matrix*

The particle shape is for the moment, taken to be arbitrary. In a Cartesian coordinate system $(x, y, z)/(\vec{e}_x, \vec{e}_y, \vec{e}_z)$, the field incident onto the particle surface may be written as [BOH 88]:

$$\begin{aligned} \vec{E}_i &= \vec{E}_0 e^{i\left(\vec{k}\bullet\vec{z}-\omega t\right)}, \\ \vec{H}_i &= \vec{H}_0 e^{i\left(\vec{k}\bullet\vec{z}-\omega t\right)}. \end{aligned} \qquad [1.21]$$

The subscripts (*i*), and latter on (*p*) and (*s*), are used to distinguish between the different contributions of the incident field, the field inside the particle and the field scattered by the particle in the surrounding medium, respectively. By definition, the scattering plane is the plane containing the wave vector of the incident wave (with $k = 2\pi m_2 / \lambda$) in the direction of the observer.

Each field can be decomposed into two components. One component is parallel (subscript: || or 2) to the scattering plane and the other is perpendicular (subscript: $\perp$ or 1) to this plane. The incident electrical field can be decomposed as follows:

$$\vec{E}_i = \left(E_{0\|}\vec{e}_{0\|} + E_{0\perp}\vec{e}_{0\perp}\right)e^{i\left(\vec{k}\bullet\vec{z}-\omega t\right)}. \quad [1.22]$$

The incident electrical field can be represented in a spherical coordinate system $(r,\theta,\phi)/\left(\vec{e}_r,\vec{e}_\phi,\vec{e}_\theta\right)$ given as follows [BOH 88]:

$$\begin{cases}\vec{e}_{\perp i} = \sin\phi\vec{e}_x - \cos\phi\vec{e}_y = -\vec{e}_\phi \\ \vec{e}_{\|i} = cos\phi\vec{e}_x + \sin\phi\vec{e}_y = \sin\theta\vec{e}_r + \cos\theta\vec{e}_\theta\end{cases} \quad \begin{cases}E_{\|i} = \cos\phi E_{xi} + \sin\phi E_{yi} \\ E_{\perp i} = \sin\phi E_{xi} - \cos\phi E_{yi}\end{cases}. \quad [1.23]$$

In the far-field (i.e. $kr \gg 1$, where r is the distance between the observer and the particle), the radial component of the electrical field scattered by the particle may be neglected:

$$\vec{E}_s \sim \frac{e^{ikr}}{-ikr}\vec{A} \quad \text{and} \quad \vec{e}_r \bullet \vec{E}_s \simeq 0 \quad \text{for } kr \gg 1. \quad [1.24]$$

Thus, the scattered field far from the particle surface may be written as [BOH 88]:

$$\begin{cases}\vec{E}_s = E_{s\|}\vec{e}_{s\|} + E_{s\perp}\vec{e}_{s\perp}, \\ \vec{e}_{s\|} \equiv \vec{e}_\theta, \ \ \vec{e}_{s\perp} \equiv -\vec{e}_\phi, \ \vec{e}_{s\perp} \times \vec{e}_{s\|} \equiv \vec{e}_r.\end{cases} \quad [1.25]$$

When the particle material is linear (and the incident wave has moderate amplitude), the amplitudes of the scattered and the incident fields are proportional to each other:

$$\begin{pmatrix}E_{s\|} \\ E_{s\perp}\end{pmatrix} = \frac{e^{i\left(\vec{k}-(\vec{r}-\vec{z})-\omega t\right)}}{-ikr}\begin{pmatrix}S_2 & S_3 \\ S_4 & S_2\end{pmatrix}\begin{pmatrix}E_{i\|} \\ E_{i\perp}\end{pmatrix}. \quad [1.26]$$

The elements $S_1, S_2, S_3, S_4 \in \mathbb{C}$ of the amplitude scattering matrix depend both on the direction angles (i.e. the scattering angle θ and the azimuthal angle ϕ) and the particle properties (shape, orientation and composition). In fact, equation [1.26] formally describes all the properties of the scattered field in the far-field.

Using the various polarizing elements (linear and circular polarizers) between the particles and a linear photodetector (i.e. the observer), several quantities of interest become accessible. In particular, the Stokes parameters, denoted by I_s, Q_s, U_s, V_s, can be expressed as follows:

$$\begin{pmatrix} I_s \\ Q_s \\ U_s \\ V_s \end{pmatrix} = \frac{1}{k^2 r^2} \begin{pmatrix} \left\langle E_{s\parallel} E_{s\parallel}^* + E_{s\perp} E_{s\perp}^* \right\rangle \\ \left\langle E_{s\parallel} E_{s\parallel}^* - E_{s\perp} E_{s\perp}^* \right\rangle \\ \left\langle E_{s\parallel} E_{s\perp}^* + E_{s\perp} E_{s\parallel}^* \right\rangle \\ i\left\langle E_{s\parallel} E_{s\perp}^* - E_{s\perp} E_{s\parallel}^* \right\rangle \end{pmatrix} = \begin{pmatrix} S_{11} & S_{12} & S_{13} & S_{14} \\ S_{21} & S_{22} & S_{23} & S_{24} \\ S_{31} & S_{32} & S_{33} & S_{34} \\ S_{41} & S_{42} & S_{43} & S_{44} \end{pmatrix} \begin{pmatrix} I_i \\ Q_i \\ U_i \\ V_i \end{pmatrix}, \qquad [1.27]$$

where $\langle\ \rangle$ represents a temporal average over a time period $1/\nu$. The matrix $S_{i=1-4,j=1-4}$ is referred to as the scattering matrix [BOH 88]:

$$\begin{aligned} S_{11} &= \frac{1}{2}\left(|S_1|^2 + |S_2|^2 + |S_3|^2 + |S_4|^2\right) \quad S_{12} = \frac{1}{2}\left(|S_2|^2 - |S_1|^2 + |S_4|^2 - |S_3|^2\right) \\ S_{21} &= \frac{1}{2}\left(|S_2|^2 - |S_1|^2 - |S_4|^2 + |S_3|^2\right) \quad S_{22} = \frac{1}{2}\left(|S_2|^2 + |S_1|^2 - |S_4|^2 - |S_3|^2\right) \end{aligned} \qquad [1.28]$$

$$\begin{aligned} S_{13} &= \mathrm{Re}\left\{S_2 S_3^* + S_1 S_4^*\right\} \quad S_{14} = \mathrm{Im}\left\{S_2 S_3^* - S_1 S_4^*\right\} \\ S_{23} &= \mathrm{Re}\left\{S_2 S_3^* - S_1 S_4^*\right\} \quad S_{24} = \mathrm{Im}\left\{S_2 S_3^* + S_1 S_4^*\right\} \\ S_{31} &= \mathrm{Re}\left\{S_2 S_4^* + S_1 S_3^*\right\} \quad S_{32} = \mathrm{Re}\left\{S_2 S_4^* - S_1 S_3^*\right\} \\ S_{41} &= \mathrm{Im}\left\{S_2 S_4^* - S_3^* S_1\right\} \quad S_{42} = \mathrm{Im}\left\{S_2 S_4^* - S_3 S_1^*\right\} \\ S_{33} &= \mathrm{Re}\left\{S_1 S_2^* + S_3 S_4^*\right\} \quad S_{34} = \mathrm{Im}\left\{S_2 S_1^* + S_4 S_3^*\right\} \\ S_{43} &= \mathrm{Re}\left\{S_1 S_2^* - S_3 S_4^*\right\} \quad S_{44} = \mathrm{Re}\left\{S_1 S_2^* - S_3 S_4^*\right\} \end{aligned} \qquad [1.29]$$

Only a few of the 16 elements of the scattering matrix are independent of each other [VAN 57]. Despite the apparent complexity of the preceding expressions, they can all be evaluated (at least in principle) by selecting the proper combination of the polarization state of the incident and the collected light [MIS 99, FUL 95].

For a particle illuminated by an unpolarized incident wave, the Stokes parameters for the scattered light reduce to the following terms:

$$\frac{I_s}{I_i} = S_{11}, \quad \frac{Q_s}{I_i} = S_{21}, \quad \frac{U_s}{I_i} = S_{31}, \quad \frac{V_s}{I_i} = S_{41}. \qquad [1.30]$$

In this case, S_{11} may be obtained by measuring the scattered intensity in one (or several) directions, depending on the polarization state of the scattered wave. S_{41} may be derived from the measurement of the intensities scattered by the particle when the incident wave is successively right-handed and left-handed circularly polarized. S_{12} is obtained in a rather similar way, but for a linearly polarized incident wave successively parallel and perpendicularly polarized.

The polarization state of the light scattered by most particles, other than spherical particles, is different from the polarization state of the illuminating wave. One of the most commonly used parameters for estimating this change is given as follows:

$$\delta = \sqrt{\left(S_{21}^2 + S_{31}^2 + S_{41}^2\right) / S_{11}^2}. \qquad [1.31]$$

Ellipsometric techniques aim to characterize the size and shape of particles by analyzing the corresponding Stokes parameters (or Muller matrix [BOH 88], see also Figure 1.19) [MIS 99, MAC 96, HON 06]. However, following this approach may be particularly difficult, or even impossible, under transient and non-stationary conditions.

1.2.4.2. *Cross-sections, symmetry parameters and radiation pressure*

The scattered intensity in any direction (θ,ϕ) and at a large distance r, from the observer, can be *formally* deduced from the scattering matrix and by calculating the Poynting vector [VAN 57]:

$$I_s(\theta,\phi) = I_i \frac{F(\theta,\phi)}{k^2 r^2}, \qquad [1.32]$$

where $F(\theta,\phi)$ is a dimensionless function describing the angular intensity distribution of the scattered light. The quantity $F(\theta,\phi)/k^2$ is homogeneous over the surface area. The total flux scattered by the particle in the surrounding media is equal to the flux of the incident wave through a reference surface denoted by C_5,

$$I_i C_s = \int_0^{2\pi}\int_0^{\pi} I_i \frac{F(\theta,\phi)}{k^2 r^2} d\Omega, \qquad [1.33]$$

where $d\Omega = \sin\theta d\theta d\phi$ is a differential solid angle in the spherical coordinate system. For a virtual sphere of radius $r = 1$ (see Figure 1.6(b)), equation [1.33] can be written as follows:

$$C_s = \frac{1}{k^2} \int_0^{2\pi} \int_0^{\pi} F(\theta,\phi)\, d\Omega. \qquad [1.34]$$

The surface area C_a related to the flux absorbed by the particle, may be defined in the same way. The global efficiency of the particle, in terms of scattering and absorption, is associated with a characteristic surface C_e such that:

$$C_e = C_s + C_a. \qquad [1.35]$$

The quantities C_e, C_s and C_a (also denoted by $C_{\text{ext}}, C_{\text{sca}}$ and C_{abs} or $\sigma_{\text{ext}}, \sigma_{\text{sca}}$ and σ_{abs}, respectively) are the *extinction* (subscript: *e*), *scattering* (subscript: *s*) and the *absorption* (subscript: *a*) cross-sections of the particle, respectively. The cross-sections depend *a priori* on the particle size, shape, orientation and composition, as well as the polarization state and the wavelength of incident wave. A transparent particle has no absorption (i.e. $k_m = 0$), so $C_a = 0$. To quantify the relative efficiency of a particle of radius a, in terms of extinction, scattering and absorption of the incident wave, the cross-sections are normalized by the particle 2D projected surface area:

$$Q_e = \frac{C_e}{\pi a^2}, \quad Q_s = \frac{C_s}{\pi a^2}, \quad Q_a = \frac{C_a}{\pi a^2}. \qquad [1.36]$$

The extinction coefficient Q_e usually differ significantly from one (Figures 1.7 and 1.13 and section 1.3.1.4). In other words, particles can scatter and absorb much more (or much less) electromagnetic energy than would do a geometrical object.

Figure 1.7. *Schematic of the extinction cross-section of a particle of radius a, depending on the point of view adopted on the nature of light: a) mechanical (geometrical optics) or b) physical (wave optics)*

Light extinction spectrometry uses the latter feature to estimate the size distribution and concentration of nano- and microparticle systems (section 2.7).

As will be shown later, the intensity scattered by particles is highly dependent on the observation direction. An *asymmetry factor*, g (also denoted by $\langle \cos\theta \rangle$), may be used to quantify the anisotropy of the scattering diagrams:

$$g = \langle \cos\theta \rangle = \frac{\int_{4\pi} I_s(\theta,\phi) \cos\theta d\Omega}{\int_{4\pi} I_s(\theta,\phi)\, d\Omega}, \qquad [1.37]$$

where the right-hand side of equation [1.37] is a normalized angular averaging of the particle scattering diagram with respect to the optical axis of the incident wave. This factor tends to unity for particles that are large compared to the wavelength (i.e. due to forward diffraction) and tends to zero for small particles (i.e. Rayleigh scattering).

The momentum of a photon is equal to $h\nu / c$, where $h \approx 6.63 \times 10^{-34}$ J s is Planck's constant. In linear optics, a photon absorbed by a particle, transfers all its energy (i.e. heating) and momentum (i.e. acceleration) to the particle. But, there is no energy transfer and only a partial momentum transfer when the photon is refracted by a transparent particle. The particle *radiation pressure* efficiency coefficient Q_{pr} and *cross-section* C_{pr} may be obtained by writing a momentum balance along the optical axis of the incident wave:

$$Q_{pr} = C_{pr} / \pi a^2 = Q_e - gQ_s. \qquad [1.38]$$

Note that with Gaussian laser beams, the radiation pressure also has a lateral component and the main component (along the beam axis) may be negative (due to an attractive force) (e.g. [ASH 70] [REN 96]). Radiation pressure is now widely used to make optical tweezers, for manipulating micrometric particles or biological cells.

1.3. Methods using separation of variables

1.3.1. *Lorenz–Mie (or Mie) theory*

Mie theory or LMT [MIE 08] is the fundamental scattering theory located in many fields and for most optical particle sizing instruments (see Chapter 2). The theory provides an exact solution for the scattering of a harmonic electromagnetic plane wave by a spherical, homogeneous, isotropic, linear and non-magnetic particle located in a non-absorbing medium (this type of particle is sometimes called a Mie scattered). The theory solves the wave equation in spherical coordinates, using the

method of separation of variables and with the appropriate boundary conditions. In the following sections, we summarize the main steps and results of this theory. The reader can find more details on this theory in the excellent books by Bohren and Huffman [BOH 88], Kerker [KER 69] and Stratton [STR 10].

1.3.1.1. *Wave equation and separation of variables*

An electromagnetic wave must satisfy the following two equations to be a solution of Maxwell's equations, with $k^2 = \omega^2 \varepsilon \mu$:

$$\begin{cases} \nabla^2 \vec{E} + k^2 \vec{E} = 0, \\ \nabla^2 \vec{H} + k^2 \vec{H} = 0. \end{cases} \quad [1.39]$$

The problem above can be reduced to solving a single scalar wave equation:

$$\nabla^2 \psi + k^2 \psi = 0, \quad [1.40]$$

where ψ is a function constructed from the spherical harmonic functions, $\vec{M}_{\text{Sph}} = \vec{\nabla} \times (\vec{r}\psi)$ and $\vec{N}_{\text{Sph}} = \left(\vec{\nabla} \times \vec{M}_{\text{Sph}}\right)/k$. The scalar wave equation may be written in spherical coordinates:

$$\frac{1}{r^2}\frac{\partial}{\partial r}\left(r^2 \frac{\partial \psi}{\partial r}\right) + \frac{1}{r^2 \sin\theta}\frac{\partial}{\partial \theta}\left(\sin\theta \frac{\partial \psi}{\partial \theta}\right) + \frac{1}{r^2 \sin\theta}\frac{\partial^2 \psi}{\partial \phi^2} + k\psi^2 = 0. \quad [1.41]$$

In the method of separation of variables, a solution with the following form is sought:

$$\psi(r, \theta, \phi) = R(r)\Theta(\theta)\Phi(\phi), \quad [1.42]$$

where R, Θ and Φ are independent functions. Substituting equation [1.42] into equation [1.41] results in a system of three equations with m and n as separation constants:

$$\begin{cases} \dfrac{d^2\Phi}{d\phi^2} + m\phi^2 = 0, & [1.43a] \\ \dfrac{1}{\sin\theta}\dfrac{d}{d\theta}\left(\sin\theta \dfrac{d\Theta}{d\theta}\right) + \left[n(n+1) - \dfrac{m^2}{\sin^2\theta}\right] = 0, & [1.43b] \\ \dfrac{d}{dr}\left(r^2 \dfrac{dR}{dr}\right) + \left[k^2 r^2 - n(n+1)\right] R = 0. & [1.43c] \end{cases}$$

For even (*e*) and odd (*o*) orders, the solutions of equation [1.43a] have the form:

$$\begin{cases} \Phi_e = \cos(m\phi), \\ \Phi_o = \sin(m\phi). \end{cases} \quad [1.44]$$

The solutions of equation [1.43b] are the associated Legendre functions, that is $P_n^m(\cos\theta)$. The solutions of equation [1.43c] are derived by changing variables as $\rho = kr$ and introducing the function $Z = R\sqrt{\rho}$, so that, the radial equation [1.43c] can be rewritten as:

$$\rho \frac{d}{d\rho}\left(\rho \frac{dZ}{d\rho}\right) + \left[\rho^2 - \left(n - \frac{1}{2}\right)^2\right] Z = 0. \quad [1.45]$$

The linearly independent solutions of equation [1.45] are spherical Bessel functions of the first type J_ν and the second type Y_ν of half-integer order $\nu = n + 1/2$ [ABR 65]:

$$j_n(\rho) = \sqrt{\frac{\pi}{2\rho}} J_{n+1/2}(\rho), \quad y_n(\rho) = \sqrt{\frac{\pi}{2\rho}} Y_{n+1/2}(\rho). \quad [1.46]$$

The solutions given above are related to Bessel functions of the third order (or Hankel functions),

$$k_n^{(1)}(\rho) = j_n(\rho) + iy_n(\rho), \quad k_n^{(2)}(\rho) = j_n(\rho) - iy_n(\rho). \quad [1.47]$$

The global solutions take the following form:

$$\begin{aligned} \psi_{emn} &= \cos(m\phi) P_n^m(\cos\theta) z_n(kr), \\ \psi_{omn} &= \sin(m\phi) P_n^m(\cos\theta) z_n(kr). \end{aligned} \quad [1.48]$$

1.3.1.2. *Field solutions and continuity constraints*

The various functions j_n, y_n, $k_n^{(1)}$, $k_n^{(2)}$ are not defined mathematically for all space (e.g. $y_n(r) \to \infty$ as $r \to 0$) [ABR 65]. Thus, $y_n(r)$ cannot be used to describe the incident and internal fields. By contrast, $y_n(r)$ can be used to describe the scattered field because the amplitude of the outgoing spherical wave field must

decrease as $1/r$ when $r \to +\infty$. Similar considerations produce the following expressions for the internal field and the far-field scattered field:

$$\begin{cases} E_p = \sum_{n=1}^{\infty} E_n \left(c_n M_{o1n}^{(1)} - i d_n N_{e1n}^{(1)} \right), \\ H_p = \dfrac{-k_p}{\omega \mu_p} \sum_{n=1}^{\infty} E_n \left(d_n M_{e1n}^{(1)} - i c_n N_{o1n}^{(1)} \right); \end{cases}$$
$$\begin{cases} E_s = \sum_{n=1}^{\infty} E_n \left(i a_n N_{e1n}^{(3)} - b_n M_{o1n}^{(3)} \right), \\ H_s = \dfrac{k}{\omega \mu} \sum_{n=1}^{\infty} E_n \left(i b_n N_{o1n}^{(3)} - a_n M_{e1n}^{(3)} \right); \end{cases} \quad [1.49]$$

with $E_n = i^n E_0 (2n+1) / n(n+1)$.

The fields in the preceding expressions are expressed as infinite linear combinations of spherical harmonics weighted by complex coefficients. a_n and b_n are usually referred to as external scattering coefficients, and c_n and d_n as internal scattering coefficients. The conditions for the continuity of the tangential components of the electromagnetic fields at the particle surface $(r = a)$ give:

$$\begin{cases} E_{i\theta} + E_{s\theta} = E_{p\theta} \\ H_{i\theta} + H_{s\theta} = H_{p\theta} \end{cases}, \quad \begin{cases} E_{i\phi} + E_{s\phi} = E_{p\phi} \\ H_{i\phi} + H_{s\phi} = H_{p\phi} \end{cases}. \quad [1.50]$$

Combining equations [1.49] and [1.50] allows us to fully determine the external scattering coefficients:

$$a_n = \frac{m\psi_n(mx)\psi'_n(x) - \psi_n(x)\psi'_n(mx)}{m\psi_n(mx)\xi'_n(x) - \xi_n(x)\psi'_n(mx)},$$
$$b_n = \frac{\psi_n(mx)\psi'_n(x) - m\psi_n(x)\psi'_n(mx)}{\psi_n(mx)\xi'_n(x) - m\xi_n(x)\psi'_n(mx)}, \quad [1.51]$$

where $x = \pi D / \lambda$ is the particle size parameter (also denoted as α), $\psi_n(\rho) = \rho j_n(x)$ and $\xi_n(\rho) = \rho h_n^{(1)}(\rho)$ are the Ricatti–Bessel functions, and the symbol $()'$ denotes the first derivative with respect to the argument of the function.

The classical procedure for computing the external scattering coefficients [ZHA 96, BAR 90] is to introduce the logarithmic derivatives of the Riccati–Bessel functions in equation [1.51]:

$$D_n^{(1)}(\rho)=\frac{\psi_n'(\rho)}{\psi_n(\rho)},\quad D_n^{(2)}(z)=\frac{\xi_n'(\rho)}{\xi_n(\rho)},\quad D_n^{(3)}(\rho)=\frac{\psi_n(\rho)}{\xi_n(\rho)}. \qquad [1.52]$$

These derivatives may be computed using upward or downward recurrences ([BOH 88, ZHA 96]), so that equation [1.51] becomes:

$$\begin{aligned} a_n &= D_n^{(3)}\frac{mD_n^{(1)}(x)-D_n^{(1)}(mx)}{mD_n^{(2)}(x)-D_n^{(1)}(mx)},\\ b_n &= D_n^{(3)}\frac{D_n^{(1)}(x)-mD_n^{(1)}(mx)}{D_n^{(2)}(x)-mD_n^{(1)}(mx)}. \end{aligned} \qquad [1.53]$$

1.3.1.3. *Solutions for phase functions and cross-sections*

The general formulations introduced in section 1.2.4 can now be expressed more explicitly for the scattered fields ($kr \gg \lambda$) ([BOH 88, KER 69, STR 10]):

$$\begin{pmatrix} E_{s\|} \\ E_{s\perp} \end{pmatrix}=\frac{e^{i(k(r-z)-\omega t)}}{-ikr}\begin{pmatrix} S_2 & 0 \\ 0 & S_1 \end{pmatrix}\begin{pmatrix} E_{i\|} \\ E_{i\perp} \end{pmatrix}, \qquad [1.54]$$

with, for the where the amplitude functions S_1 and S_2,

$$S_1=\sum_{n=1}^{\infty}\frac{(2n+1)}{n(n+1)}\left(a_n\pi_n+b_n\tau_n\right),\quad S_2=\sum_{n=1}^{\infty}\frac{(2n+1)}{n(n+1)}\left(a_n\tau_n+b_n\pi_n\right); \qquad [1.55]$$

the angular functions,

$$\pi_n=\frac{P_n^1}{\sin\theta},\qquad \tau_n=\frac{dP_n^1}{\sin\theta}; \qquad [1.56]$$

and the cross-sections,

$$C_s=\frac{2\pi}{k^2}\sum_{n=1}^{\infty}(2n+1)\left(|a_n|^2+|b_n|^2\right),\quad C_e=\frac{2\pi}{k^2}\sum_{n=1}^{\infty}(2n+1)\,\mathrm{Re}\{a_n+b_n\}. \qquad [1.57]$$

REMARKS.–

– For a spherical particle (as well as an infinite circular cylinder under normal illumination), the diagonal terms of the scattering matrix are zero, that is $S_3 = S_4 = 0$. Spherical particles are said to conserve the polarization.

– The scattered intensity is proportional to $I_1 = I_{s\perp} \propto \left|S_1 S_1^*\right|$ or $I_2 \equiv I_{\parallel} \propto \left|S_2 S_2^*\right|$ for perpendicular or parallel polarization, respectively.

– The theoretically infinite expansion series can be numerically truncated, when

$$n > n_{stop} = x + 4x^{1/3} + 2. \qquad [1.58]$$

Indeed, when n exceeds the size parameter x, the coefficients a_n, b_n decrease rapidly with r [BOH 88]. This behavior may be understood via the localization principle [VAN 57], whereby terms of order n in the expansion correspond to "rays" that impact the particle surface at a distance r_n from its center:

$$r_n = \lambda\left(n + 1/2\right)/\left(2\pi\right). \qquad [1.59]$$

– For particles significantly larger than the wavelength, $D/\lambda \gg 1$, the extinction coefficients always tend to two.

Over the last 30 years, LMT has been generalized to cases where the incident wave is an electromagnetic beam of arbitrary shape: the important practical applications are for circular [GOU 88, BAR 89] and elliptical Gaussian beams [REN 93]. LMT has been similarly generalized to various scatterers: coated and multilayered spherical or cylindrical particles (e.g. [WU 91, ONO 95, ONO 04, WU 98]), spheres with spherical inclusions [BOR 94], spheroid particles [BAR 02, XU 07, COO 91], etc.

1.3.1.4. *Numerical examples*

The electromagnetic fields inside a particle are not directly measurable, but computing these fields facilitates an understanding of some features of scattered field patterns[4]. Figure 1.8 shows the electromagnetic intensity distribution inside and around (a) a water droplet in air and (b) an air bubble in water. For the purposes of illustration, the surface of the particles is demarcated by a circle. Surprisingly, some of the patterns for a droplet (i.e. a refracting particle) are analogous to those observed when a river flows around the pier of a bridge. However, patterns such as

4 Certain laser-induced fluorescence diagnostics use these electromagnetic fields as input conditions (see Chapter 3).

the focusing spot or rainbow rays do not conform to this trivial analogy. Some of the regular patterns and variations of the electromagnetic intensity are a consequence of caustics [DES 72], interferences [VAN 57], and morphology-dependent resonances (MDRs; e.g. [CHY 78]).

Figure 1.8. *Electromagnetic intensity inside and outside a spherical particle illuminated by a plane harmonic wave: a) a water droplet in air (D = 40 μm, m = 1.332, perpendicular polarization with λ = 0.6326 μm); and b) an air bubble in water (D = 100 μm, m = 0.75, by parallel polarization with λ = 0.532 μm)*

Figure 1.9 compares the scattering diagrams (for a punctual detector located at infinity) of a water droplet whose diameter increases as $D/\lambda = 0.01,\ 0.1,\ 1,\ 10$ and 100. Clearly, the asymmetry and complexity (which manifests as oscillations or Mie's lobes) of the scattering diagrams increase drastically with the ratio D/λ. Some phenomena, such as the rainbow, are more contrasted depending on the polarization state of the incident wave, as well as the ratio D/λ.

Figure 1.10 shows the scattering diagrams of particles with diameter D = 50 μm and different relative refractive index ($m = m_1/m_2$), illuminated by a parallel or perpendicular plane wave with λ_0 = 0.532 μm. The different cases correspond to the particle as a water droplet (m_1 = 1.334), a light-oil droplet (m_1 = 1.510), an air bubble (m_1 = 1.00) and a tungsten bead ($m_1 = 3.49 + 2.71i$) in air (m_2 = 1.00), water (m_2 = 1.334) and light oil (m_2 = 1.510). Among the various interesting features, we can remark that the water droplet in oil scatters light such as an optical bubble (i.e. the near-critical-angle scattering phenomena is clearly observable); the metallic bead produces very smooth scattering diagrams (i.e. the refracted rays do not really penetrate the core of the particle), and the oil droplet scatters less light overall in water than in air (i.e. the refractive index contrast is lower).

Figure 1.9. *Scattering diagrams of water droplets in air, λ = 0.6326 μm and m_1 = 1.332, for a) perpendicular and b) parallel polarization*

Figure 1.11 uses both linear and logarithmic intensity scales to show the evolution of the scattered intensity at $\theta = 30°$ by increasing the diameter of a water droplet. With the linear scale, it is clear to see that for $D \gg \lambda$, the overall scattered intensity increases with the droplet size, with strong oscillations. The second graph shows that the scattering behavior can be separated into three size ranges: when $D \ll \lambda$, the scattered intensity evolves as $I(\theta) \propto D^6$ (this scattering regime is called the Rayleigh scattering regime; see section 1.4.1); when $D \gg \lambda$, it evolves as $I(\theta) \propto D^2$ (this scattering regime is referred to as the Mie scattering regime); and when $D \sim \lambda$, the behavior of the scattered intensity is unclear and characteristic of a transient scattering regime.

The internal structure of particles, as well as the shape and size aperture of the collection optics, may also greatly influence their scattering and detectability properties. Figure 1.12 shows scattering diagrams for various particles when the light scattered by the particles is collected by a circular detector of an aperture angle ±0.357° or ±3.57° (corresponding to collection optics of 5 or 50 mm in diameter, located at 400 mm from the particles). To perform these calculations, the optical apertures were meshed to evaluate the properties of the electromagnetic scattered fields at each mesh node (see section 2.4.2.2). Figure 1.12(a) compares the results obtained for diethyl-hexyl-sebacate (DEHS, an oily liquid used to seed gas

flows[5]) droplets in air. The droplet size distribution is either monodisperse or polydisperse (i.e. using a normal size distribution with mean $\bar{D}$ and standard deviation σ_D). Increasing the detector aperture angle by a factor of ten increases the overall collected intensity by a factor of 100; a larger collection angle also tends to smooth the oscillations of the scattering diagrams.

Figure 1.10. *Influence of the relative refractive index on the scattering properties of a spherical particle with diameter D = 50 μm, illuminated by a linear polarized and harmonic plane wave with λ = 0.532 μm*

Figure 1.12(b) shows scattering intensity diagrams for particles used to seed liquid flows[6]: solid glass beads (with a specific density of 2.5 and a glass refractive index of 1.52); hollow glass beads with an air core (with a specific density of 1.10, a ratio of glass/air radii of 0.83 and an air refractive index of 1.00); and silver-coated hollow glass beads with an air core (with an effective density of 1.4, a ratio of glass/air radii of 0.76, a refractive index of 0.129 + 3.19*i* and a coating thickness of 5 nm) [ONO 95, ONO 96a]. Clearly, the coating improves the detectability of the seeding particle when the detection optics are set above $\theta \sim 35 - 40°$ (and more particularly for $\theta = 90°$, the typical angle for the PIV technique[5]). For angles

5 See [BOU 12] by the same authors.
6 See [BOU 12] by the same authors.

below $\theta \sim 35 - 40°$ (a rather common angle for the laser Doppler velocimetry (LDV) technique[7]), the coating has an adverse effect. For $\theta = 180°$, the coating provides almost no improvement in detectability.

Figure 1.11. *Evolution of the intensity scattered by water droplets in the scattering direction $\theta = 30°$ (i.e. $\varphi = 0°$) for $\lambda = 0.532$ μm*

Figure 1.12. *Scattering diagrams obtained with circular detectors and for various seeding particles: a) DEHS droplets in air and b) glass beads in water (i.e. solid, hollow with an air core, and hollow with an air core and a silver coating), $\lambda_0 = 532$ nm*

Figure 1.13 shows the evolution of the extinction, scattering and absorption coefficients for droplets composed of a water–India ink dilution. The extinction coefficient increases rapidly with size up to a value of ≈ 3.94 (i.e. the corresponding droplet scatters and absorbs four times more energy than an object of the same geometrical size). The extinction coefficient decreases and tends to two when

7 An effective refractive index may also be defined for some particulate medium (e.g. [NIK 81, BOH 88, DOI 01b].

$D \gg \lambda$. The absorption coefficient increases continuously (see section 1.2.2.1), accompanied by some small- and high-frequency oscillations.

Figure 1.13. *Evolution of the extinction, scattering and absorption coefficients for droplets composed of a water–India ink dilution (considered here to be a homogeneous liquid with Y = 25%, m = 1.334 + 2.5 10^{-3}i and λ = 0.532 μm)*

1.3.2. *Debye and complex angular momentum theories*

1.3.2.1. *Debye theory*

Debye theory [DEB 09] shows that certain groups of terms in the infinite expansion series provided by LMT theory can be interpreted as contributions of waves that are partially reflected or refracted inside or outside the particle. By analogy with geometrical optics, reflection and transmission coefficients are introduced for these partial waves. Figure 1.14 presents a schematic of the Debye decomposition method, as reformulated by Hovenac and Lock [HOV 92]. The particle and the surrounding medium are denoted by superscripts (1) and (2), respectively, using

– $R_n^{(22)}$ for the reflection coefficient of the wave that is partially reflected (via specular reflection and diffraction) by the particles toward the external medium (the subscript n refers to the order of the LMT expansion);

– $T_n^{(21)}$ for the transmission coefficient of the waves that are partially transmitted within the particle;

– $R_n^{(11)}$ for the reflection coefficient of the partial internal waves partially reflected by the inner surface of the particle;

– $T_n^{(12)}$ for the transmission coefficient of the internal waves partially transmitted toward the external medium.

Figure 1.14. *Schematic of the Debye decomposition method*

The external scattering coefficients of the partial waves of order p and expansion order n read as:

$$\left.\begin{matrix} a_n(p) \\ b_n(p) \end{matrix}\right\} = \frac{1}{2}\begin{cases} 1 - R_n^{(22)}, \text{ for } p = 0; \\ -T_n^{(21)}\left(R_n^{(11)}\right)^{p-1} T_n^{(12)}, \text{ for } p \geq 1; \end{cases} \quad [1.60]$$

where $p = 0$ contribution corresponds to the diffracted and reflected waves (section 1.7.1); $p = 1$, to single refracted waves; $p = 2$, to the partial waves undergoing one internal reflection prior to being scattered (i.e. the first rainbow); $p = 3$, to the partial waves that experiences two internal reflections prior to being scattered (i.e. second rainbow) and so forth [HOV 92]. A strict equivalence exists between the external scattering coefficients derived by the LMT and the Debye theory when $p \to \infty$:

$$\begin{Bmatrix} a_n \\ b_n \end{Bmatrix}_{\text{LMT}} = \frac{1}{2}\left[1 - R_n^{(22)} - \sum_{p=1}^{\infty} T_n^{(21)}\left(R_n^{(11)}\right)^{p-1} T_n^{(12)}\right], \quad [1.61]$$

$$\text{with } \alpha = \begin{cases} m \\ 1 \end{cases}, \beta = \begin{cases} 1 \\ m \end{cases} \text{ and } \mathrm{p} \to \infty.$$

The Debye series can help us to better understand and validate certain hypotheses for geometrical or physical optics models [ONO 05]. As an example, Figure 1.15 presents the evolution of the normalized scattering diagrams of E-glass fibers (which have mechanical reinforcement applications) for two angular domains and various fiber diameters [ONO 04b]. The comparison of the forward scattering

pattern produced by waves $p = 0$ (which would be more or less predicted by Fraunhofer theory) with the full scattering pattern (which takes all contributions into account) shows the strong influence of the higher order contributions on the so-called diffraction. In a similar way, Figure 1.16(a) compares the partial scattering diagrams of a water droplet calculated with pure geometrical optics (i.e. without interferences), with predictions of the Debye theory. Figure 1.16(b) shows the result of interference between various partial waves.

Figure 1.15. *Iso-map levels of the logarithm of the normalized intensity scattered by E-glass fibers (for diameters ranging from 0.1 up to 30 µm) corresponding to partial waves and full scattering for a) near-forward and b) near-backward angular domains [ONO 04, LEN 04]*

Figure 1.16. *Comparison of the scattering diagrams predicted by pure geometrical optics and Debye theory for a water droplet for a) a single scattering process, and b) two scattering processes (p = 0 and p = 1; p = 0 and p = 2) [ONO 04]*

1.3.2.2. *Complex angular momentum theory*

The description of the physical and mathematical background of this electromagnetic theory goes far beyond the scope of this brief introduction to the light scattering properties of small particles. However, in a few words, let us say that the complex angular momentum (CAM) theory is based on the description of the scattering particle as an electromagnetic potential (Debye potential) and on the localization approximation principle (equation [1.58]). The general form of CAM theory requires as many (and perhaps more) computational resources than LMT. Nevertheless, various useful[8] quasi-analytic and computationally cost-effective approximations have been derived for the scattering of droplets (in the vicinity of the first rainbow angle) and bubbles (in the vicinity of the critical angle). If CAM approximation provides rather satisfactory results for the first rainbow angle scattering [NUS 92, SAE 06], the practical interest of the first-order approximation derived for the near-critical-angle scattering of large bubbles [FIE 91] appears to be more limited [KRZ 09, ONO 09a]. The reader is referred to the pioneering works of Nussensweig [NUS 92] and Fiedler-Ferrari *et al*. [FIE 91] for more details on this exciting but complex theory.

1.4. Rayleigh theory and the discrete dipole approximation

1.4.1. *Rayleigh theory*

Rayleigh theory is an asymptotic theory that describes the elastic scattering of a harmonic plane wave by a particle much smaller than the incident wavelength

8 See [BOU 12] by the same authors.

$\left(D/\lambda \ll 1\right)$ [BOH 88]; that is, the electromagnetic field gradient on the particle surface is negligible (quasi-static field approximation). The particle-induced dipole moment is given by:

$$P=\varepsilon_1\left(\lambda\right)\alpha E_i, \qquad [1.62]$$

where $\varepsilon_1(\lambda)$ and α are the particle material electrical permittivity and the particle polarizability, respectively. For a spherical particle of radius a and volume $V = 4\pi a^3/3$ in a medium of electrical permittivity $\varepsilon_2(\lambda)$, its polarizability is $\alpha = 3V[\varepsilon_1 - \varepsilon_2]/[\varepsilon_1 + 2\varepsilon_2]$ [VAN 57] or, in terms of the relative refractive index:

$$\alpha = \frac{\tilde{m}^2 - 1}{\tilde{m}^2 + 2} a^3 . \qquad [1.63]$$

The induced dipole moment radiates light, immersed in an oscillating field (i.e. the particle scatters a fraction of the incident wave). The following expressions are obtained for the scattered intensities and the cross-sections:

$$\begin{pmatrix} I_{s//} \\ I_{s\perp} \end{pmatrix} = \frac{k^4}{2r^2} \begin{pmatrix} \cos^2\theta & 0 \\ 0 & 1 \end{pmatrix} \begin{pmatrix} I_{i//} \\ I_{i\perp} \end{pmatrix}, \qquad [1.64]$$

$$\begin{aligned} C_s &= \frac{8}{3}\pi k^4 \left|\alpha\right|^2 = \frac{2^7\pi^5}{3}\frac{a^6}{\lambda^4}\left|\frac{\tilde{m}^2-1}{\tilde{m}^2+2}\right|^2, \\ C_a &= -4\pi k \,\mathrm{Im}\left\{\alpha\right\} = -8\pi^2 \frac{a^3}{\lambda}\,\mathrm{Im}\left\{\frac{\tilde{m}^2-1}{\tilde{m}^2+2}\right\}, \end{aligned} \qquad [1.65]$$

where k is the modulus of the wave vector and r is the distance between the observer (in the far-field) and the particle. For an unpolarized incident wave, the scattered intensity is equal to the average value of the two main polarization components: $I_s = (I_{s//} + I_{s\perp})/2$ (see Figure 1.17).

The following are the key results of this theory:

– The perpendicular scattering component $I_{s\perp}$ is isotropic, whereas the parallel component totally vanishes at $\theta = 90°$. A small particle illuminated by a parallel polarized beam is thus virtually undetectable; that is, the parallel polarization component must be avoided when the PIV[1] technique is applied to nanoparticle systems.

– The scattered intensity shows an overall scaling $I \propto \lambda^{-4}$. This proportionality relation was first used to explain why the sky is blue (i.e. short wavelengths from the

Sun are preferentially scattered by molecules over longer wavelengths). Note that the white color of the clouds or a glass of milk (droplets with $a > \lambda$) is due to Mie scattering ($I \propto \lambda^{-2}$).

– The scattered intensity increases with the particle radius as $I \propto a^6$ (whereas in the Mie scattering regime, $a \gg \lambda$, the increased intensity only scales as $I \propto a^2$).

– The scattering cross-section ($C_s \propto a^6$) increases much more rapidly than the absorption cross-section ($C_a \propto a^3$). In other words, regarding extinction, absorption of small absorbing particles dominate over their scattering efficiency (e.g. soot that emits light too [MIC 87]).

– The Rayleigh theory is the basis of other asymptotic theories such as the Rayleigh–Gans and the Rayleigh-Debye-Gans theories. The latter theory is used to model the scattering properties of objects with more complex shapes within the limit, where $kD|m - 1| \ll 1$ and $|m - 1| \ll 1$ (e.g. biological cells or dilute aggregates) [BOH 88, SOR 01, FAR 96, OUF 08, MRO 12].

Figure 1.17. *Rayleigh theory: scattering diagrams of a water droplet in air ($D = 0.01$ μm and $m = 1.332$) where the droplet diameter is much smaller than the incident wavelength ($\lambda_0 = 0.5$ μm)*

1.4.2. *Discrete dipole approximation*

This numerical method discretizes an arbitrarily shaped particle into N elementary dipoles of radius $a \ll \lambda$ and polarizability α [DRA 94]. The particle scattering properties are then computed by summing the contribution of all the dipoles and interactions. A large number of dipoles are necessary to obtain satisfactory results (several thousands to millions of dipoles are needed to capture

some resonance phenomena), and substantial computational resources are required (CPU, memory and disk space) [DRA 10]. As a result, and due to some other basic limits and numerical instabilities, this method is limited to objects with very small size parameters and a moderate refractive index (e.g. $\left|\tilde{m}kx\right| \leq 0.25$ and $\left|\tilde{m}-1\right| < 2$, respectively) [DRA 10]. However, this method makes it possible to calculate the scattering, absorption or radiation properties of particles with very complex shapes (see Figure 1.18). Furthermore, it is not necessary to develop a new mathematical model for each new particle shape; we must only provide an adequate mesh. The application range and the available codes [DRA 10, SCA 10] for this technique are also continuously increasing with improvements in computer capabilities.

Figure 1.18. *Particle shapes that can be accommodated by analytical, semi-analytical and numerical light scattering models or theories: a)–c) homogeneous or multilayered spheres, spheroids and cylinders, d) Tchebychev particles, e) neighboring spheres, f) sphere in the vicinity of a dielectric plane surface, g) virtually any meshed object and h) aggregates of spheres*

1.5. The T-matrix method

The T-matrix method was first introduced by Waterman [WAT 65] to calculate the scattering of an electromagnetic wave by a homogeneous, non-spherical particle. The T-matrix is a transformation matrix relating to the electromagnetic fields scattered by a complex object (such as a particle and particulate systems) with the incident field. As in LMT, the scattered, internal and incident fields are expanded in linear combinations of spherical vector wave functions [MIS 99]. There are different ways of computing the transformation matrix [MIS 02]. The null-field method, for instance, relies on the Schelkunoff equivalence principle: the electromagnetic fields outside a virtual sphere S, circumscribing the scattering object, can be expressed as surface integrals involving only the tangential components of the fields on the surface of S. The integrals vanish inside the volume defined by this surface. An integral representation of the scattered field is derived from the boundary conditions for the tangential field components on the surface of the scattering object, in terms of the tangential components of the internal fields on the surface of the scattering

object. A similar procedure is used to derive expressions for the incident field. The orthogonality of the spherical vector wave functions on spherical surfaces enables the determination of an expression for the T-matrix.

Generally speaking, T-matrix codes that are available online are limited to rather small particles $x \leq 5 \sim 40$ [SCA 10, MIS 04]. The maximum size parameter that can be calculated also depends on the particle (or particulate system) shape and refractive index. However, these codes allow the calculation of scattering properties of complex- shaped particles and particulate systems (see Figures 1.18(a)–(f)) [MIS 07, MIS 98, DOI 01a, MAC 96, AUG 07]). The T-matrix method may be used, for instance, to model the scattering properties of aggregates of nanoparticles encountered in colloidal suspensions [SOR 01, BUS 02], aerosols [ONO 12], combustion systems [FAR 96, OUF 08] or dusty plasmas [ONO 09b, ONO 11]). As an example, Figure 1.19(a) compares the extinction coefficient, the scattering diagrams and the linear polarization rate ($P = -S_{12}/S_{11} = (S_1 - S_2)/(S_1 + S_2)$) of three particles with the same mass diameter (section 1.2.2.1): a homogeneous sphere, a spheroid and a compact hexagonal aggregate of nanospheres [ONO 11, MRO 12, WOŹ 12].

The T-matrix is also a powerful approach for modeling the scattering and absorption properties of fractal aggregates of nanospheres (e.g. soots and colloidal agglomerates). The latter may be built using a diffusion-limited aggregation model [SOR 01, BUS 02, WOŹ 12] and the so-called "Fractal equation" [FOR 79]:

$$n_p = k_f \left(R_g / r_p \right)^{D_f}, \qquad [1.66]$$

where n_p and r_p represent the number and the radius of nanoparticles within the aggregate, respectively; R_g and D_f are the radius of gyration and the fractal dimension of the aggregate, respectively, and k_f is a prefactor or compacity factor [SOR 01]. As an illustration, Figure 1.20 shows three aggregates with the same volume radius, $R_v = r_p n_p^{1/3} \approx 6.69$, with $n_p = 300$, $r_p = 1$ and $k_f = 1.593$, but different fractal dimensions and radii of gyration: a) $D_f = 2.00$, $R_g = 13.73$; b) $D_f = 2.45$, $R_g = 9.69$; and c) $D_f = 2.85$, $R_g = 6.30$.

Figure 1.19(b) presents the averaged scattering diagrams of carbonaceous fractal aggregates (i.e. for 50 nearly identical randomly oriented aggregates). This scattering diagram, in log–log scale versus the scattering vector $q = 2k \sin\left(\theta / 2\right)$, is typical for fractal aggregates. Also called the optical structure factor, this diagram exhibits three distinct asymptotic behaviors related to the Guinier, Fractal and Porod regions [GUI 95, POR 51, SOR 01, FAR 96, LIU 08]. The fractal dimension of these aggregates can be estimated by analyzing the power law decay of the scattered

intensity in the fractal zone [SOR 01], whereas their mean radius of gyration can be deduced by analyzing the Guinier region (small angle scattering region). From the analysis of the Porod region, the size parameter of monomers may be estimated. However, the Porod region is rarely distinct with visible photons. X-rays or neutrons diagnostics [GUI 95] offer a good alternative to solve the latter problem but they are rarely applicable to the in situ characterization of particles encountered in most mechanical engineering problems.

Figure 1.19. *3D rendering of different fractal aggregates of spherical particles [WOŹ 12]*

Figure 1.20. *a) Extinction coefficient, scattering and linear polarization diagrams for three particles with the same mass diameter but different shapes [ONO 09b]; b) logarithm of the intensity scattered by a fractal particle (with $D_f = 2.00$) versus the logarithm of the scattering vector for perpendicular polarization [ONO 11, MRO 12]*

1.6. Physical (or wave) optics models

In the 17th Century, geometrical optics had already explained many optical phenomena (light reflection, refraction, etc.) and facilitated the development of the first optical instruments. However, phenomena such as irization and diffraction rings

in the forward domain remained unexplained. Thus, a wave optics or physical optics theory of scattering phenomena evolved in close connection with mathematical developments. Figure 1.12 shows three pure physical optics phenomena that are currently used in characterizing particulate flows: forward diffraction, the rainbow and near-critical-angle scattering. For a spherical particle, all three phenomena produce a characteristic ring (or fringe) pattern that takes the form of bright and dark cones. These conic sections originate approximately from the particle center, with the symmetry axis along the optical axis of the illumination wave. The aperture angles of these cones depend both on the diameter and refractive index of the particle. In the following sections, we summarize the basic concepts of the three physical optics models established to describe these phenomena.

Figure 1.21. *Three phenomena demonstrating the wave nature of light: forward (i.e. Fraunhofer) diffraction, rainbow scattering and near-critical-angle scattering [ONO 05]*

1.6.1. *Huygens–Fresnel integral*

The Huygens–Fresnel principle states that any point of a wavefront can be modeled by a punctual and coherent light source that emits spherical waves [BOR 02]. In an infinite, homogeneous and non-absorbing medium, the summation contributions from all these punctual sources allows the wavefront to reconstruct itself as it propagates [BOR 02].

Huygens–Fresnel theory is a scalar theory for the forward diffraction phenomenon. But, the theory does not account for the polarization state of light or the particle refractive index. As a paraxial approximation, Huygens–Fresnel theory is only valid for small scattering angles ($\theta \approx 0°$) and at large distances from the object [BOR 02, GOO 96].

Figure 1.22(a) shows a schematic of a plane harmonic wave propagating along the $z' \equiv z$ axis, from the incident wavefront $(Ox'y')$ toward the (Oxy) plane. Each differential element $dx'dy'$ radiates toward all elements of (Oxy) and more particularly, the surface $dxdy$ that is at distance r from the considered emitting element. In the $(Ox'y')$ plane, the incident electrical field E_N of the wavefront is given by:

$$E_N(x', y', t) = E_{N0} e^{-i\omega t}, \qquad [1.67]$$

where E_{N0} is the nominal amplitude of the incident field. The reconstructed field E_F is deduced from the scalar diffraction integral:

$$E_F(k_x, k_y, t) = \frac{e^{ikr}}{\lambda r} \int_{-\infty}^{+\infty} \int_{-\infty}^{+\infty} E_N(x', y', t) e^{-i(k_x x' + k_y y')} dx'dy', \qquad [1.68]$$

where the direction of the wave vector k_x and k_y may be approximated as $k_x \cong kx/r = kq\cos(\Phi)/r$ and $k_y \cong ky/r = kq\sin(\Phi)/r$, within the small angle approximation.

Figure 1.22. *Coordinate systems for Fraunhofer diffraction*

1.6.2. *Fraunhofer diffraction theory for a particle with a circular cross section*

Figure 1.22(b) shows a Cartesian coordinate system $(Ox'y')$ attached to a plane circular object with radius a that is illuminated by a plane harmonic wave. First, the object is considered to be a circular hole in an infinite plate of negligible thickness. The sources of the incident wavefront cannot participate in the reconstruction of the new wavefront if they are more than a distance a away from the optical axis, that is $r' \geq a$. For $r' < a$, the wavefront is reconstructed normally. In the new polar coordinate system (r', ϕ') and (q, Φ) the first differential surface element is $ds' = r'dr'd\phi'$ with $x' = r'\cos\phi'$ and $y' = r'\sin\phi'$. The point of the observation plane (Oxy) is obtained from $x = q\cos\phi$ and $y = q\sin\phi$. The symmetry of the problem allows the use of the method of separation of variables to replace the double integral of equation [1.68] by a product of two integrals [WAT 04a]:

$$E_F\left(k_x, k_y, t\right) = \frac{e^{ikr}}{\lambda r}\int_0^a r'dr'\int_0^{2\pi} E_{N0}e^{-i\omega t}\exp\left[-i\frac{kr'q}{r}\left(\cos\phi'\cos\phi + \sin\phi'\sin\phi\right)\right]d\phi'. \quad [1.69]$$

By rearranging the above equation, E_F can be written as follows:

$$E_F\left(k_x, k_y, t\right) = \frac{E_{N0}e^{i(kr-\omega t)}}{\lambda r}\int_0^a r'dr'\int_0^{2\pi}\exp\left[-i\frac{kr'q}{r}\cos\left(\phi' - \phi\right)\right]d\phi'. \quad [1.70]$$

The symmetry of the diffraction pattern results from the symmetry of the object with respect to the optical axis $z' \equiv z$. Thus, we can select any value ϕ' and in particular, a value that simplifies equation [1.70], that is $\phi' = 0$:

$$J = \int_0^{2\pi}\exp\left[-i\frac{kr'q}{r}\cos\left(\phi\right)\right]d\phi' = 2\pi J_0\left(\frac{kr'q}{r}\right), \quad [1.71]$$

where $J_{n=0}(z)$ with $z = kr'q/r$ is a Bessel function of the first type and order $n = 0$. The diffracted electrical field in the far-field is as follows:

$$\begin{aligned} E_F\left(q,t\right) &= \frac{2\pi E_{N0}e^{i(kr-\omega t)}}{\lambda r}\int_0^a r'dr'J_0\left(\frac{kr'q}{r}\right), \\ &= \frac{2\pi E_{N0}e^{i(kr-\omega t)}}{\lambda r}\left(\frac{r}{kq}\right)^2\int_0^{kaq/r}\nu J_0\left(\nu\right)d\nu. \end{aligned} \quad [1.72]$$

Useful recurrence relations exist between Bessel functions [ABR 65], and more particularly:

$$uJ_1(v) = \int_0^u vJ_0(v)\,dv, \qquad [1.73]$$

Substituting equation [1.73] in equation [1.72] gives:

$$E_F(q,t) = \frac{2\pi E_{N0} e^{i(kr-\omega t)}}{\lambda r}\left(\frac{r}{kq}\right)^2\left(\frac{kaq}{r}\right)J_1\left(\frac{kaq}{r}\right). \qquad [1.74]$$

For small angles, $\theta \approx q/r$, and for an object of surface area $s' = \pi a^2$, the expression for the diffracted field is:

$$E_F(\theta,t) \approx \frac{s' E_{N0} e^{i(kr-\omega t)}}{\lambda r}\frac{2J_1(ka\theta)}{ka\theta}, \qquad [1.75]$$

and the expression for the diffracted intensity is given by:

$$I_F(\theta,t) = \frac{c}{8\pi}E_F(\theta,t)E_F(\theta,t)^* = \frac{s'^2 cE_{N0}^2}{8\pi\lambda^2 r^2}\left[\frac{2J_1(ka\theta)}{ka\theta}\right]^2. \qquad [1.76]$$

Equation [1.76] is not defined for $\theta = 0°$, but as the $\lim\left(J_1(z)/z\right) = 1/2$ for $z \to 0$, we obtain $I_F(0) = s'^2 cE_{N0}^2/\left(8\pi\lambda^2 r^2\right)$ for this particular angle. Finally, the angular intensity profile of the diffraction pattern of a circular hole is given by:

$$I_F(\theta,t) = I_F(0)\left[\frac{2J_1(ka\theta)}{ka\theta}\right]^2. \qquad [1.77]$$

This function is maximal for $\theta = 0°$ (the main diffraction lobe can be seen in Figure 1.13) and decreases rapidly with large oscillations when the scattering angle increases (i.e. the diffraction pattern is composed of bright and dark rings). The angle position of the first dark ring is inversely proportional to the diameter of the diffracting object such that:

$$\theta_1 \approx 1.22\lambda/(2a). \qquad [1.78]$$

To calculate the diffraction pattern of a circular, opaque and thin disk, we can use previously obtained results. Using equation [1.71] for a circular opaque disk of radius a, the electrical field diffracted in the far-field is as follows:

$$E_F(q,t) = \frac{2\pi E_{N0} e^{i(kr-\omega t)}}{\lambda r} \int_a^{+\infty} r' dr' J_0\left(\frac{kr'q}{r}\right). \quad [1.79]$$

Integrating equation [1.79] by parts yields terms that have already been calculated:

$$E_F(q,t) = \frac{2\pi E_{N0} e^{i(kr-\omega t)}}{\lambda r}\left(\int_0^{+\infty} r' J_0\left(\frac{kr'q}{r}\right) dr' - \int_0^{a} r' J_0\left(\frac{kr'q}{r}\right) dr'\right), \quad [1.80]$$

which finally produces:

$$E_F(q,t) = E_{N0} e^{i(kz-\omega t)} - \frac{\pi a^2 E_{N0} e^{i(kr-\omega t)}}{\lambda r}\left(\frac{r}{kaq}\right) 2J_1\left(\frac{kaq}{r}\right). \quad [1.81]$$

The intensity of the diffraction pattern averaged over one temporal period is then given by:

$$I_F(q) = \left\langle I_F(q,t)\right\rangle_{1/\nu} = \frac{c}{8\pi} E_F(q,t) E_F(q,t)^*. \quad [1.82]$$

The diffraction pattern of a solid disk is also composed of concentric bright and dark rings (see Figures 1.23(b) and 2.28). A peculiarity of these diffraction patterns is the existence of a bright spot at the center, also known as the Arago–Poisson spot. The intensity of the spot depends mainly on the amplitude of the illuminating beam and the observed distance with respect to the particle. The angular width of the spot increases with the particle size and observer distance. The intensity profile of this spot is given by:

$$I_{\text{Spot}}(q) \propto J_0^2\left(\frac{kaq}{r}\right). \quad [1.83]$$

Laser diffractometers, which analyze the diffraction pattern produced by particulate systems, are probably the most widely used particle size instruments[9].

9 See [BOU 12] by the same authors.

Figure 1.23. *a) Calculation of the diffraction pattern (Airy disk) of a small circular hole and b) experimental diffraction patterns for metallic beads with diameters D = 2.4, 3.9 and 4.8 mm, observed from a distance of 5 m [FEI 97]*

1.6.3. *Airy theory of the rainbow*

Within the context of geometrical optics (section 1.7), the first rainbow is related to the maximum angle of deviation for rays that are refracted after one internal reflection by spherical and transparent particles. Figure 1.24(a) shows that the scattering angle of these particular rays (denoted by $p = 2$) increases up to a maximum θ_{ac} and then decreases as the impact parameter of the incident rays increases. This maximum scattering angle θ_{ac} is referred to as the first rainbow angle. None of the rays of type $p = 2$ are scattered in the angular domain, $\theta < \theta_{ac}$ (and more particularly, within the Alexander's dark band [VAN 57, NUS 92]). For $\theta > \theta_{ac}$, two types of rays, $p = 2$, superimpose on each other to interfere at infinity.

In fact, a similar angular condition exists for all rays, where $p \geq 2$. It is only for the purposes of illustration that the rays associated with the second ($p = 3$), third ($p = 4$) and higher rainbows are not shown in Figure 1.24. As mentioned in Figure 1.24(b), the intensity of successive rainbows decreases rapidly due to the multiple internal reflections experienced by high-order rays. This explains why when the Sun illuminates raindrops in nature, it is difficult (but possible) to observe the third- and fourth-order rainbows ($p = 4, 5$) [THE 11] and almost impossible to observe in nature higher order rainbows.

For a spherical particle (or a circular cylinder under normal incidence), rays of order p emerge at the scattering angle θ [VAN 57, BUL 98]:

$$\theta(p,m) = q_1\left(2p\tau' - 2\tau - 2q_2\pi\right), \qquad [1.84]$$

where q_2 is a natural integer and $q_1 = \pm 1$ is a parameter, which allows us to obtain a scattering angle in the desired angular range (i.e. $0 - \pi$ or $-\pi - 0$). The derivative of the preceding equation is equated to zero to find the maximum deviation angle:

$$\frac{d\theta}{d\tau} = q_1\left(2p\frac{d\tau'}{d\tau} - 2\right) = 0. \qquad [1.85]$$

Figure 1.24. *(a) The first rainbow occurs in the vicinity of the maximum deviation angle of the refracted rays that undergone one internal reflection (p = 2). (b) The evolution of the Fresnel intensity coefficients for rays scattered by a water droplet versus the normalized path length of the rays inside the droplet [ONO 05]*

Using the second Snell–Descartes relation, $\cos\tau = m\cos\tau'$, we obtain:

$$\frac{d\tau'}{d\tau} = \frac{\sin\tau}{m\sin\tau'} = \frac{\tan\tau}{\tan\tau'}, \qquad [1.86]$$

and equation [1.85] gives:

$$\tan\tau' = p\tan\tau. \qquad [1.87]$$

The Snell–Descartes relations may be reformulated as [BUL 98]:

$$\frac{1}{\sqrt{1+\tan^2\tau'}} = \frac{1}{m}\frac{1}{\sqrt{1+\tan^2\tau}}. \qquad [1.88]$$

Equations [1.87] and [1.88] yield:

$$\tan^2\tau = \frac{m^2-1}{p^2-m^2},\ \tan^2\tau' = p^2\frac{m^2-1}{p^2-m^2}. \qquad [1.89]$$

Finally, the angular position of the rainbow of order $p-1$ produced by rays of order $p \geq 2$ is:

$$\theta_{ac}(p,m) = q_1\left[2p\arctan\left(\sqrt{p^2\frac{m^2-1}{p^2-m^2}}\right) - 2\arctan\left(\sqrt{\frac{m^2-1}{p^2-m^2}}\right) - 2q_2\pi\right], \qquad [1.90]$$

which depends only on the particle relative refractive index (i.e. the dispersion equation of the particle and surrounding materials). This explains the origin of the rainbow of colors observed in the sky. In fact, a water droplet in air typically has m = 1.3404 for λ = 0.488 μm (blue) and m = 1.3315 for λ = 0.6328 μm (red), so that for blue and red light, the first rainbow is localized at θ_{ac} = 139.0° and θ_{ac} = 137.7°, respectively. As mentioned previously, for a spherical particle, the rainbows form cones of light with an aperture angle of $\theta_{ac}(p,m)$. For a circular jet illuminated under normal incidence, the rainbows form fringes parallel to the jet axis [SAE 06, LOC 00].

Despite the successes of pure geometrical optics, two important characteristics of rainbows cannot be accounted for: the angular dependence on the particle size, the presence of supernumery bows (even for monochromatic illumination[10]) and a finite intensity when $\theta = \theta_{ac}$.

To explain the aforementioned observations, Young, Fresnel and Airy proposed a physical optics theory of the rainbow around the beginning of the 19th Century. This theory, now called the Airy theory of the rainbow, is based on the Huygens–Fresnel principle (section 1.6.1) [AIR 38]. The starting point is the existence of a singularity at $\theta = \theta_{ac}$: geometrical optics predicts an infinite intensity gradient (i.e. a caustic; see Figure 1.8 and section 1.7) at this angle. This singularity generates a pure wave optics (or diffraction) phenomena. A careful examination of Figure 1.24(a) reveals that the p = 2 rays are phase-shifted with respect to each other. Let us assume that the associated wavefront can be defined by a relation $u(v)$, where u is along a direction that exactly corresponds to the rainbow angle predicted by geometrical optics, and v is along the particle radius a and perpendicular to u. A Cartesian coordinate system is defined by (u, v). In the vicinity of the direction

10 See [BOU 12] by the same authors.

defined by the angle θ_{ac} (only the first rainbow is considered henceforth), the wavefront [WAT 04b, WAT 04c, ADA 02] can be expressed by:

$$E_N(v,t) = e^{-i\omega t} e^{iku(v)}, \qquad [1.91]$$

where $u(v)$ can be derived from basic trigonometric calculations. To obtain an integral that can be calculated in the end, let us simplify the problem by replacing this function by its first-order approximation. For this purpose, this function is expanded with a Taylor expansion at the vicinity of $\theta - \theta_{ac} = 0°$. After some calculations, it can be shown that the first non-zero term that describes the shape of the wavefront is cubic:

$$u = -\frac{hv^3}{3a^2}, \text{ with } h \equiv \frac{3\tan\theta_{ac}}{4\cos^2\theta_{ac}}. \qquad [1.92]$$

The angular deviation, $\theta - \theta_{ac} = du/dv = k_v$, corresponds to the tangential component of the wave vector (see the magnified image in Figure 1.24(a)). By a proper substitution in equation [1.91], the amplitude of the electrical field diffracted in the far-field and in the vicinity of the rainbow angle is computed to be:

$$E_F(v,t) = \frac{E_0 e^{i(kR-\omega t)}}{\lambda R} \int_r e^{-ikhv^3/3a^2} e^{i(\theta-\theta_{ac})v} dv. \qquad [1.93]$$

Let us introduce the constants, $l = \sqrt[3]{3\lambda a^2/4h}$, and $z = 4l(\theta - \theta_{ac})/\lambda$ [WAT 04b], along with a change of variable $\eta = v/l$. Then, by requiring that the scattered intensity has the form $I_F = (8/\pi c) E_F E_F^*$ ([DAV 55, VAN 57, ONO 12b]), the intensity profile of the first rainbow is given by:

$$I_F(\theta) = \frac{cE_0^2}{8\pi\lambda^2 R^2} \left(\frac{3\lambda D^2}{16h}\right)^{2/3} \left| \int_0^\infty \cos\left[\frac{\pi}{2}\left(z\eta - \eta^3\right)\right] d\eta \right|^2, \qquad [1.94]$$

where the integral was unknown in Airy's time. He simply called it the rainbow integral. Currently, the integral is related to the well-known Airy function so that equation [1.94] may be reformulated as [ABR 65]:

$$\int_0^\infty \cos\left[\frac{\pi}{2}\eta^3 - \frac{\pi z}{2}\eta\right] d\eta = \left(\frac{2\pi^2}{3}\right)^{1/3} Ai\left[-\left(\frac{\pi^2}{12}\right)^{1/3} z\right]. \qquad [1.95]$$

For a particle of refractive index m and diameter $D = 2a$, which is illuminated by a plane harmonic wave of wavelength λ, the intensity profile of the first rainbow with $q_1 = -1$ is:

$$I_F(\theta) = \frac{cE_0^2}{R^2}\left(\frac{3}{\pi h^2}\right)^{1/3}\left(\frac{D}{\lambda}\right)^{4/3} Ai^2\left[-\left(\frac{\pi^2}{12}\right)^{1/3} z\right]. \quad [1.96]$$

By taking into account the second radius of the curvature of the particle (i.e. in the plane perpendicular to the scattering plane) [ONO 05, ONO 12], we finally arrive at the following result:

$$I_F(\theta) = \frac{cE_0^2}{R^2}\left(\frac{3}{\pi h^2}\right)^{1/3}\left(\frac{D}{\lambda}\right)^{7/3} Ai^2\left[-\left(\frac{\pi^2}{12}\right)^{1/3} z\right]. \quad [1.97]$$

Equation [1.97] clearly shows that the rainbow pattern oscillates in the scattering plane (corresponding to oscillations of the Airy function) and that the 3D pattern is composed of bright and dark cones whose angular aperture depends both on the particle size and on the refractive index (via h and z). More surprisingly, the intensity of the rainbow pattern is found to increase with the particle size as a power law with exponent 7/3.

The Airy theory allows fast and rather accurate predictions, two particularly important advantages for inverse methods [VET 04]. However, the quality of its predictions decreases rapidly when the particle size decreases and/or for scattering angles that deviate too greatly from the geometrical rainbow angle (i.e. where the Taylor expansion was performed). The Airy theory tends to minimize the intensity decay of the supernumerary bows and does not account for the high-frequency ripple structure of the rainbow (due to interferences of the $p = 2$ and $p = 0$ rays) and the effect of the polarization of the incident wave (i.e. the rainbow obtained for the perpendicular polarization always shows higher contrast) [ONO 04].

1.6.4. *Marston's physical-optics approximation*

In optics, a bubble is a particle with a refractive index that is lower than the refractive index of the surrounding medium, $m = m_1/m_2 < 1$ (e.g. this situation can either correspond to an air bubble rising in water or a water droplet sinking in silicon oil). From geometrical optics, a total reflection angle $\phi_c = \sin^{-1}(m^{-1})$ exists, above which the rays impinging onto the bubble surface are totally reflected ($p = 0$). The corresponding scattering angle is referred to as the near-critical-scattering angle with $\theta_c = \pi - 2\phi_c$ (see Figure 1.25(a)). The reflection coefficient of the totally reflected

rays is a unimodular complex number. This coefficient decreases continuously for partially reflected rays, as shown in Figure 1.25(b).

Figure 1.25. *a) Near-critical-angle scattering of a bubble. b) Comparison of the scattering diagrams for an air bubble in water from the physical optics approximation (POA), pure geometrical optics and the Lorenz–Mie Theory [ONO 99a]*

In Marston's physical optics approximation (POA) [MAR 79, MAR 81, LAN 84] for near-critical-angle scattering (see Figure 1.21), the semi-discontinuity (weak caustic) of the reflected coefficient provides a starting point for describing the propagation of a "steep wavefront" in the far-field. The procedure used is reminiscent of Airy's theory of the rainbow. Indeed, the POA uses a Taylor expansion to derive a first-order approximation of the reflected wavefront (which turns out to be a quadratic function) and the Huygens–Fresnel principle to study propagation of this approximated wavefront. Figure 1.25 shows that the POA dramatically improves the geometrical optics prediction of the near-critical scattering pattern. Note that near-critical-angle scattering patterns show substantial similarities to the rainbow patterns (see, for instance, Figures 2.19 and 2.24). Analytical relationships may be derived between the angular positions of the bright and dark fringes and the bubble characteristics [ONO 99a]. If, for instance, the bubble relative refractive index is known *a priori*, the bubble diameter can be directly deduced from the measurement of the angular position θ_n of the *n*th fringe with:

$$a_n = \frac{\lambda_0 m \omega_n^2}{\sin^2\left(\theta_c - \theta_n\right)\cos\phi_c}, \qquad [1.98]$$

where ω_n are tabulated integral constants [ONO 09a]: $\omega_1 = 1.2171983$, $\omega_2 = 1.87252$, $\omega_3 = 2.34485$, etc. If both the relative refractive index and the bubble size are

unknown, they can be both deduced from the measurement of the angular positions of two fringes of order υ and κ with $\kappa > \upsilon$ [ONO 09a] such that:

$$m_{\upsilon\kappa} = \sin\left[\left(\pi - \theta_\upsilon - \Omega_{\upsilon\kappa}\right)/2\right], \qquad [1.99]$$

$$a_{\upsilon\kappa} = \lambda_0 m_{\upsilon\kappa} \frac{\omega_\upsilon^2 + \omega_\kappa^2 - 2\omega_\upsilon\omega_\kappa \cos\Delta_{\upsilon\kappa}}{\sin^2\left(\Delta_{\upsilon\kappa}\right)\sin\left[\left(\theta_\upsilon - \Omega_{\upsilon\kappa}\right)/2\right]}, \qquad [1.100]$$

where $\Omega_{\upsilon\kappa} = \tan^{-1}\left[\sin\Delta_{\upsilon\kappa} / \left(\cos\Delta_{\upsilon\kappa} - \omega_\kappa / \omega_\upsilon\right)\right]$ and $\Delta_{\upsilon\kappa} = \theta_\kappa - \theta_\upsilon$. As an illustration of the accuracy of POA, Figure 1.26 compares the POA and LMT predictions for the angular position of the first bright fringe θ_1 for (a) air bubbles in water and (b) bubbles of various compositions. The agreement between these two theories is found to be reasonable, although the POA accuracy decreases rapidly for larger order fringes. To improve the predictions of POA, the contribution of other rays needs to be accounted for (i.e. at least the rays p = 1, 2 for the coarse structure and the rays p = 2' for the ripple structure). This is a major difference between near-angle-critical scattering and rainbow scattering.

Recent extensions of the POA are focused on the scattering of spheroid bubbles and cloud of bubbles ([ONO 07, ONO 09a, ONO 12b]).

Figure 1.26. *Comparison of the POA and LMT results for the angular position of the first bright fringe for a) air bubbles in water and b) various liquid–liquid or gas–liquid bubbles [ONO 99a]*

1.7. Geometrical optics

Pure geometrical optics is based on a mechanistic view of the nature of light. The theory consists of decomposing the incoming wave into rays ("pencils of light" [VAN 57] or into "virtual photons"), that are reflected or refracted by the particle. The direction of propagation and the intensity of these rays are described by the Snell–Descartes laws and the Fresnel coefficients, respectively. The reflected or refracted rays are within the plane defined by the incident ray and the normal to the particle surface at the point of impact such that:

$$m\cos\tau' = \cos\tau, \qquad [1.101]$$

where τ and τ' are the complementary angles of the usual incident and refraction angles, and m is the real part of the particle relative refractive index. Except for grazing incidence or total reflection, all incident rays are partially reflected into the surrounding medium (rays noted as $p = 0$) or refracted inside the particle, see Figure 1.27.

Figure 1.27. *Geometrical model: a) the path of rays of order p scattered by a spherical particle with relative refractive index $m = m_1/m_2$ and diameter D; b) ray tracing for $m_1 = 1.332$, $m_2 = 1$, $D = 100\ \mu m$, $\lambda_0 = 0.6328\ \mu m$ and $p < 4$*

The refracted rays can be transmitted into the surrounding medium directly (i.e. single refraction: $p = 1$) or after having undergone several internal reflections (one internal reflection: $p = 2$, two internal reflections: $p = 3$, etc.). Without the influence of the Fresnel coefficients, as well as absorption, this cycle would continue indefinitely.

1.7.1. *Calculation of the scattering angle*

For a spherical particle, there is a recurrence relation between the incident angle and the scattering angles [VAN 57, BUL 98]:

$$\theta_p = q_1\left(2p\tau' - 2\tau + 2\pi q_2\right), \qquad [1.102]$$

where q_2 is a natural integer and $q_1 = \pm 1$ is a coefficient that helps selecting the angular range of the scattering domain. From equation [1.102], it is easy to show that for rays $p = 1$ and refracting particles $\left(m \geq 1\right)$, there is a maximum scattering angle $\theta_{\text{refrac.}}$; for rays $p = 0$ reflecting onto the surface of a bubble ($m < 1$), there exists a critical scattering angle θ_c below which total reflection occurs:

$$\begin{cases} \theta_{\text{refrac.}} = 2\cos^{-1}\left(1/m\right), \ m > 1; \\ \theta_c = \pi - 2\sin^{-1}(m), \ m < 1; \\ \theta_B = 2\tan^{-1}(1/m), \ m > 1. \end{cases} \qquad [1.103]$$

The Brewster angle θ_B is introduced in the following section. Note that for all rays $p \geq 2$, there exists a ($p-1$) rainbow angle (section 1.6.3).

1.7.2. *Calculation of the intensity of rays*

The amplitude of the rays reflected by a plane surface is given by the complex coefficients of Fresnel [BOH 88]:

$$r_1 \equiv r_\perp = \frac{\sin\tau - m\sin\tau'}{\sin\tau + m\sin\tau'}, \; r_2 \equiv r_\parallel = \frac{m\sin\tau - \sin\tau'}{m\sin\tau + \sin\tau'}, \qquad [1.104]$$

where the subscripts 1 (or $\perp$) and 2 (or $\parallel$) denote the perpendicular and parallel polarization, respectively. The amplitude of the different rays is given by:

$$\begin{aligned} &\varepsilon_{p(\perp,\parallel)} = r_{\perp,\parallel} \quad \text{for } p = 0, \\ &\varepsilon_{p(\perp,\parallel)} = \left(1 - r_{\perp,\parallel}^2\right)^2 \left(-r_{\perp,\parallel}\right)^{p-1} \quad \text{for } p \geq 1. \end{aligned} \qquad [1.105]$$

The Fresnel coefficients provide many interesting results. For instance, when a parallel polarized ray impinges onto a dielectric material with an angle of incidence equal to the Brewster angle, its reflection coefficient is zero (see equation [1.103] and Figure 1.16).

The curvature of the particle surface is not accounted for in equations [1.104] and [1.105], but it is obvious that curvature generates dispersion and focusing effects even for an infinitesimal ray [DES72]. The effect of curvature for a sphere may be accounted for by introducing a divergence term Θ_p for the energy of the scattered rays. This divergence is calculated by writing an energy balance for the flux of the incident ray through a differential surface element of the particle surface and the flux of the scattered ray at infinity ([DAV 55, VAN 57, ONO 12b]), which yields:

$$\Theta_p = \frac{\sin\tau\cos\tau}{\sin\theta_p \left| d\theta_p / d\tau \right|}. \qquad [1.106]$$

If the material of the particle is absorbing, the Beer–Lambert law can be used to estimate the absorption rate of the transmitted rays (section 1.2.2.1). The amplitude of the transmitted ray decreases exponentially with the absorption constant $K = 4\pi k_m/\lambda$ and the ray path length $L = pD\sin\tau'$ inside the particle. The intensity of the ray thus decreases as $\exp[-pKD\sin\tau']$.

Finally, at large distances from the particle center (i.e. $kr \gg D$), the intensity of the ray p takes the following general form:

$$I_{1,2} \equiv I_{\perp,\parallel}(\theta) \propto I_0 \frac{D^2}{r^2} \varepsilon^2_{p(\perp,\parallel)} \Theta_p e^{-pKD\sin\tau'}. \qquad [1.107]$$

1.7.3. *Calculation of the phase and amplitude of rays*

The predictions of pure geometrical optics can be significantly improved by accounting for the phase ϕ_p of the rays. Three other contributions must be considered in addition to the phase shift associated with reflection phenomena (which is already accounted for by the complex coefficients of Fresnel)

$$\phi_p = \phi_{r,p} + \phi_{f,p} + \pi/2. \qquad [1.108]$$

The first phase term $\phi_{r,p}$ accounts for the total ray path length regarding to a reference ray. The latter passes through the center of the particle before following the direction of the scattering angle (see Figure 1.29 and section 2.12). For two reference surfaces, Σ and Σ', $\phi_{r,p}$ is given by:

$$\phi_{r,p} = \frac{2\pi D}{\lambda} m_2 (\sin\tau - pm_1 \sin\tau'). \qquad [1.109]$$

The second phase term $\phi_{f,p}$ comes from the curvature of the various dioptric interfaces encountered by the ray. These interfaces generate focal points and focal lines. For a ray passing through a focal point, $\phi_{f,p}$ increases by $+\pi/2$ when the direction of the electrical field is reversed. In the case of a sphere, van de Hulst [VAN 57] has established a general relation for these additional phase shifts:

$$\phi_{f,p} = \frac{\pi}{2}\left(p - 2k + \frac{1}{2}s + \frac{1}{2}q \right), \qquad [1.110]$$

where $s = \pm 1$ depends on the sign of the derivative $d\theta_p / d\tau$, that is $s = \left(d\theta / d\tau\right) / \left|d\theta / d\tau\right|$, with according van de Hulst [VAN 57] notations $k = q_1 q_2$ and $q = -q_1$. Finally, far from the particle center, the amplitude of the ray p may be expressed as:

$$S_{1,2} \equiv S_{s\perp,s\parallel} \propto \sqrt{I_{s\perp,s\parallel}}\, \mathrm{e}^{i\phi_p} . \qquad [1.111]$$

Equation [1.105] allows the direct calculation of the scattering diagrams of a particle for a particular ray p (i.e. similar to the Debye theory for the partial waves p), whereas equation [1.111] enables us, for instance, to calculate the interference between different scattering phenomena or the integral response of a real detector (section 1.4.2) (e.g. [SAN 91, NAQ 93, WU 07, REN 11]).

In summary, geometrical optics has three main advantages: it is intuitively easy to grasp and to implement, and it is computationally efficient. The shortcomings of geometrical optics are related to its asymptotic nature of the theory. The theory is limited to large particles ($D \gg \lambda$) and fails to predict pure wave phenomena that are now commonly used to characterize particle systems[11]: forward diffraction (which can represent up to 50% of the total scattering of large particles), rainbow scattering and near-critical-angle scattering.

Current developments in geometrical optics are focused on the incident beam description (e.g. wave front curvature), the scattering of non-spherical particles and the coupling of geometrical with physical-optics or electromagnetic models (e.g. [MAC 95, WU 07, REN 11, ONO 12b]).

1.8. Multiple scattering and Monte Carlo models

1.8.1. *Scattering by an optically diluted particle system*

When most virtual photons (i.e. rays) reaching a photodetector have statistically undergone less than one scattering event with a particle in the system, we face a

11 See [BOU 12] by the same authors.

single scattering regime and the particulate medium is considered to be optically diluted (Figure 1.28). The scattering, absorption and extinction properties of the illuminated particles may be obtained by summation of the individual contributions. The single scattering assumption is utilized by most, if not all, of the optical particle size instruments used in fluid mechanics[12].

Figure 1.28. *Sketch of the single, multiple and dependent scattering regimes*

Let C_N be the particle concentration by number (per cubic meter) and $n(D)$ be the corresponding normalized particle size distribution by number (section 1.2.2.3). The total extinction cross-section and intensity scattered by all illuminated particles are given by:

$$\begin{aligned} \overline{C}_e &= C_N \int_0^\infty n(D) C_e(D, \tilde{m}, \lambda)\, dD, \\ \overline{I}_{\perp,\parallel}(\theta) &= C_N \int_0^\infty n(D) I_{\perp,\parallel}(\theta, D, \tilde{m}, \lambda)\, dD. \end{aligned} \qquad [1.112]$$

1.8.2. *Multiple scattering*

If a non-negligible number of the virtual photons reaching the photodetector have undergone more than one scattering event, we face a multiple scattering regime and the particulate medium is said to be optically dense [VAN 80, WOL 87]. Multiple scattering can be treated as a succession of single scattering events because each particle scatters light as if it was the only particle. In the case where the particles are very close to each other, the particles scatter light as aggregates and we face a dependent scattering regime (or a coherent scattering regime if the particles are spatially organized [WOL 85]). With dependent scattering, the scattering problem can no longer be decomposed into a succession of single scattering events.

12 See [BOU 12] by the same authors.

As previously mentioned, most OPC techniques used in fluid mechanics are limited to optically diluted flow, that is they assume a single scattering regime. Thus, given a particulate system and an experimental setup, it is imperative to ensure that operation occurs in the single scattering regime. Unfortunately, it is not easy to give a universal criterion for the transition between the single regime and the other regimes. Indeed, this transition depends on the properties of the system of particles (particle size distribution, refractive index and concentration, and thickness of the particulate medium), as well as the optical setup itself (wavelength and polarization of the incident wave, angular aperture and position of the detectors, etc.). Nevertheless, an order of magnitude expression for this criterion can be derived: to be in the single scattering regime, the mean free path Λ of the collected photons must be much greater than the minimum distance L that the photons would travel in the absence of particles. That is to say:

$$\Lambda = \left(C_N \overline{C}_{ext}\right)^{-1} \gg L. \qquad [1.113]$$

Equivalently, the optical thickness $C_N \overline{C}_{ext} L$ of the particulate medium must be sufficiently low and the attenuation A of the illumination beam must be negligible:

$$A = 1 - T = 1 - \exp\left(-C_N \overline{C}_{ext} L\right) \ll 1. \qquad [1.114]$$

If the above criteria are not fulfilled, the easiest solution is to dilute or reduce the dimensions of the particulate system, or to change the incident wavelength. In some cases, the reduction of the angular aperture of the collection optics [XU 07], the use of ultra fast laser sources and detection optics [ROZ 03], controlling the polarization state [DIL 06] or the cross correlation of the collected photons [WOL 85, PHI 81] can minimize or even cancel out some of the effects of multiple scattering.

1.8.3. *Monte Carlo method*

Geometrical optics is an invaluable tool for large scatterers with a complex shape, or when a scattering process needs to be modeled in a complex environment (walls, mechanical supports, detector aperture shapes, etc.). However, tracking multiple paths of the virtual photons (or ray) in complex systems quickly becomes impossible. Indeed, without absorption, the interaction of a virtual photon with any object requires following two photons in each successive step (i.e. $p = 0$ and $p = 1$). Continuation of this process results in a dramatic increase in the number of virtual photons that must be tracked.

To circumvent the latter difficulty, the Monte Carlo method considers all scattering phenomena as stochastic events and converts all previously established

scattering properties into probability density functions. For instance, the scattering diagram calculated with LMT is transformed into a probability that a virtual photon with a given intensity is scattered in a given direction (θ, ϕ). Geometrical laws, Fresnel coefficients and the results of physical optics theories can also be processed in the same way. This procedure facilitates the modeling of scattering properties of complex systems. The main limit of the Monte Carlo method is that it requires the launching of a huge number of virtual photons to observe the weakest phenomena (i.e. less probable events) with a reasonable level of stochastic noise.

As a concrete example, let us consider a colloidal suspension of monodisperse, spherical nanoparticles (with diameter D, number concentration C_N and refractive index m_4) in a liquid of refractive index m_3 (see Figure 1.29). A sample of this suspension is placed in a rectangular spectrophotometer cell (internal dimensions $l_x \times l_y \times h$, glass wall thickness e and refractive index m_2) [ONO 09c]. This cell is itself placed in a medium of refractive index m_1. The glass cell is illuminated by a collimated and unpolarized beam with wavelength λ_0 and diameter w. We will only consider the simplest case of scattering in the (Oxy) plane, neglecting polarization and interference phenomena.

Figure 1.29. *Monte Carlo prediction of the scattering properties of a colloidal suspension within a spectrophotometer cell*

The trajectories of the virtual photons reflected and refracted by the glass walls of the cell are well described by the Snell–Descartes laws. Thus, the description of these trajectories requires only simple vector calculations. For each interaction of the virtual photon with the surrounding medium/cell wall or the cell wall/liquid interfaces, the corresponding reflected intensity can be calculated using Fresnel coefficients, that is $0 \le r_{\perp,\parallel}^2(\theta) \le 1$. Let us generate a random number H_r, which is

homogeneously distributed such that $H_r = 0-1$. The following equation shows when the virtual photon will be reflected or refracted.

$$\begin{cases} r_{\perp,\parallel}^2 \le H_r \Rightarrow \textit{reflected}, \\ r_{\perp,\parallel}^2 > H_r \Rightarrow \textit{refracted}. \end{cases} \quad [1.115]$$

Next, we consider that a virtual photon has successfully entered the suspension. As nanoparticles are spherical, LMT (and subsequently, Rayleigh theory) can be used to calculate their scattering diagrams, cross-sections and the virtual photon mean free paths Λ (section 1.8.2). For an infinite suspension, the distance L_Λ at which the virtual photon interacts (by scattering or absorption) with a particle is given by $L_\Lambda = -\Lambda \ln(H_\Lambda)$, where $H_\Lambda = 0-1$ is a new random number. On the other hand, we can easily calculate the distance L_∞ that the virtual photon could have traveled into the cell in the absence of particles in the liquid. Thus, the interaction of the virtual photon with a particle of the suspension is:

$$\begin{cases} L_\Lambda < L_\infty \Rightarrow \textit{effective}, \\ L_\Lambda \ge L_\infty \Rightarrow \textit{not effective}. \end{cases} \quad [1.116]$$

It is important to emphasize that the positions of the particles are only defined statistically within this method. In fact, due to the limitation of computational resources, it would be impossible to pre-allocate the positions of all the nanoparticles in a typical colloidal suspension (see Table 1.3). If there is no effective interaction, it means that the virtual photon has directly reached one of the walls of the glass cell, and the entire procedure beginning with equation [1.115] must be repeated.

An effective interaction can be either due to a scattering or due to an absorption event. With a new random number $\mathrm{H}_{s,a} = 0-1$, the behavior of the photons can be inferred by using the scattering and absorption cross sections of the particle,

$$\begin{cases} Q_s / (Q_s + Q_a) \le H_{s,a} \Rightarrow \text{scattered}, \\ Q_s / (Q_s + Q_a) > H_{s,a} \Rightarrow \text{absorbed}. \end{cases} \quad [1.117]$$

A virtual photon is no longer tracked after absorption: a new virtual photon is generated from the light source, and the entire procedure described above is repeated from the beginning. For a scattered photon, it is necessary to first estimate its

probability P to be scattered in the scattering angle direction θ_0 (i.e. 2D scattering is assumed for simplicity):

$$P(\theta_0, D, m, \lambda / m_3) = \int_0^{\theta_0} I(\theta, D, m, \lambda / m_3)\, d\theta \Big/ \int_0^{\pi} I(\theta, D, m, \lambda / m_3)\, d\theta. \quad [1.118]$$

A new random number is generated, $H_\theta = 0 - 1$, and the virtual photon is found to be scattered in the direction defined by the scattering angle $\theta = \{\theta_0 \,|\, P(\theta_0) = H_\theta\}$.

The next step is to determine whether the photon will interact with another particle of the suspension, a wall of the glass cell or reach the surface of a detector (e.g. a partially absorbing surface), or escape from the calculation domain of computation (e.g. through the cell base and lid).

Figure 1.30 represents some of the numerical results obtained with a more complete algorithm. For the purposes of illustration, the paths of only 10 photons are shown. The parameters of these simulations are C_N = 0, 310^{23}, 3×10^{24}, 3×10^{25} part/m^3 for $m_1 = 1$, m_2 = 1.51, m_3 = 1.334, m_4 = 1.627, λ = 405 nm, w = 1 mm, $l_x x l_y$ = 10 × 10 mm, h = 50 mm, $e_x = e_x$ = 1 mm and D = 10 nm (Table 1.3). The effects of multiple reflections and refractions at the glass cell interfaces and corners are clearly observable, as is the effect of the particle number concentration on the number of scattering events. Multiple scattering tends to increase the backward and near-backward scattering contributions and decrease the beam transmission.

Figure 1.30. *Tracing 10 rays (virtual photons) within a nanoparticle suspension in a rectangular glass cell*

Concentration, C_N (part/m^3)	Mean free path, Λ (m)	Turbidity, τ (m^{-1})	Transmission rate, T (–)
0	∞	0	1.00
3.00×10^{22}	7.12×10^{-2}	0.140	0.87
3.00×10^{23}	7.12×10^{-3}	1.40	0.25
3.00×10^{24}	7.12×10^{-4}	14.0	7.97×10^{-6}

Table 1.3. *Orders of magnitude for the mean free path, turbidity and transmission rate with increasing particle number concentration*

For the same parameters in Figure 1.30, Figure 1.31 shows the scattering diagrams obtained for the launching of 10^5 photons (a small number) for detection localized at r = 120 mm from the center of the cell (the far-field condition is fulfilled, but the remote sensing approximation is not). The scattering diagrams thus obtained, deviate significantly from what is expected for optically diluted nanoparticulate systems. The effects of the glass cell corners are clearly observable, as the effects of multiple scattering when $C_N = 3 \times 10^{24}$ part/m^3 (i.e. the scattering diagram is no longer homothetic to the diagrams obtained at lower concentrations). Note that the high-frequency oscillations observed for all diagrams are mainly attributed to the statistical noise of the Monte Carlo method. It would be necessary to launch more virtual photons to reduce the amplitude of this noise.

Figure 1.31. *Monte Carlo simulation of scattering diagrams for a colloidal suspension inside a rectangular glass cell [ONO 09]*

The Monte Carlo method has also been used to describe the scattering properties of colloidal droplets (e.g. [ONO 99b, DOI 01b]) as well as many other complex systems (e.g. [BRI 92]).

1.9. Conclusion

In this chapter, the elementary properties of electromagnetic waves have been summarized. In the same way, a few rigorous theories or approximations used to calculate various light scattering properties of small particles in flow have been reviewed and illustrated in a concise and accessible format. Figure 1.32 presents an attempt to synthesize the ranges of validity of these various theories and models that are used in Chapter 2 (on OPC techniques) to solve direct or inverse problems.

Figure 1.32. *Schematic of the ranges of validity of the main theories and models used to predict the light scattering properties of small particles [ONO 09b]*

The refractive index of materials encountered in fluid mechanics are usually difficult to determine, but a number of useful databases do exist [AST 10, HIT 10, REF 10, TEX 10, ILI 10, SOP 08]. Databases with executable or source codes for calculating the scattering properties of particles and particulate systems can also be found (e.g., [DRA 10, SCA 10, MIS 04, ONO 10, MÄT 02]). For more details on the various theories and models that have been briefly reviewed in this chapter, the reader can consult various reference books and articles in the field [BOH 88, KER 69, VAN 57, NUS 92, VAN 80, MIS 02, MIS 00, DOI 00, KOK 09, GOU 09, WRI 98, FUL 95].

1.10. Bibliography

[ABR 65] ABRAMOWITZ M., STEGUN I.A., *Handbook of Mathematical Functions*, Dover Inc., New York, NY, 1965.

[ADA 02] ADAM J.A., "The mathematical physics of rainbows and glories", *Physics Reports*, vol. 356, pp. 229–365, 2002.

[AIR 38] AIRY G.B., "On the intensity of light in the neighbourhood of a caustic", *Transactions of the Cambridge Philosophical Society*, vol. 6, no. 3, pp. 397–403, 1838.

[ASH 70] ASHKIN A., "Acceleration and trapping of particles by radiation pressure", *Physical Review Letters*, vol. 24, no. 4, pp. 156–159, 1970.

[AST 10] ASTER. Spectral library (reflectances) – Jet Propulsion Laboratory (NASA), 2010, available at http://speclib.jpl.nasa.gov.

[AUG 07] AUGER J.C., MARTINEZ V., STOUT B. "Absorption and scattering properties of dense ensembles of non-spherical particles", *Journal of the Optical Society of America A*, vol. 24, pp. 3508–3516, 2007.

[BAR 90] BARBER P.W., HILL S.C., *Light Scattering by Particles: Computational Methods*, World Scientific, New York, NY, 1990.

[BAR 89] BARTON J.P., ALEXANDRE D.R., SCHAUB S.A., "Theoretical determination of net radiation force and torque for a spherical particle illuminated by a focused laser beam", *Journal of Applied Physics*, vol. 66, no. 10, pp. 4594–4603, 1989.

[BAR 02] BARTON J., "Electromagnetic field calculations for an irregularly shaped, near-spheroidal particle", *Journal of the Optical Society of America A*, vol. 19, pp. 2429–2435, 2002.

[BAS 95a] BASS M., *Handbook of Optics, Volume 1: Fundamentals, Techniques, and Design*, McGraw-Hill, New York, NY, 1995.

[BAS 95b] BASS M., *Handbook of Optics, Volume 2*, McGraw-Hill, New York, NY, 1995.

[BOH 88] BOHREN C.F., HUFFMAN D.R., *Absorption and Scattering of Light by Small Particles*, John Wiley & Sons, New York, NY, 1988.

[BOR 94] BORGHESE F., DENTI P., SAIJA R., "Optical properties of spheres containing spherical inclusions", *Applied Optics*, vol. 33, no. 3, pp. 484–493, 1994.

[BOR 02] BORN M., WOLF P.-E., *Principles of Optics,* 7th ed., Cambridge University Press, Cambridge, 2002.

[BOU 12] BOUTIER A. (Ed), *Laser Velocimetry in Fluid Mechanics*, ISTE Ltd, London and John Wiley & Sons, New York, 2012.

[BRI 92] BRITON J.P., MAHEU B., GRÉHAN G., GOUESBET G., "Monte Carlo simulation of multiple scattering in arbitrary 3-D geometry", *Particle & Particle Systems Characterization,* vol. 9, pp. 52–58, 1992.

[BUL 98] BULTYNCK H., Développements de sondes laser Doppler miniatures pour la mesure de particules dans des écoulements réels complexes, PhD Thesis, University of Rouen, France, 1998.

[BUS 02] BUSHELL G.C., YAN Y.D., WOODFIELD D., RAPER J., AMAL R. "On techniques for the measurement of the mass fractal dimension of aggregates", *Advances in Colloid and Interface Science*, vol. 95, pp. 1–50, 2002.

[CHÝ 78] CHÝLEK P., KIEHL J.T., KO M.K.W., "Narrow resonance structure in the Mie scattering characteristics", *Applied Optics*, vol. 17, pp. 3019–3021, 1978.

[CHY 80] CHÝLEK P., KIEHL J.T., KO M. K.W., ASHKIN A. "Surface waves in light scattering by spherical and non-spherical particles", in: *Light scattering by irregular particle*. SCHUERMAN D.W. (ed.), Plenum Press, New-York, pp. 153–164, 1980.

[COO 91] COORAY M.F.R., CIRIC I.R., "Scattering by systems of spheroids in arbitrary configurations", *Computational Physics Communication*, vol. 68, pp. 279–305, 1991.

[DAV 55] DAVIS G.E., "Scattering of light by an air bubble in water", *Journal of the Optical Society of America* A, vol. 45, p. 572, 1955.

[DEB 09] DEBYE P., "Der Lichtdruck auf Kugeln von Beliebigem Material", *Annalen Physik*, vol. 30, pp. 57–136, 1909.

[DES 72] DESCHAMPS G.A., "Ray techniques in electromagnetic", *Proceedings of the IEEE* vol. 60, no. 9, pp. 1022–1035, 1972.

[DIL 06] DILLET J., BARAVIAN C., CATON F., PARKER A., "Size determination by use of two-dimensional mueller matrices backscattered by optically thick random media", *Applied Optics*, vol. 45, pp. 4669–4678, 2006.

[DOI 00] DOICU A., EREMIN Y., WREIDT T., *Acoustic and Electromagnetic Scattering Analysis Using Discrete Sources*, Academic Press, New York, NY, 2000.

[DOI 01a] DOICU A., WRIEDT T., "T-matrix method for electromagnetic scattering from scatterers with complex structure", *Journal of Quantitative Spectroscopy & Radiative Transfer*, vol. 70, pp. 663–673, 2001.

[DOI 01b] DOICU A., WRIEDT T., "Equivalent refractive index of a sphere with multiple spherical inclusions", *Journal of Optics A: Pure and Applied Optics*, vol. 3, pp. 204–209, 2001.

[DRA 94] DRAINE B.T., FLATAU P.J., "Discrete dipole approximation for scattering calculations", *Journal of the Optical Society of America A*, vol. 11, pp. 1491–1499, 1994.

[DRA 10] DRAINE B.T., FLATAU P.J., "Discrete dipole approximation scattering (DDSCAT) code", 2010, available at http://code.google.com/p/ddscat.

[FAR 96] FARIAS T.L., KOYLU U.O., CARVALHO M.G., "Range of validity of the Rayleigh–Debye–Gans theory for optics of fractal aggregates", *Applied Optics*, vol. 35, pp. 6560–6567, 1996.

[FIE 91] FIEDLER-FERRARI N., NUSSENZWEIG H.M., WISCOMBE W.J., "Theory of near-critical-angle scattering from a curved interface", *Physical Review A*, vol. 43, no. 2, pp. 1005–1038, 1991.

[FEI 97] FEIER I., FRIEDSAM H., PENICKA M., "The poisson alignment reference system implementation at the advanced photon source", *5th International Workshop on Accelerator Alignment, ANL/FNAL*, 13–17 October, paper 47, Argonne, IL, 1997.

[FOR 79] FORREST S.R., WITTEN T.A., "Long-range correlations in smoke-particle aggregates", *Journal of Physics A*, *Mathematical and General,* vol. 12, pp. 109–117, 1979.

[FUL 95] FULLER G.G., *Optical Rheometry of Complex Flows*, Oxford University Press, New York, NY, 1995.

[GOO 96] GOODMAN J.W., *Introduction to Fourier Optics*, McGraw-Hill, New York, 1996.

[GOU 88] GOUESBET G., MAHEU B., GRÉHAN G., "Light scattering from a sphere arbitrarily located in a Gaussian beam, using a Bromwich formulation", *Journal of the Optical Society of America*, vol. 5, no. 9, pp. 1427–1443, 1988.

[GOU 09] GOUESBET G., "Generalized Lorenz–Mie theories, the third decade: a perspective", *Journal of Quantitative Spectroscopy & Radiative Transfer*, vol. 110, no. 14–16, pp. 1223–1238, 2009.

[GUI 95] GUINIER A., FOURNET G., WALKER C.B., YUDOWITCH K.L., *Small Angle Scattering of X-Rays*, Wiley, New York, NY, 1995.

[HIT 10] HITRAN, "The HITRAN database, smithsonian astrophysical observatory in Cambridge", 2010, available at http://www.cfa.harvard.edu/hitran.

[HON 06] HONG S.H., WINTER J., "Size dependence of properties and internal structure of plasma grown carbonaceous nanoparticles studied by in situ Rayleigh–Mie scattering ellipsometry", *Journal of Applied Physics*, vol. 100, p. 064303, 2006.

[HOU 95] HOUAS L., TOUAT A., JOURDAN G., "Richtmyer–Meshkov mixing zone study by a multidirectional laser absorption technique", *Physical Review E*, vol 52, pp. 5344–5351, 1995.

[HOV 92] HOVENAC E.A, LOCK J.A., "Assessing the contribution of surface waves and complex rays to far-field scattering by use of the Debye series", *Journal of the Optical Society of America* A, vol. 9, no. 5, pp. 781–795, 1992.

[ILI 10] IL'IN V.B., "Database of optical properties of small particles (Sobolev astronomical institute, DOP)", 2010, available at http://www.astro.spbu.ru/DOP.

[KAY 98] KAYE P.H., "Spatial light scattering as a means of characterising and classifying non-spherical particles", *Measurement Science and Technology*, vol. 9, pp. 141–149, 1998.

[KER 69] KERKER M., *The Scattering of Light, and Other Electromagnetic Radiations*, Academic Press, New York, NY, 1969.

[KOK 09] KOKHANOVSKY A.A., *Light Scattering Reviews 1–4*, Springer Praxis Books, London, 2009.

[KRZ 09] KRZYSIEK M., Particle systems characterization by inversion of critical light scattering patterns, PhD Thesis, Aix-Marseille University, Marseille, France, 2009.

[LAN 84] LANGLEY D.S., MARSTON P.L., "Critical scattering of laser light from bubbles in water: measurements, models and application to sizing bubbles", *Applied Optics*, vol. 23, no. 7, pp. 1044–1054, 1984.

[LAV 99] LAVIGNE C., ROBLIN A., OUTTERS V., LANGLOIS S., GIRASOLE T., ROZE C., "Comparison of iterative and Monte Carlo methods for calculation of the aureole about a point source in the earth's atmosphere", *Applied Optics*, vol. 38, no. 30, pp. 6237–6246, 1999.

[LEN 04] LENOBLE A., Caractérisation optique et étude de la stabilité d'un procédé de fibrage du verre, PhD Thesis, Aix-Marseille University, Marseille, France, 2004.

[LIP 95] LIPSON S.G., LIPSON H., TANNHAUSSER D.S., *Optical Physics*, Cambridge University Press, Cambridge, 1995.

[LIU 08] LIU L., MISHCHENKO M.I., ARNOTT W.P., "A study of radiative properties of fractal soot aggregates using the superposition T-matrix method", *Journal of Quantitative Spectroscopy & Radiative Transfer*, vol. 109, pp. 2656–2663, 2008.

[LOC 96] LOCK J.A., "Ray scattering by an arbitrarily oriented spheroid: II. Transmission and cross-polarization effects", *Applied Optics*, vol. 35, pp. 515–531, 1996.

[LOC 00] LOCK J.A., "Supernumerary spacing of rainbows produced by an elliptical-cross-section cylinder. I. Theory", *Applied Optics*, vol. 39, no. 27, pp. 5440–5451, 2000.

[MAC 95] MACKE A., MISHCHENKO M.I., MUINONEN K., CARLSON B.E., "Scattering of light by large nonspherical particles: ray tracing approximation versus T-matrix method", *Optics Letters*, vol. 20, pp. 1934–1936, 1995.

[MAC 96] MACKOWSKI D.W., MISHCHENKO M.I., "Calculation of the T-matrix and the scattering matrix for ensembles of spheres", *Journal of the Optical Society of America*, vol. 13, pp. 2266–2278, 1996.

[MAR 79] MARSTON P.L., "Critical scattering angle by a bubble: physical optics approximation and observations", *Journal of the Optical Society of America A*, vol. 69, no. 9, pp. 1205–1211, 1979.

[MAR 81] MARSTON P.L., KINGSBURY D.L., "Scattering by a bubble in water near the critical angle: interference effects", *Journal of the Optical Society of America A*, vol. 71, pp. 358–361, 1981.

[MÄT 02] MÄTZLER C., Matlab functions for Mie scattering and absorption – version 2, Research Report no. 2002–11, Institut für Angewandte Physik, Bern, Switzerland, 2002.

[MEI 02] MEIER G. "Computerized background oriented Schlieren", *Experiments in Fluids*, vol. 33, pp. 181–187, 2002.

[MIC 87] MICHELSEN H., *et al*., "Modeling laser-induced incandescence of soot: a summary and comparison of LII models", *Applied Physics B*, vol. 87, pp. 503–521, 1987.

[MIE 08] MIE G., "Beitrâge zur optik truber medien, speziell kolloidaler metallosungen", *Annalen der Physik*, vol. 25, pp. 377–452, 1908.

[MIS 98] MISHCHENKO M.I., TRAVIS L.D., "Capabilities and limitations of a current FORTRAN implementation of the T-matrix method for randomly oriented, rotationally symmetric scatterers", *Journal of Quantitative Spectroscopy and Radiative Transfer*, vol. 60, no. 3, pp. 309–324, 1998.

[MIS 99] MISHCHENKO M.I., HOVENIER J.W., TRAVIS L.D., *Light Scattering by Nonspherical Particles: Theory, Measurements and Applications*, Academic Press, San Diego, CA, 1999.

[MIS 02] MISHCHENKO M.I., TRAVIS L.D., LACIS A.A., *Scattering, Absorption, and Emission of Light by Small Particles*, Cambridge University Press, Cambridge, UK, 2002.

[MIS 04] MISHCHENKO M.I., TRAVIS L.D., "Electromagnetic and Light Scattering by Small Particles", 2004, available at http://www.giss.nasa.gov/~crmim/index.html.

[MIS 07] MISHCHENKO M.I., VIDEEN G., BABENKO V.A., KHLEBTSOV N.G., WRIEDT T., "Comprehensive T-matrix reference database, A 2004–06 update", *Journal of Quantitative Spectroscopy & Radiative Transfer*, vol. 106, pp. 304–324, 2007.

[MIS 10] MISHCHENKO M.I., TRAVIS L.D., "Electromagnetic Scattering by Particles and Surfaces", NASA GISS, 2010, available at http://www.giss.nasa.gov/ staff/mmishchenko.

[MRO 12] MROCZKA J., WOŹNIAK M., ONOFRI F.R.A., "Algorithms and methods for analysis of the optical structure factor of fractal aggregates", *Metrology and Measurement Systems*, vol. 19, no. 3, pp. 459–470, 2012.

[NIK 81] NIKLASSON G.A., GRANQVIST C.G., HUNDERI O., "Effective medium models for the optical properties of inhomogeneous materials", *Applied Optics*, vol. 20, pp. 26–30, 1981.

[NUS 92] NUSSENZWEIG H.M., *Diffraction Effects in Semiclassical Scattering*, Cambridge University Press, Cambridge, 1992.

[ONO 95] ONOFRI F., GRÉHAN G., GOUESBET G., "Electromagnetic scattering from a multilayered sphere located in an arbitrary beam", *Applied Optics*, vol. 34, no. 30, pp. 7113–7124, 1995.

[ONO 96a] ONOFRI F., BLONDEL D., GRÉHAN G., GOUESBET G., "On the optical diagnosis and sizing of spherical coated and multilayered particles with phase-Doppler anemometry", *Particle & Particle Systems Characterization*, vol. 13, pp. 104–111, 1996.

[ONO 96b] ONOFRI F., GIRASOLE T., GRÉHAN G., GOUESBET G., BRENN G., DOMNICK J., XU T.-H., TROPÉA C. "Phase-Doppler anemometry with the dual burst technique for measurement of refractive index and absorption coefficient simultaneously with size and velocity", *Particle & Particle Systems Characterization*, vol. 13, pp. 112–124, 1996.

[ONO 99a] ONOFRI F., "Critical angle refractometry for simultaneous measurement of particles in flow size and relative refractive index", *Particle & Particle Systems Characterization*, vol. 13, pp. 119–127, 1999.

[ONO 99b] ONOFRI F., BERGOUGNOUX L., FIRPO J.-L., MISGUICH-RIPAULT J., "Size, velocity, and concentration in suspension measurements of spherical droplets and cylindrical jets", *Applied Optics*, vol. 38, pp. 4681–4690, 1999.

[ONO 04] ONOFRI F., LENOBLE A., BULTYNCK H., GUÉRING P.-H., "High-resolution diffractometry for the on-line sizing of small transparent fibres", *Optics Communication*, vol. 234, pp. 183–191, 2004.

[ONO 05] ONOFRI F., Diagnostics optiques des milieux multiphasiques, Habilitation Thesis, Aix-Marseille University, Marseille, France, 2005.

[ONO 07] ONOFRI F., KRZYSIEK M., MROCZKA J., "Critical angle refractometry and sizing for bubbly flow characterization", *Optics Letters*, vol. 32, pp. 2070–2072, 2007.

[ONO 09a] ONOFRI F.R.A., KRZYSIEK M., MROCZKA J., REN K.-F., RADEV S., BONNET J.-P., "Optical characterization of bubbly flows with a near-critical-angle scattering technique", *Experiments in Fluids*, vol. 47, pp. 721–732, 2009.

[ONO 09b] ONOFRI F., REN K.-F., GRISOLIA C., "Development of an in situ ITER dust diagnostic based on extinction spectrometry", *Journal of Nuclear Materials,* vol. 390–391, pp. 1093–1096, 2009.

[ONO 09c] ONOFRI F., Modélisation par Méthode Monte Carlo de la diffusion statique de nanosuspensions, Internal report CN2, IUSTI, UMR 6595, CNRS University of Provence, Marseille, France, 2009.

[ONO 10] ONOFRI F., "Small Software for the Calculate the Light Scattering Properties of Single Particles (Delpi v1.1)", 2010, available at http://iusti.univ-provence.fr/document.php?pagendx=12070&project=iusti.

[ONO 11] ONOFRI F.R.A., WOŹNIAK M., BARBOSA S., "On the optical characterization of nanoparticles and their aggregates in plasma systems", *Contributions to Plasma Physics*, vol. 51, nos. 2–3, pp. 228–236, 2011.

[ONO 12a] ONOFRI F.R.A, BARBOSA S., TOURÉ O., WOZNIAK M., GRISOLIA C., "Sizing highly-ordered buckyball-shaped aggregates of colloidal nanoparticles by light extinction spectroscopy", *Journal of Quantitative Spectroscopy & Radiative Transfer,* 2012.

[ONO 12b] ONOFRI F.R.A., RADEV ST., SENTIS M., BARBOSA S., "A physical-optics approximation of near-critical-angle scattering by spheroidal bubbles", *Optics letters*, forthcoming Doc. ID 173169

[OUF 08] OUF F.-X., VENDEL J., COPPALLE A., WEILL M., YON J., "Characterization of soot particles in the plumes of over-ventilated diffusion flames", *Combustion Science and Technology*, vol. 180, pp. 674–698, 2008.

[PHI 81] PHILLIES G.D., "Suppression of multiple scattering effects in quasielastic light scattering by homodyne cross-correlation techniques", *Journal of Chemical Physics*, vol. 74, pp. 260–262, 1981.

[POR 51] POROD G., Die Röntgenkleinwinkelstreuung von dichtgepackten kolloiden Systemen, *Kolloid Z.*, vol. 124, pp. 83–114, 1951.

[REF 10] REFRACTIVEINDEX.INFO, "Refractive Index Database", 2010, available at http://refractiveindex.info.

[REN 93] REN K.-F., GRÉHAN G., GOUESBET G., "Laser sheet scattering by spherical particles", *Particle & Particle Systems Characterization*, vol. 10, pp. 146–151, 1993.

[REN 11] REN K.-F., ONOFRI F.R.A., ROZÉ C., GIRASOLE T., "Vectorial complex ray model and application to 2D scattering of plane wave by a spheroidal particle", *Optics Letters,* vol. 36, no. 3, pp. 370–372, 2011.

[ROZ 03] ROZÉ C., GIRASOLE T., MÉÈS L., GRÉHAN G., HESPEL L., DELFOUR A., "Interaction between ultra short pulses and a dense scattering medium by Monte Carlo simulation: consideration of particle size effect", *Optics Communications*, vol. 220, pp. 237–245, 2003.

[SAE 06] SAENGKAEWA S., CHARINPANITKUL T., VANISRI H., TANTHAPANICHAKOON W., MEES L., GOUESBET G., GRÉHAN G. "Rainbow refractrometry: on the validity domain of Airy's and Nussenzveig's theories", *Optics Communications*, vol. 259, pp. 7–13, 2006.

[SAN 91] SANKAR S.V., BACHALO W.D., "Response characteristics of the phase doppler particle analyzer for sizing spherical particles larger than the light wavelength", *Applied Optics*, vol. 30, no. 12, pp. 1487–1496, 1991.

[SCA 10] SCATTPORT, "Scattering programs, University of Bremen", 2010, available at http://www.scattport.org.

[SEG 81] SEGELSTEIN D.J., The complex refractive index of water, Master Thesis, Kansas City, MO, 1981.

[SHE 73] SHEALY D.L., BURKHARD D.G., "Caustic surfaces and irradiance for reflection and refraction from an ellipsoid, elliptic paraboloid, and elliptic cone", *Applied Optics*, vol. 12, no. 12, pp. 2955–2959, 1973.

[SOP 08] SOPRA, "Optical Database from Sopra SA", 2008, available at http://www.sspectra.com/sopra.html.

[SOR 01] SORENSEN C.M., "Light scattering by fractal aggregates: a review", *Aerosol Science and Technology*, vol. 35, pp. 648–687, 2001.

[STR 10] STRATTON J.A., *Electromagnetic Theory*, McGraw-Hill, New York, NY, 1941.

[TEX 10] TEXLOC, Refractive Index of Polymers, 2010.

[VAN 57] VAN DE HULST H.C., *Light Scattering by Small Particles*, Dover Publications, New York, NY, 1957.

[VAN 97] VAN BEECK J.P.A.J., Rainbow phenomena: on development of a laser-based, non intrusive technique for measuring droplet size, temperature and velocity, PhD Thesis, Technical University of Eindoven, Netherlands, 1997.

[VAN 80] VAN DE HULST H.C., *Multiple Light Scattering*, vols. 1 and 2, Academic Press, New York, NY, 1980.

[VET 04] VETRANO M.R., VAN BEECK J.P.A.J., RIETHMULLER M.L., "Global rainbow thermometry: improvements in the data inversion algorithm and validation technique in liquid–liquid suspension", *Applied Optics*, vol. 34, pp. 3600–3607, 2004.

[WAT 65] WATERMAN P.C., "Matrix formulation of electromagnetic scattering", *Proceedings of the IEEE*, vol. 53, no. 8, pp. 805–812, 1965.

[WAT 04a] WATSON D.M., "Diffraction by a circular aperture or obstacle (Physics lecture notes, outline, and readings)", 2004, available at http://www.pas.rochester.edu/~dmw/phy218/Lectures.htm.

[WAT 04b] WATSON D.M., "Diffraction of rain drops (Physics lecture notes, outline, and readings)", 2004, available at http://www.pas.rochester.edu/~dmw/phy218/Lectures.htm.

[WAT 04c] WATSON D.M., "Rainbows (Physics lecture notes, outline, and readings)", 2004, available at http://www.pas.rochester.edu/~dmw/phy218/Lectures.htm.

[WOL 85] WOLF P.-E., MARET G., "Weak localization and coherent backscattering of photons in disordered media", *Physical Review Letters*, vol. 55, pp. 2696–2699, 1985.

[WOL 87] WOLF P.-E., MARET G., "Multiple light scattering from disordered media. The effect of Brownian motion of scatterers", *Zeitschrift für Physik B (Condensed Matter)*, vol. 65, pp. 409–413, 1987.

[WOŹ 12] WOŹNIAK M., ONOFRI F.R.A., BARBOSA S., YON J., MROCZKA J., "Comparison of methods to derive morphological parameters of multi-fractal samples of particle aggregates from TEM images", *Journal of Aerosol Science*, vol. 47, pp. 12–26, 2012.

[WRI 98] WRIEDT T.A., "Review of elastic light scattering theories", *Particle & Particle Systems Characterization*, vol. 15, no. 2, pp. 67–74, 1998.

[WU 91] WU Z.S., WANG Y.P., "Electromagnetic scattering from multilayered sphere: recursive algorithms", *Radio Science*, vol. 25, pp. 1393–1401, 1991.

[WU 98] WU Z., GUO L., "Electromagnetic scattering from a multilayered cylinder arbitrarily located in a Gaussian beam, a new recursive algorithm", *Progress in Electromagnetics Research*, vol. 18, pp. 317–333, 1998.

[WU 07] WU L., YANG H., LI X., YANG B., LI G., "Scattering by large bubbles: comparisons between geometrical-optics theory and Debye series", *Journal of Quantitative Spectroscopy & Radiative Transfer*, vol. 108, p. 54, 2007.

[XU 07] XU F., Shaped beam scattering by a spheroid and online wet steam measurement by using spectral light extinction method, PhD Thesis, University of Rouen, France, 2007.

[XU 10] XU F., LOCK J.A., GOUESBET G., "Debye series for light scattering by a nonspherical particle", *Physical Review A*, vol. 81, p. 43824, 2010.

[ZHA 96] ZHANG S., JIN J., *Computations of Special Functions*, John Wiley & Sons, New York, NY, 1996.

Chapter 2

Optical Particle Characterization

2.1. Introduction

Optical particle sizing techniques aim to provide statistical data on the shape, size distribution and concentration of small particles (crystals, dust, fibers, cement particles, pollen grains, red blood cells, etc.). There are two main types of techniques. In the first type, a particle sample is examined ex situ without real-time constraints. In the second type, the analysis is performed in situ and in real time, whenever possible, either because no other options are available (access problems, sensitivity of the particulate system to external disturbances, etc.) or because the dynamics of the particulate system are also of interest (such as in studies on combustion, plasmas, suspensions, etc.). Only techniques of the second type are considered in this chapter. Various scientific disciplines require this type of analysis. In astrophysics, for instance, both the size distribution and the composition of interstellar dust need to be characterized. In plasma physics, the nucleation and growth mechanisms of nanocrystals, dust and flakes are still not well understood. This book focuses on fluid mechanics, where it is crucial to characterize the size distribution, concentration, composition and dynamics[1] of the dispersed phase (droplets, bubbles, etc.) interacting with the fluid flow, in real time and with a high spatial resolution, without disturbing the flow itself.

Most optical particle characterization (OPC) techniques require an accurate description of the interaction between light and matter, that is, between the physical properties (shape, material composition, etc.) of the particles of interest and the

---

Chapter written by Fabrice ONOFRI and Séverine BARBOSA.

1 See the book "Laser Velocimetry in Fluid Mechanics" by the same authors [BOU 12].

properties (intensity, phase, etc.) of the light they scatter and absorb (e.g. see Chapter 1). OPC techniques have to characterize as many properties as possible on the flowing particles (whose diameter ranges from nanometers to a few millimeters, see Figure 2.1), by simply analyzing, in a few microseconds or milliseconds, a scattered intensity in a particular angular range, a fringe spacing or a spectrum, etc.

Optics may be viewed as a length-measuring tool whose length scale is in the order of fractions of a micrometer (λ = 0.38–0.78 μm in the visible spectrum). Chapter 1 emphasizes the differences in particle light scattering and absorption depending on whether the particle diameter D is much smaller $\left(D/\lambda \ll 1\right)$, on the order of magnitude $\left(D/\lambda \approx 1\right)$ or much larger $\left(D/\lambda \gg 1\right)$ than the illumination wavelength λ. The incident wavelength also affects the diffusive or specular nature of the particle surface, and its sphericity, to some extent. Given the extent of the field, the authors choose to review only the principles of the most widely used techniques, as well as those thought to be the most promising, for the optical characterization of the size, shape and composition of particles (drops, bubbles, nanoparticles and the aggregates of these particles) that are observed in common particulate systems and multiphase flows (suspensions, sprays, bubbly flows, dusty plasmas, etc.). Special emphasis is placed on those techniques facilitating in situ and dynamic measurements.

Figure 2.1. *Size range for particles encountered in nature and industry*

Figure 2.2. *Scanning electron microscope (SEM) images of solid particles: a) crystals, b) abrasive particles, c) silica beads, d) cotton fibers, e) pollen grains and f) bacteria*

2.2. Particles in flows

2.2.1. *Diameter, shape and concentration*

For particle characterization, it is important to have *a priori* estimates for the size range, shape and concentration of the particles in the flow:

$$\begin{pmatrix} \text{Diameter} \\ D << \lambda \\ D \sim \lambda \\ D >> \lambda \end{pmatrix} \cap \begin{pmatrix} \text{Sphericity} \\ \varepsilon / \lambda >> 1 \\ \varepsilon / \lambda \sim 1 \\ \varepsilon / \lambda << 1 \end{pmatrix} \cap \begin{pmatrix} \text{“Concentration”} \\ \Lambda / L > 1 \\ \Lambda / L \sim 1 \\ \Lambda / L < 1 \end{pmatrix} \qquad [2.1]$$

These parameters determine both the light scattering model and the experimental setup that will be used. Note that the relative refractive indices of the particles are not explicitly given in equation [2.1], but play an important (see Chapter 1) role in the system formulation. Figure 2.1 provides a few orders of magnitude for the mean diameters of particles typically encountered in nature and industry, and Figure 2.2 shows a few scanning electron microscope (SEM) images of these particles. Clearly,

the solid particles have an extremely complex shape. On the one hand, industry also produces very useful spherical glass, plastic or metallic beads. On the other hand, when they are small and not subject to overly strong deformations, liquid droplets and gas bubbles can be modeled as perfect spheres with an unmatched specular surface $(\varepsilon / \lambda \ll 1)$. This is an important feature because most of the OPC techniques used in fluid mechanics are limited to the characterization of perfectly spherical (or slightly irregular) particles, as shown in Table 2.1.

Table 2.1. *The most commonly used optical particle characterization methods for measuring particle size distributions in flows, where T, S and C denote temporal, spatial and field methods, respectively. Some of these techniques also provide information on quantities such as the particle velocity (1, 2 or 3 components), fluxes, concentration or refractive index*

2.2.2. *Statistical representation of particle size data*

2.2.2.1. *Various diameters*

The size of particles within a system can be represented by a mean diameter and a corresponding standard deviation. The mean diameter is usually an equivalent spherical diameter (i.e. the mean diameter of a spherical particle with the same volume, the same specific surface area or the same number). Furthermore, the mean diameter is frequently defined in terms relevant to flow criteria: dynamics, transfers,

physicochemical processes, etc. Thus, different mean diameters can be calculated depending on the type of information sought:

$$\bar{D}_q^p = \left(\frac{\int_{D_{\min}}^{D_{\max}} D^p n(D) \mathrm{d}D}{\int_{D_{\min}}^{D_{\max}} D^q n(D) \mathrm{d}D} \right)^{1/(p-q)} \qquad [2.2]$$

where p and q are integers with $p \neq q$ and $p, q \leq 4$, $n(D)$ is the probability density function (or the particle size distribution (PSD)) in numbers of particles. The PSD is normalized and bounded by a minimum $D_{\min}$ and a maximum $D_{\max}$ diameter. The mean diameter D_0^1 (p = 0; q = 1) is referred to as the mean number diameter. This diameter is an averaged quantity, with no weighting factors. D_0^2 and D_0^3 are the surface and the volume mean diameters, respectively. D_0^2 is an average value that accounts for the specific surface area of the particles, relevant in processes such as evaporation and polymerization, among others. D_0^3 is an average value that is appropriate for describing volume and mass transport by the flow or inertia phenomena. The following inequality always holds true: $D_0^3 \geq D_0^2 \geq D_0^1$. For a given particulate system, the volume PSD is always shifted toward larger diameter particles relative to the PSD number (see Figure 2.3). The Sauter mean diameter D_2^3 accounts for and compares volume (momentum, inertia) and surface effects (drag, evaporation) in the particulate system. Thus, the Sauter diameter is widely used in both modeling and experimental studies in fluid mechanics.

OPC techniques are associated with a particular mean diameter. For instance, imaging techniques provide usually raw particle sizes as number D_0^1 or as surface D_0^2, whereas the rainbow diffractometry provides raw particle sizes with a complex weighting factor $D_0^{7/3}$. Indeed, when comparing statistical data obtained with different techniques, the statistics must be converted to the same and most appropriate format regarding the system under study.

The number N of particles being characterized is always limited in practice. Thus, a useful discrete form of equation [2.2] is:

$$\bar{D}_q^p \approx \left(\frac{\sum_i D_i^p n_i(D_i) \Delta D_i}{\sum_i D_i^q n_i(D_i) \Delta D_i} \right)^{1\backslash(p-q)} \qquad [2.3]$$

where n_i is the number of particles with diameters that pertain to the bin (i.e. size class) centered on D_i with a width ΔD_i, and $N = \sum_i n_i$ denotes the total number of sampled particles.

The median diameter, denoted by $D_{(50)}$ or $D(50)$, divides the PSD into two equal parts in terms of the number or volume of the particles in the sample:

$$\left[\int_{D_{\min}}^{D_{(50)}} D^p n(D)\mathrm{d}D\right]^{1/p} = \frac{1}{2} \qquad [2.4]$$

The Stokes' diameter D_{St} is the mean diameter of a sphere with the same terminal velocity (sedimentation at low Reynolds numbers) and specific mass as the particles in the sample:

$$D_{\mathrm{St}} = \sqrt{\frac{18\mu V_{\mathrm{St}}}{(\rho_p - \rho_f)g}} \qquad [2.5]$$

where $\mu, V_{\mathrm{St}}, D_{\mathrm{St}}, \rho_p, \rho_f$ and g represent the dynamic viscosity of the flow, the Stokes' velocity (i.e. the sedimentation velocity) of the particle, the particle mass density, the density of the surrounding gas or liquid, and the acceleration due to gravity, respectively. The aerodynamic mean diameter, which is sometimes denoted by D_a, is the diameter of a sphere of unit density with the same terminal velocity as the mean terminal velocity of the particles in the sample. The Stokes' diameter and the aerodynamic diameter are frequently extracted from optical measurements (i.e. using imaging or laser velocimetry techniques). Strictly speaking, D_{St} and D_a are deduced not from the light scattering properties of the particles but from hydrodynamic and aerodynamic considerations. Therefore, these diameters can significantly differ from those measured by conventional optical methods. Many other definitions exist for the mean diameter [REN 98, XU 02, PRO 04].

2.2.2.2. *Higher-order statistical moments*

The standard deviation σ_D provides information on the width of the PSD:

$$\sigma_D^2 = N^{-1}\sum_i n_i \left(D_i - \bar{D}\right)^2 \qquad [2.6]$$

The PSD is considered to be a monodisperse when the standard deviation is small relative to the mean diameter, and polydisperse when the standard deviation is

non-negligible relative to the mean diameter. The relative width of a distribution is a rather subjective point, which may differ significantly from one application (or field) to the next. Nevertheless, generally speaking a PSD is considered as monodisperse when $\sigma_D / \bar{D} \leq 0.1$. The PSD is said to be unimodal when the distribution clearly shows a single peak (i.e. a mode, as in a normal distribution) and multimodal when the distribution shows several modes (as in the superimposition of several normal distributions). More information on the shape of the size distribution and higher-order statistical moments of the particle diameter are provided by the degree of asymmetry (the skewness, *S*) and flatness (the kurtosis factor, *K*):

$$S \approx \left((N-1)\sigma_D^3\right)^{-1} \sum_i \left(D_i - \bar{D}\right)^3;\ K \approx \left((N-1)\sigma_D^4\right)^{-1} \sum_i \left(D_i - \bar{D}\right)^4 \qquad [2.7]$$

$S = 0$ for a perfectly symmetrical distribution (e.g. a normal distribution); $S > 0$ for the most commonly encountered cases where there is a PSD tail toward larger particle diameters (e.g. a log-normal PSD) and $S < 0$ if the tail is directed toward smaller particle diameters. Briefly, the kurtosis factor ($K \approx 3$ for a normal distribution) quantifies the weight of the tail relative to the mode of the distribution [REN 98, XU 02].

2.2.2.3. *Size distributions*

The PSD representation may be considered to be the ultimate description of the system, but it must be emphasized that it is fundamental to ensure which type of distribution is obtained, number $n(D)$, surface $s(D)$ or volume $v(D)$, with:

$$\int_0^\infty n(D)\,\mathrm{d}D = \int_0^\infty s(D)\,\mathrm{d}D = \int_0^\infty v(D)\,\mathrm{d}D = 1 \qquad [2.8]$$

These various distributions describe the same particulate medium but are usually very different (except if the sample is monodisperse, see Figure 2.3). In many situations, the shape of the PSD of real particle systems (e.g. sprays and powders) is close to those of well-known analytical distributions. The most commonly observed and used one is the log-normal distribution (see Figure 2.3), which is a two-parameter distribution:

$$n(D)_{\mu,s} = \frac{1}{Ds\sqrt{2\pi}} \exp\left[-\frac{\left(\ln D - \mu\right)^2}{2s^2}\right] \qquad [2.9]$$

where the parameters μ and s correspond to the mean and standard deviation of the logarithm of the particle diameter. These parameters can be related to the more intuitive mean diameter and standard deviation of the particles as follows:

$$\mu = \ln \bar{D} - s^2/2; s^2 = \ln\left(\sigma_D{}^2/\bar{D}^2 + 1\right) \quad [2.10]$$

$$\bar{D} = \exp\left[\mu + s^2/2\right]; \quad \sigma_D^2 = \bar{D}^2\left[\exp\left(s^2\right) - 1\right] \quad [2.11]$$

Other important distributions (gamma, Rosin–Rammler, power law, etc.) may be more or less relevant depending on the size range, the physical processes or the field being studied (e.g. [REN 98, XU 02, PRO 04]).

Figure 2.3. *Log-normal particle size distributions, in number, surface and volume, for different moments (mean sizes and standard deviations)*

2.2.3. *Concentrations and fluxes*

The spatial concentration and the flux of particles are also fundamental quantities required for characterizing particle flows and performing mass balance calculations. Thus, the number of particles per unit volume, or per unit surface and per second, is often required in addition to the PSD. The measurement of a particle concentration requires the characterization of the dimensions of the optical probe volume and a

reference surface needs to be defined in order to estimate the particle flux and the particle size–velocity correlation. The sign of the particle velocity is required to calculate the net flux. Unfortunately, very few OPC techniques can simultaneously characterize particle size and dynamics. In most cases, the measured concentration and fluxes are only estimated as relative values requiring a calibration step.

For a given particulate medium, the concentration per unit volume may be described in terms of the number C_N, specific surface area C_S and volume C_V of the particles. For spherical particles, these concentrations are related to each other as follows:

$$C_V v(D) = \frac{\pi D^3}{6} C_N n(D), \quad C_S s(D) = \frac{\pi D^2}{2} C_N n(D) \qquad [2.12]$$

In fluid mechanics[2] (e.g. [TRO 11]), the particle concentration reflects the strength of the interactions between the particles and the fluid flow (in terms of momentum transfer, induced turbulence, etc.). For optical techniques, the effective density of a particulate system is related to the local optical thickness, which itself depends on both the system turbidity (particle shape, size, refractive index, illuminating wavelength, etc.) and dimensions (see section 1.8 for details).

2.3. An attempt to classify OPC techniques

A first classification was operated at the beginning of this chapter. OPC techniques may also be distinguished apart each other, depending on whether the measured quantity is fundamentally time dependent (dynamic) or not (static), or whether particle size–velocity correlations are accessible or not. Obviously, there exist many other classification criteria as detailed later on and in Table 2.1.

2.3.1. *Physical principles and measured quantities*

When light interacts with particles, the light probes and transports different information toward the observer and the detection optics. A brief classification of techniques grouped by common hypotheses and constraints is given below:

– static intensity: analysis is performed over a certain spectral range (light extinction spectrometry, section 2.11), an angular range (diffractometry techniques, section 2.6 and section 2.7) and/or spatial range (e.g. shadowgraph imaging, section 2.8);

2 See [BOU 12] by the same authors.

– polarization state of the scattered light (e.g. ellipsometry techniques, section 2.5);

– inelastic scattering intensity or frequency shift (e.g. laser-induced fluorescence, section 2.13 and Chapter 3) or other inelastic or nonlinear scattering (e.g. Chapter 5);

– phase delay (phase Doppler interferometry, section 2.4; out-of-focus interferometric imaging, section 2.8) and quasi-static scattering (dynamic light scattering, section 2.12).

2.3.2. *Nature and procedure to achieve statistics*

How the statistics are obtained is also a feature that distinguishes OPC techniques from a fluid mechanics perspective (see Table 2.1 and Figure 2.4).

Figure 2.4. *Schematic of different approaches for obtaining particle statistical properties: a) counting methods (temporal averaging); b) spatial (spatial integration and averaging) and c) field methods (spatio-integral averaging)*

Counting, punctual or temporal techniques characterize the individual particles passing through a small optical probe volume (see Figure 2.4). The PSD is obtained by integrating the properties of a large number of single particles over time. These techniques provide a number of particle. Some techniques simultaneously measure the velocity of each detected particle and the effective dimensions of the probe volume for each size class (as in phase Doppler interferometry). Thus, net fluxes are deduced, as well as the size–velocity correlation and the concentration of particles in the flow. These techniques usually have a high spatial and temporal resolution, making them particularly suitable for rather dense (but still dilute) flows or for boundary layer investigations. Unfortunately, these are time-consuming techniques due to the small probe volume involved and are inappropriate for characterizing flows with spatial instabilities.

With integral or spatial techniques, the ensemble of particles located in a large optical probe volume is characterized quasi-instantaneously, that is, in a snap shot.

The resulting statistics correspond to spatially averaged flow properties. These techniques are not suitable for studying particle dynamics in flow. Some of these techniques can measure the absolute particle concentration (such as forward diffractometry), but none of them can measure fluxes.

Field methods or spatio-temporal techniques have emerged over the last few years. Imaging (section 2.8) and digital holography (section 2.10) techniques (using a fast video camera and a high-frequency pulsed laser) are representative of these techniques. Both the spatial and the temporal properties of the particulate flow are recorded in a given sequence. Analyzing the sequence of images or holograms by a particle tracking method allows determining the position (2D/3D), the velocity (2C/3C) and the diameter of each particle. These are spatial techniques because the particle ensemble-averaged properties can be calculated over a rather large spatial domain. However, these are also punctual techniques in the sense that the position of each particle is known and temporal statistics can be evaluated at a specified point within the flow. These techniques are still under development, and the reliability of the measurements of the concentration and fluxes remains to be demonstrated. They are also limited to particle sizes much larger than the wavelength.

2.4. Phase Doppler interferometry (or anemometry)

2.4.1. *Principle*

This technique is an extension of the well-known laser Doppler velocimetry (or anemometry) technique (i.e. LDV or LDA, [BOU 12]) and is commonly referred to as phase Doppler anemometry (PDA) or when implemented in instrumentation as a phase Doppler particle analyzer (PDPA) [DUR 75, BAC 84, BUE 88]. It is more accurate and preferable to call this technique phase Doppler interferometry (PDI) [ONO 03].

PDI exploits the fact that the phase ϕ of the optical Doppler signal generated by a spherical particle crossing the optical probe volume of a laser Doppler velocimeter is directly related to the particle diameter and, to a lesser extent, the particle refractive index. For known system optical parameters, the theoretical phase–diameter relationship of the PDI system can be determined from geometrical optics or Lorenz–Mie theory (LMT) (see Chapter 1) (Figure 2.6(c) and section 2.4.2).

It is impossible to measure an absolute phase in practice. Thus, these interferometers deduce the particle diameter from the phase-delay measurement between the Doppler signals, recorded by different detectors. To minimize alignment labor and for more complex reasons, the detectors are placed side-by-side behind a single collection lens. Using the principles of LDV, one component of the

particle velocity is obtained from the measurement of the heterodyne Doppler frequency ν_D of one of the collected signals, given the spacing δ_f of the fringes within the optical probe volume. As shown in Figure 2.5, the particle velocity component V_x is calculated from $V_x = \delta_f \nu_D$. The other velocity components of the particle are accessible when two other probe volumes are used [BOU 12]. For size measurements, using three detectors $\left(D_i,\ i = 1-3\right)$ provides more sensitivity to the particle size than two detectors, without decreasing the size dynamics (i.e. due to an ambiguity of 2π in any phase measurement). Indeed, three-detectors PDI operates like a Vernier system. An initial estimate of the diameter D_{12}^{Mes} is obtained from the measured phase delay $\Delta\phi_{12}^{\text{Mes}}$. This initial estimate compensates for the possible ambiguity in 2π in the phase delay $\Delta\phi_{13}^{\text{Mes}}$ that is used to obtain an improved estimate of the diameter, D_{13}^{Mes} [ONO 96b]:

$$
\begin{aligned}
D_{12}^{\text{Mes}} &\equiv \Delta\phi_{12}^{\text{Mes}} \left(\frac{D^{\text{Th}}}{\Delta\phi_{12}^{\text{Th}}} \right), \\
D_{13}^{\text{Mes}} &\equiv \left(\Delta\phi_{13}^{\text{Mes}} + 2\pi q \right) \left(\frac{D^{\text{Th}}}{\Delta\phi_{13}^{\text{Th}}} \right), \\
q &= \text{INT}\left\{ \frac{1}{2\pi} \left[\Delta\phi_{12}^{\text{Mes}} \left(\frac{D^{\text{Th}}}{\Delta\phi_{12}^{\text{Th}}} \right) \left(\frac{\Delta\phi_{13}^{\text{Th}}}{D^{\text{Th}}} \right) - \Delta\phi_{13}^{\text{Mes}} \right] + \frac{1}{2} \right\}
\end{aligned}
\qquad [2.13]
$$

Figure 2.5. *Geometry of a PDI system with a) one velocity component; b) form of the nominal probe volume of the system and c) illustration of the virtual fringe pattern at the crossing of two coherent beams that are either both parallel or perpendicularly polarized*

The superscript (Th) in equation [2.13] denotes the theoretical phase delay for a given diameter, q is an integer that accounts for possible 2π-jumps in the phase delay and INT symbolizes the nearest integer function. As depicted in Figure 2.6(c), the ratio of the slopes of the relationships between the diameters and the phase delays is of the order from two to four. This ratio, or the two estimated diameters, may also be exploited to detect erroneous measurements from particle trajectory effects (that are observed when the probe volume diameter $2\omega_x$ is not sufficiently large relative to the particle size, i.e., $2\omega_0 / D \leq 3-5$) or from particle non-sphericity [AIZ 94, TRO 96].

The length $2\omega_z \sim 1/\tan\alpha$ of the nominal probe volume of a PDI can vary from a few to tens of millimeters, whereas the lateral probe dimensions only range from a few tens to hundreds of micrometers, that is, $2\omega_x \sim 2\omega_y \sim$ 30–800 μm. The problem with this excessive length is that there must be only one particle within the probe volume at a given time for accurate interpretation of the Doppler signal. Thus, the nominal probe volume length limits the applicability of the technique to highly dilute particulate flows. One way of reducing this length is to use a spatial filter, common to all detectors, into the detection optics. A slit of a width of L = 50–200 μm and a height of few millimeters is used for this purpose. The longitudinal width that can be observed by the detection optics is limited to gL, where g is the optical magnification of the detection optics (typically g = 1–4). The effective probe volume length is thus reduced to a dimension more compatible with fluid mechanics requirements, that is, $2\omega_z \sim$ 50–800 μm. Matters are slightly more complicated as the detection optics may be located at different off-axis ϕ and elevation ψ angles. As a simplification, the probe volume of a PDI is modeled as a truncated cylinder, yielding an expected probe volume $\sim\pi(\omega_x)^2 gL$ (e.g. ~0.016 mm^3 for the classical optical parameters L = 100 μm, g = 2.5, $2\omega_x$ = 100 μm and ϕ = 30°) [BER 07, ALB 03].

Figure 2.6. *a) Experimental cross-section of the optical probe volume of a phase Doppler interferometer; b) typical electrical Doppler signals produced by three photodetectors when a small particle is passing through the probe volume; c) schematic of the phase–diameter relationship of a phase Doppler system*

The intensity of an optical signal must exceed a certain threshold to be detected. With a photomultiplier, the signal must exceed a threshold voltage. For a set detection threshold, the dimensions of the effective optical probe volume depend on the particle diameter, the trajectory within the probe volume, the gain of the detectors, the laser power (which may depend on the room temperature), the particle concentration in the flow surrounding the PDI probe volume and even the fouling of the experimental optical windows. Thus, one can understand why optical techniques do not generally measure concentration or flux accurately. However, PDI uses a unique probe volume correction to improve accuracy. This method is based on measuring the particle transit time (TT) within the probe volume. The highest accuracy is typically achieved with a two- or three-velocity component system, but the method is described here for a system with a single velocity component system, for simplicity (see Figure 2.7(b)). Given the particle transit time and a velocity component V_x, one projection of the particle path length inside the optical probe volume can be deduced from the current flow conditions, electronics settings and the particle size, $L_x = V_x TT$. By repeating this procedure for all the detected particles (where there are hundreds or thousands of particles per size class), PDI can estimate the actual width of the measuring volume for each size class [SAF 84]. With some additional assumptions [BER 07, ALB 03], this method normalizes the particle count rate for each size class to obtain absolute values of the local particle concentration in the flow and the corresponding flux (i.e. across a reference surface perpendicular to the *x*-axis). To our knowledge, PDI is the only OPC technique that integrates real-time, in situ and self-calibration measurements of the optical probe volume dimensions. However, the characterization of the local statics (e.g. time averaged diameters, velocities, inter-distances, fluxes, etc.) and correlations (e.g. size-velocity) requires to analyze dozens or even hundreds of thousands of particles.

Figure 2.7. *Schematic of the principles of a) spatial filtering methods for reducing the effective length of the nominal probe volume and b) the procedure for estimating the lateral dimensions of the probe volume on-line*

2.4.2. *Modeling the phase–diameter relationship*

A model at varying levels or rigor and accuracy can explain the relationship between the particle diameter and the phase delays between Doppler signals. In section 2.4.2.1, we first present a heuristic approach that was originally (and still is) used to introduce the principles of LDV. More rigorous models are based on geometrical optics and LMT.

2.4.2.1. *Fringe model and geometrical optics*

The reader must keep in mind that the fringe model [DUR 81] is a heuristic model that is presented more as a curiosity than for rigor. The model has almost no practical application [ONO 02], but it is commonly used, and thus, we have tried to elucidate its origins.

Figure 2.8. *Interpretation of the phase–diameter relationship using the heuristic fringe model*

The focal length of a spherical particle in air may be expressed, within the paraxial approximation, as follows:

$$f \approx m\frac{D}{2}\left[2\left(m-1\right)\right]^{-1} \qquad [2.14]$$

Within the fringe model, the optical probe volume of a PDI or a LDV interferometer contains parallel fringes with $\delta_f = \lambda/\left(2\sin\alpha\right)$, where α is the half-angle between the two incident laser beams. Neglecting reflection and diffraction effects, the particle projects (or scatters) these fringes in the forward region (see Figure 2.8). On a plane (P) located at a large distance L from the particle $\left(L \gg D\right)$, the fringe spacing of the projected fringes is $\delta_p = \delta_f L/f$.

Now consider two photodetectors in the plane (P) that are symmetrical with respect to the optical axis z of the PDI system. The distance between the optical axes of the photodetectors is $l_{12} \approx 2L\psi$ and the detectors makes an angle $\psi_1 \approx -\psi_2 \approx tg\psi$ with the z-axis. The intensity of the projected fringes varies periodically for continuous particle motion perpendicular to the probe volume fringe pattern. One velocity component of the particle $|V_x| = \nu_D \delta_f$ can be measured from the heterodyne Doppler frequency ν_D of the projected fringes. The electrical Doppler signals are phase-shifted by $\Delta\phi_{12}^{\mathrm{Th}} = 2\pi\left(l_{12} / \delta_p\right)$ with respect to each other due to the relative position of the photodetectors. From previous considerations, the phase delay between the signals from the two photodetectors depends on both the particle size and the relative refractive index [ONO 02]:

$$\frac{\Delta\phi_{12}^{\mathrm{Th}}}{D^{\mathrm{Th}}} \approx \frac{\pi}{\lambda}\frac{m}{m-1}\alpha\psi \quad [\mathrm{rad/\mu m}] \qquad [2.15]$$

Simulations using a model based on geometrical optics show that equation [2.15] is accurate within 2.5% for $\alpha, \psi \in [0-5°]$ and $m \in [1.1-1.7]$. However, the accuracy of the previous equation is only relative because the diffraction and reflection effects are far from negligible in the expected validity angular range of this heuristic model.

2.4.2.2. *Model based on geometrical optics*

Here, the phase delay of the Doppler signals is attributed to the difference between the paths of the rays from each beam that are scattered by the particle toward the photodetectors. Within the remote sensing approximation, these coherent rays interfere with each other, producing signals showing a beating frequency, that is, the heterodyne Doppler frequency. For simplicity, only three ray orders are considered here: the reflected $(p=0)$ rays, the directly refracted $(p=1)$ rays and those rays that are refracted after one internal refraction $(p=2)$ (section 1.7). D_1 represents a punctual photodetector placed at a large distance $(r \gg D \gg \lambda)$ from the particle. The particle is located at the center of the optical probe volume. The angular position of the detector is defined by the off-axis Φ_1 and elevation ψ_1 angles (see Figures 2.5 and 2.9). Notice that the photodetectors are located in different scattering planes relative to the incident rays I and II. However, the scattering angles $\theta_{1,I}$ and $\theta_{1,II}$ corresponding to D_1 may be deduced from the following relations [BUL 98, NAQ 93]:

$$\begin{aligned}\cos\theta_{1,I} &= -\sin\alpha + \cos\alpha\cos\psi_1\cos\Phi_1 \\ \cos\theta_{1,II} &= +\sin\alpha + \cos\alpha\cos\psi_2\cos\Phi_1\end{aligned} \qquad [2.16]$$

The notation can be simplified using the particle symmetry. The phase delay is calculated for a general scattering angle θ and the geometry of the phase system will be retroactively accounted for by successively substituting $\theta = \theta_{n,I}$, followed by $\theta = \theta_{n,II}$ (with n = 1, 2 or 3 for each photodetector). Thus, an initial solution is obtained for a plane containing the incident beam, the particle and the photodetector centers. As an additional simplification, the beam is modeled as a plane harmonic wave of wavelength λ_0. The phase–diameter relationship can then be calculated (see Figure 2.35). For convenience, two reference wavefronts are defined: the incident (Σ) wavefront and the exiting wavefront (Σ'). In the absence of particles, the optical path length of a ray passing through the probe volume (and particle) center, perpendicular to the two reference planes, equals $\delta_{\text{Ref}} = m_2 D$.

Figure 2.9. *Schematic of a typical setup for a commercial phase Doppler interferometer*

2.4.2.2.1. Reflected rays (p = 0)

The optical path length of a ray reflected at $\left(\theta_{p=0} \equiv \theta_{1,I,p=0}, \theta_{1,II,p=0}\right)$ is denoted by $\delta_{p=0}$. The differential optical path length relative to the reference path length δ_{Ref} is as follows:

$$\delta_{p=0} - \delta_{\text{Ref}} = m_2\left(a_1 + a_2\right) - m_2 D = -m_2 D\sin\left(\theta_{p=0}/2\right) \qquad [2.17]$$

The scattering angle $\theta_{p=0}$ may be derived from van de Hulst [VAN 57] relations (section 1.7.1) for the relative phase $\phi_{p=0}(\theta, \lambda, m, D)$:

$$\phi_{p=0} = \frac{2\pi}{\lambda_0}\left(\delta_{p=0} - \delta_{\text{Ref}}\right) = -\frac{2\pi}{\lambda_0} m_2 D \sqrt{\frac{1-\cos\theta_{p=0}}{2}} \qquad [2.18]$$

For a PDI system using two beams, two reflected rays interfere at the photodetector. Assuming that these rays have about the same amplitude, the phase of the beating signal is equal to the phase delay between the two reflected rays:

$$\phi_{1,I-II,p=0} = \frac{\pi}{\lambda_0} m_2 D\left[\sqrt{2\left(1-\cos\theta_{1,I,p=0}\right)} - \sqrt{2\left(1-\cos\theta_{1,II,p=0}\right)}\right] \qquad [2.19]$$

For two photodetectors, D_1 and D_2, the phase delay between the two Doppler signals read as:

$$\Delta\phi_{12,I-II,p=0} = \phi_{1,I,p=0} - \phi_{2,II,p=0} \qquad [2.20]$$

Equation [2.20] establishes an implicit relation between both the phase delay and the particle properties (the particle diameter and relative refractive index).

2.4.2.2.2. Refracted rays ($p = 1$)

For refracted rays scattered in the direction θ, the differential optical path length reads as:

$$\delta_{p=1} - \delta_{\text{Ref}} = \left(m_2 b_1 + m_1 b_2 + m_2 b_3\right) - m_2 D \qquad [2.21]$$

where $b_3 = b_1 = R\left(1-\sin\tau\right)$ and $b_2 = D\sin\tau'$ (see Figure 2.35). The phase $\phi_{p=1}$ of these rays is as follows:

$$\phi_{p=1} = \frac{2\pi}{\lambda_0}\left(\delta_1 - \delta_{\text{Ref}}\right) = \frac{2\pi}{\lambda_0} D\left[m_1 \sin\tau'\left(\theta_{p=1}\right) - m_2 \sin\tau\left(\theta_{p=1}\right)\right] \qquad [2.22]$$

The angles τ and τ' may be cancelled out of the equation [2.22] by substituting $m = m_1 / m_2$ and using the two relations $\cos\tau = m\cos\tau'$ and $\theta_{p=1} = 2\tau - 2\tau'$ (section 1.7.1):

$$\phi_{p=1} = \frac{2\pi}{\lambda_0} m_2 D\sqrt{m^2 + 1 - 2m\cos\left(\theta_{p=1}/2\right)} \qquad [2.23]$$

Because $\cos(\theta/2) = \sqrt{(1+\cos\theta)/2}$, the phase of the ray refracted in the $\theta_{p=1}$-direction becomes:

$$\phi_{p=1} = \frac{2\pi}{\lambda_0} m_2 D \sqrt{m^2 + 1 - 2m\sqrt{(1+\cos\theta_{p=1})/2}} \qquad [2.24]$$

The phase of the Doppler signal detected by the photodetector D_1 for the two incident beams is then:

$$\phi_{1,I\text{-}II,p=1} = \frac{2\pi}{\lambda_0} m_2 D \left[\begin{array}{l} \sqrt{m^2 + 1 - 2m\sqrt{(1+\cos\theta_{1,I,p=1})/2}} \\ -\sqrt{m^2 + 1 - 2m\sqrt{(1+\cos\theta_{1,II,p=1})/2}} \end{array} \right] \qquad [2.25]$$

Finally, the phase delay between the signals from the photodetectors D_1 and D_2 is $\Delta\phi_{12,I-II,p=1} = \phi_{1,I,p=1} - \phi_{2,II,p=1}$.

2.4.2.2.3. Refracted rays with one internal reflection ($p = 2$)

Following the same procedure, it is easy to show that the phase of the $p = 2$ rays scattered in the $\theta_{p=2}$ – direction is:

$$\phi_{p=2} = \frac{2\pi}{\lambda_0} D\left[2m_1 \sin\tau'(\theta_{p=2}) - m_2 \sin\tau(\theta_{p=2})\right] \qquad [2.26]$$

The calculation of the scattering angle $\theta_{p=2}$ involves solving a transcendental equation that depends on both τ and τ', with $\theta_{p=2} = 4\tau' - 2\tau$. Thus, it is not possible to obtain an analytical expression for the phase-dependence of these rays on the particle properties. Equation [2.26] is valid, but must be solved iteratively.

The geometrical model produces fairly good results provided that a single scattering mechanism (reflection, single refraction, etc.) dominates the other mechanisms. Until recently, all commercial PDI systems used such a geometrical optics model to derive the phase–diameter relationship. Note that with a little effort, the geometrically based model above can be extended to account for the relative intensity of the various rays (via the Fresnel and divergence coefficients), interferences between different types of rays (e.g. $p = 0$ and $p = 1$), and detectors with a finite aperture, among others (section 1.7, e.g. [SAN 91, NAQ 93, REN 11]).

2.4.2.3. *Electromagnetic model*

Here, we consider a planar PDI system with a symmetrical configuration [AIZ 94], where both the detectors and the incident beams are within the scattering plane (i.e. the off-axis angle $\Phi = 0°$). The photodetector D_1 is positioned at an elevation angle ψ_1, which produces the scattering (or collection) angles $\psi_1 + \alpha$ and $\psi_1 - \alpha$, depending on whether the particle is lighted by beam I or beam II, respectively. The electrical field scattered by the particle in the $\psi_1 -$direction is defined by the superimposition of two fields [ONO 03]:

$$\vec{\mathbf{E}}_s(\psi_1) = \left[E_{s\|I}(\psi_1+\alpha) + E_{s\|II}(\psi_1-\alpha)\right]\vec{\mathbf{e}}_{\|} + \left[E_{s\perp I}(\psi_1+\alpha) + E_{s\perp II}(\psi_1-\alpha)\right]\vec{\mathbf{e}}_{\perp} \quad [2.27]$$

Averaging over a frequency period $1/\nu$ and using the Poynting vector results in the following expression for intensity of the field on the detector surface:

$$\langle \mathbf{S_s} \rangle_{1/\nu} = \frac{1}{4\pi\mu_0 \nu} \mathrm{Re}\left\{\vec{\mathbf{E}}_\mathbf{s} \times \left(\vec{\mathbf{k}} \times \vec{\mathbf{E}}_\mathbf{s}\right)\right\} = \frac{E_s E_s^*}{4\pi\mu_0 \nu} \quad [2.28]$$

Separating the real and complex terms yields:

$$\langle \mathbf{S_s} \rangle_{1/\nu} = \frac{\mathbf{k}}{2\pi\mu_0 \nu}\begin{bmatrix} \left|E_{s\|I}\right|^2 + \left|E_{s\|II}\right|^2 + \left|E_{s\perp I}\right|^2 + \left|E_{s\perp II}\right|^2 \\ +2\,\mathrm{Re}\left\{E_{s\|I}E_{s\|II}^* + E_{s\perp I}E_{s\perp II}^*\right\} \end{bmatrix} \quad [2.29]$$

such that

$$\langle \mathbf{S}_s \rangle_{1/\nu} = \frac{\mathbf{k}}{4\mu_0 \pi \nu}\left(G + \mathrm{Re}\left\{H \exp\left[-2i\pi\nu_D(t)\right]\right\}\right) \quad [2.30]$$

with

$$\begin{cases} \nu = \left(\nu_I + \nu_{II}\right)/2, \\ H = E_{s\|I}E_{s\|II}^* + E_{s\perp I}E_{s\perp II}^*, \\ G = \left|E_{s\|I}\right|^2 + \left|E_{s\|II}\right|^2 + \left|E_{s\perp I}\right|^2 + \left|E_{s\perp II}\right|^2, \\ 2\pi\nu_D(t) = \left(\vec{\mathbf{k}}_I - \vec{\mathbf{k}}_{II}\right)\cdot\vec{\mathbf{V}}(t) + 2\pi\nu_s \equiv \dfrac{4\pi\sin\alpha}{\lambda}V_x(t) + 2\pi\nu_s \end{cases} \quad [2.31]$$

where $V_x(t)$ is the component of the particle velocity in the scattering plane and perpendicular to the main optics axis, and ν_s is the frequency shift of the

two incident beams (details will be provided later) [ONO 03]. Notice that PDI systems use exclusively parallel $\left(E_{s\perp I} \approx E_{s\perp II} \approx 0\right)$ or perpendicular beams $\left(E_{s\parallel I} \approx E_{s\parallel II} \approx 0\right)$. For a photodetector with a solid aperture Ω and a linear response (the intensities of electrical and optical Doppler signals are proportional to each other), the detected signal is:

$$\begin{aligned}
&\left\langle I(t)\right\rangle \propto \int_{\Omega} \left|S_s(t)\right| \mathrm{d}\Omega \\
&= \left\langle G\right\rangle_{\Omega} + 2\sqrt{\left\langle H_i\right\rangle_{\Omega}^2 + \left\langle H_r\right\rangle_{\Omega}^2}\cos\left[\tan^{-1}\left(\left\langle H_i\right\rangle_{\Omega} / \left\langle H_r\right\rangle_{\Omega}\right) - 2\pi\nu_D t\right] \\
&\text{with} \\
&\left\langle G\right\rangle_{\Omega} = \int_{\Omega} G\mathrm{d}\Omega,\ \left\langle H_r\right\rangle_{\Omega} = \int_{\Omega} \mathrm{Re}\left\{H\right\}\mathrm{d}\Omega \text{ and } \left\langle H_i\right\rangle_{\Omega} = \int_{\Omega} \mathrm{Im}\left\{H\right\}\mathrm{d}\Omega
\end{aligned} \qquad [2.32]$$

The three characteristic parameters of the electrical Doppler signals, the pedestal P, visibility V and phase Φ (see Figure 2.6) [ADR 71, NAQ 93, ONO 03, ONO 06] are defined as follows:

$$\begin{aligned}
&P = \left\langle G\right\rangle_{\Omega} / \left(2\pi\mu_0 \nu r\right), \\
&V = 2\sqrt{\left\langle H_r\right\rangle_{\Omega}^2 + \left\langle H_i\right\rangle_{\Omega}^2} / \left\langle G\right\rangle_{\Omega}, \\
&\Phi = \tan^{-1}\left(\left\langle H_i\right\rangle_{\Omega} / \left\langle H_r\right\rangle_{\Omega}\right)
\end{aligned} \qquad [2.33]$$

and

$$\left\langle I(t)\right\rangle = P\left[1 + V\cos\left(2\pi\nu_D t + \Phi\right)\right] \qquad [2.34]$$

Equation [2.34] represents the Doppler signal produced by the particle[3]. A PDI equipped with three photodetectors produces three Doppler signals (I_1, I_2, I_3) and two phase delays, $\Phi_{12} = \Phi_1 - \Phi_2$ and $\Phi_{13} = \Phi_1 - \Phi_3$.

The models above can be directly extended to other PDI configurations, particularly those referred to as conventional, extended and dual mode configurations.

2.4.3. *Experimental setup and typical results*

2.4.3.1. *Optical configuration*

The optical parameters of the PDI system must be optimized to obtain a one-to-one, almost linear phase–diameter relationship (modulus 2π). Good linearity is

3 That is, the same formulation is obtained for illumination by a Gaussian beam [GRÉ 93, ALB 03, ONO 06], a multilayered particle [ONO 96a] or, under certain conditions, a fiber jet [MIG 96, ONO 03].

obtained when the photodetectors collect only light that is purely reflected ($p = 0$) or refracted ($p = 1$) by the particle. This point has already been elucidated with the geometrical optics model. For metallic beads, or strongly absorbing particles, the aforementioned condition is always fulfilled except in the diffraction zone. However, optimization is much more complicated for optically transparent particles (water droplets, air bubbles, etc.) as only optical parameters for which one of the scattering processes is dominant can be used. Given a size range and relative refractive indices for the particles, the corresponding optimized PDI setup may be obtained from parametric studies of the relative weights of the Fresnel coefficients or Debye series (e.g. $I_{p=0} / I_{p=1}$) (see Chapter 1). The key parameter in the optimization procedure, the off-axis angle, is usually set in the range $\phi = 25$–$75°$ for $1.33 \leq m \leq 1.52$ and parallel polarized beams [ONO 03, ALB 03]. Other important parameters are the polarization of the incident beams (e.g. the Brewster condition) and the size (e.g. small for large particles and vice versa) and shape (usually rectangular) of the apertures of the detectors. The elevation and half-beam angles mostly affect the slope of the phase–diameter relationship (which increases with both angles). For practical reasons, most users set the detection optics at an angle of $\phi = 30°$, which is rarely optimal. The detection optics can also be located in the near-backward region (e.g. [BLO 01, ONO 03]) for a more compact setup.

2.4.3.2. *Classical experimental setup*

As already mentioned, a PDI system is very similar to a LDV system, particularly regarding the optics used to form the optical probe volume (see Figures 2.9 and 2.10). A conventional PDI uses (1) an argon laser (more recent systems preferentially use DPSS lasers) with an optical power ranging from a few hundred milliwatts to several watts. The laser output beam is directed to (2) an optoelectronic device that splits the different laser lines into beam pairs of dissimilar colors (corresponding to usually two and sometimes three wavelengths) and frequency shifts one beam of each pair. This is usually accomplished with (3) an acousto-optic modulator (i.e. a Bragg cell with $\nu_s = 40$ or 80 MHz). The frequency shift of the beams shifts the Doppler signal spectra toward higher frequencies in order to allow the measurement of velocities that are zero as well as to determine the direction of propagation of the particles. Optical fiber couplers (4) and a polarization-maintaining, single-mode optical fiber (5) are used to route the beam pair to the emission optics (6) of the PDI system. The PDI emission optics adjusts the beam expansion (7) and focus (8) of the beam pair within the particulate flow. The nominal optical probe volume (9) is thus defined.

Figure 2.10. *Pictures (1–19) of a commercial phase Doppler interferometer (from Dantec MT [DAN 10]); screen copies of the software windows for (22) control of the optical and electronic setup of the system and (21) the automatic displacement of the optical bench that sets the whole phase Doppler system*

Figure 2.11. *Examples of local statistics obtained for a fluidized bed (glass beads in air) [BER 07] by a phase Doppler system: a), b) velocity histograms (U: axial; V: radial velocity components), c) histogram of the particle sizes, d), e) size–velocity correlation for the two velocity components and f) particle transit time (TT) versus arrival time (AT) within the probe volume*

The collection optics (10) is basically composed of a group: of collecting lenses (11) (whose focal length, as for the emission optics, allows the measurement distance to be adjusted); optical masks (12) to differentiate and control the aperture of each detector; spatial filtering optics (basically, a slit (13)); and optical coupler (14) and multimode optical fibers (15) to collect and direct the collected light fluxes toward the photodetectors. The photodetectors are equipped with interferential filters (17) and often located in a separate device, integrated with a phase calibration unit. The electrical Doppler signals are thus amplified, band-pass filtered, digitized and analyzed by a processor (18). The entire system is controlled via a personal computer (19) that facilitates the following actions:

– parameterization and calibration of different elements (band-pass filters, photomultiplier tension, Fourier transform parameters, etc.);

– post-processing of the raw data: arrival time (e.g. to study cluster formation), transit time (e.g. to estimate probe volume dimensions), heterodyne frequencies (i.e. velocity components) and phase delays (particle size);

– performance and statistical calculations (e.g. data and validation rate, mean diameters, histograms, correlations, etc.) and light scattering calculations (phase–diameter relationship, nominal probe volume size, etc.);

– digitization of external signals (flow temperature and pressure, engine phase angle, etc.);

– control of the motorized optical bench, allowing the PDI to automatically scan the particulate flow, and measure profiles, using a pre-defined mesh and parameter set.

2.4.4. *Conclusion*

This technique has found application in various fields. However, due to the constraints imposed on the form and nature of the particles (homogeneous spheres of a known refractive index), it is mainly used to characterize sprays, bubbly flows and fluidized beds (with industrial beads). Manufacturers, [DAN 10, ART 10, TSI 10] in promoting their systems, report an accuracy of approximately 1% for the velocity and from 1 to 2% for the size of spherical particles. These systems can size particles ranging from $D_{\min} \approx 0.5\,\mu\text{m}$ to $D_{\max} \approx 2-3\,\text{mm}$. For a given optical configuration, the maximum dynamic range is on the order of $D_{\max} / D_{\min} < 50$, but $D_{\max} / D_{\min} \leq 30$ is more reasonable for obtaining accurate measurements. However, to completely change the size range, it may be necessary to simultaneously modify the focal length of the transmission and reception optics, as well as the angular position and the mask of the detectors. The maximum velocity range is $V_{\max} / V_{\min} \leq 30$, with $V_{\max} \sim 200-300\,\text{m/s}$. The measurement accuracy for the

concentration and fluxes may be more problematic. This accuracy is approximately 5–20% for an optically dilute particulate flow with a low turbulence rate and a reasonable particle size polydispersity. The error may be much larger for more complex flows. Nevertheless, despite the aforementioned limits, PDI is still the standard technique for the experimental characterization of particle dynamics and size in two-phase flows or multiphase flows. Research laboratories have greatly extended the capabilities of this technique beyond commercial systems as follows:

– Accounting and correction of phenomena related to trajectory effects (that become significant when $2\omega_x / D \leq 3-5$, e.g. [GRÉ 93, AIZ 94, XU 94, TRO 96]);

– Improvement of concentration and flux measurements under normal operating conditions [AIZ 94, TRO 96, BER 07, SOM 04, ROI 01];

– Improvement of the spatial resolution for dense [BUE 01] or microflows [ONO 06];

– Simultaneous measurement of the size, velocity and real and/or imaginary refractive index of particles (for multiphase flows or droplet coalescence studies) [ONO 96b, NAQ 91, ONO 95];

– Characterization of inhomogeneous spherical particles that are stratified (due to heat, thermal or concentration gradients [ONO 96a, RHE 95]) or heterogeneous (paints,suspensions [MAN 94, ONO 99b]);

– Estimation of the size of rough [NAQ 96, ONO 05] or irregular [BLO 01] particles, aggregates [DOI 98a], fibers [ONO 03, MIG 96], and spheroid particles [DOI 98b].

2.5. Ellipsometry

Ellipsometric techniques are used to analyze the polarization properties of scattered light using single particles [MAS 89] or ensembles of particles [MAN 97]. The experimental setup and the signal analysis method may take various forms, ranging from simple (presented here) to more complex.

For spherical particles, the simplest method (known as the polarization technique) analyzes the rate (or modulus) and the phase angle of the linear polarization degree of the scattered light, at a given scattering angle (usually $\theta = 90°$) and wavelength. The emission optics, shown in Figure 2.12(a), are composed of a linear polarized and continuous laser (1), and a set of optical components for controlling the polarization state (e.g. a retardation plate, $\lambda / 2$) (2) and focusing (3) the incident beam. The incident beam creates the optical probe volume (4). Optical detection consists of the collection optics (5), which collects the light scattered by the small particles passing through the measured volume, a spatial

filter (6), an interference filter (7), optics (8) splitting the parallel and perpendicular components of the scattered field and two photodetectors (9). This arrangement, with an incident beam polarized at 45° to the scattering plane, facilitates the measurement of the modulus $\tan\psi$ and phase angle Δ of the collected light, where $P = \tan\psi e^{i\Delta}$ and

$$\begin{aligned} \Delta &= tg^{-1}\left[\mathrm{Im}\left(S_2 / S_1\right) / \mathrm{Re}\left(S_2 / S_1\right)\right] \\ \psi &= tg^{-1}\sqrt{S_2\overline{S}_2 / S_1\overline{S}_1} \end{aligned} \qquad [2.35]$$

Figure 2.12(b) shows the simulated evolution of these two quantities upon increasing the diameters of two types of particles [ONO 11b]. In zone (A), a one-to-one relation exists between the diameter and the phase angle. Thus, the diameters of small particles can be found directly by measuring the phase angle (similar to finding the refractive index from the modulus [MAS 89]). For large particles, see zones (B, C), the situation is more complex, and the method fails [HON 06].

More generally, the other coefficients of the scattering matrix (section 1.2.4.1 and section 1.5) can be determined by modulating the polarization of the incident beam (linear and circular polarizations) and the intrinsic axis of the analyzer (8). Thus, further information on the nature and shape of the particles (or clouds of particles) can be found. Unfortunately, this is a rather time-consuming approach that can hardly be applied to transient regimes or to naturally non-stationary particulate systems [OKA 08, MAN 97].

Figure 2.12. *a) Schematic of an ellipsometer for measuring only the module and phase angle of the scattered light; b) evolution of the two measured parameters versus particle size or refractive index*

2.6. Forward (or "laser") diffraction

2.6.1. *Principle*

It has long been known that the diameter of a spherical particle may be deduced from the measurement of the angular position of the first minimum θ_1 of the diffraction pattern[4]. In the Fraunhofer theory, a spherical and opaque particle has a diameter $D \approx 1.22\lambda_0/\theta_1$ (section 1.6.2). Figure 2.13 shows experimental diffraction patterns for particles of various shapes [2.47].

In the 1970s and 1980s, the principle of what is now referred to as the "laser diffraction" technique was extended to characterize an ensemble of particles by an analysis of scattering patterns at small angles [XU 02]. Figure 2.14(a) shows the basic setup of a conventional forward diffractometer (sometimes, incorrectly called a "laser particle sizer"). This system probes the particulate medium using a parallel beam a few millimeters in diameter, which is produced by a stabilized laser source with an optical power of a few milliwatts. A lens, with focal length f, collects the light scattered in the forward region (diffraction zone) by all the particles that are illuminated by the incident beam and separated by less than, typically, $L \leq 3f/2$, from the collection lens. A photodetector array (usually a CCD or CMOS device)[5] is placed in the Fourier plane of the collection lens to record the far-field intensity of the diffraction pattern of the particulate medium. This setup uses what is sometimes referred to as a direct Fourier transform setup (note that an "inverse Fourier transform setup" may be useful for sizing small particles).

Figure 2.13. *Diffraction patterns for single particles: spheroids, crystals and fibers (source: P.H. Kaye, University of Hertfordshire, Hatfield [KAY 98])*

The photodetector array (or sensor) is unique in many aspects. First, a tiny optical hole in the center of the array allows for the passage of the direct beam.

4 That is, the same formulation is obtained for illumination by a Gaussian beam [GRÉ 93, ALB 03, ONO 66], a multilayered particle [ONO 96a] or, under certain conditions, a fiber jet [MIG 96, ONO 03].

5 CCD (charge coupled device) and CMOS (complementary metal oxide semiconductor).

The small dimension of this hole limits the detection of multiple scattered photons. The intensity of the direct beam is measured by a photodiode in the absence of particles (i.e. reference signal intensity: $I_0(0,\lambda)$) and with particles in the medium (i.e. extinction signal intensity: $\overline{I}(0,\lambda)$). The concentration of particles in the medium may be calculated (section 2.11) from these two intensities, provided the PSD (measured from the analysis of the diffraction pattern) and relative refractive index (generally assumed) of the particles are known *a priori*. The second unique feature of the sensor is related to the diffraction pattern. The diffraction pattern for a spherical particle is composed of bright and dark rings whose intensity decreases rapidly with increasing scattering angles (section 1.6.2). Therefore, the sensor is ideally composed of photoelements whose shape takes the form of concentric rings, where the photosensitive surface increases with the scattering angle. Due to technological constraints, the photoelements may be only portions or sectors of rings (Figure 2.14(b)). The characteristics of the photoelements may also be subject to other constraints, such as the capability to detect irregular particles or for obtaining a matrix with a lower condition number (inversion methods will be covered later). The recording rate is limited by the "frame-rate" of the sensor (a few tens of photosensitive elements are read at a few tens of hertz to kilohertz), as well as by the minimum signal-to-noise ratio (SNR). In addition to providing virtually instantaneous statics, one of the main advantages of this OPC technique is that deviations in the expected properties of the particle have little effect (e.g. in comparison to rainbow diffractometry). This relative tolerance of particle shapes and compositions can be intuitively understood as forward scattering being an "edge" phenomenon, where the average contour of randomly oriented irregular particles may not be very dissimilar from those for equivalent spherical particles. These elementary considerations do not hold for monodisperse particles, i.e. MDRs of spherical and transparent particles, and particles that are small relative to the incident wavelength (section 1.4.1) or particles oriented by the flow (fibers, platelets).

Figure 2.14. *Principle of a) a forward diffractometer (direct Fourier transform) for the characterization of the size distribution and spatial concentration of spherical to slightly irregular particles in flow; b) the CCD sensor of the diffractometer*

Laser diffractometers are widely used in industry and by academic laboratories to size powders, suspensions, and sprays, among others, for scatterer size ranges from a few hundred nanometers to several hundred micrometers. The optical thickness of the particulate medium must be low enough to neglect multiple scattering effects. If this is not the case, the particle fraction or the geometrical thickness of the medium must be reduced so that the beam transmission is typically between 36% and 95%, depending on the particle size range and composition. This limited transmission range drastically reduces the minimum and maximum concentrations that can be measured. Some systems include a correction algorithm for the first effects of multiple scattering to operate at transmission rates as low as 5% [HIR 88, DUM 09].

2.6.2. *Modeling and inversion of diffraction patterns*

Manufacturers publish very little on this strategic component of the system. Consequently, details of the procedure and the regularization schemes used to invert the scattering problem are unknown. Until recently, commercial systems used Fraunhofer diffraction theory (whose limits are well-known)[6] for the direct calculation of diffraction patterns. Currently, LMT is commonly used, especially for small particles. The first inverse methods were based on an iterative procedure assuming a particular PSD shape (e.g. log-normal, power law or gamma distribution) or a direct estimate of the statistical moments of the PSD (e.g. [MRO 93]). Nowadays, most systems appear to use an algebraic inversion procedure [XU 02, HAN 94], which is very similar to that used to invert extinction spectra (section 2.11.2) or near-critical-angle and rainbow scattering patterns (section 2.7).

2.6.2.1. *Algebraic inversion*

Recall that when a particulate medium is optically dilute and the particles are randomly distributed in space, the diffraction pattern can be estimated by summing the individual contributions of all the illuminated particles. The averaged angular intensity profile $\overline{I}(\theta)$ of the diffraction pattern formed by spherical particles, for a number PSD $n(D)$ and concentration C_N, is given by:

$$\overline{I}(\theta) = C_N \int_0^\infty I(\theta, \lambda, D, \tilde{m}) n(D) \, \mathrm{d}D \qquad [2.36]$$

6 That is, the same formulation is obtained for illumination by a Gaussian beam [GRÉ 93, ALB 03, ONO 66], a multilayered particle [ONO 96a] or, under certain conditions, a fiber jet [MIG 96, ONO 03].

where the kernel of the integral $I(\theta,\lambda,D,\tilde{m})$ will be determined using LMT, or, later on, the Fraunhofer theory. Thus, for a volume PSD $v(D)$ bounded by $D_{\min}$ and $D_{\max}$:

$$\overline{I}(\theta) \propto \frac{6C_V}{\pi}\int_{D_{\min}}^{D_{\max}} \frac{I(\theta,\lambda,D,\tilde{m})}{D^3} v(D)\mathrm{d}D \qquad [2.37]$$

where C_V denotes the local particle volume concentration in the particulate medium. Setting $\kappa = 6/\pi$, the algebraic form of the previous integral is $\overline{\mathbf{I}} \equiv \mathbf{I}\cdot\mathbf{V}$, with:

$$\overline{I}_i = \kappa C_V \sum_{j=1}^{M} I_{i,j} v_j \qquad [2.38]$$

where the quantity to be determined $v(D)$ is written as a vector of elements v_j, with j = 1, 2, …, M. $\mathbf{I}$ is a scattering (or diffraction) matrix of dimension $N \times M$. The element $I_{i,j} = I(\theta_i,\lambda,\tilde{m},D_j)/D_j^3$ has to be evaluated for each scattering angle θ_i, $i = 1,2\cdots N$, and the diameters D_{j-1} to D_j within the particle size class such that:

$$I_{i,j} = \int_{D_{j-1}}^{D_j} \frac{I(\theta_i,\lambda,\tilde{m},D)}{D^3}\mathrm{d}D \qquad [2.39]$$

For photosensitive elements with complex shapes and a large aperture angle, the surface Ω_i must be discretized before evaluating the optical response (which is assumed to be linear). Thus, equation [2.39] may be rewritten as:

$$I_{i,j} \propto \iint_{\Omega_i}\int_{D_{j-1}}^{D_j} \frac{I(\theta_i,\lambda,\tilde{m},D)}{D^3}\mathrm{d}D\mathrm{d}\Omega. \qquad [2.40]$$

To determine $V = C_V\, v(D)$, the following equation must be solved: $\overline{\mathbf{I}} \equiv \mathbf{I}\cdot\mathbf{V}$. However, this direct method is unstable, as for extinction (section 2.11). It is preferable to converge iteratively toward the desired solution by minimizing the differences between the measured and the reconstructed intensity profiles. This procedure can be performed using a non-negative least-square (NNLSQ) algorithm [HAN 94]:

$$\left\|\mathbf{I}\cdot\mathbf{V} - \overline{\mathbf{I}}\right\|_{V>0}^2 \qquad [2.41]$$

The Twomey–Philips algorithm [TWO 79] is commonly used [CRA 97, ONO 12a] to stabilize the inversion procedure. The algorithm consists of smoothing the solution during the reconstruction procedure:

$$\left\| \left(\mathbf{I}^{\mathrm{T}}\mathbf{I} + \gamma \mathbf{H} \right) \mathbf{V} - \mathbf{I}^{\mathrm{T}} \overline{\mathbf{I}} \right\|^2_{V>0} \qquad [2.42]$$

where $\mathbf{H}$ is a smoothing matrix and γ is a regularization parameter (section 2.11).

In the single scattering regime (section 1.8.2), the intensity scattered in any direction is proportional to the particle concentration in the medium. Thus, the PSD can be derived in a straightforward manner from any normalized scattering pattern at any particle concentration. Once the PSD is determined, the particle concentration can be estimated from the transmission rate $\overline{T}$ of the direct beam:

$$\overline{T}\left(\theta = 0, \lambda\right) = \overline{I}\left(0, \lambda\right) / I_0\left(0, \lambda\right) = \exp\left(-C_N \overline{C}_e L\right) \qquad [2.43]$$

where

$$C_N \overline{C}_e = C_V \kappa \int_{D_{\max}}^{D_{\max}} C_e\left(D, \tilde{m}, \lambda\right) \frac{v(D)}{D^3} \mathrm{d}D \qquad [2.44]$$

Thus,

$$C_V = -\ln \overline{T} \Big/ \left\{ \kappa L \int_{D_{\max}}^{D_{\max}} C_e\left(D, \tilde{m}, \lambda\right) \frac{v(D)}{D^3} \mathrm{d}D \right\} \qquad [2.45]$$

2.6.2.2. *Simplified inversion*

As previously mentioned, the earliest inversion methods assumed a PSD model. Due to limited computational resources, the Fraunhofer theory (valid for $\pi D / \lambda \gg 1$) was preferred to LMT for solving the direct problem [XU 02]:

$$\overline{I}\left(\theta\right) \propto C_N \int_{D_{\min}}^{D_{\max}} \left[\frac{J_1\left(\pi D \lambda^{-1} \sin\theta\right)}{\lambda \sin\theta} \right]^2 D^2 n(D) \mathrm{d}D \qquad [2.46]$$

If we assume that the PSD of the cloud of particles is of a log-normal type (with $\mu, s,$ see section 2.2.2.3), the intensity profile of the ensemble diffraction pattern is given by:

$$\overline{I}\left(\theta\right) \propto \frac{C_N}{s\sqrt{2\pi}} \int_{D_{\min}}^{D_{\max}} \left[\frac{J_1\left(\pi D \lambda^{-1} \sin\theta\right)}{\lambda \sin\theta} \right]^2 \exp\left[\frac{-1}{2} \left(\frac{\ln D - \mu}{s} \right)^2 \right] D \mathrm{d}D \qquad [2.47]$$

The theoretical intensity profile above can be rapidly compared to the experimental profile as there are only four variables in equation [2.47]: the two parameters of the log-normal distribution and the bounds of the integral. The values of the bounds are generally assumed from physical considerations, whereas (μ, s) may be estimated using a non-negativity-constrained least squares algorithm, for instance. The latter algorithm seeks values of (μ, s) that minimize a χ^2 – test, quantifying the differences between the experimental and reconstructed diffraction intensity profiles (e.g. [ONO 12a]). Obviously, if this procedure is simple to implement, the uniqueness of the solution is not guaranteed. The procedure also fails to reconstruct irregular and multimodal PSDs.

2.6.3. *Typical experimental setup and results*

Most of the laser diffractometers available on the market perform off-line analyses of test samples (e.g. Figure 2.15(a)). The collected sample may be diluted in water or ethanol or dispersed in a gas flow prior to analysis. To limit particle agglomeration or sedimentation problems before and during measurement, liquid suspensions are generally shaken (in a mechanical shaker or ultrasound bath). Despite the interest in these high-resolution instruments, they cannot perform in situ characterization of particulate flows. To the best of our knowledge, only two commercial systems allow characterizing two- and multiphase particulate flows in situ (Figures 2.15(b) and (c)). One diffractometer is dedicated to sizing spherical and slightly irregular particles [MAL 10], while the other diffractometer is dedicated to sizing small fibers [POW 10]. For these two systems, the particulate flow is located in zone 3, that is, between the collimation (zone 2) and Fourier optics (zone 4).

The implementation of a laser diffractometer is particularly simple, at least compared to a PDI system. The alignment procedure consists of optimizing the transmission of the direct beam (maximum intensity at $\theta = 0$ and ideally, zero intensity for $\theta > 0$). Afterwards, the laser is successively turned off and on to record the electrical dark noise of the sensor and the optical background of the experimental room, respectively. These two signals are subtracted from all subsequent measured signals. This procedure limits the application of this technique, as the temperature and the lighting in the room must remain constant, as well as the particulate system radiation (a condition that may be difficult to ensure with dusty plasmas, for instance). The intensity of the direct beam is then measured in the absence of any particles in the flow. This requirement is necessary to obtain an absolute particle concentration but it is also difficult to fulfill in many situations (e.g. for colloidal suspensions).

Figure 2.15. *Pictures of commercial forward diffractometers from a) CILAS (integrated system) [CIL 10]; b) Malvern Instruments (flows) [MAL 10] and c) PowerScope Technologies [POW 10] with (1) a laser source (usually a He–Ne laser of a stabilized laser diode), (2) collimated emission optics, (3) probing zone, (4) detection (i.e. Fourier) optics, (5) photodetectors (usually a dedicated CCD sensor) and (6) electronics hardware and PC link*

Figure 2.16 shows the background noise and a typical measurement signal (i.e. the intensity profile of the diffraction pattern) recorded by a Spraytec system when characterizing spherical glass beads fluidized in dry air. Note that the signal is discretized into 32 bins, that is, the number of photosensitive elements of the optical sensor. Figure 2.17 presents typical inversion results that include the following: time-averaged mean diameters and the corresponding PSD, and the temporal evolution of a few statistical parameters. This laser diffractometer, from Malvern Instruments, characterizes particulate media with widths ranging from approximately 150 mm (particle size range: 0.5–200 μm) to 675 mm (particle size range: 3–850 μm). Note that the measurement distance and the particle size range are related by the proper selection of the focal length of the Fourier optics. From the technical data sheet of this system, the accuracy and reproducibility are 3% and 0.5%, respectively, for a maximum measurement rate of 2.5 or 10 kHz. This system also includes a correction algorithm for the first effects of multiple scattering (optical thickness up to four) and can digitize external signals (temperature, pressure, etc.).

Figure 2.16. *Screen copies of the intensity profiles of the diffraction pattern (32 photoelements) recorded by a Spraytec system: a) optical background noise (without particles) and b) corrected intensity profile of the diffraction pattern obtained for flowing glass beads*

Figure 2.17. *Screen copy of the main window of the Spraytec system showing the averaged particle size distribution and related statistics, as well as the online evolution of statistical properties of the PSD*

2.6.4. *Conclusion*

In summary, laser diffractometry is one of the most widely used OPC techniques for characterizing particulate flows (suspensions, sprays, bubbly and biological flows, etc.) even when the particle shapes and composition deviate (slightly) from what is expected. Except for imaging techniques, laser diffractometry is probably the technique that is easiest to implement and can cover the widest size range for a given configuration. It is also one of those rare techniques that provide a reliable estimation of the particle concentration in the flow. The main limitations of this technique for particulate flows are that no information can be obtained on particle flow dynamics (velocities and fluxes) and that laser diffractometers have a rather limited spatial resolution.

Recent developments concern the inversion procedure (for monodisperse, highly polydisperse or multimodal systems), particles with complex shapes (spheroids, fibers [ONO 04], crystals [KAY 98], and particle aggregates [SOR 01, ONO 11b]) or very small particles [SCH 09].

2.7. Rainbow and near-critical-angle diffractometry techniques

2.7.1. *Similarities to forward diffraction*

In the previous chapter, similarities between the scattering patterns of spherical particles at the forward, rainbow and near-critical scattering angles (Figure 1.21) were indicated. These three phenomena originate from the following:

– A discontinuity in the refractive index for forward diffraction: "rays" propagate in media having refractive indices dissimilar to either side of the particle edges.

– A maximum deviation angle and an internal caustic in the case of the first rainbow: according to geometrical optics the intensity of rays $p = 2$ tends to infinity at the rainbow angle (i.e. the denominator of equation [1.106] is zero).

– A total reflection phenomenon and a weak caustic: the first derivative of the Fresnel coefficient of the rays $p = 0$ is discontinuous for the near-critical angle.

Forward (or "edge") diffraction is easily observable for any particle whose size and relative refractive index are not negligible relative to the incident wavelength and unity, respectively [BOH 88]. Forward diffraction is weakly sensitive to the polarization state of the incident wave. On the other hand, the rainbow scattering pattern is only observed for large and highly symmetric particles (spheres, cylinders, spheroids, etc.) whose refractive index is real (transparent particles) and greater than one. This phenomena is more intense and contrasted for a perpendicular polarized incident wave (section 2.7.2). Near-critical-angle scattering is also observed for large and symmetric particles (which are also smooth) whose refractive index is real (this condition is less drastic than for the rainbow, section 2.7.3) and less than one. Because of the symmetry of spherical particles, these three phenomena cause the scattering of more or less bright or dark, right circular cones of light. The apex of the cones nearly coincides (but not exactly) with the particle center (Figure 1.21). In forward diffraction, the axes of the cones are always directed in the forward direction, $\theta = 0°$. The angular apertures of these cones depend on the particle size and also slightly on the particle relative refractive index. For the first rainbow, the axis of the cones is usually directed in the backward region, $\theta = 180°$, but not always (it is directed in the forward direction for very low relative refractive indices). The angular aperture is also highly dependent on both the size parameter and the refractive index of the particle. In near-critical-angle scattering, the axes of the cones are oriented in the forward or the backward direction, depending on the particle relative refractive index and size [ONO 99a]. Their aperture also depends strongly on the size parameter and the relative refractive index of the particle.

Figure 2.18. *Schematic of the optical setup for a), b) rainbow and c), d) near-critical-angle scattering techniques for characterizing a), c) single particles or b), d) particulate systems; (3) probe volume; (4) far-field detection optics with focal length f; (5) 1D or 2D CCD or CMOS video camera; (6) beam expander (and collimating) optics; (7) cell and (8) mirrors*

The observer must be located at large distance from the particle to analyze these phenomena independently of the relative position of the particle within the optical probe volume. In practice, it is sufficient to place the observer in the back focal plane of a lens (Fourier configuration). In this scheme, the 2D cross sections of the cones are usually seen as full rings with forward diffraction and always as partial rings for the other phenomena (see Figure 2.21). Therefore, it is not surprising that the experimental setups used to record these three phenomena are practically identical (see Figure 2.14 and Figure 2.18).

2.7.2. *Rainbow diffractometry*

Rainbow diffractometry is also known as rainbow angle refractometry or rainbow angle refractometry and sizing technique. The technique is referred to herein as rainbow diffractometry, for the reasons discussed in the previous section.

2.7.2.1. *Principle*

The first systems were dedicated to the characterization of single particles [ROT 90, SAN 93,VAN 94a, HAN 98]. Now, most systems are designed to perform global analyses [VAN 99, VET 04, LEM 06].

For the analysis of individual particles, a coherent and perpendicular polarized laser beam is focused in the flow. The beam waist diameter, that is the optical probe volume formed, is approximately the maximum particle size (see Figure 2.18a). The detection optics is essentially composed of Fourier optics and a CCD video camera (1D or 2D array). To better control the effective dimensions of the optical probe volume, spatial filtering optics may also be integrated into the detection optics (see Figure 2.20). The first rainbow is essentially the superimposition of two fringe patterns: a strong and low-frequency pattern with a low-intensity and a high-frequency pattern. The first pattern is the result of the rainbow phenomena (i.e. rays $p = 2$), which is reasonably well described by the Airy theory [AIR 38] (section 1.6.3). The second pattern, which is also called a ripple structure, is the result of the interference between rays $p = 2$ and $p = 0$. This interference is usually regarded as a parasitic phenomenon (although some studies have capitalized on this phenomenon [VAN 94a, HAN 98]), as it considerably increases the difficulty of the rainbow pattern analysis (detection of peaks or inflection points, etc.). Classically, the particle diameter and refractive index can be deduced from the measurement of the angular position of two fringes of the rainbow pattern. Note that within the framework of the Airy theory, the particle refractive index can be deduced directly from the angular position of the first inflection point of the rainbow intensity profile (see Figure 2.21) [VET 04]. Unfortunately, under real flow conditions, the rainbow signals are noisy and highly sensitive to the particle trajectory within the probe volume (section 2.7.2) [SAE 10], as well as to particle non-sphericity [MAR 94, ADL 98] or non-homogeneity [VET 05]. Therefore, rainbow diffractometry for individual particles is limited to basic studies in well-controlled environments [WIL 07, HAN 98, BOD 10, SAE 10].

To minimize these problems, rainbow refractometry is now principally exploited for characterizing particle ensembles [VAN 99, VET 04, LEM 06, SAE 06] for which it is sufficient to expand the incident beam and develop an inversion procedure. The beam expansion considerably increases the intensity and the SNR of the rainbow signals, while drastically reducing particle trajectory effects. According to some authors, this configuration can also minimize detrimental effects related to particle sphericity and/or non-homogeneity.

For an optically dilute flow, the intensity scattered in the vicinity of the rainbow angle θ by all the particles within the effective probe volume could be approximated by:

$$\overline{I}\left(\theta \sim \theta_{ac}\right) = C_N \int_0^{\infty} I\left(\theta \sim \theta_{ac}, \lambda, D, m\right) n\left(D\right) dD \qquad [2.48]$$

To obtain the number PSD $n(D)$ from the integral above, $\bar{I}$ and I must be measured and calculated, and an inverse problem must be solved. For the calculation of the kernel I, Airy theory [AIR 38, VET 04, WAT 04], Complex Angular Momentum theory [NUS 92, SAE 06] and LMT or Debye theory[7] [BOH 88, HOV 92, ONO 04] are all used. An algebraic or a more phenomenological method may be used for the inversion. Using the phenomenological approach, Figure 2.19 shows the dependence of the rainbow intensity profiles on the main properties of the particulate medium (i.e. the particle relative refractive index, mean diameter and standard deviation for a log-normal PSD):

– Changes in the refractive index primarily induce an angular shift (i.e. rotation) of the entire rainbow pattern;

– The width of the size distribution plays a dominant role in the contrast (i.e. visibility) of the higher order fringes;

– The particle mean diameter mainly controls the angular spreading of the rainbow pattern.

These features have been already exploited to invert rainbow and near-critical-angle signals (section 2.7.3, [ONO 09b, ONO 07]).

Figure 2.19. *Simulation of rainbows produced by different clouds of spherical particles with a Gaussian size distribution: a) influence of the particle mean diameter, when both the related standard deviation and the refractive index are constant; b) influence of the standard deviation, when the mean diameter and refractive index are constant; c) influence of the real part of the refractive index, when the size distribution is constant (λ = 0.6328 μm and perpendicular polarization)*

7 That is, the same formulation is obtained for illumination by a Gaussian beam [GRÉ 93, ALB 03, ONO 06], a multilayered particle [ONO 96a] or, under certain conductions, a fiber jet [MIG 96, ONO 03].

Figure 2.20. *Illustration of the experimental setup for a rainbow diffractometer*

2.7.2.2. *Experimental setup and typical results*

Figure 2.20 shows a schematic of an experimental setup for characterizing dry spraying of glass beads [ONO 05]. The nominal optical probe volume is produced by a fiber-coupled He–Ne laser of 10 mW power, a beam expander and collimating optics. The volume of the optical probe volume is approximately 1 cm^3 for the following collection optics parameters: focal lengths $f_1 = f_2 = 100$ mm, $f_3 = 75$ mm, and a 1,024 × 1,024 pixels and 12 bits CCD. Figure 2.21 compares the intensity profiles of a recorded pattern (1 s exposure time) with those reconstructed by using the Airy and Debye theories $(p = 2)$ and matching the positions of the various fringes. Clearly, the angular positions of the experimental and reconstructed profiles fit quite well, which is not the case for the intensities.

Figure 2.21. *Rainbow pattern recorded for glass beads in flow and comparison between the experimental and reconstructed (simple inversion) intensity profiles*

Figure 2.22. *Comparison of the PSD reconstructed with a rainbow (Figure 2.21) and a forward diffractometer*

The latter effect is due to vignetting effects occurring with these detection optics (i.e. the Fourier configuration does not ensure absolute intensity measurements). However, vignetting effects can be strongly reduced by selecting better-quality optics and by using a diaphragm (this effect has been quantified in [ONO 11a]). Figure 2.22 compares the PSD reconstructed from the data in Figure 2.21 with the PSD measured by a laser diffractometer [MAL 10]. Note that the estimated refractive index (m = 1.503) from these data was also compatible with the glass bead specifications (m = 1.5–1.51) provided by the manufacturer. Figure 2.23 shows that rainbow diffractometry can also be used to characterize liquid–liquid particle systems [VET 04].

2.7.2.3. *Conclusion*

Rainbow diffractometry is relatively easy to implement, although the angular calibration of the setup may be rather tricky. Spatial statistics for flow properties at a well-defined scale can be obtained using this technique. Virtually instantaneous, these statistical values may also be time-averaged (via the exposure time). The ability of this laboratory technique to measure the mean refractive index of the particles is a unique advantage for particle composition or temperature studies.

Figure 2.23. *a) Shadowgraph image and b) rainbow pattern obtained for a suspension of silicone oil droplets in water; c) comparison of the experimental and reconstructed intensity profiles of the rainbow pattern; and d) comparison of the PSD estimated using shadowgraph and rainbow techniques (source: M.R. Vetrano, Institut Von Karman, Rhode-Saint-Genèse [VET 04])*

Despite its strengths, the sensitivity of rainbow diffractometry is detrimental in case of particles exhibiting internal refractive index gradients or inclusions, or particles being non-spherical. Its inability to measure absolute particle concentrations is also clearly a strong limitation. The maximum particle size that can be measured with this technique is approximately 1–3 mm, depending on the sphericity of the particles. A size of 10 μm is probably a minimum particle size for visible light because the angular broadening of the rainbow pattern increases drastically (and the rainbow phenomena disappear gradually) for smaller particles. A ratio of $D_{\max} / D_{\min} \sim 10 - 20$ is probably a maximum value, for a given optical configuration and refractive index.

2.7.3. *Near-critical-angle diffractometry*

2.7.3.1. *Principle*

This technique characterizes the PSD and the mean refractive index of individual [ONO 09b], or an ensemble [ONO 07], of spherical particles, with $m = m_1 / m_2 < 1$ [DAV 55]. These particles are optical bubbles, such as gas bubbles in a liquid (density ratio $\rho_1 / \rho_2 < 1$) or droplets within a liquid (density ratio $\rho_1 / \rho_2 > 1$). The diffraction pattern of the ray $p = 0$ is analyzed in the vicinity of the near-critical scattering angle $\theta_c = \pi - 2\phi_c$, where $\phi_c = \sin^{-1}(m)$ is the critical angle (section 1.6.4). The scattering pattern of a bubble at $\theta \sim \theta_c$ mainly consists of the

superimposition of two fringe patterns (similar to the rainbow diffractometry, section 2.7.2). In the physical optics approximation (POA) introduced by Marston [MAR 79], the low-frequency pattern is directly attributed to the diffraction of the ray $p = 0$, whereas the high-frequency pattern is mainly attributed to the interference between the rays $p = 0$ and $p > 1$. This laboratory technique, as currently implemented, does not provide particle concentration (i.e. absolute) or velocities. Nevertheless, its ability for characterizing the relative refractive index of the particles enables the study of unmatched multiphase flow systems (such as coalescence and mixing) [ONO 09b].

Figure 2.24. *Simulation of the intensity profile of the near-critical scattering patterns of different clouds of bubbles. a) Influence of the bubble mean diameter, when both the related standard deviation and the refractive index are constant. b) Influence of the standard deviation, when the mean diameter and refractive index are constant. c) Influence of the real part of the refractive index, when the size distribution is constant (log-normal size distribution, λ = 0.532 µm and parallel polarization) [ONO 07]*

When this technique is used as a particle counting method or a spatial method, the optical setups and inversion procedures are very similar to those used in forward and rainbow diffractometry techniques. The main difference lies by the angular position of the detection optics, which is close to one side $\theta_c \approx 82.7°$ for air bubbles in water [ONO 09b], and the scattering model employed. For an optically dilute flow, the spatial averaged intensity profile collected at $\theta \sim \theta_c$ is given as:

$$\overline{I}\left(\theta \sim \theta_c\right) = C_N \int_0^\infty I\left(\theta \sim \theta_c, \lambda, D, m\right) n\left(D\right) dD \qquad [2.49]$$

The kernel of the integral above may be computed by using LMT [BOH 88], the POA [ONO 09b, MAR 79, MAR 81] or the CAM theory [NUS 92]. Figure 2.24 shows the influence of the particle composition, mean diameter and standard

deviation for a cloud of bubbles with a log-normal PSD. Note that the behaviors shown are similar to those observed for rainbow patterns (see Figure 2.19).

Figure 2.25. *Schematic of a near-critical-angle refractometer and sizing instruments for the characterization of bubbly flows*

2.7.3.2. *Experimental setup and typical results*

Figure 2.25 shows a block diagram of a laboratory setup [ONO 09b]. Bubbles of various relative refractive indices (air in water, water–ethanol or water–glycerin mixtures, etc.) are produced by different systems (17): a piezoelectric injector, an injector-attended system or porous electrodes [KRZ 09]. The near-critical-angle scattering setup is very simple. A 50-mW Nd-YAG laser, operating at $\lambda_0 = 532$ nm (2), is coupled to a single-mode polarization-maintaining fiber (3) that is mainly used to control the laser beam intensity during the calibration procedure (see Figure 2.25). The laser beam (4) is expanded to achieve a collimated beam with a beam waist diameter $2\omega \approx 12$ mm where the probe volume is located. A half-wave plate (5) allows the polarization state of the beam (usually parallel) to be adjusted. The collection optics (7–11) operate in a Fourier mode and consists of the following components: a wide aperture camera lens (7), a circular diaphragm (to control the probe volume length and limit optical aberrations) (8), two achromatic doublets (9),

a CCD sensor (11) (1,024 × 1,024 pixels; 12 bits) and an interferential filter centered on λ_0 (10). The angular calibration of the system is performed using a goniometer (16). For aqueous bubbly flows, the angular resolution of this optical setup is of $\Delta\theta \approx 0.02°$ for a maximum angular range of $\theta = 70.3–82.8°$. The setup depicted in Figure 2.25 includes two other systems: an interferometric imaging system (using the Nd-YAG laser as the illuminating beam) (14) and a shadowgraph system (equipped with a long-working-distance microscope and a conventional or high-speed video camera) (13). The camera uses a flash lamp (12) and triggering optics (15) to illuminate and detect single bubbles passing through the center of the probe volume.

Figure 2.26. *Air bubble in water: shadowgraph image, near-critical-angle scattering pattern and comparison of the experimental and the reconstructed intensity profiles [ONO 11a]*

Figure 2.26 shows the following typical experimental results obtained for a single air–water bubble: the shadowgraph image, the corresponding near-critical-angle scattering pattern, the intensity profile of the scattering pattern and the reconstructed scattering pattern (using classical LMT). The agreement between the two intensity profiles is astonishing as this large bubble is clearly ellipsoidal, with an ellipticity of $\xi \approx 0.89$ and the major axis within the scattering plane (corresponding to a diameter $D \approx 1{,}040$ μm). Although this technique is used to size spherical particles, the good agreement is because near-critical-angle diffractometry deduces the bubble size from the measurement of the radius of curvature of the bubble in the scattering plane and in the vicinity of the critical impact parameter. If the symmetry of the ellipsoidal bubbles is tilted relative to the scattering plane, the agreement worsens. Note that the refractive index deduced from Figure 2.26, that is $m = 1.3355$, is also in good agreement with that found using an Abbe refractometer, $m = 1.3345$.

Figure 2.27. *Cloud of rising air bubbles in water: a) near-critical-angle scattering pattern; b) experimental and reconstructed intensity profiles (inversion method: LMT-LogNorm); c)–e) comparison of the PSD reconstructed with c) shadowgraph and near-critical-angle scattering techniques (inverse methods: d) LMT-LogNorm and e) LMT-NNLSQ))*

This technique is also used to characterize real bubbly flows. Various results for an air–water bubbly flow with a bimodal PSD (generated by a piezoelectric valve operating in an anharmonic mode) are compared in Figure 2.27, as an example. Shadowgraph statistics are compared to near-critical-angle scattering statistics, depending on whether a PSD model is used to reconstruct the intensity profile (LMT-LogNorm) or not (i.e. algebraic method, LMT-NNLSQ) (see section 2.11.2) [ONO 09b]. The two inverse methods produce a good estimate of the mean diameter and standard deviation of the PSD (as well as the mean refractive index). Only the algebraic method detects the two PSD modes, as expected.

2.7.3.3. *Conclusion*

This technique provides an individual (a counting technique providing temporal statistics) or global (spatial technique providing spatial statistics) characterization of the size distribution and mean relative index of the disperse phase of bubbly flows [ONO 09b, ONO 11a]. When operating in a spatial mode, statistics (recording and inversion) may be acquired in a few seconds with rather limited computational resources. As the statistics are derived from the analysis of the averaged near-critical-angle scattering pattern, it is not necessary to record and store thousands of images before running complex (but not always accurate) blob

analyses, as with the shadowgraph systems. Some evidence also suggests that this diffractometry technique can address more dense flows than the shadowgraph technique, as well as size spheroid bubbles [REN 11, ONO 12b]. A unique feature of the technique is that the mean composition of the bubbles can be estimated, which can be applied to bubble mixing and coalescence studies, for instance. It also allows sizing spherical [ONO 11a, REN 11]) and spheroid bubbles [ONO 12b]. For air bubbles flows, the size dynamic range of this technique is about $D_{max}/D_{min} \leq 15–25$ with $D_{min} \approx 20–30$ μm and $D_{max} \approx 1–2$ mm. Nonetheless, the technique has some drawbacks and limits. As a far-field technique, it fails to analyze bubbly flows showing refractive index gradients and, like most OPC techniques, it does not provide information about the particle absolute concentration or fluxes.

2.8. Classical shadowgraph imaging

Formally, particle imaging techniques record and analyze 2D images, coded as intensity, to characterize the shape and size of particles. The shadowgraph optical configuration is preferred for flow studies because high contrast images can be provided for reasonably high optical magnifications and working distances.

2.8.1. *Principle and classical setup*

To improve image contrast, the illumination source is pulsed, collimated (incident rays are parallel to the optical axis of the imaging system) and set to back-illuminate the particulate system. The imaging optics (magnification optics, color filter and video camera) are placed on the opposite side (Figure 2.28). Such an imaging system, operating in a transmission mode, is usually referred to as a shadowgraph imaging system.

The short exposure time of the video camera (typically, $\delta t \sim 1–100$ μs) and the short duration of the light source pulse Δt limit the particle image blur as the particles move in the flow. In typical applications, a simple flash lamp or a light-emitting diode are sufficient ($\Delta t \geq 10–100$ μs) to freeze the particle motion. In addition, the low coherence of these light sources (spectral bandwidth, $\Delta\lambda \geq 30$ nm) reduces the intensity of the speckle noise (see Figure 2.29). For high speed flows, or when larger flow fields are required, Nd:YAG lasers are usually used for their higher fluence and shorter pulse duration ($\Delta t \sim 3–10$ ns). Unfortunately, the coherence of these lasers ($\Delta\lambda \leq 0.2$ nm) produces an intense speckle noise that hinders particle detection. An optical diffuser (depolished or holographic glass plate), or preferably a fluorescence cell or a fluorescent glass plate, can be used to reduce the laser light coherence. Laser-induced fluorescence significantly enlarges the spectral range of the incident pulse ($\Delta\lambda_F \geq 30$ nm) without prohibitively

increasing the duration time. The trade-off is a drastically reduced fluence and the difficulty to collimate the fluorescent light emission. The high-resolution digital video camera is equipped with a macro-lens or preferably a telecentric video lens or a long-working-distance microscope. The microscope integrates high optical magnifications (0.5×–5×) with working distances (30–500 mm) that are compatible with flow studies. For larger working distances, Schmidt–Cassegrain telescopes may also be used [LAV 12]. In any case, the field-of-view and the effective depth-of-field of the system are directly related to the working distance and the particle properties (see section 2.8.3).

Figure 2.28. *a) Schematics of typical setups employed for the shadowgraph technique; b) typical shadowgraph images of air bubbles in water (D = 400—2,000 μm) illuminated by a flash lamp*

The recorded images can be analyzed using the commercial software supplied with the system [DAN 10, TSI 10, CIL 10, LAV 12, KAN 12, OXF 12, RD 12], or with general purpose imaging software (e.g. with Matlab® [MAT 12] or ImageJ [IMA 12]). Common blob analyses provide particle diameter statistics (e.g. an equivalent spherical diameter based on the particle image surface area or contour), as well as more advanced morphological properties (e.g. particle orientation, surface roughness). When two images are captured with a short interframe delay, a particle-tracking algorithm can be used to measure the particle displacements and consequently, the 2D particle velocity[8].

Reliable PSD estimation requires the recording and processing of a large number of images. In addition, the blob analysis should be able to treat not only "perfect" particle images but also particles that are out-of-focus, incomplete or hidden by other particles (see Figure 2.28(b)). It is obvious, for instance, that the problem

8 See [BOU 12] by the same authors.

arising from screening effects (i.e. hidden particles) affects preferentially the count and validation rate of the smallest particles. In section 2.8.3, a simple model is introduced to account for some these effects.

Figure 2.29. *a) Illustration of the effect of the speckle noise on particle detection; b) shadowgraph image of the atomization of a capillary jet (D=100 µm) by a thermal plasma [GUÉ 08])*

2.8.2. *One-dimensional shadow Doppler technique*

In this variation of the conventional shadowgraph technique (also called shadow Doppler technique [HAR 94]), a shadowgraph system is coupled with a LDV system[9]. The transmission image of each particle passing through the small illuminated region is recorded by a high-frequency linear video camera. By measuring the appropriate particle velocity component (with the LDV system), a 2D image of each particle can be reconstructed line by line. The camera is positioned either directly behind the imaging optics or at the output of a fiber bundle [MAT 04].

Figure 2.30. *a) Classical optical setup for a shadow Doppler system and b) typical images recorded for aluminum particles (mean diameter = 25 µm and velocity = 15 m/s; linear camera: 128 pixels, 64 kHz) [HAR 94]*

9 See [BOU 12] by the same authors.

This interesting OPC technique has been commercialized [KAN 12]. This technique provides valuable information about the particle size, shape and dynamics, but it is limited to optically dilute particulate flows. The resolution for particle diameters at velocities up to 100 m/s is estimated at 4% and 10% for spherical or irregular particles [KAN 12, HAR 94], respectively.

2.8.3. *Calculation of particle images using the point spread function*

The precise calculation of the formation of a particle image by a single lens requires extensive electromagnetic calculations [SCH 89, REN 96, HES 08]. However, this problem can be addressed to some extent with a simplified image formation model (see Figures 2.31 and 2.32).

Figure 2.31. *Schematic for the formation of a shadowgraph image*

In this model, a spherical particle is considered to be a more or less opaque disk, whereas the imaging optics is modeled by its point spread function (PSF) [FDI 10, GOO 96, PEN 87]. The intensity $i(x,y)$ of the particle image on the video camera photoarray is expressed as the convolution product of the object (i.e. particle) function $o(x,y)$ and the PSF $s(x,y)$ of the imaging system:

$$i(x,y) = o(x,y) \otimes s(x,y) \qquad [2.50]$$

The object function reduces to an opaqueness function [PEN 87]:

$$o(x,y) = 1-(1-\tau)\text{circ}\left(\frac{\sqrt{x^2+y^2}}{\gamma a}\right) \text{ with } \text{circ}(r) = \begin{cases} 1, & r \le a \\ 0, & r > a \end{cases} \qquad [2.51]$$

where $r = \sqrt{x^2 + y^2}$ is the radial distance from the disk center (located in the object plane of the imaging optics), γ is the lateral optical magnification of the imaging system (assumed constant in the entire field), a is the particle radius and τ is the particle transmission factor (or contrast factor; $\tau = 0$ for a fully opaque particle). The PSF is a Gaussian function for axisymmetrical imaging optics illuminated by a completely incoherent light source [PEN 87]:

$$s(r) = \frac{2}{\pi\chi^2}\exp\left(-\frac{2r^2}{\chi^2}\right) \qquad [2.52]$$

where χ is the PSF half-width [PEN 87], which depends on the solid aperture A of the imaging optics, the wavelength or the particle distance z_p relative to the object plane (this distance is neglected henceforth). Denoting ρ as the integration variable and I_0 as the modified Bessel function of the first kind, the intensity profile of the image may be expressed as follows:

$$i(r) = 1 - \frac{4(1-\tau)}{\chi^2}\int_0^a \exp\left(-2\frac{r^2\gamma a}{\chi^2}\right) I_0\left(\frac{4\rho r}{\chi^2}\right) d\rho \qquad [2.53]$$

Figure 2.32. *The intensity profile of the image i(r) is calculated using the convolution of the intensity profile corresponding to the particle luminance o(r) and the intensity profile s(r) of the PSF of the detection optics*

Let us introduce the following dimensionless parameters: the radius $\tilde{a}$, the radial coordinate $\tilde{r}$ and the integration parameter,

$$\tilde{a} = \frac{\sqrt{2}\gamma a}{\chi},\ \tilde{r} = \frac{\sqrt{2}r}{\chi},\ \tilde{\rho} = \frac{\rho}{\gamma a} \qquad [2.54]$$

such that the dimensionless intensity profile of the image becomes [FDI 10]:

$$i(\tilde{r}) = 1 - 2(1-\tau)\exp\left(-\tilde{r}^2\right)\int_0^{\tilde{a}} \rho \exp\left(-\rho^2\right) I_0\left(2\tilde{r}\rho\right) d\rho. \qquad [2.55]$$

Figure 2.33(a) shows the evolution of this profile for various particle radii and transmissions. The transmission factor τ controls the particle image contrast, that is the relative amplitudes of the extrema $i_{\min}$ and $i_{\max}$ of the particle image (see Figure 2.33(b)). The dimensionless particle radius $\tilde{a}$ has a drastic influence on the shape of the image profile. For a given object of radius a, $\tilde{a}$ is maximized when the particle is in focus (U-shaped image profile: image in focus with sharp edges) and tends to zero (V-shaped image profile: blurred image) as the object becomes increasingly out-of-focus, because defocusing increases the PSF half-width χ. For a given PSF half-width χ, the edges of the images of small particles are more blurred than images of large particles. The remarks above imply that the detection and validation rate of particle images decreases with the particle size for a given setup and a given set of detection parameters (i.e. $i_{\min}$, image edge gradient, etc.). These effects bias the PSD and related statistics if the effects are not corrected for.

Figure 2.33. *Normalized intensity profiles for the images of spherical particles using the PSF model a) for different values of the particle transmission and radius. b) Illustration of some of the criteria used to evaluate the particle image contrast and the particle diameter*

It is difficult to relate the relative particle width to the particle diameter for particle images with a flared intensity profile. As already mentioned, the height of the profile is controlled by the parameter τ, for a given $\tilde{a}$ value. A low τ value implies a high image contrast and vice versa. The normalized minimum level $\tilde{i}_{\min} = \tilde{i}(0)$ decreases with $\tilde{a}$ and reaches the limit $\tilde{i}_{\min} = \tau$ (i.e. the maximum image

contrast) at sufficiently large $\tilde{a}$. A dimensionless image half-width $\tilde{r}_i(l)$ can be defined from the profile height $h = \tilde{i}_{\max} - \tilde{i}_{\min}$, for a given level *l*. Let us introduce the absolute reference level $\tilde{i}_{\text{ref}}(l)$, $\tilde{i}_{\min} \le \tilde{i}_{\text{ref}}(l) \le \tilde{i}_{\max}$ as follows:

$$\tilde{i}_{\text{ref}}(l) = \tilde{i}_{\min} + lh \qquad [2.56]$$

The dimensionless image half-width $\tilde{r}_i(l)$ is thus independent of the transmission parameter τ:

$$i(\tilde{r}_i) = \tilde{i}_{\text{ref}}(l) \qquad [2.57]$$

The image width is directly related to the particle width if $\tilde{a} \ge 1$. For spherical particles, a value of $l \approx 0.61$ seems to be the best compromise [FDI 10, MAL 00].

This model allows us to understand and quantify the influence of the basic parameters of a shadowgraph system, the aperture of the video imaging system, the particle transmission factor or position relative to the object plane, etc. However, the model is in many ways limited. For instance, it does not predict the presence of a bright spot (the "Arago-Poisson spot", see Figure 2.28) at the center of each particle image that is in focus and the model cannot predict the formation of particles images under coherent illumination (i.e. interference phenomena) [REN 96].

2.8.4. *Conclusion*

The 2D shadowgraph technique (i.e. with the setups depicted in Figure 2.28) is virtually the most powerful OPC technique available, being both intuitive and flexible, with a large size dynamic range and unique capabilities for particle morphology analyses. The technique is also rather cost-effective sharing many common components with PIV, PTV[10] and out-of-focus interferometric imaging techniques. Commercial systems [DAN 10, TSI 10, CIL 10, LAV 12, KAN 12, OXF 12, RD 12] are mostly used to characterize sprays, fibers, crystals, biological cells, etc. From the manufacturer's data sheets, the dynamic range of these systems can reach $D_{\max} / D_{\min} < 100$ with $D_{\min} > 5$ µm for working distances and fields of view ranging from 30 mm to 1 m and 1 to 1,000 mm^2, respectively. The particle velocity may also be measured using particle tracking algorithms[1]. The limit of this technique lies in the minimum measureable particle size, the large computational resources required to store and process the raw data, and all the hidden statistical biases. It is important to realize that the statistics provided by most systems are not corrected for the probe volume dependence on the particle size or for screening effects.

10 See [BOU 12] by the same authors.

2.9. Out-of-focus interferometric imaging

2.9.1. *Principle*

The principle of this technique was developed around 1990–2000 (e.g. [RAG 90, GLO 95, HES 98, MOU 99, MAE 02, KAW 02, DEH 05, PU 05], although many physical aspects were previously known. Depending on the authors or manufacturer, the technique is referred to as Interferometric Laser Imaging Droplet Sizing (ILIDS) or Interferometric Particle Imaging (IPI). As the technique is still under development and to avoid controversy, we shall call this technique out-of-focus interferometric imaging (OFII).

In its basic configuration, this technique characterizes the diameter and two velocity components of all the spherical particles within an optical probe volume produced by a polarized and coherent laser sheet. The optical setup shows several similarities to the PIV setup[11], with a few important differences. The first difference is that the video camera observing the illuminated particles is located at a scattering angle where two scattering processes of nearly equal strength dominate the other processes. This optimum angle is $\theta \approx 67°$ for water droplets, a perpendicularly polarized illuminating beam, specular reflection $(p=0)$ and single refraction $(p=1)$. Other angles are possible, but only this angle will be considered here. When the camera lens is adjusted so that the particle images are perfectly in focus, the particle contours cannot be distinguished. In fact, it is easy to show by simple trigonometric calculations that none of the rays scattered by the particle corresponding contour can reach the video camera at this focus setting. However, the particle image shows two bright spots called "glare spots" (denoted by g_0 and g_1 in Figures 2.34 and 2.35) instead of a demarcated contour. These glare spots are related to the impact $(p=0)$ and exit $(p=1)$ points of the rays that are reflected and refracted by the particle surface in the direction of the video camera. For a given aperture, the camera lens forms the images (denoted by G_0 and G_1, see Figure 2.34) of these glare spots on the camera chip.

The particle diameter can be estimated from the measurement of the distance l_{01} between the images of the two glare spots for a known magnification factor of the camera lens [HES 08, VAN 91]. However, the resolution and dynamics of this method are quite limited. When the particle images are out of focus (i.e. the camera lens is intentionally defocused), the particle image is transformed into a circular disk containing a specific number of fringes (dark and bright, see Figure 2.34). These fringes result from the interference between the images of the two glare spots that superimpose and interfere on the camera chip. The number of fringes in the circular

11 See [BOU 12] by the same authors.

disk depends on both the particle diameter D and refractive index m, as well as the wavelength λ_0 of the illuminating beam and the camera lens angular aperture. Therefore, the principle of the out-of-focus interferometric imaging technique is to analyze the angular frequency of the fringes inside each detected disk to determine the particle size distribution. The two velocity components of each particle are measured by applying PTV onto the associated disk. Next, we detail the principle of this OPC technique, first within the framework of geometrical optics and then, using LMT.

Figure 2.34. *Illustration of the principle of the out-of-focus interferometric imaging technique for a refracting particle (m > 1) [ALB 03]*

2.9.2. *Modeling the diameter–angular frequency relationship*

2.9.2.1. *Geometrical optics model*

Glare spots could be regarded as punctual and coherent light sources that can interfere at infinity, as in Young's famous double slit experiment. When the video camera lens is defocused, the images of the glare points are enlarged and may overlap and interfere on the video camera chip (Figure 2.34). The diameter a_{Dk} of the disk containing the interference fringes can be derived from simple geometrical considerations (e.g. [ALB 03]):

$$a_{Dk}\left(z_P\right) = A\left|1 - z\left(f^{-1} - z_P^{-1}\right)\right|, \qquad [2.58]$$

where A, z, f and z_p denote the diameter of the camera lens (or input diaphragm), the distance between the camera lens and the camera chip (modified by the defocusing), the back focal length of the camera lens and the distance between the camera lens and the particle [SEM 04], respectively. It is clear from equation [2.58] that the diameter of the disk containing the fringes depends on the particle distance z_p, that is the 3D position of the particle may be estimated from the measurement of the diameter of the aforementioned disk and the determination of the 2D position of its centroid.

Figure 2.35. *Out-of-focus interferometric imaging technique: geometrical optics model in the near-forward scattering domain for a) a droplet or beads (m > 1) or b) a bubble (m < 1)*

Let us now calculate the properties of the fringe pattern produced by the interference of the rays refracted and reflected by a spherical particle in the scattering direction θ. The particle, with diameter $D = 2R$ and real refractive index m_1, is illuminated by a plane wave of wavelength λ_0 propagating in a non-absorbing medium of refractive index m_2. For future convenience, let us define a reference ray and two reference surfaces, the initial surface Σ and the final surface Σ' (see Figure 2.35). In the absence of a particle, the reference ray is a ray coming from Σ that passes through the center of the particle, then it is scattered in the θ-direction and reaches the surface Σ'. The optical path difference between the reflected rays δ_0 and the reference ray δ_{Ref} in the θ-direction is given by:

$$\delta_0 - \delta_{\text{Ref}} = m_2\left(a_1 + a_2\right) - m_2 D = -m_2 D \sin\left(\theta/2\right) \qquad [2.59]$$

The corresponding phase delay ϕ_0 is equal to:

$$\phi_0 = \frac{2\pi}{\lambda_0}\left(\delta_0 - \delta_{\text{Ref}}\right) = -\frac{2\pi}{\lambda_0} m_2 D \sin\left(\theta/2\right) \qquad [2.60]$$

Similarly, the optical path difference between the single refracted rays δ_1 and the reference ray δ_{Ref} is given by:

$$\delta_1 - \delta_{\text{Ref}} = \left(m_2 b_1 + m_1 b_2 + m_2 b_3\right) - m_2 D \qquad [2.61]$$

with $b_3 = b_1 = R(1-\sin\tau)$ and $b_2 = D\sin\tau'$. The phase delay ϕ_1 of these rays is expressed as:

$$\phi_1 = \frac{2\pi}{\lambda_0}\left(\delta_1 - \delta_{\text{Ref}}\right) = \frac{2\pi}{\lambda_0} D\left(m_1 \sin\tau' - m_2 \sin\tau\right) \qquad [2.62]$$

It is preferable to derive relations that depend explicitly on the scattering angle. The expression above is therefore manipulated by introducing the particle relative refractive index as follows [BUL 08]:

$$\left(m_1 \sin\tau' - m_2 \sin\tau\right)^2 = m_2^2 \begin{bmatrix} m^2 + 1 - \left(m\cos\tau' - \cos\tau\right)^2 \\ -2m\cos\tau\cos\tau' - 2m\sin\tau'\sin\tau \end{bmatrix} \qquad [2.63]$$

Using the Snell–Descartes relation yields [VAN 57]:

$$\left(m_1 \sin\tau' - m_2 \sin\tau\right)^2 = m_2^2\left(m^2 + 1 - 2m\cos\left(\tau - \tau'\right)\right) \qquad [2.64]$$

From geometrical optics[12], we know that the rays $p = 1$ are scattered in the direction $\theta = 2\tau - 2\tau'$, reducing equation [2.64] to:

$$\left(m_1 \sin\tau' - m_2 \sin\tau\right)^2 = m_2^2\left(m^2 + 1 - 2m\cos\left(\theta/2\right)\right) \qquad [2.65]$$

Using equation [2.65], equation [2.62] simplifies to:

$$\phi_1 = \left(-1\right)^i \frac{2\pi}{\lambda_0} m_2 D\sqrt{m^2 + 1 - 2m\cos\left(\theta/2\right)} \qquad [2.66]$$

In the equation above, $i = 2$ for a droplet ($m > 1$) and $i = 1$ for a bubble ($m < 1$). This distinction is introduced due to the square root and to take into account that $\delta_1 - \delta_{\text{Ref}} \geq 0$ for a droplet (i.e. $m_1 \sin\tau' - m_2 \sin\tau \geq 0$) and $\delta_1 - \delta_{\text{Ref}} \leq 0$ for a bubble (i.e. $m_1 \sin\tau' - m_2 \sin\tau \leq 0$) (see equation [2.62] and Figure 2.35). Finally, the phase delay between the reflected and refracted rays scattered in the θ-direction are written as follows:

$$\Delta\phi_{01} = \phi_0 - \phi_1 = -\frac{2\pi m_2 D}{\lambda_0}\left[\sin\left(\theta/2\right) + \left(-1\right)^i\sqrt{m^2 + 1 - 2m\cos\left(\theta/2\right)}\right] \qquad [2.67]$$

12 That is, the same formulation is obtained for illumination by a Gaussian beam [GRÉ 93, ALB 03, ONO 06], a multilayered particle [ONO 96a] or, under certain conditions, a fiber jet [MIG 96, ONO 03].

For simplification, let us assume that the rays interfering on the CCD chip have nearly the same amplitude[13], denoted as $\sqrt{I}$. Classically, the interference function of these two rays has the following form:

$$I\left(\theta, m, \lambda_0, D\right) = 2I_0\left[1+\cos\left(\Delta\phi_{01}\right)\right] \qquad [2.68]$$

We are seeking a function that is periodic in the scattering angle θ such that $I\left(\theta, m, \lambda_0, D\right) = I\left(\theta + d\theta, m, \lambda_0, D\right)$. The maxima of $\Delta\phi_{01}$ can be determined by $d\left(\Delta\phi_{01}\right)/d\theta = 2\pi N$, where N is a integer representing the number of periods (or bright fringes).

By differentiating equation [2.68] using equation [2.67], we find that the particle diameter is related to the optical parameters (scattering angle, refractive index, etc.) and the number of fringes within the disk over a small angular range $\Delta\theta \approx 0°$ around the scattering angle θ:

$$D \approx \frac{2\lambda_0}{m_2}\frac{N}{\Delta\theta}\left[\cos\left(\theta/2\right)+\frac{\left(-1\right)^i m\sin\left(\theta/2\right)}{\sqrt{m^2+1-2m\cos\left(\theta/2\right)}}\right]^{-1} \qquad [2.69]$$

where $\Delta\theta$ represents the collection angle of the camera lens (aperture of the detection optics) in radians. For small apertures, this angle may be approximated by $\Delta\theta \approx A/f$. This aperture angle can also be measured precisely using a goniometer or estimated from the numerical aperture (N.A.) or the aperture $\#f/d$ of the camera lens:

$$\Delta\theta \approx 2N.A. \approx \left(f/d\right)^{-1} \quad \left[rad\right] \qquad [2.70]$$

The ratio $F_a = N/\Delta\theta$ represents the average angular frequency of the fringes per micrometer (for wavelength units in micrometers). The theoretical calibration curve relates this angular frequency F_a to the particle diameter D (and the relative refractive index m) as follows:

13 When water droplets in air are illuminated by a plane and perpendicular polarized incident wave, this condition is fulfilled for the reflected and refracted rays a $\theta \approx 67°$ [ONO 96b].

$$D \approx \omega\left(m_1, m_2, \lambda_0, \theta\right) F_{\mathrm{a}},$$
$$\omega \approx \left(2\lambda_0 / m_2\right)\left[\cos\left(\theta/2\right) + \frac{\left(-1\right)^i m \sin\left(\theta/2\right)}{\sqrt{m^2 + 1 - 2m\cos\left(\theta/2\right)}}\right]^{-1} \qquad [2.71]$$

where ω may be considered to be an optical constant in many situations (for a given optical setup and particle composition). This simple model, based on geometrical optics, is commonly used to invert experimental data (to find the particle diameter from the measured number of fringes per disk). The predictions of this model can also be compared to Lorenz–Mie calculations by expressing the angular frequency in degrees^{-1}:

$$F_{\mathrm{a}} = \frac{\pi}{180}\frac{D}{\omega} \qquad [2.72]$$

As an illustration, consider a water droplet in air with D = 200 μm, λ_0 = 0.532 μm, m_1 = 1.334, m_2 = 1.0 and θ = 67°. In this case, one obtains $\omega \approx 0.584$ μm/rad and $F_{\mathrm{a}} \approx 5.98$ deg^{-1}, which corresponds to $\Delta\theta$ = 5°, $N = \Delta\theta F_{\mathrm{a}} \approx 30$ fringes for a disk of diameter a_{Dk}. This result is in good agreement with the predictions of LMT (see Figure 2.37).

2.9.2.2. *Electromagnetic model*

From LMT, the fringes observed in the disk of the out-of-focus image correspond to the natural oscillations (or Mie lobes) of the particle scattering diagram. Thus, the out-of-focus interferometric imaging technique may be regarded as an OPC technique relating the particle diameter to the number of lobes within an angular portion $\Delta\theta$ of the scattering diagram. The angular frequency–diameter relationship can be determined from the theory by estimating the angular frequency of the scattering diagram in the vicinity of the collection angle θ for various diameters (and later on, dissimilar refractive indices).

As an illustration, Figure 2.36 presents the scattering diagrams and the corresponding angular spectra for water droplets of different sizes, a detection optics localized at θ = 67° with aperture $\Delta\theta$ = 10°, and for (a) a perpendicular (b) a parallel polarized incident wave. As already mentioned[14], for this configuration, the perpendicular polarization produces the highest contrasted and more regular fringe pattern. Figure 2.37(a) compares the numerical calibration curves of this system for water droplets ranging from D = 5–200 μm. The agreement is almost perfect except for

14 When water droplets in air are illuminated by a plane and perpendicular polarized incident wore, this condition is fulfilled for the reflected and refracted rays a $\theta \approx 67°$ [ONO 96b].

minor oscillations related to MDRs (section 1.3.1.4), which the geometrical optics model does not take into account.

Figure 2.36. *LMT simulations of the scattering diagrams and the related angular frequency spectra for water droplets in air illuminated by a plane wave of a) perpendicular or b) parallel polarization*

Figure 2.37. *a) LMT and geometrical optics: comparison of the relationship between the dominant angular frequency of the scattering diagrams of water droplets and the diameter of the droplets; b) evolution of the slope of the previous relationship and the corresponding signal-to-noise ratio, versus the angular position of the detection optics*

Figure 2.37(b) shows the evolution of the angular frequency of the local scattering diagram of a water droplet of $D = 100$ µm versus the detection angle θ. The corresponding SNR (in decibels) is also shown and is defined as the integral of the angular frequency peak divided by the total power of the angular frequency spectrum. The SNR can be used to evaluate the harmonic nature and contrast of

the fringes to some extent. As expected, Figure 2.37(b) shows that the SNR decreases for perpendicular polarization greater than the refraction angle limit $\theta > \theta_{\text{Refrac.}} \approx 82.7°$ (section 1.7). In contrast, for parallel polarization, the SNR rapidly increases for $\theta > \theta_{\text{Refrac.}}$ before reaching a maximum value at $\theta = 90–100°$ (i.e. Scheimpflug optics are not really necessary for these angles[15]). The parallel polarization configuration appears to be ideal, but this is not necessarily true. In fact, for this particular angular range, we are observing the result of interference between the reflected rays $p = 0$ and rays that have undergone two internal reflections $(p = 3)^2$ in this angular range. The problem is that the rays $p = 3$ are very sensitive to particle non-sphericity. A small deformation from the ideal spherical shape can result in a strong perturbation to the fringe pattern, inducing a tilt in the fringes (see Figure 2.34), for example. Note that the geometrical model described above can easily be extended to predict the calibration curve associated with the rays $p = 0$ and $p = 3$, or any other pair or rays.

Figure 2.38. *a) Images of glare spots produced by a water droplet; b) out-of-focus interferometric image corresponding to a); c) out-of-focus interferometric image recorded for decane droplets (D ≈ 60 µm) transported by an oscillating gas flow (source: C. Lacour and D. Durox, EM2C, École Centrale, Paris [LAC 08, LAC 11])*

2.9.3. *Conclusion*

The principle of the out-of-focus interferometric imaging technique is a combination of the principles of classical imaging and far-field techniques.

15 See [BOU 12] by the same authors.

In addition to providing aesthetic raw data, the technique provides the following information for each particle in the observation field: its diameter, the 2D (or 3D) position and two velocity components (if image pairs are recorded and analyzed with a PTV algorithm[16]). Unfortunately, this technique is also limited in several ways. First, the technique can only be used for very dilute flows. If the flow is not very dilute, the interferograms start to overlap and are particularly difficult to analyze. The use of spatial filtering or cylindrical optics (i.e. to compress the fringes, see Figure 2.39) can accomodate slightly more dense flows [SHE 12]. This configuration has been used to characterize sprays [MAE 00]: for instance, the spray of water droplets was meshed in 10 × 10 mm interrogation windows, each containing up to 300 droplet interferograms ranging from 10 to 150 μm. The resolution of the droplets diameter was estimated using a monodisperse droplet generator to be approximately 4% for a validation count of 90%. Commercial systems have nearly the same resolution. The technique also has quite a limited dynamic range (i.e. $D_{max}/D_{min} < 10–15$ with $D_{min} > 10–20$ μm, as there is less than one fringe per disk for smaller particles) and only provides a relative particle concentration [DAN 10, TSI 10, LAV 12, KAN 12]. Despite these limitations, the out-of-focus interferometric imaging technique is almost fully compatible with PIV/PTV[17] equipment and is developing rapidly. This technique is commonly presented as an add-on to the PIV/PTV software and is used for analyzing interferograms and extracting particle displacements.

Figure 2.39. *Techniques for the optical compression of out-of-focus interferometric images: spatial filtering method and cylindrical magnification (source: K. Hishida, Keio University, Yokohama [SHE 12])*

The requirement for transparency (or low absorption) of the particles is another limitation of the basic tenet of this technique. Nevertheless, two ingenious solutions have been proposed to solve this problem. The first uses two coherent laser sheets with a small crossing angle to form the probe volume [SEM 04]. This so-called

16 See [BOU 12] by the same authors.
17 See footnote 16.

Global Phase Doppler configuration allows the analysis of the interference fringe pattern produced by the glare points generated by each laser sheet. Thus, metallic particles or highly absorbing particles can be measured using the contribution of only the two glare spots generated by the rays $p = 0$. An additional advantage of this configuration, for transparent particles, is that the laser sheet crossing angle allows the sensitivity of the angular frequency of the fringes to be adjusted to the particle size (as in phase Doppler interferometry, section 2.4). The main limitations of this approach are linked to the probe volume size and shape (which deviate significantly from that for the PIV/PTV technique[18]) and the complexity of the relationship between the angular frequency and the particle size (e.g. for water droplets with detection optics at $\theta = 67°$, each interferogram results from the interference of four glare spots). The second solution consists in using a mirror to reflect the laser sheet directly transmitted through the particulate medium, so that the transmitted sheet superimposes with the incident laser sheet. For highly absorbing particles, the illumination on two opposite sides generates two reflected glare spots. This configuration can also be applied to size bubbles (e.g. [DEH 05, KAW 02]).

2.10. Holography of particles

2.10.1. *Gabor holography for holographic films*

Holography is an optical technique where 3D images of objects are recorded within an optically transparent and continuous medium. Many recording and reconstruction configurations exist (e.g. [JÜP 10]).

Figure 2.40. *Schematic diagram of the two basic steps of the holography technique using holographic plates in the Gabor setup: a) recording and b) reconstruction*

The recording setup for characterizing particulate systems is referred to as the Gabor (or inline) setup, where the positions $\{x_k, y_k, z_k\}$ and radii r_k of the $k = 1,2,\ldots,n$ spherical particles localized in a given probe volume are to be determined. The optical setup is essentially composed of a coherent laser source, a

18 See [BOU 12] by the same authors.

set of expanding and collimating optics, and a holographic plate (or film). The specificity of the Gabor configuration is due to the incident beam acting as both the probing beam and the reference beam. A hologram results from the interference of the reference beam and the scattered light from the particles illuminated by the probing beam. Up until the beginning of the 1990s, holograms were primarily recorded on holographic plates (e.g. glass plates coated with dichromated gelatin) [ROY 77, TRI 92]. Unlike classical photographic films, these holographic plates have the unique ability to record both the amplitude and the phase of the electromagnetic field incident on their surfaces. Particle positions can be estimated relative to the recording plane with holography because the phase of the electromagnetic field is a direct coding of the light propagation distance[19]. After exposure, the holographic plate must be developed in the laboratory using various chemical processes. The reconstruction (or restitution) step follows this tedious development step: the holographic plate is illuminated by the same reference beam used in the recording step to view the 3D images of the particles recorded a few hours before. A classical imaging system (i.e. a CCD video camera with a high-magnification camera lens, positioned on a 3D optical bench) is then used to analyze each particle image.

Inline holography on holographic plates can record a huge amount of data (corresponding to a probe volume of several cubic decimeters with a high spatial resolution) in a single acquisition. This feature is particularly useful for studies limited by reproducibility constraints (i.e. single-shot experiments). Nevertheless, the technique is limited to rather large particles (greater than 5–10 μm in diameter) and to very dilute particulate systems (corresponding to a reference beam obscuration of less than ≈1 %) [TRI 92]. The reconstruction step is also particularly labor intensive and time consuming. Consequently, interest in this technique has declined significantly over the last two decades, in favor of reconstruction steps using photorefractive crystals [MEN 04] or digital holography.

2.10.2. *Inline digital holography*

This is a rapidly developing technique. The experimental setup is the same as for classical Gabor holography, except that a digital video camera without any imaging optics records the intensity of the hologram. The 3D field is reconstructed numerically.

---

19 That is, the same formulation is obtained for illumination by a Gaussian beam [GRÉ 93, ALB 03, ONO 06], a multilayered particle [ONO 96a] or, under certain conditions, a fiber jet [MIG 96, ONO 03].

2.10.2.1. *Direct calculation and reconstruction of a hologram*

2.10.2.1.1. Direct problem

Consider a 2D photoarray composed of $N \times M$ square pixels of size $\Delta\xi$, with $i = 1,2,\ldots,N$ and $j = 1,2,\ldots,M$, illuminated by a plane harmonic electromagnetic wave of wavelength λ (see Figure 2.41(a)). A spherical particle is located between the illuminating light source and the photosensor. Within the framework of Fresnel–Kirchoff diffraction theory [GIR 08], the intensity of the electromagnetic field scattered by this particle on the photosensor surface can be expressed as follows:

$$i_k\left(i,j\right) = \frac{\pi r_k^2}{\lambda z_k} J_1\left(\frac{2\pi r_k \sqrt{\Delta x_k^2 + \Delta y_k^2}}{\lambda z_k}\right) \sin\left(\frac{\pi\left[\Delta x_k^2 + \Delta y_k^2\right]}{\lambda z_k}\right) \qquad [2.73]$$

where $\Delta x_k = i\Delta\xi - x_k$, $\Delta y_k = j\Delta\xi - y_k$ and J_1 is the spherical Bessel function of the first kind. For an optically dilute particulate medium, the intensity distribution of the ensemble hologram produced by n illuminated particles is as follows:

$$I^{\mathrm{Th}}\left(i,j\right) = I_0\left(i,j\right) + I_{\mathrm{b}}\left(i,j\right) - \sum_{k=1}^{n} \alpha_k i_k\left(i,j\right) \qquad [2.74]$$

where $I_0\left(i,j\right)$ and $I_{\mathrm{b}}\left(i,j\right)$ represent the intensity of the incident beam and the background noise for the pixel $\left(i,j\right)$, respectively, and α_k is a weighting factor to account for the local attenuation of the incident beam.

2.10.2.1.2. Reconstruction

A large variety of approaches exist to invert holograms of particulate systems. Inverse methods (e.g. [GIR 08, SOU 07]) search for the parameters $\left\{x_k, y_k, z_k, \alpha_k, r_k; k = 1,2,\cdots,n\right\}$ that minimize (using least squares) the global difference between the reconstructed $I^{\mathrm{Th}}\left(i,j\right)$ and the measured $I^{\mathrm{Meas}}\left(i,j\right)$ holograms. In fact, most of the approaches in current use are based on a direct reconstruction scheme. The direct scheme simply identifies the contribution of each illuminated particle to the global hologram. For spherical particles, these contributions take the form of "ring patterns" that can be modeled by equation [2.73] or with simpler, but more computationally efficient, models (such as the PSF [TIA 10, MÜL 04]). Some authors perform a wavelet analysis (e.g. [LEB 99, ONU 93]) to detect each ring pattern; briefly, the 2D wavelet transform of the entire hologram shows maxima corresponding to the positions where the analyzing (or daughter) wavelet $\psi_a\left(x,y\right)$ is centered around a particle ring pattern and the wavelet scale $a\left(= f\left(z\right)\right)$ is on the scale of the local ring pattern. The size and distance (relative to the photosensor) of all the particles contributing to the entire hologram are evaluated

by iterating over the z-coordinates. Different wavelets analyses may be used, such as $\psi_a(x,y) = a^{-2}\sin\left[a^{-2}\left(x^2+y^2\right)\right]$, with $a = \sqrt{\lambda z/\pi}$ [ONU 93].

2.10.2.2. *Example results*

Figure 2.41(b) shows the entire hologram recorded by a CCD video camera $\left(N \times M = 2048 \times 2048 \text{ pixels};\ \Delta\xi = 7.4\ \mu\text{m}\right)$ for three free-falling water droplets, with D = 18 µm. Note that the hologram has been exposed eight times (i.e. eight laser shots for a single hologram). Figure 2.41(c) presents the image field that has been reconstructed with the wavelet transform method [SAL 08] for a distance $z_k = 246.16$ mm. The images of droplets (ii) and (iii) appear to be reconstructed well enough to estimate the droplet sizes, 3D positions and accelerations. In contrast, droplet (i) appears more distant (the ring patterns are still visible). In this case, the numerical reconstruction must be continued for distances $z > 246.16$ mm. Figure 2.42(a) shows the digital hologram of an air–water bubbly flow [TIA 10]. Figures 2.42(b) and (c) show the data reconstruction (PSD and 3D positions) by the PSF. The authors of this impressive work report a resolution of 100 µm for the z-coordinate [TIA 10].

Figure 2.41. *a) Schematic of the recording and reconstruction steps of the inline digital holography of particles. Reconstructed multiple-exposure (eight exposures) holograms of water droplets of diameter D = 18 µm and vertical velocity V_y=-0.5 m/s, b) for z = 0 mm and c) z = 246.19 mm (source: D. Lebrun, CORIA, Rouen [SAL 08])*

2.10.3. *Conclusion*

Inline Digital Holography has potentially huge advantages for studying particulate flow, while being limited to dilute flows and rather large particles. The setup is also rather inexpensive; it is hardly negligible compared to other OPC techniques. The quality of the measurements and the dimensions of the field of view are strongly dependent on the photosensor characteristics and the quality of the

reconstruction (including the direct calculation of the holograms). Large photosensors allow better resolution of the axial coordinates of the particles and wider fields of view. Reconstruction may be prohibitive for some applications, even when graphical power units (GPU; e.g. [TIA 10]) are used to speed up the calculations. Nevertheless, the applicability of the digital holography technique [JÜP 10] is continuously increasing with computer resource capabilities. Among the current developments of this technique [LAM 12], we can cite the use of focused laser beams for near-wall and small particle measurements, the correction of optical aberrations induced by dioptric surfaces and the use of more sophisticated scattering models (e.g. [LAM 12, ALL 13, WU 12]).

Figure 2.42. *a) Digital hologram pattern recorded for air bubbles in water; b) reconstructed PSD (raw, log-normal and gamma fitting models) and c) full 3D reconstruction of the bubbly flow structure (source: G. Barbastathi, MIT, Cambridge [TIA 10])*

2.11. Light extinction spectrometry

2.11.1. *Principle*

The principle of this technique is quite similar to that of molecular absorption spectrometry, so we will refer to it as “light extinction spectrometry” (LES)

rather than by "turbidimetry". Molecular absorption spectrometry analyzes the composition of a sample from molecular absorptivity measurements over a broadband spectrum. LES characterizes the PSD and concentration of small particles suspended in a continuous medium from spectral extinction measurements.

Figure 2.43. *Sketch of the laser extinction spectrometry technique*

LMT can be used to compute the extinction cross-section of a spherical particle illuminated by a plane wave. The quantity C_e represents the homogeneous surface area of the incident wave that it is scattered and absorbed by the particle. C_e is the sum of two surface areas: $C_e = C_{\mathrm{a}} + C_{\mathrm{s}}$, a scattering area and an absorbing area, respectively. Let z be the direction of propagation of an incident wave in an optically dilute particulate system containing C_N particles per unit volume, with diameter D and relative refractive index $\tilde{m}$. In addition, we assume that the total forward scattering of these particles is negligible with respect to the variation of the intensity of the wave throughout the particulate medium [XU 07]. The variation of the intensity of this wave as it passes through an infinitesimal slab of thickness dz is then proportional to the local extinction cross section of the particulate medium and the slab width (see Figure 2.43(a)):

$$I(z+dz) - I(z) = -C_N C_e(D, \tilde{m}, \lambda)\, dz \qquad [2.75]$$

Integrating equation [2.75] produces an exponentially decreasing wave intensity from the initial intensity $I_0 = I(z=0)$, as the wave propagates:

$$I(z) = I_0 \exp\left[-C_N C_e(D, \tilde{m}, \lambda) z\right] \qquad [2.76]$$

Note that only the axial dimension of the particulate system appears explicitly in equation [2.76]: see Figure 2.43(b) for the effective shape of the optical probe volume (i.e. the shaded area) of a LES system. The product $\tau(\lambda) = C_N \overline{C}_e$ represents the particulate medium turbidity.

Basic turbidimeters estimate the turbidity of a particulate medium from L and the measured transmission ratio $T(\lambda) = I(z)/I_0$, at a single wavelength λ. In this case, C_e is estimated via an experimental calibration procedure (the PSD is simply assumed to be constant during the entire experiment). More advanced LES systems simultaneously characterize the PSD and concentration of the entire particulate system by measuring the transmission $T(\lambda_i)$ of a collimated and broadband light beam passing through the particulate medium, where $I_0(\lambda_i)$ and $\overline{I}(\lambda_i)$ denote the initial and final spectral intensity, respectively:

$$\overline{T}(\lambda_i) = \overline{I}(\lambda_i)/I_0(\lambda_i) = \exp(-\tau L) \qquad [2.77]$$

where $\overline{C}_e$ represents the average extinction cross-section of the system:

$$\overline{C}_e = \int_0^{\infty} C_e(D, \tilde{m}, \lambda)\, n(D) dD \qquad [2.78]$$

The integral equation above is a Fredholm equation of the first kind. Thus, an inverse problem must be solved to simultaneously determine C_N and the normalized PSD by number $n(D)$, from the measured $\overline{T}(\lambda_i)$ and the calculated kernel of the integral $\overline{C}_e(D, \tilde{m}, \lambda)$ [HAN 94, TWO 79].

2.11.2. *Algebraic inverse method*

There are many ways to regularize and solve this inverse problem [HAN 94, TIK 95, XU 02, SCH 91b, ONO 12a], but we present only the simplest and most widely used methods here. For numerical stability, it is preferable to rewrite equation [2.78] in terms of volumes rather than numbers. For particles that can be represented as equivalent spheres, the volume particle concentration C_v is related to the number particle concentration C_N by $V(D) = C_v v(D) = C_N(\pi/6) D^3 n(D)$, where $V(D)$ is the particle volume distribution and $v(D)$ is the normalized particle volume distribution such that:

$$\int_{-\infty}^{+\infty} v(D) dD = \int_{-\infty}^{+\infty} n(D) dD = 1 \qquad [2.79]$$

Introducing the constant $\varphi = -3\ L/2$ and the physical boundaries $\left(D_{\min}, D_{\max}\right)$ for the integral [2.78], equation [2.77] becomes (e.g. [ONO 09a]):

$$\ln\left[\overline{T}\left(\lambda_i\right)\right] = \varphi\int_{D_{\min}}^{D_{\max}} C_e\left(D,\tilde{m},\lambda_i\right)\frac{V\left(D\right)}{D}dD \qquad [2.80]$$

The equation above may be discretized as follows:

$$\int_{D_{\min}}^{D_{\max}} \frac{C_e\left(D,\tilde{m},\lambda_i\right)}{D}V\left(D\right)dD = \sum_{j=1}^{M} S_{i,j}V_j \qquad [2.81]$$

where the distribution to be determined $V\left(D\right)$ is written as a vector V_j with $j = 1,2,\cdots,M$. $\mathbf{S}$ is an extinction matrix of size $N \times M$ that is normalized by the particle diameter. The element $S_{i,j} = C_e\left(D,\tilde{m},\lambda_i\right)/D_j$ is evaluated for a given wavelength λ_i, $i = 1,2,\cdots,N$ and the size interval (class or bin) $\left[D_{j-1}, D_j\right]$:

$$S_{i,j} = \int_{D_{j-1}}^{D_j} \frac{C_e\left(D,\tilde{m},\lambda_i\right)}{D}dD \qquad [2.82]$$

The spectral transmission $\overline{\mathbf{T}}$ is a unidimensional vector whose elements $\overline{T_i}$ have to be measured. To obtain $\mathbf{V}$, one has to solve the algebraic equation $\overline{\mathbf{T}} \equiv \mathbf{S}\cdot\mathbf{V}$, which has the trivial solution:

$$\mathbf{V} \equiv \left(\mathbf{S^T S}\right)^{-1}\mathbf{S^T}\overline{\mathbf{T}} \qquad [2.83]$$

This solution is numerically unstable because the problem is usually overdetermined and ill-posed. To overcome this issue, it is preferable to search for the vector $\overline{\mathbf{T}}$ that minimizes $\mathbf{S}\cdot\mathbf{V} - \overline{\mathbf{T}}$, recognizing that the PSD is a positive quantity ($V_j > 0$, $j = 1,2,\ldots,M$) with a more or less regular behavior. The minimization process is often based on an NNLSQ algorithm [HAN 94, MAT 12]:

$$\left\|\mathbf{S}\cdot\mathbf{V} - \overline{\mathbf{T}}\right\|^2_{V>0} \qquad [2.84]$$

The aforementioned inverse method produces satisfactory results for the reconstruction of near-critical-angle scattering diagrams (section 2.7.3) [ONO 09b] but not for extinction spectra. The condition number κ of the extinction matrix $\mathbf{S}$ is always too large $\kappa = \left\|S\right\|.\left\|S^{-1}\right\| \gg 1$. There are various methods for regularizing this

problem (Tikhonov's method, Singular Value Decomposition and filtering, etc.) [HAN 94, ONO 09a, TIK 95]. In the Phillips–Twomey method, a smoothing matrix $\mathbf{H}$ and a regularization (or Lagrangian) parameter γ are introduced to "stabilize" the reconstruction procedure [TWO 79]:

$$\left\|\left(\mathbf{S}^{\mathrm{T}}\mathbf{S}+\gamma\mathbf{H}\right)\mathbf{V}-\mathbf{S}^{\mathrm{T}}\overline{\mathbf{T}}\right\|^{2}_{V>0} \qquad [2.85]$$

The choice of the regularization parameter is rather tricky (i.e. values that are too large oversmooth the PSD and generate artificial modes, whereas values that are too small have no effect on the reconstruction process). Nevertheless, different solutions exist for estimating the optimum value of a given set of parameters (such as the L-curve method [HAN 94]). Depending on the problem, the smoothing matrix may be the identity matrix or one of its derivatives (we use the matrix in equation [2.86]) [ONO 09a, ONO 12a]. Once $\mathbf{V}(D)$ is estimated, C_v is obtained by integrating $\mathbf{V}(D)$. $v(D)$, $n(D)$ and C_N are then deduced from the relations existing between all these quantities (which were presented at the beginning of section 2.11.2).

$$\mathrm{H}=\begin{bmatrix} 1 & -2 & 1 & 0 & \dots & \dots & \\ -2 & 5 & -4 & 1 & 0 & \dots & \\ 1 & -4 & 6 & -4 & 1 & 0 & \dots \\ 0 & 1 & -4 & 6 & -4 & 1 & 0 \\ \vdots & 0 & 1 & -4 & 6 & -4 & \cdots \\ \vdots & \vdots & 0 & 1 & -4 & 6 & \ddots \\ \vdots & \vdots & \vdots & \vdots & \vdots & \vdots & \ddots \end{bmatrix} \qquad [2.86]$$

To provide examples of extinction spectra, Figure 2.44(a) shows the broadband spectral transmission of clouds of monodisperse and polydisperse carbonaceous beryllium and tungsten spherical microparticles. Figure 2.44(b) compares the various PSDs reconstructed with equation [2.85]) for clouds that are assumed to consist of spherical particles or of a mixture of spherical and spheroidal particles [ONO 09a].

2.11.3. *Experimental setup and conclusion*

A basic system (single wavelength) is composed of a stabilized monochromatic light source, collimating and focusing optics, and a photodetector equipped with a spatial filter (case one in Figure 2.45). The spatial filter minimizes the collection of rays that have undergone single scattering and multiple scattering events. The

particulate media under study may or may not be inside a test chamber, a spectrophotometric cell, a multipass cell, etc. The first step is to measure the beam transmission without any particles (which is not always possible). This reference intensity accounts for all phenomena that are not described by equation [2.76], such as optical windows transmission and absorptions. When the particles are in the probe zone, the measured beam transmission may be too low or too high. The transmission may be too low for basic and prohibitive reasons (multiple scattering, see section 1.8.2) or technical reasons (detection limit, SNR considerations, etc.). However, in both cases, the optical thickness of the medium should be decreased (e.g. by diluting the sample, by reducing the distance L or by changing the spectral range). If the beam transmission is too high, converse solutions to those recommended for weak transmissions should be used. When all these issues are resolved, the absolute particle concentration can be obtained, provided that the PSD is known *a priori* (from another technique) and equations [2.77] and [2.78] are used to calculate the average extinction of the medium. If the PSD is not known but can be assumed to be constant during the entire experiment, the particle concentration can only be estimated from a calibration procedure (using calibrated particles, for instance).

Figure 2.44. *Simulations of a) light extinction spectra of spherical, carbonaceous Beryllium and Tungsten particles (Log-Normal PSD with mean and standard deviation D = 3 µm and σ_D = 1 µm, respectively), b) a typical reconstructed PSD for carbonaceous particles, depending on the kernel used for the inversion (spheres, or a mixture of spheres and spheroids) [ONO 09a]*

As mentioned above, more advanced systems use a broadband illumination light source (cases two and three in Figure 2.45). In principle, the light source may be a halogen, deuterium, xenon lamp or flash lamp, as well as a supercontinuum light source or an OPO laser. However, the output beam must be stable (in intensity and frequency) and collimated with achromatic optics. The scanning of the spectrum may be ensured by the emission unit (case two) or the detection unit (case three).

Case three is a system where a broadband light source is coupled with a monochromator (motorized diffraction gratings, filter wheels, etc.). In this case, the detection unit may be composed of only one or two photodetectors (to cover the UV/mid-IR range). Case two shows the most widely used configuration where a spectrophotometer is used to sample the spectrum. For obvious reasons, it is preferable to use diode-array spectrophotometers when characterizing non-stationary and transient particulate flows, rather than spectrophotometers using a Fourier-transform or scanning grating setup.

Figure 2.45. *a) Setup of various light extinction spectrometers: using a single wavelength (e.g. laser source (case one)); a broadband light source in combination with a spectrometer (case two); or a photodetector (case three). b) Picture of a type 2 system: (i) stabilized UV-NIR light source (deuterium–halogen); (ii) solarized optical fibers; (iii) achromatic emission and collection optics (parabolic mirrors); (iv) alignment components; (v) spectrometer; (vi) in-line attenuator and laser diode (for alignment purposes); (vii) probe zone; (viii) Laskin-nozzle and (ix) diffusion drier [ONO 09a, ONO 12a]*

LES is mainly used to characterize suspensions and aerosols of spherical particles where the particles dimensions are on the order of the wavelength [XU 02, XU 07]. In fact, for $D \ll \lambda$, the extinction coefficient decreases rapidly with the particle diameter (i.e. the extinction coefficient is very sensitive to D), whereas for $D \gg \lambda$, this coefficient tends towards two (i.e. the coefficient becomes almost insensitive to the particle diameter)[20]. For technical and economic reasons, and also due to the limited transparency of classical materials outside this spectral range, the spectrum of a LES system is frequently limited to the UV-NIR $(\sim 0.2-1\,\mu\text{m})$ range and a maximum particle size range of approximately $0.01-1\,\mu\text{m}$. For example, Figure 2.46 shows the results of the temporal analysis of the growth of silicon nanoaggregates in a discharge plasma [ONO 11b, ONO 12a]. The reconstructions

20 That is, the same formulation is obtained for illumination by a Gaussian beam [GRÉ 93, ALB 03, ONO 06], a multilayered particle [ONO 96a] or, under certain conditions, a fiber jet [MIG 96, ONO 03].

were performed with the algebraic method, using the T-Matrix and a fractal particle model to compute the extinction matrix ($D_f = 2.85,$ see section 1.5). The minimum measureable particle size depends strongly on the particle concentration. For instance, as observed in Figure 2.46, silicon nanoparticles as small as $D = 20$ nm can be measured provided that the volume concentration exceeds 10 ppb for a probe length of $L = 0.13$ m.

Figure 2.46. *Real-time evolution of a) extinction spectra and b) reconstructed statistical properties of silicon nanoaggregates produced by a dusty plasma (compared with SEM off-line analyses [BOU 04]) [ONO 11b, ONO 12a]*

To conclude on this point, we can say that LES is the only OPC technique that provides an accurate estimation of the absolute particle concentration. In addition, no other OPC technique characterizes either transparent or absorbing particles in this challenging size range (in between the Rayleigh and Mie scattering regimes). The measurements can be performed at rather long distances and with only two optical accesses (and even one if a mirror is used to reflect the probing beam). The main drawbacks of the LES technique are the limited capabilities of current inversion procedures and, more profoundly, the need for a good estimate of the complex refractive index dependence of the particles on the wavelength.

Current research and development is focused on improving the reconstruction procedure [SCH 91b, SU 02] and the characterization of complex particles such as dust [ONO 09a], crystals [CRA 97] and aggregates [SOR 01, ONO 11b, ONO 12a].

2.12. Photon correlation spectroscopy

Dynamic light scattering (DLS), also known as photon correlation spectroscopy (PCS) or quasi-elastic light scattering (QELS), has become an important tool in

characterizing the size distribution of ultrafine particles found in colloidal suspensions and, more generally, Brownian suspensions [XU 02, BER 00].

When a dilute suspension of nanometric- to micron-sized particles is illuminated by a stabilized laser source, the scattered light shows a characteristic temporal fluctuation. This phenomenon is linked to the Brownian motion of the particles (i.e. the molecular collisions induced by thermal agitation), which induces a loss of coherence of the scattered light (i.e. the Fizeau–Doppler effect). The autocorrelation function Γ (ACF) of the scattered signal $I(t)$ shows a characteristic decay time depending on the temperature T and the viscosity η of the fluid, as well as on the translational (i.e. linear displacement) diffusion coefficient D_T of the particles. For spherical and monodisperse particles, Γ can be directly related to the diffusion constant as follows:

$$\Gamma = q^2 D_T \qquad [2.87]$$

where $q = (4\pi m_2 / \lambda)\sin(\theta/2)$ is the scattering vector for the scattering angle θ. The Stokes–Einstein relation relates the particle hydrodynamic diameter to the translational diffusion coefficient in the fluid:

$$D \equiv D_h = k_B T / (3\pi\eta D_T) \qquad [2.88]$$

where k_B is Boltzmann's constant. Figure 2.47(a) shows the ACFs for ovalbumin and titanium dioxide suspensions [MAL 00]. The spherical equivalent mean diameters are estimated at 6 and 95 nm, respectively, using the two characteristic decay times from the ACFs.

For polydisperse samples, an inverse problem needs to be solved for the ACF analysis. For direct calculation purposes, the ACF may be viewed as the superimposition of the contributions of monodisperse particles (whose ACFs are given by exponentially decreasing functions):

$$\left|g^1(q,\tau)\right| = \int_0^\infty G_N(\Gamma)\exp(-\Gamma\tau)\,d\tau \qquad [2.89]$$

where $G_N(\Gamma)$ represents the number distribution of the characteristic time decays. To determine $G_N(\Gamma)$, the first-order autocorrelation function $|g^1(q,\tau)|$ must be measured and a model is required for the kernel $\exp(-\Gamma\tau)$ of the integral [2.89]

(such as equation [2.88]). The first-order ACF is derived from the second-order ACF $g^2(q,t)$ and the measured intensity $I(t)$ [XU 02]:

$$g^2(q,\tau) = \frac{\langle I(t) I(t+\tau) \rangle}{\langle I(t) \rangle^2} = 1 + \beta \left[g^1(q,\tau) \right]^2 \qquad [2.90]$$

where β is a geometrical constant that accounts for the optical probe volume and the properties of the detection optics. Various semi-analytical and inverse methods have been developed to solve the problem above (e.g. [BER 00, PRO 04]).

Figure 2.47. *a) Autocorrelation functions measured for two colloidal suspensions [MAL 10]; schematic of two DLS setups: b) fiberized heterodyne and c) homodyne with variable analysis angle*

For particles of a complex shape or particles interacting with each other, such as macromolecules and aggregates, the translational (and rotational) diffusion coefficient is a multiparametric function. The common procedure for dealing with many additional unknown parameters is to collect and analyze ACFs at different scattering angles (Figure 2.47(c)). In this case, the sample analysis can take a few minutes. Some systems use a heterodyne setup where a part of the incident beam is directed onto the photodetector surface area. This solution, which may be fiberized (see Figure 2.47(b)), compensates for drifts in the laser intensity and frequency stability. For semi-dilute to dense suspensions, conventional data analysis of DLS signals is compromised by multiple scattering effects. Nevertheless, various efficient methods exist for minimizing the harmful effects of multiple scattering (e.g. cross-correlation measurements [BER 00, SCH 87, SCH 91a] or which take advantage of multiple scattering (e.g. diffusion wave spectroscopy [MAR 87]).

2.13. Laser-induced fluorescence and elastic-scattering imaging ratio

The OPC technique is mostly used to characterize spray nozzles and the properties of sprays (e.g. [DOM 03, YEH 93, BAZ 95, SAN 99, LEG 99, ZIM 02])

such as the cone angle, droplet size distribution, etc. The technique is referred to as the spray paternator or planar droplet sizing technique, depending on the authors.

2.13.1. *Principle*

The two primary requirements of this technique are that the particles are spherical and emit fluorescent light when excited by a laser beam (i.e. laser-induced fluorescence (LIF), see Chapters 3 and 5). There are two main assumptions: in the Mie scattering regime (elastic), the particles scatter incident light proportionately to their surface area $\left(I_e \propto D^2\right)$ and the fluorescent emission (inelastic) is proportional to the number of fluorescent molecules, that is to the particle volume $\left(I_f \propto D^3\right)$. By measuring both the elastic and the inelastic signals generated by a particle, the particle diameter can be estimated from the ratio $I_f / I_e \propto D^3 / D^2 = D$. In practice, this technique is mostly used to perform locally averaged characterizations. Two video cameras are used to simultaneously record two images of the spray: one image is produced by the elastic scattering $I_e(x,y)$ and the second image is produced by the inelastic scattering $I_f(x,y)$. It is generally assumed [KOH 03] that these two intensity distributions depend only on the local intensity of the incident beam $I_0(x,y)$, the local droplet concentration of the spray $C_N(x,y)$, and two optical constants c_f and c_e, which depend on numerous factors (probe volume dimension, electronic gain, etc).

$$\begin{aligned} I_f(x,y) &= c_f I_0(x,y) \int_0^\infty C_N(x,y) D^3 dD \\ I_e(x,y) &= c_e I_0(x,y) \int_0^\infty C_N(x,y) D^2 dD \end{aligned} \qquad [2.91]$$

The local value of the Sauter diameter can be estimated by calculating the ratio $I_f(x,y) / I_e(x,y)$ and using the definition of the Sauter diameter (see section 2.2.2.1).

$$D_2^3(x,y) \equiv \frac{\int_0^\infty C_N(x,y) D^3 dD}{\int_0^\infty C_N(x,y) D^2 dD} = \frac{1}{K_{fe}} \frac{I_f(x,y)}{I_e(x,y)}, \text{ with } K_{fe} = \frac{c_f}{c_e} \qquad [2.92]$$

2.13.2. *Experimental setup and results*

The setup is composed of a high-energy pulsed Nd-YAG laser (λ_0 = 532 nm, or λ_0 = 355 nm; I_0 > 20–30 mJ/pulse) (1); beam-shaping optics producing a laser sheet (2, 3); a video camera CCD (4), equipped with an optical filter (5) to collect the elastic scattering centered on λ_0; an intensified (or high-sensitivity) video camera (6), equipped with a optical filter (7) to collect a portion of the laser-induced fluorescence (e.g. $\lambda_f > \lambda_e$) (see Figure 2.48). Note that the two cameras must have a highly dynamic range to compensate for the $I_e \propto D^2$ and $I_f \propto D^3$ laws (i.e. for a dynamic range of 12 bits, the maximum dynamic size is far below $\sqrt[3]{2^{12}} = 16$). The experiment starts with various calibration steps: dye dosing, adjustment of the fields of view of both cameras, evaluation of the intensity $I_0(x, y)$ distribution of the laser sheet, measurement of the constant K_{fe} using calibrated droplets, etc. When the calibration is completed, the electrical and optical background noise of both images must be measured and subtracted from the measured images, before calculating the ratio defined by equation [2.92]. The two cameras can be placed on the same side, as depicted in Figure 2.48, where a dichroic filter or a semi-transparent plate (8) is used to separate the elastic and inelastic scattering. The cameras can also be placed on opposite sides to obtain a higher SNR (but this configuration is more sensitive to spray asymmetries).

Figure 2.48. *Setup schematic for simultaneous laser-induced fluorescence (LIF) and elastic-scattering (Mie scattering) imaging of a spray of liquid droplets (dye seeding)*

Figure 2.49. *Corrected elastic-scattering and fluorescence emission images obtained for a hollow cone spray (60° cone angle) generated by an air-assisted nozzle. Water droplets seeded with a Rhodamine 6G dye solution and a Sauter diameter of 10–50 μm (source: Y. Hardalupas, Imperial College of Science, London [DOM 02a, CHA 04, DOM 02b])*

2.13.3. *Conclusion*

This technique is mainly used to characterize transient sprays [YEH 93, CHA 04, DUC 08]. The operating principle is simple and the results are particularly commendable, but its applicability is limited in several ways. First, the fluorescence signal depends strongly on the concentration of dye molecules and the operating temperature (and pressure). The fluorescence signal may also be absorbed by the liquid vapor. Thus, it is crucial to operate at constant temperature and to limit evaporation. Furthermore, equation [2.92] is a very simple approximation [DOM 02b]. For instance, it is well known that elastic scattering shows strong oscillations (section 1.3.1.4). The amplitude of these oscillations may be damped by increasing the fluorescent dye concentration in the sprayed liquid, but geometrical (volume/surface absorption) and quenching (or bleaching) phenomena may produce severe distortions of the $I_f \propto D^3$ law [DOM 02b]. It is very difficult to provide order of magnitude estimates for the resolution and dynamics of this technique. In any case, the technique is most likely limited to $D_{\max} / D_{\min} \leq 10$ with $D_{\min} \geq$ 10–20 μm.

2.14. Laser-induced incandescence

Laser-induced incandescence (LII) occurs when a laser beam encounters solid absorbing particles [MEL 84, VAN 94b, SCH 06, FRA 10]. The absorbed energy causes an increase in the particle temperature. The particles simultaneously lose energy through heat transfer to the surroundings. For a sufficiently high-energy absorption rate, the temperature can reach high levels where significant incandescence

(essentially blackbody emissions) and vaporization phenomena can occur. The inversion of the LII signal intensity and time decay is performed assuming a PSD model to determine the volume concentration, the mean size of all monomers and the small aggregates within the measurement volume. The measurement can be local (when the detector is a photomultiplier; PM) or 2D (when the detector is a streak camera with a time resolution of a few nanoseconds, e.g. [FRA 10, NI 95, DEL 05]).

The LII basic setup is composed of a pulsed laser, focusing optics, collection (1D) or imaging optics (2D) with an interference filter (i.e. the central wavelength is selected to improve detection of the LII signal against background optical noise). Depending on the probe volume size, the particle absorption, and the external medium temperature and pressure, the laser fluence is in the 0.05−0.7 J/cm^2 range (e.g. for a Nd:YAG laser at 1,064 or 532 nm [SCH 06]). This technique is used commercially [ART 10] to characterize nanoparticles and aggregates produced by combustion (soot) and plasma (ceramics) systems [ONO 11b]. The current limitations and developments of the technique [SCH 06, FRA 10, DES 08, NI 95, DEL 05, MIC 07, LIU 06, JEN 01] are mainly related to or focused on the following:

– Particle properties (shape and refractive index; e.g. [MIC 07]);

– Particle scattering and emission models (based on the Rayleigh theory, or Rayleigh–Gans–Debye theory[21]) inverse methods for the analysis of the LII raw data (which all assume a PSD model) [SCH 06, LIU 06];

– The attenuation of the incident laser beam or the LII signal by particles outside the probe volume [VAN 94b, SCH 06];

– The superimposition of a detrimental fluorescent emission onto the LII signal (due to hydrocarbon molecules [VAN 94b, SCH 06]));

– The calibration of the system (the detection of the peak LII signal can be evaluated at two wavelengths as a partial solution to this problem, e.g. [JEN 01]).

2.15. General conclusions

In this chapter, we have attempted to briefly review the most important concepts and techniques for optical characterization of the size, shape and composition of particles (drops, bubbles, nanoparticles and their aggregates). We have especially emphasized the most widely used and promising optical particle characterization techniques, for in situ and dynamic measurements, and the investigation of particulate

21 That is, the same formulation is obtained for illumination by a Gaussian beam [GRÉ 93, ALB 03, ONO 06], a multilayered particle [ONO 96a] or, under certain conditions, a fiber jet [MIG 96, ONO 03].

systems and multiphase flows (suspensions, sprays, bubbly flows, dusty plasmas, etc.). This overview has highlighted several criteria to differentiate between these techniques:

– the underlying principles (light angular intensity distribution, polarization, phase, or coherence) which determine the capabilities and operating conditions of the techniques;

– the ability to accommodate particle morphology (spherical, irregular, fractal, etc.);

the maximum particle size range (from nanometers to millimeters) and the particle size range for given settings (which rarely exceed $D_{max}/D_{min} \approx 15–50$);

– the ability to provide measurements of concentrations or fluxes;

– the method used to obtain statistics (temporal, spatial, and spatiotemporal), which is a determining factor when comparing results from different OPC techniques to other measurements or the predictions of multiphase flow models;

– the absolute or relative nature of the measurements (autocalibration of the optical probe volume dimensions) and some related statistical biases (detection of smaller and larger particles, screening effects, etc.);

– the ability to retrieve other particle information: composition (via the refractive index), dynamic properties (spatial coordinates, velocity, acceleration) or position within the flow.

In Table 2.1, we have attempted to synthesize these different criteria and techniques. For more details on these aspects, please refer to the biblioghraphy of the present chapter. This chapter has also focused on the light scattering and absorption properties of particles.

2.16. Bibliography

[ADL 98] ADLER C.L., LOCK J.A., STONE B.R., "Rainbow scattering by a cylinder with a nearly elliptical cross section", *Applied Optics*, vol. 37, no. 9, pp. 1540–1550, 1998.

[ADR 71] ADRIAN R.J., GOLDSTEIN R.J., "Analysis of a laser Doppler anemometer", *Journal of Physics E*, vol. 4, pp. 505–511, 1971.

[AIR 38] AIRY G.B., "On the intensity of light in the neighborhood of a caustic", *Transactions of the Cambridge Philosophical Society*, vol. 6, no. 3, pp. 397–403, 1838.

[AIZ 94] AIZU Y., DOMNICK J., DURST F., GRÉHAN G., ONOFRI F., QIU H.H., SOMMERFELD M., XU T-H., ZIEMA M., "A new generation of phase Doppler instruments for particle velocity, size and concentration measurements", *Particle & Particle Systems Characterization*, vol. 2, pp. 43–54, 1994.

[ALB 03] ALBRECHT H.-E., DAMASCHKE N., BORYS M., TROPEA C., *Laser Doppler and Phase Doppler Measurement Techniques*, Springer, Berlin, 2003.

[ALL 13] ALLANO D., MALEK M., WALLE F., CORBIN F., GODARD G., COËTMELLEC S., LECORDIER B., FOUCAUT J.-M., LEBRUN D., "Three-dimensional velocity near-wall measurements by digital in-line holography: calibration and results", *Applied Optics*, vol. 52, no. 1, pp. 9–17, 2013.

[ART 10] ARTIUM TECHNOLOGIES INC., 2010, available at http://www.artium.com.

[BAC 84] BACHALO W.D., HOUSER, M.J., "Phase/Doppler spray analyzer for simultaneous measurements of drop size and velocity distributions", *Optical Engineering*, vol. 23, pp. 583–590, 1984.

[BAZ 95] BAZILE R., STEPOWSKI D., "Measurements of vaporized and liquid fuel concentrations in a burning spray jet of acetone using planar laser-induced fluorescence", *Experiments in Fluids*, vol. 10, pp. 1–9, 1995.

[BER 07] BERGENBLOCK T., ONOFRI F., LECKNER B., TADRIST L. "Experimental estimation of particle flow fluctuations in dense unsteady two-phase flow using phase Doppler anemometry", *International Journal of Multiphase Flow*, vol. 33, pp. 849–872, 2007.

[BER 00] BERNE B.J., PECORA R., *Dynamic Light Scattering: With Applications to Chemistry, Biology, and Physics*, Dover Inc., Toronto, Canada, 2000.

[BLO 01] BLONDEL D, BULTYNCK H., GOUESBET G., GRÉHAN G., "Phase Doppler measurements with compact monoblock configurations", *Particle & Particle Systems Characterization*, vol. 18, no. 2, pp. 79–90, 2001.

[BOD 10] BODOC V., ROUZAUD O., LAVERGNE G., "Measurement of bi-component droplet vaporization using global rainbow refractometry", *ILASS – Europe 2010, 23rd Annual Conference on Liquid Atomization and Spray Systems*, Brno, Czech Republic, September 2010.

[BOH 88] BOHREN C.F., HUFFMAN D.R., *Absorption and Scattering of Light by Small Particles*, John Wiley & Sons, New York, NY, 1988.

[BOU 94] BOUFENDI L., BOUCHOULE A., "Particle nucleation and growth in a low-pressure argon-silane discharge", *Plasma Sources Science and Technology*, vol. 3, pp. 262–270, 1994.

[BUE 88] BAUCKHAGE K., "The phase Doppler difference method, a new laser Doppler technique for simultaneous size and velocity measurements", *Particle & Particle Systems Characterization*, vol. 5, pp. 66–71, 1988.

[BUE 01] BUETTNER L., CZARSKE J., "A Multimode-fibre laser-Doppler anemometer for highly spatially resolved velocity measurements using low-coherence light", *Measurement Science and Technology*, vol. 12, pp. 1891–1903, 2001.

[BUL 98] BULTYNCK H., Développements de sondes laser Doppler miniatures pour la mesure de particules dans des écoulements réels complexes, PhD Thesis, University of Rouen, Rouen, France, 1998.

[CHA 04] CHARALAMPOUS G., HARDALUPAS Y., TAYLOR A.M.K.P., "Optimisation of the droplet sizing accuracy of the combined scattering (Mie)/laser induced fluorescence (LIF) technique", *12th International Symposium on Applications of Laser Techniques to Fluid Mechanics*, Lisbon University Ed., Portugal, Lisbon, 2004.

[CIL 10] CILAS, 2010, available at http://www.cilas.com.

[COË 11] COËTMELLEC S., REMACHA C., BRUNEL M., LEBRUN D., JANSSEN A.J.E.M., "Digital in-line holography with a spatially partially coherent beam", *Journal of the European Optical Society – Rapid Publications,* Vol. 6, p.11060, 2011

[CRA 97] CRAWLEY G., DI BENEDETTO M.C., "Size analysis of fine particle suspensions by spectral turbidimetry: potential and limits", *Powder Technology*, vol. 91, pp. 197–205, 1997.

[DAN 10] DANTEC DYNAMICS, 2010, available at http://www.dantecdynamics.com.

[DAV 55] DAVIS G.E., "Scattering of light by an air bubble in water", *Journal of the Optical Society of America A*, vol. 945, pp. 572–581, 1955.

[DEH 05] DEHAECK S., VAN BEECK J.P.A.J., RIETHMULLER M.L., "Extended glare point velocimetry and sizing for bubbly flows", *Experiments in Fluids*, vol. 39, no. 2, pp. 407–419, 2005.

[DEL 05] DE LULIIS S., CIGNOLI F., ZIZAK G., "Two-color laser-induced incandescence (2C-LII) technique for absolute soot volume fraction measurements in flames", *Applied Optics*, vol. 44, pp. 7414–7422, 2005.

[DES 08] DESGROUX P., MERCIER X., LEFORT B., LEMAIRE R., THERSSEN E., PAUWELS J.F., "Induced incandescence and cavity ring-down spectroscopy: effect of pressure on soot formation", *Combustion and Flame*, vol. 155, pp. 289–301, 2008.

[DOI 98a] DOICU A., GÖBEL G., WRIEDT T., BAUCHKAGE K., "Influence of agglomerates of conducting spheres on the response of a phase-Doppler anemometer", *Particle & Particle Systems Characterization*, vol. 15, no. 5, pp. 225–229, 1998.

[DOI 98b] DOICU A., KÖSER J., WRIEDT T., BAUCKHAGE K., "Light scattering simulation and measurement of monodisperse spheroids using a phase Doppler anemometer", *Particle & Particle Systems Characterization*, vol. 15, pp. 257–262, 1998.

[DOM 02a] DOMANN R., HARDALUPAS Y., "Planar droplet sizing for quantification of spray unsteadiness", *ILASS-Europe*, Zaragoza, 9–11 September 2002.

[DOM 02b] DOMANN R., HARDALUPAS Y., JONES A.R., "A study of the influence of absorption on the spatial distribution of fluorescence intensity within large droplets using Mie theory, geometrical optics and imaging experiments", *Measurement Science and Technology*, vol. 13, pp. 280–291, 2002.

[DOM 03] DOMANN R., HARDALUPAS Y., "Quantitative measurement of planar droplet Sauter mean diameter in sprays using planar droplet sizing", *Particle & Particle Systems Characterization*, vol. 20, pp. 209–218, 2003.

[DUC 08] DUCHAINE P., LACOSTE D., SCHULLER T., ZIMMER L., "Caractérisation de l'interaction d'un jet modulé et d'un spray dilué par imagerie Mie et LIF", Paper 7.2, *11ème congrès francophone de techniques laser*, Poitiers, 2008.

[DUM 09] DUMOUCHEL C., YONGYINGSAKTHAVORNA P., COUSIN J., "Light multiple scattering correction of laser-diffraction spray drop-size distribution", *International Journal of Multiphase Flow*, vol. 35, no. 3 pp. 277–287, 2009.

[DUR 75] DURST F., ZARÉ M., "Laser Doppler Measurements in Two-Phase Flows", *LDA Symposium*, Ed. P.O. Box 70 1740, Skovlunde, Copenhagen, 1975.

[DUR 81] DURST F., MELLING A., WHITELAW J.H., *Principles and Practice of Laser-Doppler Anemometry*, Academic press, New York, NY, 1981.

[FDI 08] FDIDA N., Développement d'un système de granulométrie par imagerie. Application aux sprays larges et hétérogènes, PhD Thesis, University of Rouen, Rouen, France, 2008.

[FDI 10] FDIDA N, BLAISOT J.-B., "Drop size distribution measured by imaging: determination of the measurement volume by the calibration of the point spread function", *Measurement Science and Technology*, vol. 21, no. 2, p. 025501, 2010.

[FRA 10] FRANCQUEVILLE L., BRUNEAUX G., THIROUARD B., Soot volume fraction measurements in a gasoline direct injection engine by combined laser induced incandescence and laser extinction method, *SAE International Journal of Engines*, vol. 3, no. 1, pp. 163–182, 2010.

[GIR 08] GIRE J., DENIS L., FOURNIER C., THIEBAUT E., SOULEZ F., DUCOTTET C., "Digital holography of particles: benefits of the 'inverse problem' approach", *Measurement Science and Technology*, vol. 19, no. 7, p. 074005, 2008.

[GLO 95] GLOVER A.R., SKIPPON S.M., BOYLE R.D., "Interferometric laser imaging for droplet sizing: a method for droplet-Size measurement in sparse spray systems", *Applied Optics*, vol. 34, no. 36, pp. 8409–8421, 1995.

[GOO 96] GOODMAN J.W., *Introduction to Fourier Optics*, McGraw-Hill, New York, 1996.

[GRÉ 93] GRÉHAN G., GOUESBET G. , NAQWI A., DURST F., "Particle trajectory effects in phase Doppler systems: computations and experiments", *Particle & Particle Systems Characterization*, vol. 10, pp. 332–338, 1993.

[GUÉ 08] GUÉNADOU D., LORCET H., BROTHIER M., GRAMONDI P., MICHON U., ONOFRI F., VARDELLE M., MARIAUX G., "Gasification of Biomass by Thermal Plasma", *7th International Symposium of High Temperature Air Combustion and Gasification (HiTACG)*, Phuket, Thailand, 13–16 January 2008.

[HAN 94] HANSEN P.C., "Regularization tools, a Matlab package for analysis and solution of discrete ill-posed problems", *Numerical Algorithms*, vol. 6, pp. 1–35, 1994.

[HAN 98] HAN H., REN K-F., ZHENSEN W., GREHAN G., GOUESBET G., CORBIN F., "Characterization of initial disturbances in liquid jet by rainbow sizing", *Applied Optics*, vol. 37, no. 36, pp. 8498–8503, 1998.

[HAR 94] HARDALUPAS Y., HISHIDA K., MAEDA M., MORIKITA H., TAYLOR A.M.K.P., WHITELAW J.H., "Shadow Doppler technique for sizing particles of arbitrary Shape", *Applied Optics*, vol. 33, no. 36, pp. 8417–8426, 1994.

[HES 98] HESS C.F., "Planar particle image analyzer", *9th International Symposium on Applications of Laser Techniques to Fluid Mechanics*, Lisbon University Ed., Portugal, 13–16 July 1998.

[HES 08] HESPEL H., REN K.-F., GRÉHAN G., ONOFRI F., "Numerical study of glare spot phase Doppler anemometry", *Optics Communications*, vol. 281, no. 6, pp. 1375–1383, 2008.

[HIR 88] HIRLEMAN E.D., "Modeling of multiple scattering effects in Fraunhofer diffraction particle size analysis", *Particle & Particle Systems Characterization*, vol. 5, pp. 57–65, 1988.

[HON 06] HONG S.H., WINTER J., "Size dependence of optical properties and internal structure of plasma grown carbonaceous nanoparticles studied by in situ Rayleigh-Mie scattering ellipsometry", *Journal of Applied Physics*, vol. 100, pp. 064–303, 2006.

[HOV 92] HOVENAC E.A., LOCK J.A., "Assessing the contribution of surface waves and complex rays to far-field scattering by use of the Debye series", *Journal of the Optical Society of America A*, vol. 9, no. 5, pp. 781–795, 1992.

[IMA 12] IMAGE J, 2012, available at http://rsbweb.nih.gov/ij.

[JEN 01] JENKINS T.P., HANSON R.K., "Soot pyrometry using modulated absorption/ emission", *Combustion and Flame*, vol. 126, pp. 1669–1679, 2001.

[JÜP 10] JÜPTNER W., *Digital Holography: Digital Hologram Recording, Numerical Reconstruction, and Related Techniques*, Springer, Berlin, 2010.

[KAN 12] KANOMAX, 2012, available at http://www.kanomax.co.jp.

[KAW 02] KAWAGUCHI T., AKASAKA Y., MAEDA M., "Size measurements of droplets and bubbles by advanced interferometric laser imaging technique", *Measurement Science and Technology*, vol. 13, no. 3, pp. 308–316, 2002.

[KAY 98] KAYE P.H., "Spatial light scattering as a means of characterising and classifying non-spherical particles", *Measurement Science and Technology*, vol. 9, pp. 141–149, 1998.

[KOH 03] KOH H., JEON J., KIM D., YOON Y., KOO J.-Y, "Analysis of signal attenuation for quantification of a planar imaging technique", *Measurement Science and Technology*, vol. 14, pp. 1829–1838, 2003.

[KRZ 09] KRZYSIEK M., Particle systems characterization by inversion of critical light scattering patterns, Ph.D. Thesis, University of Provence, Marseille, France, 2009.

[LAB 95] LABRUNIE L., PAULIAT G., ROOSEN G., LAUNAY J.C., "Simultaneous acquisition of π/2 phase-stepped interferograms with a photorefractive bi12GeO20 crystal: application to real-time double-pulse holography", *Optics Letters*, vol. 20, pp. 1652–1654, 1995.

[LAC 08] LACOUR C., DUROX D., CNRS Images, 2008, available at http://www.cnrs.fr.

[LAC 11] LACOUR C., DUROX D., DUCRUIX S., MASSOT M., "Interaction of a polydisperse spray with vortices", *Experiments in Fluids*, vol. 51, NO. 2, pp. 295–311, 2011.

[LAM 12] LAMADIE F., BRUEL L., HIMBERT M., "Digital holographic measurement of liquid–liquid two-phase flows", *Optics and Lasers in Engineering*, vol. 50, no. 12, pp. 1716–1725, 2012.

[LAV 12] LAVISION, 2012, available at http://www.lavision.de/en.

[LEB 99] LEBRUN D., BELAÏD S., ÖZKUL C., "Hologram reconstruction by use of optical wavelet transform", *Applied Optics*, vol. 38, no. 17, pp. 3730–3734, 1999.

[LEG 99] LEGAL P., FARRUGIA N., GREENHALGH D.A., "Laser sheet drop sizing of dense sprays", *Optics Laser Technology*, vol. 31, pp. 75–83, 1999.

[LEM 06] LEMAITRE P., PORCHERON E., GRÉHAN G., BOUILLOUX L., "Development of a global rainbow refractometry technique to measure the temperature of spray droplets in a large containment vessel", *Measurements Science and Technology*, vol. 17, no. 6, pp. 1299–1306, 2006.

[LIU 06] LIU F., DAUN K.J., SNELLING D.R., SMALLWOOD G.J., "Heat conduction from a spherical nano-particle: status of modeling heat conduction in laser-induced incandescence", *Applied Physics B*, vol. 83, no. 3, pp. 355–382, 2006.

[MAE 00] MAEDA M., KAWAGUCHI T., HISHIDA K., "Novel interferometric measurement of size and velocity distributions of spherical particles in fluid flows", *Measurement Science and Technology*, vol. 11, pp. 13–18, 2000.

[MAE 02] MAEDA M., KASAKA Y.A., KAWAGUCHI T., "Improvement of the interferometric technique for simultaneous measurement of droplets size and velocity vector field and its application to a transient spray", *Experiments in Fluids*, vol. 33, no. 1, pp. 125–133, 2002.

[MAL 00] MALOT H., BLAISOT J.B., "Droplet size distribution and sphericity measurements of low-density sprays through image analysis", *Particle & Particle Systems Characterization*, vol. 17, no. 4, pp. 146–158, 2000.

[MAL 10] MALVERN INSTRUMENTS, 2010, available at http://www.malvern.com.

[MAN 94] MANASSE U., WRIEDT T., BAUCKHAGE K., "Reconstruction of real size distributions hidden in phase Doppler anemometry results obtained from droplets of inhomogeneous liquids", *Particle & Particle Systems Characterization*, vol. 11, pp. 84–90, 1994.

[MAN 97] MANICKAVASAGAM S., MENGÜÇ M.P., "Scattering matrix elements of fractal-like soot agglomerate", *Applied Optics*, vol. 36, no. 6 pp. 1337–1351, 1997.

[MAR 87] MARET G., WOLF P.E., "Multiple light scattering from disordered media. The effect of Brownian motion of scatterers", *Zeitschrift für Physik B (Condens Mater)*, vol. 65, pp. 409–413, 1987.

[MAR 79] MARSTON P.L., "Critical scattering angle by a bubble: physical optics approximation and observations", *Journal of the Optical Society of America A*, vol. 69, no. 9, pp. 1205–1211, 1979.

[MAR 81] MARSTON P.L., KINGSBURY D.L., "Scattering by a bubble in water near the critical angle: interference effects", *Journal of the Optical Society of America A*, vol. 71, no. 3, pp. 358–361, 1981.

[MAR 94] MARSTON P.L., KADUCHAK G., "Generalized rainbows and unfolded glories of oblate drops: organization for multiple internal reflections and extension of cusps into Alexander's dark band", *Applied Optics*, vol. 33, no. 21, pp. 4702–4713, 1994.

[MAS 89] MASSOLI P., BERRETA F., D'ALLESSIO A., "Single droplet size, velocity and optical characteristics by the polarization properties of the scattered light", *Applied Optics*, vol. 6, no. 28, pp. 1200–1208, 1989.

[MAT 04] MATSUURA K., KOMAKI M., UEYAMA K., HIRONAGA K., "Shadow Doppler velocimetry with double fiber-array sensors", *Experiments in Fluids*, vol. 36, no. 1, pp. 11–22, 2004.

[MAT 12] MATLAB, 2012, available at http://www.mathworks.fr.

[MEL 84] MELTON L., "Soot diagnostics based on laser heating", *Applied Optics*, vol. 23, pp. 2201–2208, 1984.

[MEN 04] MENG H., PAN G., PU Y., WOODWARD S.H. "Holographic particle image velocimetry: from film to digital recording", *Measurement Science and Technology*, vol. 15, pp. 673–685, 2004.

[MIC 07] MICHELSEN H.A., LIU F., KOCK B.F., BLADH H., BOIARCIUC A., CHARWATH M., DREIER T., HADEF R., HOFMANN M., REIMANN J., WILL S., BENGTSSON P.-E., BOCKHORN H., FOUCHER F., GEIGLE K.-P., MOUNAÏM-ROUSSELLE C., SCHULZ C., STIRN R., TRIBALET B., SUNTZ R., "Modeling laser-induced incandescence of soot: a summary and comparison of LII models", *Applied Physics B*, vol. 87, pp. 503–521, 2007.

[MIG 96] MIGNON H., GRÉHAN G., GOUESBET G., XU T.-H., TROPEA C., "Measurement of cylindrical particles with phase Doppler anemometry", *Applied Optics*, vol. 35, no. 25, pp. 5180–5190, 1996.

[MOU 99] MOUNAÏM-ROUSSELLE C., PAJOT O., "Droplet sizing by Mie scattering interferometry in S.I engine", *Particle and Particle Systems Characterization*, vol. 16, pp. 160–168, 1999.

[MRO 93] MROCZKA J., "Method of moments in light scattering data inversion in the particle size distribution function", *Optics Communications*, vol. 99, pp. 147–151, 1993.

[MÜL 04] MÜLLER J., KEBBEL V., JÜPTNER W., "Characterization of spatial particle distributions in a spray-forming process using digital holography", *Measurement Science and Technology*, vol. 15, pp. 706–710, 2004.

[NAQ 91] NAQWI A., DURST F., LIU X., "Extended phase-Doppler system for characterization of multiphase-flows", *Particle & Particle Systems Characterization*, vol. 8, pp. 16–22, 1991.

[NAQ 93] NAQWI A., DURST F., "Analysis of the laser light scattering interferometric devices for the in-line diagnostic of moving particles", *Applied Optics*, vol. 32, pp. 4003–4018, 1993.

[NAQ 96] NAQWI A., "Sizing of irregular particles using a phase Doppler system", *Particle & Particle Systems Characterization*, vol. 8, pp. 343–349, 1996.

[NI 95] NI T., PINSON J.A., GUPTA S., SANTORO R.J., "Two-dimensional imaging of soot volume fraction by the use of laser-induced incandescence", *Applied Optics*, vol. 34, no. 30, pp. 7083–7091, 1995.

[NUS 92] NUSSENZWEIG H.M., *Diffraction Effects in Semiclassical Scattering*, Cambridge University Press, Cambridge, 1992.

[OKA 08] OKADAA Y., MANNA I., MUKAIA T., KÖHLERB M., "Extended calculation of polarization and intensity of fractal aggregates based on rigorous method for light scattering simulations with numerical orientation averaging", *Journal of Quantitative Spectroscopy and Radiative Transfer*, vol. 109, pp. 2613–2627, 2008.

[ONO 95] ONOFRI F., Prise en compte des dimensions finies des faisceaux d'éclairage en granulométrie optique: anémométrie phase Doppler, applications aux diagnostics des milieux diphasiques, PhD Thesis, University of Rouen, Rouen, France, 1995.

[ONO 96a] ONOFRI F., BLONDEL D., GRÉHAN G., GOUESBET G., "On the optical diagnosis and sizing of spherical coated and multilayered particles with phase-Doppler anemometry", *Particle & Particle Systems Characterization*, 13, pp. 104–111, 1996.

[ONO 96b] ONOFRI F., GIRASOLE T., GRÉHAN G., GOUESBET G., BRENN G, DOMNICK J., XU T.-H, TROPÉA C., "Phase-Doppler anemometry with the dual burst technique for measurement of refractive index and absorption coefficient simultaneously with size and velocity", *Particle & Particle Systems Characterization*, vol. 13, pp. 112–124, 1996.

[ONO 99a] ONOFRI F., "Critical angle refractometry for simultaneous measurement of particles in flow size and relative refractive index". *Particle & Particle Systems Characterization*, pp. 119–127, 1999.

[ONO 99b] ONOFRI F., BERGOUNOUX L., FIRPO J.-L., MESGUISH-RIPAULT J., "Velocity, size and concentration measurements of optically inhomogeneous cylindrical and spherical particles", *Applied Optics*, vol. 38, pp. 4681–4690, 1999.

[ONO 00] ONOFRI F., "Etude numérique et expérimentale de la sensibilité de l'anémométrie phase Doppler à l'état de surface des particules détectées", *7ème congrès francophone de vélocimétrie laser*, Marseille, September 2000.

[ONO 02] ONOFRI F., LENOBLE A., RADEV S., "Superimposed non interfering probes to extend the phase Doppler anemometry capabilities", *Applied Optics*, vol. 41, no. 18,pp. 3590–1600, 2002.

[ONO 03] ONOFRI F., LENOBLE A., RADEV S., BULTYNCK H., GUERING P.-H., MARSAULT N., "Interferometric sizing of single-axis birefringent glass fibres", *Particle & Particle Systems Characterization*, vol. 20, no. 3, pp. 171–182, 2003.

[ONO 04] ONOFRI F., LENOBLE A., BULTYNCK B., GUÉRING P.-H, "High-resolution laser diffractometry for the on-line sizing of small transparent fibres", *Optics Communications*, vol. 234, pp. 183–191, 2004.

[ONO 05] ONOFRI F., Diagnostics optiques des milieux multiphasiques, Habilitation thesis, University of Provence, Marseille, France, 2005.

[ONO 06] ONOFRI F., "3-Interfering beams laser Doppler velocimetry for particle position and flow velocity profile measurements", *Applied Optics*, 45, pp. 3317–3324, 2006.

[ONO 07] ONOFRI F., KRZYSIEK M., MROCZKA J., "Critical angle refractometry and sizing for bubbly flow characterization", *Optics Letters*, vol. 32, pp. 2070–2072, 2007.

[ONO 09a] ONOFRI F., REN K.-F., GRISOLIA C., "Development of an in situ ITER dust diagnostic based on extinction spectrometry", *Journal of Nuclear Materials*, vol. 390–391, pp. 1093–1096, 2009.

[ONO 09b] ONOFRI F.R.A., KRZYSIEK M., MROCZKA J., REN K.-F., RADEV ST., BONNET J.-P., "Optical characterization of bubbly flows with a near-critical-angle scattering technique", *Experiments in Fluids*, 47, pp. 721–732, 2009.

[ONO 11a] ONOFRI F.R.A., KRZYSIEK M.A., BARBOSA S., MESSAGER V., REN K-F., MROCZKA J., "Near-critical-angle scattering for the characterization of clouds of bubbles: particular effects", *Applied Optics*, vol. 50, no. 30, pp. 5759–5769, 2011.

[ONO 11b] ONOFRI F., WOZNIAK M., BARBOSA S., "On the optical characterisation of nanoparticle and their aggregates in plasma systems", *Contributions to Plasma Physics*, vol. 51, no. 2–3, pp. 228–236, 2011.

[ONO 12a] ONOFRI F.R.A., BARBOSA S., TOURÉ O., WOŹNIAK M., GRISOLIA C., "Sizing highly-ordered buckyball-shaped aggregates of colloidal nanoparticles by light extinction spectroscopy", *Journal of Quantitative Spectroscopy & Radiative Transfer*, 2012.

[ONO 12b] ONOFRI F.R.A, RADEV St., SENTIS M., BARBOSA S., "A physical-optics approximation of the near-critical-angle scattering by spheroidal bubbles", *Optics Letters*, 2012, forthcoming.

[ONU 93] ONURAL L., "Diffraction from a wavelet point of view", *Optics Letters*, vol. 18, no. 11, pp. 846–848, 1993.

[OXF 12] OXFORD LASERS, 2012, available at http://www.oxfordlasers.com.

[PEN 87] PENTLAND A.P., "A new sense for depth of field", *IEEE Transactions on Pattern Analysis and Machine Intelligence*, vol. 9, no. 4, pp. 523–531, 1987.

[POW 10] POWERSCOPE TECHNOLOGIES, 2010, available at http://www.powerscopetech.com.

[PRO 04] PROVDER T., TEXTER J. (ed), *Particle Sizing And Characterization, ACS Symposium Series 881*, American Chemical Society, Washington, DC, 2004.

[PU 05] PU S., Développement de méthodes interférométriques pour la caractérisation des champs de particules, PhD Thesis, University of Rouen, Rouen, France, 2005.

[RAG 90] RAGUCCI R., CAVALIERE A., MASSOLI P., "Drop sizing by laser light scattering exploiting intensity angular oscillation in the Mie regime", *Particle & Particle Systems Characterization*, vol. 7, pp. 221–225, 1990.

[RD 12] R&D VISION, 2012, available at http://www.rd-vision.com.

[REN 96] REN K.F., LEBRUN D., ÖZKUL C., KLEITZ A., GOUESBET G., GRÉHAN G., "On the measurement of particles by imaging methods: theoretical and experimental aspects", *Particle & Particle Systems Characterization*, vol. 13, pp. 156–64, 1996.

[REN 98] RENOUX A., BOULAUD D., *Les aérosols, Physique et métrologie*, Lavoisier, Tec & Doc, Paris, 1998.

[REN 11] REN K-F., ONOFRI F.R.A., ROZÉ C., GIRASOLE T., "Vectorial complex ray model and application to 2D scattering of plane wave by a spheroidal particle", *Optics Letters*, vol. 36, no. 3 pp. 370–372, 2011.

[RHE 95] RHEIMS J., DAHL H., WRIEDT T., BAUCKHAGEN K., "Sizing coated spheres with phase Doppler anemometry", *4th International Congress on Optical Partical Sizing Conference-Partec95*, Nuremberg, Germany, 1995.

[ROI 01] ROISMAN I.V., TROPEA C., "Flux measurements in sprays using phase Doppler techniques", *Atomization Spray*, vol. 11, pp. 667–669, 2001.

[ROT 90] ROTH N., ANDERS K., FROHN A., "Simultaneous measurement of temperature and size of droplets in micrometer range", *Applied Optics*, vol. 2, no. 1, pp. 37–42, 1990.

[ROY 77] ROYER H., "Holographic Velocimetry of Submicron Particles", *Optics Communications*, vol. 20, pp. 73–75, 1977.

[SAE 06] SAENGKAEW S., CHARINPANITKUL T., VANISRI H., TANTHAPANICHAKOON W., MEES L., GOUESBET G., GREHAN G., "Rainbow refractometry: on the validity domain of Airy's and Nussenzveig theories", *Optics Communications*, vol. 259, pp. 7–13, 2006.

[SAE 10] SAENGKAEW S., CHARINPANIKUL T., LAURENT C., BISCOS Y., LAVERGNE G., GOUESBET G., GRÉHAN G., "Processing of Individual Rainbow Signals", *Experiments in Fluids*, vol. 48, pp. 111–119, 2010.

[SAF 84] SAFFMAN, M., BUCHHAVE, P., TANGER, H., "Simultaneous measurement of size, concentration and velocity of spherical particles by a laser Doppler method", *2nd International Symposium on Applications of Laser Anemometry to Fluid Mechanics*, University of Lisbon Ed, paper 8.1, Lisbon, Portugal, 2–5 July 1984.

[SAL 08] SALAH N., GODARD G., LEBRUN D., PARANTHOËN P., ALLANO D., COËTMELLEC S., "Application of multiple exposure digital in-line holography to particle tracking in a Benard-von Karman vortex Flow", *Measurement Science and Technology*, vol. 19, p. 074001, 2008.

[SAN 91] SANKAR S.V., BACHALO W.D., "Response characteristics of the phase Doppler particle analyzer for sizing spherical particles larger than the light wavelength", *Applied Optics*, vol. 30, no. 12, pp. 1487–1496, 1991.

[SAN 93] SANKAR S.V., IBRAHIM K.H., BUERMANN D.H., FIDRICH M.J., BACHALO W.D., "An Integrated Phase Doppler/Rainbow Refractometer System for Simultaneous Measurement of Droplet Size", Velocity and Refractive Index, *3rd International Congress on Optical Partical Sizing*, Yokohama, Japan, pp. 275–284, 23–26 August 1993.

[SAN 99] SANKAR S.V., MAHLER K.E., ROBART D.M., "Rapid characterization of fuel atomizers using an optical patternator", *Journal of Engeenering for Gas Turbine and Power*, vol. 121, pp. 409–414, 1999.

[SCH 09] SCHALL P., "Laser diffraction microscopy", *Reports on Progress in Physics*, vol. 72, p. 076601, 2009.

[SCH 87] SCHÄTZEL K., PETERS W., "Two-colour dynamic light scattering", *Journal of Modern Optics*, vol. 42, pp. 1929–1935, 1987.

[SCH 91a] SCHÄTZTE K., "Suppression of multiple-scattering by photon cross-correlation techniques", *Journal of Modern Optics*, vol. 38, pp. 1849–1855, 1991.

[SCH 89] SCHAUB S.A., ALEXANDER D.R., BARTON J.P., "Theoretical model for the image formed by a spherical particle in a coherent imaging system: comparison to experiment", *Optical Engineering*, vol. 28, no. 5, pp. 565–573, 1989.

[SCH 91b] SCHNABLEGGER H., GLATTER O., "Optical sizing of small colloidal particles: an optimized regularization technique", *Applied Optics*, vol. 30, pp. 4889–4896, 1991.

[SCH 06] SCHULZ C., KOCK B.F., HOFMANN M., MICHELSEN H., WILL S., BOUGIE B., SUNTZ R., SMALLWOOD G., "Laser-induced incandescence: recent trends and current questions", *Applied Physics B*, vol. 83, pp. 333–340, 2006.

[SEM 04] SEMIDETNOV N., TROPEA C., "Conversion relationships for multidimensional particle sizing techniques", *Measurement Science and Technology*, vol. 15, vol. 1, pp. 112–120, 2004.

[SHE 12] SHEN H., COËTMELLEC S., GRÉHAN G., BRUNEL M., "Interferometric laser imaging for droplet sizing revisited: elaboration of transfer matrix models for the description of complete systems", *Applied Optics*, vol. 51, no. 22, pp. 5357–5368, 2012.

[SOM 04] SOMMERFELD M., QIU, H.H., "Particle concentration measurements by phase-Doppler anemometry in complex dispersed two-phase flows", *Experiment in Fluids*, vol. 18, no. 3, pp. 187–198, 2004.

[SOR 01] SORENSEN C.M., "Light scattering by fractal aggregates: A review", *Aerosol Science Technology*, vol. 35, pp. 648–687, 2001.

[SOU 07] SOULEZ F., DENIS L., THIÉBAUT E., FOURNIER C., GOEPFERT C. "Inverse problems approach in particle digital holography: out-of-field particle detection made possible", *Journal of the Optical Society of America A*, vol. 24, no. 12, pp. 3708–3716, 2007.

[SU 02] SU M., XU F., CAIA X., REN K-F., SHENA J., "Optimization of regularization parameter of inversion in particle sizing using light extinction method", *China Particuology*, vol. 5, pp. 295–299, 2002.

[SWI 91] SWITHENBANK J., CAO J., HAMIDI A.A., "Spray diagnostics by laser diffraction", in CHIGIER N. (ed), Combustion measurements, Hemisphere Publishing Corporation, New York, pp. 179–228, 1991

[TIA 10] TIAN L., LOOMIS N., DOMÍNGUEZ-CABALLERO J.A., BARBASTATHIS G., "Quantitative measurement of size and three-dimensional position of fast-moving bubbles in air-water mixture flows using digital holography", *Applied Optics*, vol. 49, no. 9, pp. 1549–1554, 2010.

[TIK 95] TIKHONOV A.N, GONCHARSKY A, STEPANOV V.V, YAGOLA A.G., *Numerical Methods for the Solution of Ill-posed Problems*, Kluwer Academic Publisher, Dordrecht, 1995.

[TRI 92] TRIBILLON J-L., "Développements actuels des matériaux d'enregistrement pour l'holographie", *Opto92*, Paris, France, 1992.

[TRO 96] TROPEA C., XU T-H., ONOFRI F., GRÉHAN G., HAUGEN P., "Dual-mode phase Doppler anemometer", *Particle & Particle Systems Characterization*, vol. 13, pp. 165–170, 1996.

[TRO 11] TROPEA C., "Optical particle characterization in flows", *Annual Review of Fluid Mechanics*, vol. 43, pp. 399–426, 2011.

[TSI 10] TSI inc. 2010; available at http://www.tsi.com.

[TWO 79] TWOMEY S., *Introduction to the Mathematics in Remote Sensing and Indirect Measurement*, Elsevier, New York, 1979.

[VAN 94a] VAN BEECK J.P.A., RIETHMULLER M.L., "Non intrusive measurements of temperature and size of raindrops", *Applied Optics*, vol. 34, pp. 1633–1639, 1994.

[VAN 99] VAN BEECK J.P.A.J., GIANNOULIS D., ZIMMER L., RIETHMULLER M.L., "Global rainbow thermometry for droplet-temperature measurement", *Optics Letters*, vol. 24, pp. 1696–1705, 1999.

[VAN 57] VAN DE HULST H.C., *Light Scattering by Small Particles*, Dover Publications, New York, 1957.

[VAN 91] VAN DE HULST H.C., WANG R.T., "Glare points", *Applied Optics*, vol. 30, pp. 4755–4763, 1991.

[VAN 94b] VANDER WAL R.L., WEILAND K.J., "Laser-induced incandescence: development and characterization towards a measurement of soot-volume fraction", *Applied Physics B*, vol. 59, pp. 445–452, 1994.

[VET 04] VETRANO M.R., VAN BEECK J.P.A.J., RIETHMULLER M.L., "Global rainbow thermometry: improvements in the data inversion algorithm and validation technique in liquid–liquid suspension", *Applied Optics*, vol. 34, pp. 3600–3607, 2004.

[VET 05] VETRANO M.R., VAN BEECK J.P.A.J., RIETHMULLER M.L., "Generalization of the rainbow Airy theory to nonuniform spheres", *Optics Letters*, vol. 30, no. 6, pp. 658–660, 2005.

[WAT 04] WATSON D.M., Physics lecture notes, outline, and readings, 2004, available at http://www.pas.rochester.edu/~dmw/phy218/Lectures.htm.

[WIL 07] WILMS J., WEIGAND B., "Composition measurements of binary mixture droplets by rainbow refractometry", *Applied Optics*, vol. 46, no. 11, pp. 2109–2118, 2007.

[WU 12] WU X., MEUNIER-GUTTIN-CLUZEL S., WU Y., SAENGKAEW S., LEBRUN D., BRUNEL M., CHEN L., COETMELLEC S., CEN K., GREHAN G., "Holography and micro-holography of particle fields: a numerical standard", *Optics Communications*, vol. 285, no. 13–14, pp. 3013–3020, 2012.

[XU 94] XU T.-H., TROPEA C., "Improving the performance of two-component phase Doppler anemometry", *Measurement Science and Technology*, vol. 5, pp. 969–975, 1994.

[XU 02] XU R., *Particle Characterization: Light Scattering Methods*, Kluwer Academic Publishers, Dordrecht, Nederland, 2002.

[XU 07] XU F., Shaped beam scattering by a spheroid and online wet steam Measurement by using spectral light extinction method, PhD Thesis, University of Rouen, France, 2007.

[YEH 93] YEH C.-N., KOSAKA H., KAMIMOTO T., "A fluorescence/scattering imaging technique for instantaneous 2-D measurements of particle size distribution in a transient spray", *Proceedings 3rd Congress on Optical Paricle Sizing*, Yokohama, Japan, pp. 355–361, 1993.

[ZIM 02] ZIMMER L, DOMANN R., HARDALUPAS Y., IKEDA Y., "Simultaneous LIF and Mie scattering measurements for branch-like spray cluster in industrial oil burner", *40th Aerospace Sciences Meeting & Exhibit (AIAA 02-0349)*, Reno, NV, 2002.

Chapter 3

Laser-Induced Fluorescence

Practical interest in using laser-induced fluorescence (LIF) to measure a physical quantity, which characterizes the medium in which fluorescent species is present results from several factors such as:

– detection threshold, as a few parts per million of fluorescent molecule, having an intense high absorption cross-section, is sufficient to produce a measurable and usable signal;

– response time linked to the short lifetime of the excited molecule state (10^{-9}–10^{-6} s), which allows investigating physical phenomena that rapidly vary;

– shift between absorption and fluorescence spectra, allowing an easy separation between exciting radiation and fluorescence signal.

3.1. Recall on energy quantification of molecules

Atomic energy is determined by the orbital movement of electrons. The presence of several atoms inside a molecule leads to a very complex spectrum, as internuclear vibration movements and rotation movements of the molecule around its center of gravity must be also considered. Energies from vibration and rotation are also quantified, which provides a fine and a complex energetic structure to the molecule, and then a very high number of possible transitions. The Born–Oppenheimer approximation assumes that nucleus movement is slow compared to electron displacement, which allows decoupling excitations of various types: electronic, vibrational, rotational. In order to simplify explanations, in this chapter we limit

---

Chapter written by Fabrice LEMOINE and Frédéric GRISCH.

arguments to diatomic molecules; polyatomic molecules representing more complex situations requiring us to take into account the couplings between rotational and vibrational energies, etc. Therefore, the total energy of a molecule is expressed as the sum of electronic, vibrational and rotational energies:

$$E_T = E_e + E_v + E_r \qquad [3.1]$$

Molecule electronic energy exclusively comes from electron orbital movement and from electron spin. Vibration levels are equally distributed and spaced by hv (v being the vibration frequency) and may be approached by an assumption of the harmonic oscillator for small displacements r of nuclei relative to their position of equilibrium. For larger displacements r, a non-harmonic assumption must be introduced and molecule dissociation must then be taken into account (for instance a diatomic molecule that may dissociate into two atoms).

An important number of energy states of the molecule states offers possibility for multiple transitions for absorption, as well as for photon emission. The whole potential of transitions starting from a fundamental state toward an excited state constitutes the molecule absorption spectrum.

Vibration energy is expressed as a function of the vibrational quantum number v (v = 1, 2, 3, etc.) as follows:

$$G(v) = \frac{E_v}{hc} = \frac{\nu}{c}(v+1/2) - \frac{\nu}{c}x_e(v+1/2)^2 + \frac{\nu}{c}y_e(v+1/2)^3 \qquad [3.2]$$

with vibrational energy E_y, $\frac{\nu}{c}y_e$ and $\frac{\nu}{c}x_e << \frac{\nu}{c}$, x_e and y_e being parameters linked to considered molecule.

In order to define rotational energy, the molecule is initially considered as a rigid rotating system. Rotational energy is written as a function of the rotational quantum number (J = 1, 2, 3, etc.) as follows:

$$F(J) = \frac{E_r}{hc} = BJ(J+1) \qquad [3.3]$$

with E_r being the rotational energy, $B = \frac{h}{8\pi^2 cI}$ the inertia constant and I the molecule inertia moment defined relative to the line passing through the mass center and perpendicular to the molecule axis. Nevertheless, an increase of rotational energy provokes an increase of internuclei distance, inducing a variation in molecule

inertia moment. Moreover, internuclei vibration movements and rotational movements being simultaneous, the inertia moment is modified as the distance between nuclei varies. Taking into account these effects, rotational energy is thus expressed as:

$$F(J) = B_v J(J+1) - D_v J^2 (J+1)^2 \qquad [3.4]$$

with
$$B_v = \mathrm{B}_e - \alpha_e (v+1/2)$$
$$D_v = D_e + \beta_e (v+1/2)$$

D_v is a centrifugal distortion constant ($B_v >> D_v$). B_e, D_e, α_e and β_e are constants such as α_e and $\beta_e << B_e$ and D_e.

Each vibrational level has sub-rotational levels given that a number of rotational levels correspond at each vibrational level. To illustrate this, Figure 3.1 presents an energetic diagram (potential energy as a function of a internuclei distance r) of the diatomic iodine (I_2) molecule.

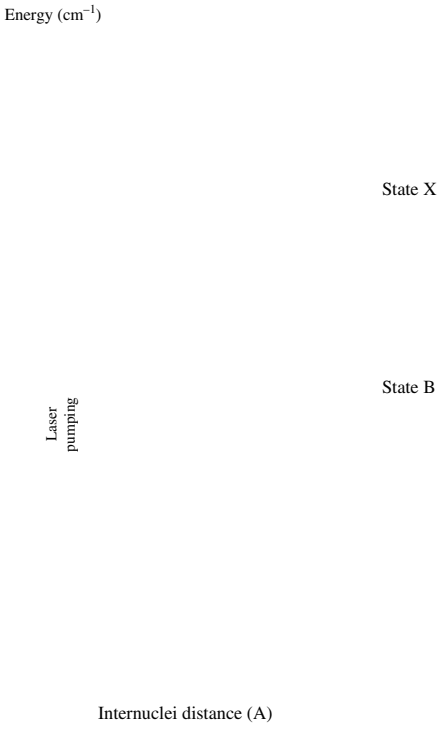

Figure 3.1. *Energetic diagram of iodine molecule (I_2)*

3.1.1. *Radiative transitions*

In order to describe radiative transitions, a molecule will be considered, which has two energetic states 1 and 2, excited by an electromagnetic wave of frequency v_{12} such as $E_2 - E_1 = hv_{12}$.

3.1.1.1. *Absorption*

The molecule, *M*, in fundamental state 1 absorbs a photon and goes into excited state 2 along reaction $M + hv \rightarrow M^*$. The population of excited state is described by the following kinetic law:

$$\frac{dN_1}{dt} = N_1 B_{12} W \qquad [3.5]$$

with B_{12} ($m^3.J^{-1}.s^{-2}$) being the Einstein coefficient for transition from state 1 toward state 2 and W ($J.m^{-3}.s$) being the spectral energy density, as far as transition of frequency v is concerned.

3.1.1.2. *Spontaneous emission (or fluorescence)*

There is a spontaneous return from excited state 2 toward fundamental state 1 by a photon emission along reaction: $M^* \rightarrow M + hv$. The depopulation rate of the excited state is expressed by kinetic equation:

$$\frac{dN_2}{dt} = N_2 A_{21} \qquad [3.6]$$

with A_{21} (s^{-1}) being the Einstein coefficient for spontaneous emission, representing transition probability by the spontaneous emission per unit of time.

The natural lifetime of the excited state τ_0 (s) is also defined as the inverse of a deactivation velocity by spontaneous emission:

$$\tau_0 = \frac{1}{A_{21}} \qquad [3.7]$$

3.1.1.3. *Stimulated emission*

Contrary to the previous case, the return to the fundamental state does not occur in a spontaneous manner, but a photon of energy hv is required to stimulate the passage from excited state to fundamental state, along reaction: $M^* \; hv \rightarrow M + 2hv$.

Note that the emitted photon possesses the same characteristics as the incident photon for phase, energy and propagation direction. This medium thus behaves as an amplifier with a gain of two, a phenomenon that is the basis for a laser effect.

The depopulation rate of an excited state by stimulated emission is expressed by the following kinetic equation:

$$\frac{dN_2}{dt} = N_2 B_{21} W \qquad [3.8]$$

B_{21} ($m^3.J^{-1}.s^{-2}$) being the Einstein coefficient for stimulated emission.

Einstein coefficients are linked by the following relationships:

$$g_1 B_{12} = g_2 B_{21}$$
$$B_{21} = \frac{A_{21} c^3}{4h\nu^3} \qquad [3.9]$$

g_1 and g_2 are degenerations of states 1 and 2, respectively, representing the number of sublevels having the same energy.

We then observe that the ratio between spontaneous emission and stimulated emission is given by:

$$\frac{B_{21} W}{A_{21}} \qquad [3.10]$$

In order to obtain a ratio close to one, in other words, a stimulated emission equivalent to the spontaneous emission rate, it is necessary to have a spectral energy density W of approximately 1.2×10^{-14} $J.m^{-3}.s$ for a wavelength λ = 600 nm ($\nu = 5.10^{14}$ Hz). For a spectral bandwidth $\Delta\lambda$ of 0.01 nm ($\Delta\nu = \frac{c\Delta\lambda}{\lambda^2} = 8.3 \times 10^{10}$ Hz), the obtained flux density is equal to:

$$\Phi = W.c.\Delta\nu = 3.10^5 \text{ W/m}^2$$

This flux is very important, compared to that emitted by a mercury vapor lamp ($\Phi \propto 10^4$ W/m^2).

3.1.2. *Energy level thermo-statistics*

For a local thermodynamic equilibrium, and for a temperature T, the populations of energy levels are distributed along a Boltzmann law:

$$N_i = N \frac{g_i e^{-E_i/kT}}{\sum_i g_i e^{-E_i/kT}} \quad [3.11]$$

N_i is the number of molecules per unit volume in state i, N is the total number of molecules per unit volume, k the Boltzmann constant.

The Boltzmann fraction $f(T)$ of the fundamental state (of energy E_1) is designated by the ratio:

$$f(T) = N_1/N = \frac{g_1 e^{-E_1/kT}}{\sum_i g_i e^{-E_i/kT}} \quad [3.12]$$

3.1.3. *Franck–Condon principle*

Transition time from the fundamental state toward the excited state is very short, that is approximately 10^{-15} s; there is no modification of the geometric position of atomic nuclei during the transition, as rotational and vibrational movements have a characteristic timescale of 10^{-12} s. The stable structure of the molecule in the fundamental state does not correspond to the stable structure in the excited state: absorption is generally followed by a vibrational relaxation at excited state, bringing back the molecule at the lowest vibrational state of the electronic excited state. Then, fluorescence emission of a molecule will always occur at wavelengths superior to those of the exciting radiation; therefore, fluorescence spectrum is shifted relative to excitation radiation. Figure 3.2 shows an example of sulforhodamine B in a water solution. In practice, it will be easy to separate excitation radiation from fluorescence radiation emitted by fluorescence.

3.1.4. *Non-radiative transitions*

Other mechanisms contribute to deactivate the excited state, each one being characterized by its own transition rate:

– collision deactivation or quenching;

– internal conversion, corresponding to the population passage from a given state toward neighboring energetic states;

– passage from a singlet electronic state (*S*) toward a triplet electronic state (*T*), leading to phosphorescence phenomena, which may compete with a collision relaxation process.

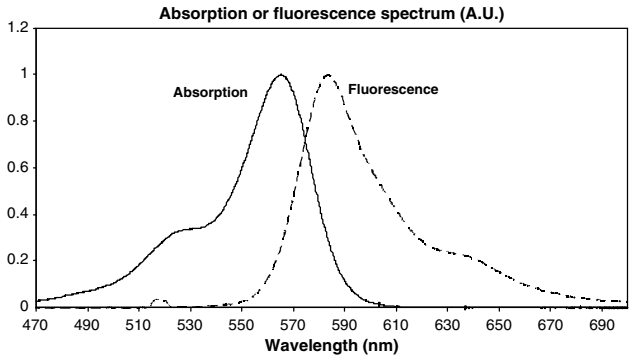

Figure 3.2. *Illustration of Franck–Condon principle (spectrum of sulforhodamine B in a water solution)*

Thus, the real lifetime τ of the excited state is plainly shorter due to various physical phenomena competing with fluorescence:

$$\tau = \frac{1}{A_{21} + k_Q + k_{ST} + k_{CI}} \qquad [3.13]$$

k_Q, k_{ST} and k_{CI} respectively represent population transfer rates by collision relaxation, passage from a singlet electronic state toward a triplet electronic state and internal conversion.

3.1.5. *Line width*

In any physical environment, spectral lines are broadened; the width is linked to the following mechanisms.

3.1.5.1. *Natural width*

Natural width results from the Heisenberg uncertainty principle, applied to the lifetime of the excited state:

$$\Delta E.\tau = \frac{h}{2\pi} \qquad [3.14]$$

ΔE being the uncertainty on energy $h\nu$ of transition, that is $\Delta E = h\Delta\nu$.

Emission (or absorption) will occur over a frequency bandwidth called natural line width:

$$\Delta\nu = \frac{1}{2\pi\tau} \qquad [3.15]$$

Yet, this width is not really observed because it is masked by other broadening phenomena linked to the thermodynamic conditions of medium in which a molecule is present (pressure, temperature).

3.1.5.2. *Doppler width*

Thermal agitation of molecules induces them to move in a random manner. When radiation emitted by these molecules (moving at a velocity V along detector direction or in opposite direction) is measured, frequency of the analyzed radiation is shifted by a $\Delta\nu$ value, called Doppler shift (Figure 3.3):

$$\Delta\nu = \nu - \nu_0 = \nu_0 \left(V/c\right) \qquad [3.16]$$

ν_0 is the center frequency of the radiation spectral profile emitted by molecules and ν is a frequency. Statistical distribution of molecule's velocities is given by Maxwell–Boltzmann law:

$$f\left(\nu\right) = \sqrt{m/2\pi kT}\, e^{\left(-mV^2/2kT\right)} \qquad [3.17]$$

with m being the mass of the molecule and T absolute temperature.

Global statistical velocity distribution of molecules provokes line broadening, called Doppler broadening, characterized by an emission or absorption probability $g_D(\nu)$ around a central frequency ν_0:

$$g_D\left(\nu\right) = \frac{2\sqrt{\ln 2}}{\sqrt{\pi}\Delta\nu_D} e^{-\frac{mc^2}{2kT}\left(\frac{\nu-\nu_0}{\Delta\nu_D}\right)^2} \qquad [3.18]$$

where $\Delta\nu_D$ is the Doppler line width at half-maximum:

$$\Delta\nu_D = \sqrt{\frac{8kT\ln 2}{mc^2}}\nu_0 \qquad [3.19]$$

The Doppler line width exclusively depends on temperature for given molecular species. The Doppler line width is only visible in a low pressure environment, typically less than 1,000 Pa. In addition, the collision broadening becomes predominant.

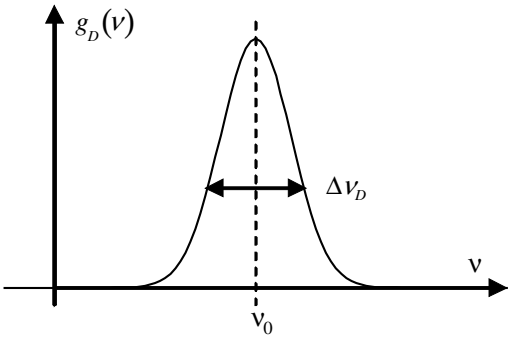

Figure 3.3. *The Doppler line width*

3.1.5.3. *Collision width or Lorentz width*

For pressure typically greater than 1,000 Pa, the high frequency of molecular collisions induces a line width much greater than the Doppler width. In fact, if a photon is absorbed or emitted when the molecule undergoes a collision, the phase of emitted or absorbed wave train varies along a random and discontinuous manner, which induces a line broadening around the central frequency ν_0. Emission probability at a frequency ν is expressed by a Lorentz distribution (Figure 3.4):

$$g_c(\nu) = \frac{2}{\pi\Delta\nu_c\left[1+\left(2\left(\frac{\nu-\nu_0}{\Delta\nu_c}\right)\right)^2\right]} \qquad [3.20]$$

with $\Delta\nu_c$, collision width at mid-height:

$$\Delta\nu_c = \frac{1}{\pi T_{\mathrm{m}}} \qquad [3.21]$$

where T_{m} is the mean time between two molecular collisions, which may be expressed by gas kinetic theory, which thus allows providing a line collision width:

$$\Delta\nu_c = K_c \frac{P}{\sqrt{T}} \qquad [3.22]$$

K_c represents a constant depending upon thermodynamic conditions of the considered molecule.

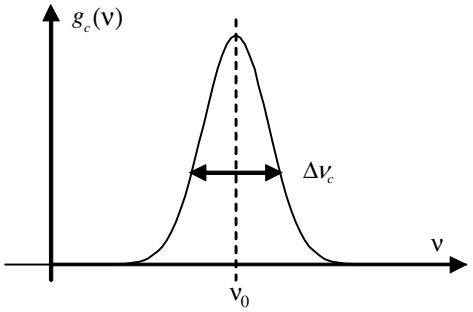

Figure 3.4. *Lorentz line width*

At atmospheric pressure, the broadening of the spectral line is very important, so we cannot distinguish the various lines corresponding to the different transitions: rather a continuum is observed. It is the same in liquids where emission and absorption bands (the word band is preferred to line in this situation) are very large and spread over more than 100 nm.

3.2. Laser-induced fluorescence principles

Laser-induced fluorescence (LIF) is a quantitative measuring technique particularly used in fluid mechanics and transport phenomena domains. This application is not exclusive, as this technique is also used in the domain of physical-chemistry, as well as in the living sciences and in microscopy [VAL 04].

Fluorescence corresponds to spontaneous de-excitation of a singlet excited state of atomic or of a molecular species. The excited state may be populated by different means, using electrical discharges (this technique is used in ionized gas lasers for instance) or chemical reactions or electromagnetic radiation absorption. The last mode is discussed in this chapter. Using laser radiation allows for the delivery of a huge amount of energy in an extremely reduced spectral band. Therefore, for a fluorescent molecule, a polychromatic light is emitted, situated at wavelengths superior to exciting radiation (Stokes fluorescence), though an anti-Stokes fluorescence might also be observed. As described earlier, fluorescence emission competes with other transition types (collision relaxation, internal conversion, the passage to triplet state (Figure 3.5)). For the following uses, stimulated emission phenomena will be neglected, the excitation energies involved being considered insufficient to obtain a significant contribution of this phenomenon.

The fluorescence emission (which will be further designated as the “fluorescence signal”) depends on the intrinsic characteristics of the emitting system (i.e. the

fluorescent molecule), and also on medium thermodynamics parameters. In fact, the intensity of this fluorescent emission particularly depends upon the number of emitting molecules per volume unit (volume concentration), the temperature, the medium viscosity, and the pH in liquid phase and the eventual presence of other molecules. In the gas phase, fluorescence intensity may also depend on pressure; in a liquid phase, such a pressure dependence may occur, but not for pressure variations found in usual situations.

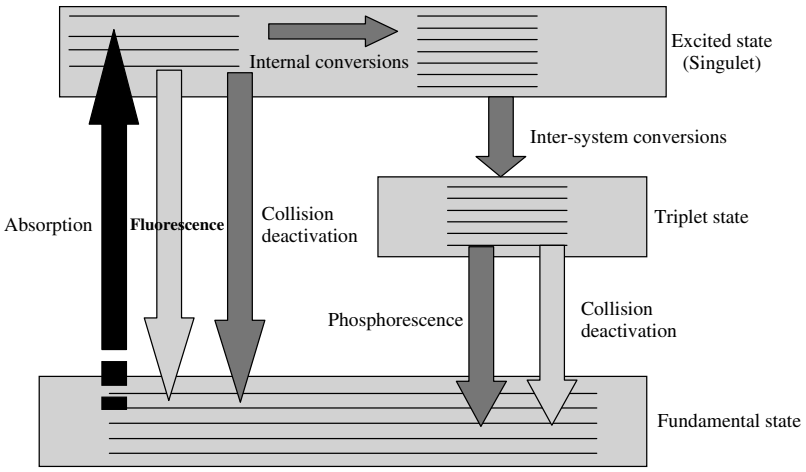

Figure 3.5. *Principle scheme of laser-induced fluorescence*

3.2.1. *Absorption kinetics*

The population variation of the excited state by transitions starting from a fundamental state is given by:

$$\frac{dN_2}{dt} = B_{12} W N_1 \qquad [3.23]$$

The spectral profile of the absorption line $g(\nu)$, combined with all the broadening mechanisms described before, as well as the spectral extent of the laser line must be taken into account through the convolution product between both line profiles:

$$\frac{dN_2}{dt} = B_{12} W N_1 \int_{-\infty}^{+\infty} g(\nu) E(\nu) d\nu \qquad [3.24]$$

with an $E(\nu)$ spectral profile of a laser line such as $\int_{-\infty}^{+\infty} E(\nu) d\nu = 1$.

When the width of the laser line is very narrow compared to the width of the absorption line, we may simply write:

$$\frac{dN_2}{dt} = B_{12} W N_1 g\left(\nu_e\right) \Delta\nu_e \qquad [3.25]$$

where ν_e is the central frequency of the laser line and $\Delta\nu_e$ its spectral width. In the general case, we must refer to relation [3.24].

3.2.2. *Fluorescence signal*

Luminous energy emitted for a molecule transition from an excited state toward the fundamental state is called the fluorescence signal. In a two-level model (1: fundamental state, 2: excited state) the number of radiative transitions (fluorescence) per unit time is given by:

$$\frac{dN_2}{dt} = -A_{21} N_2 = -\frac{N_2}{\tau_0} \qquad [3.26]$$

Luminous power $P(t)$ emitted during transition 2 –> 1 is thus:

$$P\left(t\right) = \frac{dN_2}{dt} h\nu_{12} \qquad [3.27]$$

Let us consider the case where the absorption line width is much higher than the laser line width (equation [3.25]). Neglecting all mechanisms of non-radiative transition, except collision deactivation, calculation of dN_2/dt is obtained using the balance equation. Let us note that the Boltzmann fraction $f(T)$ is introduced in order to determine the population of the sublevel of the fundamental state, which may be able to absorb incident laser radiation.

$$\frac{dN_2}{dt} = B_{12} W f\left(T\right) N_1 g\left(\nu_e\right) \Delta\nu_e - \left(A_{21} + k_q\right) \qquad [3.28]$$

When introducing population balance:

$$N_1 + N_2 = N_1^0 \qquad [3.29]$$

where N_1^0 corresponds to a fundamental state population in equilibrium conditions.

Therefore:

$$\frac{dN_2}{dt} = -N_2\left(B_{12}Wf(T)g(\nu_e)\Delta\nu_e + A_{21} + k_q\right) + f(T)B_{12}Wg(\nu_e)\Delta\nu_e N_1^0$$
$$= -\frac{N_2}{\tau_f} + f(T)B_{12}Wg(\nu_e)\Delta\nu_e N_1^0 \qquad [3.30]$$

with $\tau_f = \dfrac{1}{B_{12}Wf(T)g(\nu_e)\Delta\nu_e + A_{21} + k_q}$, the characteristic time of the fluorescence emission.

Finally, the number of transitions per unit of time is expressed by:

$$\frac{dN_2}{dt} = -\frac{N_2}{\tau_f} + B_{12}Wg(\nu_e)\Delta\nu_e f(T)N_1^0 \qquad [3.31]$$

Using initial condition $t = 0$, $N_2 = 0$, the number of molecules N_2 being in the excited state, is given by:

$$N_2 = \left(\frac{1}{\tau_f}B_{12}Wg(\nu_e)\Delta\nu_e f(T)N_1^0\right)\left(1 - e^{-t/\tau_f}\right) \qquad [3.32]$$

Energy $F(t)$ emitted by the fluorescence during transition 2 –> 1 is then given by:

$$F(t) = N_2 h\nu_{12} \qquad [3.33]$$

Using expression [3.6]:

$$N_2 = \left(\frac{1}{\tau_f}B_{12}Wg(\nu_e)\Delta\nu_e f(T)N_1^0\right)h\nu_{12}\left(1 - e^{-t/\tau_f}\right) \qquad [3.34]$$

A permanent regime is reached for excitation duration, notably longer, than the lifetime of the excited state:

$$N_2 = \frac{1}{\tau_f}B_{12}Wg(\nu_e)\Delta\nu_e f(T)N_1^0 h\nu_{12} \qquad [3.35]$$

Using definition of τ_f:

$$F = \frac{B_{12} W g(\nu_e) \Delta\nu_e f(T) N_1^0 h\nu_{12}}{B_{12} W g(\nu_e) \Delta\nu_e f(T) + A_{21} + k_q} = \frac{N_1^0 h\nu_{12}}{1 + ((A_{21} + k_q) / (B_{12} W g(\nu_e) \Delta\nu_e f(T)))} \quad [3.36]$$

Let us introduce the spectral density of saturation energy W_{sat} defined by:

$$W_{sat} = \frac{A_{21} + k_q}{B_{12} g(\nu_e) \Delta\nu_e f(T)} \quad [3.37]$$

which corresponds to the spectral density of energy leading to all the molecules that are in the excited state. Thus, energy becomes:

$$F = \frac{N_1^0 h\nu_{12}}{1 + \frac{W_{sat}}{W}} \quad [3.38]$$

If $W >> W_{sat}$, it is the saturation regime.

If $W << W_{sat}$, the linear regime is obtained:

$$F = \frac{B_{12} W g(\nu_e) \Delta\nu_e f(T) N_1^0 h\nu_{12}}{A_{21} + k_q} \quad [3.39]$$

Equation [3.39] may be rewritten using the definition of fluorescence quantum yield η:

$$F = \frac{1}{A_{21}} B_{12} W g(\nu_e) \Delta\nu_e f(T) \eta N_1^0 h\nu_{12} \quad [3.40]$$

The luminous power emitted over a spectral width $\Delta\nu$ is then:

$$F = \frac{1}{A_{21}} B_{12} W N f(t) g(\nu_e) \Delta\nu_e \eta \int_{\Delta\nu} hS(\nu) d\nu \quad [3.41]$$

where $S(\nu)$ represents the normalized spectral distribution of fluorescence intensity, such as $\frac{1}{\Delta\nu}\int_{\Delta\nu_e} S(\nu)d\nu = 1$.

Introducing the absorption cross-section, it may be defined in this case by:

$$\sigma = \frac{B_{12}}{c} f(T) h\nu_e g(\nu_e) \qquad [3.42]$$

which results in:

$$F = \frac{1}{A_{21}} \frac{\sigma c}{h\nu_e} W N_1^0 \Delta\nu_e \eta \int_{\Delta\nu} hS(\nu)\, d\nu \qquad [3.43]$$

The incident energy spectral density W may be written:

$$W = \frac{I_0}{\Delta\nu_e c} \qquad [3.44]$$

with I_0 being the incident power density (W/m^2).

Now, let us determine the energy ρ emitted per volume unit and introduce the molar absorption coefficient k_λ at the laser emission wavelength, expressed in moles^{-1}.m^2:

$$\rho = \frac{1}{A_{21}} \frac{k_\lambda}{h\nu_e} I_0 C \eta \int_{\Delta\nu} hS(\nu)\, d\nu \qquad [3.45]$$

where C is the molar volume concentration (moles.m^{-3}) and $k_\lambda = \sigma A$ (A is the Avogadro number).

3.2.3. *Fluorescence detection*

The signal formed by fluorescence emission is collected by an optical system that creates a probe volume V_{mes}, defined by the intersection between the volume excited by incident radiation and the collecting volume imposed by the optical system (Figure 3.6). The optical signal thus collected is converted into an electric signal by a photodetector, which might be a photodiode, a photomultiplier or a matrix camera of a Charge-Coupled Device (CCD) type, for instance.

The photodetector integrates the polychromatic fluorescence over a spectral window $[\nu_1;\nu_2]$ with a particular efficiency function $H(\nu)$. Moreover, the various components of the used optical chain introduce an optical constant K_{opt}. The fluorescence intensity collected in the probe volume is then expressed by:

$$I_f = K_{\text{opt}} \frac{1}{A_{21}} \frac{k_\lambda}{h\nu_e} I_0 C V_{\text{mes}} \eta \int_{\sup(\Delta\nu,[\nu_1,\nu_2])} H(\nu) \otimes hS(\nu) d\nu \qquad [3.46]$$

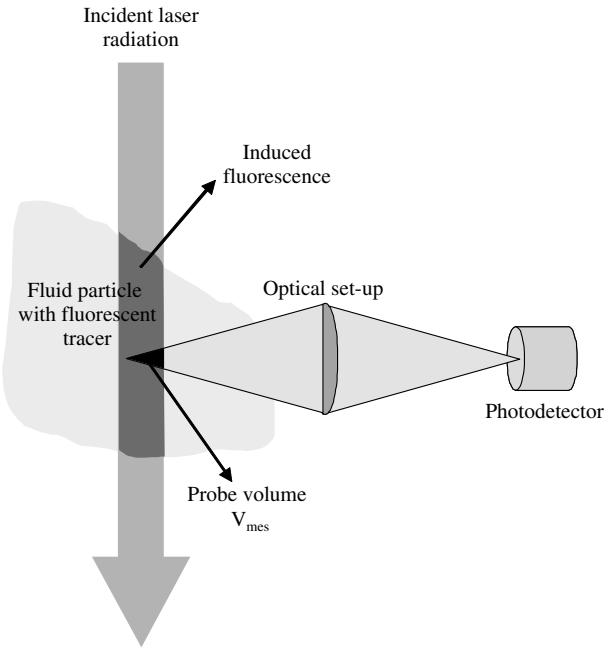

Figure 3.6. *Typical scheme of a laser-induced fluorescence device*

3.2.4. *Absorption along optical path*

All previous equations do not take into account the attenuation of an incident laser beam that crosses a medium seeded with fluorescent tracers, as well as the reabsorption of fluorescence relative to partial overlapping of fluorescence emission and absorption spectra. The Beer–Lambert law allows us to describe this absorption under the form:

$$I_\lambda = I_{\lambda 0} e^{-\int_0^l k_\lambda C(y) dy} \qquad [3.47]$$

where $I_{\lambda 0}$ is the incident intensity and l the crossed optical path (Figure 3.7), and $C(y)$ the molar concentration of fluorescent tracer at abscissa y. k_λ is the molar absorption coefficient at a λ wavelength corresponding either to the laser wavelength or to a fluorescence wavelength.

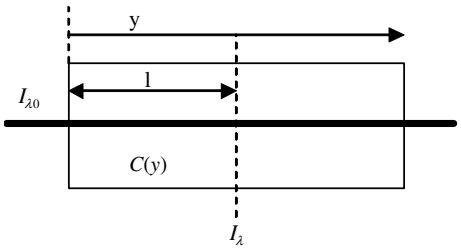

Figure 3.7. *Attenuation of the fluorescence signal along the optical path*

3.2.5. *Fluorescence measurement device*

In this section, components of a LIF device are described. Two types of methods may be implemented: the punctual method or the two-dimensional method. Advantages and drawbacks of both methods are similar to those that may be invoked for Laser Doppler Velocimetry and Particle Image Velocimetry.

3.2.5.1. *Pointwise methods*

Laser excitation is deposited in a precise flow zone and a fluorescence signal is gathered in this same zone. It is thus possible to follow over time a scalar magnitude (temperature, concentration, etc.) in one point, with an important temporal resolution, which may reach several kHz. On the other hand, the measurement must be realized point-by-point and requires stationarity or ergodicity of the studied phenomenon.

Elements of a punctual measuring chain are as follows:

– An optical collection device with the aim of forming the probe volume and of collecting fluorescence photons in a precise point.

– A continuous or pulsed laser (pulse duration must be larger than the lifetime of the excited state).

– Optical filters allowing separation between the laser source emission and fluorescence emission.

– A photodetector: photomultipliers are the most widely used devices. In such a setup, the luminous signal reaches the photosensitive surface of a photocathode:

photoelectrons are thus extracted by an photoelectric effect. These photoelectrons are then accelerated by an adjustable high voltage in order to hit a dynode, which in turn will emit secondary electrons that will be accelerated and will impact a second dynode, and so forth. Generally, in a photomultiplier there are about 10 dynodes, leading to an important gain that may reach 10^6. The resulting current is collected at the device anode (Figure 3.8).

– An amplifier of the current-voltage type, permits the conditioning of the signal along a usable form by an acquisition card for instance.

– Acquisition card and treatment software.

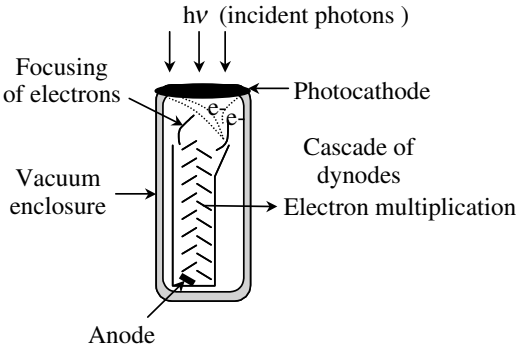

Figure 3.8. *Principle scheme of a photomultiplier*

3.2.5.2. *Two-dimensional methods*

Laser excitation is achieved using a laser sheet. A fluorescence signal produced by illumination of a flow zone by the laser sheet is thus collected and detected by a matrix detector. This method has the advantage of giving access to the instantaneous two-dimensional distribution of the fluorescence signal emitted by a given molecule. The temporal resolution obtained when using pulsed laser sources is thus a few nanoseconds. Measurement accuracy depends upon the signal-to-noise ratio of CDD-type detectors, offering lower characteristics than photomultipliers.

The elements of a two-dimensional measuring chain are as follows:

– a pulsed laser in order to instantaneously deposit an important energy;

– an optical device producing the laser sheet;

– a matrix CCD camera, eventually equipped with a light intensifier, which allows managing very short shutter durations (up to 1 ns);

– an optical system forming the image of the laser sheet on the detector of the matrix camera (Figure 3.9);

– optical filters allowing the separation of the laser source emission from the fluorescence emission.

It must also be noted that techniques based on images require a large number of corrections and special care to make them really quantitative. It is necessary to take into account response heterogeneity of a CCD camera matrix, lack of spatial uniformity in luminous energy inside the laser sheet and energy variations from one laser pulse to another.

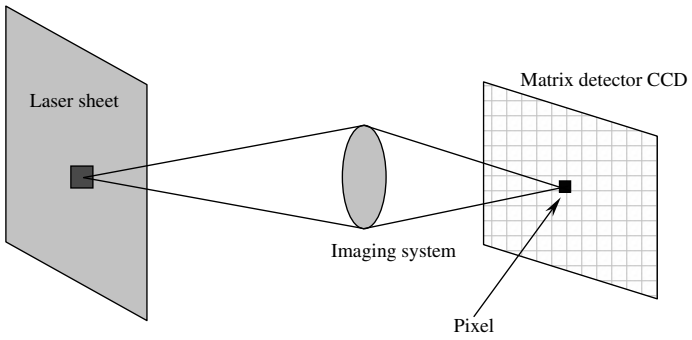

Figure 3.9. *Two-dimensional measurement principle in a laser sheet*

3.3. Applications of laser-induced fluorescence in gases

3.3.1. *Generalities*

Generally speaking, LIF requires use of chemical fluorescent tracers, having spectroscopic properties that allow for measuring scalar magnitudes: temperature, concentration and pressure. These measurements are mostly achieved in reacting flows on diatomic molecules as OH radical (a species naturally present in reactive zones) or other intermediate species such as CH, CH_2O, C_2, NO, etc. Concentrations in radicals are used to localize flame zones and to evaluate the reaction rate of analyzed combustions. It is also judicious to use other chemical tracers; they are artificially introduced into the flow with the aim that they provide markers for temperature, concentration and even pressure. The tracer is then selected in order as it possesses a chemical behavior similar to that of the analyzed fluid and it emits an intense fluorescence signal, when it is excited by wavelengths mostly situated in the UV domain. Several molecules are used, such as iodine molecule, ketones (acetone, 3-pentanone, etc.) and aromatics (toluene, 1-2-4 trimethylbenzene, naphtalene, etc.).

These species offer the advantage of having important fluorescence efficiency and a fluorescence that evolves in a different manner depending on magnitudes such as temperature, chemical composition and pressure. A concentration measurement is obtained because the fluorescence signal is proportional to the molecule number. Pressure occurs in the quenching rate k_q, as well as in the absorption line profile $g(\nu)$, when the collision broadening regime dominates. Temperature is present in the collision spectral width, quenching rate, and also in the Boltzmann population distribution $f(T)$.

3.3.2. *Diatomic molecules*

Two applications of use of diatomic molecular tracers are presented in this section. In the first application, I_2 is the tracer. Its use is dedicated to temperature and pressure measurements in inert flows developing inside rotating machines as compressors or turbines. The second application deals with analysis possibilities in reactive flows, by determining the quantity of chemical species naturally produced in the combustion of a fuel/air mixture.

3.3.2.1. *Iodine use*

Possibilities for using the molecular tracer I_2 in order to perform analysis of non-reactive flows are now detailed [MCD 83, HIL 90, HAR 93, LEM 95].

Let us consider an isolated absorption line excited by a laser line having a very narrow spectral width (Figure 3.10), centered on this absorption line of the fluorescent tracer. In this situation, the spectral overlapping term $\int_{-\infty}^{+\infty} g(\nu)E(\nu)\,d\nu$ may be expressed by using the collision line profile:

$$\int_{-\infty}^{+\infty} g(\nu)E(\nu)\,d\nu = \int_{-\infty}^{+\infty} \frac{2}{\pi\Delta\nu_c\left[1+\left(2\left(\nu-\nu_e\right)/\Delta\nu_c\right)^2\right]}\delta\left(\nu-\nu_e\right)d\nu = \frac{2}{\pi\Delta\nu_c} = \frac{2\sqrt{T}}{\pi K_c P} \quad [3.48]$$

where δ is the Dirac function.

The collision deactivation term can be expressed in a simplified manner as [CAP 73]:

$$k_q = C_q\, P/\sqrt{T} \quad [3.49]$$

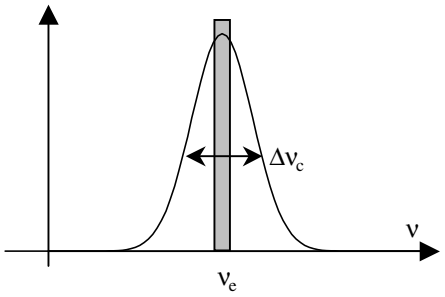

Figure 3.10. *Tuning a narrow laser line on an enlarged absorption line*

The molar concentration C of a fluorescent tracer is expressed with the help of molar fraction X_t of the fluorescent tracer by:

$$C = X_t \frac{P}{RT} \qquad [3.50]$$

where R is the perfect gas constant.

Fluorescence intensity collected inside an appropriate spectral band is thus given by:

$$I_f = KX_t f(T)\frac{1}{P} \qquad [3.51]$$

K is a constant depending upon spectroscopic parameters and optical constants.

3.3.2.2. *Pressure measurement*

Equation [3.51] shows that the fluorescence signal depends upon both pressure and temperature. Using LIF to measure pressure (equation [3.51]) in a gaseous flow requires either knowing temperature in any flow location, or minimizing temperature influence in Boltzmann fraction $f(T)$. In this last case, it will be necessary to tune the excitation laser line on an absorption line of the molecular tracer, having a Boltzmann fraction not very sensitive to temperature. Therefore, variations of fluorescence intensity will be essentially sensitive to flow pressure variations. Calculation examples of Boltzmann fractions are provided in Figure 3.11 for different absorption lines of molecular iodine. It seems possible to observe absorption lines presenting enough wide domains on which temperature dependence of Boltzmann fraction is negligible. In order to efficiently measure pressure, it will be necessary to tune excitation laser wavelength on one of these lines; use of a tunable laser source is also required.

Figure 3.11. *Evolution of Boltzmann fraction as a function of temperature for different rotational states (j″) of the same vibrational level (v″ = 0)*

Nevertheless, we must remain cautious about the validity of the application domain of equation [3.51]. For pressures close to atmospheric pressure, collision line broadenings are so large that the influence of neighbor lines becomes important, so this phenomenon should be taken into account [LEM 95]. An example of pressure measurement on the axis of a supersonic axisymmetric jet (Figure 3.12) is given in Figure 3.13.

Figure 3.12. *Pressure field Euler calculation of a supersonic jet*

3.3.2.3. *Temperature measurement*

In this case, it is necessary to use temperature dependence in equation [3.51], issued from a Boltzmann fraction. Two situations may occur:

– Flow has a constant pressure or pressure is known at any point; equation [3.51] can be directly used to determine temperature from the fluorescence signal.

– Pressure is unknown and varies in any flow location; pressure dependence in equation [3.51] must be eliminated.

Figure 3.13. *Application example: determination of a pressure field in a supersonic jet (reservoir pressure: 5.5 bars, initial temperature: 298 K) [LEM 95]*

In the second case, a molecule excitation at two wavelengths is recommended, in order to excite two different transitions (Figure 3.14). These two transitions will be chosen in such a way that they have very different Boltzmann fractions, in order to optimize their temperature dependence. The two excitation laser wavelengths will be slightly time-shifted in order to separate emissions due to each transition. Excitation to wavelength λ_1 will lead to the following expression:

$$I_{f1} = K_1 X_t f_1(T) \frac{1}{P} \qquad [3.52]$$

and excitation at wavelength λ_2:

$$I_{f2} = K_2 X_t f_2(T) \frac{1}{P} \qquad [3.53]$$

A ratio calculation of fluorescence intensities obtained on both transitions (equations [3.26] and [3.27]) allows eliminating pressure dependence:

$$\frac{I_{f1}}{I_{f2}} = \frac{K_1 f_1(T)}{K_2 f_2(T)} \qquad [3.54]$$

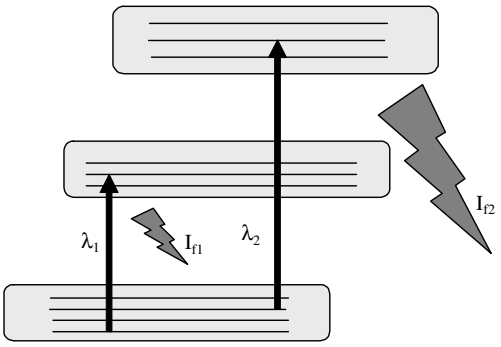

Figure 3.14. *Principle of excitation at two wavelengths*

3.3.2.4. *Measurements in reactive flows*

Generally, LIF is applied to study reactive flows via the quantity determination of reactive species, such as intermediate combustion products, which are radicals such as OH, C_2 and CH. Concentrations of these species allow determining positions of reactive zones and characterizing reactive rates of studied combustions. Particularly, the instantaneous spatial distribution of OH radical represents important information for analysis of primary reaction zone [KOH 94]. A structure of OH fluorescence images helps in the localization of high stretching zones, where a local reduction of signal and thickness of layer containing OH occurs. The analysis of other chemically stable species may also complete and facilitate these flow studies. Therefore, it is convenient to make use of fluorescent chemical tracers, which are artificially introduced into the flow. Fluorescence properties of these markers are used to obtain experimental information about temperature and concentration fields in the zones where radicals, listed earlier, are not present. Among these species, ketones and aromatics are the most employed and effective candidates (see section 3.3.3).

Some examples illustrating the application of LIF to temperature and concentration measurements in reactive flows are now presented. The first concerns the study of an ethylene/air subsonic diffusion flame in order to evaluate pollutant formation (soot, NO_x, etc.). The experiment is achieved at 0.2 MPa pressure, with the following mass rate: 6 g/s for CH_4 and 200 g/s for air. A frequency-doubled dye laser, delivering 10 ns pulses of 10 mJ, is tuned in wavelength on an absorbing rotational transition of OH. Transition $Q_1(5)$ is selected in order to produce a fluorescence signal proportional to concentration and independent of temperature. Figure 3.15 displays an example of an instantaneous image of OH concentration, giving information about the interaction effect of large and small turbulence scale structures with flame front production.

Figure 3.15. *Instantaneous image of OH radical concentration in a C_2H_4/air diffusion flame*

The second application example refers to a supersonic combustion produced in a turbulent mixing layer, inside which reaction rates are finite [BRE 01]. This mixing layer is produced between two air and hydrogen flows that separately develop at Mach 2. A hydrogen jet issued from a nozzle 6 mm in diameter is injected into a coaxial hot airflow. Combustion conditions are stabilized over 15 s. Results presented below are obtained with a fuel-air ratio of 0.29. Nominal initial air temperature is brought to 1,800 K by auxiliary hydrogen combustion, followed by a 21% reoxygenation of the hot flow at the combustion chamber entrance. PLIF is applied on OH to describe a flame front structure. Figure 3.16 shows an instantaneous and a mean OH distribution in a section of 186 mm downstream of the injector.

Figure 3.16. *Mean and instantaneous images of OH radical concentration at a distance situated between 186 and 286 downstream of the nozzle. For a color version of this figure, see www.iste.co.uk/boutier/lasermetro.zip*

Flow is running from left to right, with hydrogen flux centered on the coaxial airflow. The reaction zone, visualized by OH fluorescence, is confined into a narrow

and wrinkled region situated at the periphery of the mixing layer. Reacting flow turbulence is pointed out by the presence of easily observable large-scale coherent structures. Instantaneous flame front appears as a tiny layer linking thicker OH pockets. These measurements, associated with OH fluorescence models representing temperature and quenching effects, and being calibrated on a premixed H_2/air flame stabilized on a porous medium, allow measuring OH concentrations with an accuracy of approximately 10%.

These experiments have also been used to validate the possibility for the simultaneous sampling of several molecular tracers. The flame front structure and gaseous fuel distribution (before it disappears in combustion) have thus been observed by joint use of OH and acetone fluorescence. Acetone is injected as a vapor into a hydrogen flow with a 2% molar fraction, which is sufficient to avoid any modification of combustion performances. Simultaneity of fluorescence measurements is obtained by using only one laser excitation at λ = 282.75 nm and collecting both fluorescence emissions by two intensified ICCD (Intensified Charge-Coupled Device) cameras equipped with the appropriate optical filters. Figure 3.17 represents an instantaneous section of OH distribution inside the mixing zone; an illustration of PLIF (Planar Laser-Induced Fluorescence) measurements on acetone is also presented. Fluorescence images indicate that acetone fluorescence is displayed along coherent structures such as vortices. The number of large-scale structures in the mixing layer varies from one image to another, their scale being in the order of the hydrogen jet diameter. Let us note that OH and acetone fluorescence signals never overlap. The turbulent structures observed in a central jet and in the flame front are systematically adjoining. Absence of overlapping between both fluorescence images shows that the mixing layer is not very thick and that the fuel decomposition kinetics is very quick. Correlation between OH and acetone fluorescence signals also points out that there is a preferred consumption of acetone, thus hydrogen, by the attack of radicals. As the acetone fluorescence signal disappears near the flame front, acetone pyrolysis may be neglected in this high velocity regime. This is in agreement with similar results indicating that the disappearing rate by chemical reaction is one order of magnitude quicker than a pyrolysis one [MIL 94].

a) b) c)

Figure 3.17. *Instantaneous PLIF images PLIF: a) OH concentration, b) acetone concentration and c) combination of both images in a H_2/air supersonic flame at Mach 2. For a color version of this figure, see www.iste.co.uk/boutier/lasermetro.zip*

The concept of using PLIF with two colors on an acetone as a means to measure temperature has also been validated in this experiment. Acetone is now used as a temperature tracer in order to measure temperature distribution inside jet fuel (see section 3.3.3.1 for method details). Both wavelengths 266 nm (laser Nd:YAG quadrupled) and 308 nm (excimer laser XeCl) are selected to obtain a good sensitivity of fluorescence signals with temperature in the range of 300–1,300 K. The laser pulse at 308 nm is delayed by 500 ns relative to a pulse produced at 266 nm in order to separate the two fluorescence emissions on two ICCD cameras, each being open for 100 ns. Figure 3.18 presents some typical instantaneous images of the temperature field in the hydrogen jet seeded with acetone. The turbulent structure of the temperature field is pointed out in the explored zone (40×50 mm^2), especially in the mixing zone showing coherent structures at a large scale.

Figure 3.18. *Instantaneous images of fuel temperature distribution measured by PLIF at two colors on acetone molecule. For a color version of this figure, see www.iste.co.uk/boutier/lasermetro.zip*

A OH radical may also be used as a temperature tracer in reactive flows. A quasi-simultaneous excitation of two OH rotational transitions by two laser beams of different wavelengths is used. As before, both rotational transitions are selected as a function of their capability to produce fluorescence signals that evolve

differently with temperature. Processing of the two instantaneous OH fluorescence images, in association with theoretical evolutions of OH fluorescence signal, allows instantaneous measurement of temperature distribution in the flame (Figure 3.19(a)).

Temperature measurement accuracy with one laser shot and on one camera pixel is approximately 10 % (± 150 K). A comparison between PLIF-OH measurements and temperature measurements by Coherent Raman Anti-Stokes technique (CARS) on N_2, achieved in the same experimental conditions, shows a very good agreement on absolute temperature values, which validates this experimental approach (Figure 3.19(b)).

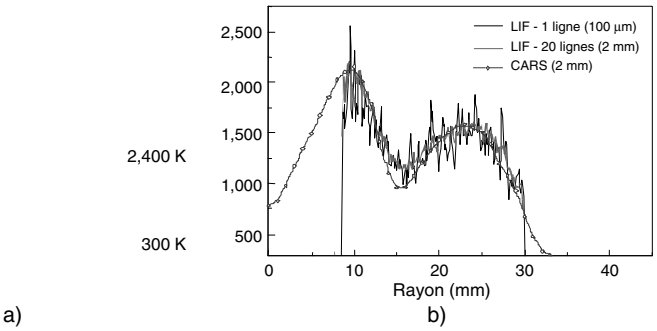

Figure 3.19. *a) An instantaneous temperature image issued from excitation of lines $Q_2(9)$ and $P_1(1)$; b) comparison of temperature profiles between PLIF-OH and CARS measurements. For a color version of this figure, see www.iste.co.uk/boutier/lasermetro.zip*

3.3.3. *Poly-Atomic molecular tracers*

As evoked before, the injection of fluorescent molecules in reactive flow appears judicious to measure fuel temperature and concentration. This approach may also be used for analysis of non-reactive turbulent, one-phase or two-phase, flows. Molecular tracers are thus selected as a function of their capability to emit fluorescence evolving with experimental conditions. Fluorescent tracers having more complex molecular chains are then used to perform concentration measurements in gaseous phases. These chemical tracers are generally composed of organic components belonging to ketone and aromatic families.

3.3.3.1. *Ketones*

The interest in using ketones are now detailed. As an illustration, the acetone case is retained [LOZ 92] because this molecule presents very attractive thermodynamic and spectroscopic properties. Other ketones such as 3-pentanone and 5-noanone may also be used as fluorescent tracers because they present similar

properties. The high saturation vapor pressure of acetone at ambient temperature (~24,000 Pa) and its weak noxiousness allow easy gaseous flow seeding. Acetone fluorescence is situated in a large spectral domain among the visible part of electromagnetic spectrum, which facilitates its detection, even by a non-intensified CCD camera. Moreover, this molecule fluorescence is not too much disturbed by the quenching of oxygen in air, opposed to diatomic or organic (aromatic) molecules (see section 3.3.3.2), which simplifies data interpretation. Use of acetone has been largely developed at the end of the 1990s in order to perform concentration and/or temperature measurements to study turbulence or mixing layers. Let us note that acetone use remains limited to low velocity gaseous flows with a temperature less than 900 K, and for supersonic flows having a temperature less than 1,300 K (beyond this temperature, the molecule is chemically destroyed by pyrolysis).

Regarding the opposite of diatomic molecules, the acetone absorption spectrum appears as a wide band spectrum, without the tiny resolved structure (rotational and vibrational structures are confound). Absorption domain spreads between 225 and 325 nm, with a maximal absorption toward 275 nm [GRI 97]. Fluorescence is emitted between 350 and 550 nm. The fluorescent yield is relatively low (approximately 0.21%), due to quick non-radiative de-excitations by internal conversion.

From equation [3.46], the fluorescence signal produced by an excitation wavelength λ_e and detected on a given spectral band is expressed as:

$$I_f\left(\lambda_e\right) = K_{opt}\frac{k_\lambda}{hc/\lambda_e} I_0 C V_{\text{mes}} \eta \int_{\Delta\nu} hS\left(\nu\right) d\nu \qquad [3.55]$$

Absorption coefficient k_{λ_e} and fluorescence quantum efficiency η depend upon temperature and the excitation wavelength. A pressure dependence of these two parameters is not found. The molar concentration C in fluorescent molecules is proportional to P/T, where P is the local pressure:

$$C \propto P/T \qquad [3.56]$$

Equation [3.55] shows that the acetone fluorescence signal may thus be used into two objectives:

– When pressure and temperature are constant, molar concentration C of fluorescent molecules may be measured, especially in mixing processes;

– When the acetone fraction and medium pressure are constant, the temperature is directly deduced from a fluorescence signal, when temperature dependencies of absorption coefficient k_{λ_e} and of fluorescence quantum efficiency η are previously known.

For instance, Figure 3.20 presents the temperature dependence of an acetone cross-section as a function of the excitation wavelength [THU 98]. It is the same for the fluorescence quantum efficiency, measured for excitation wavelengths varying between 248 and 320 nm, in a temperature range of 300–900 K (Figure 3.21). From these evolutions, the temperature dependence of an acetone fluorescence signal may be deduced, which is determined per molecule and per incident photon, for several excitation wavelengths (248, 266, 282, 300 and 320 nm) (Figure 3.22).

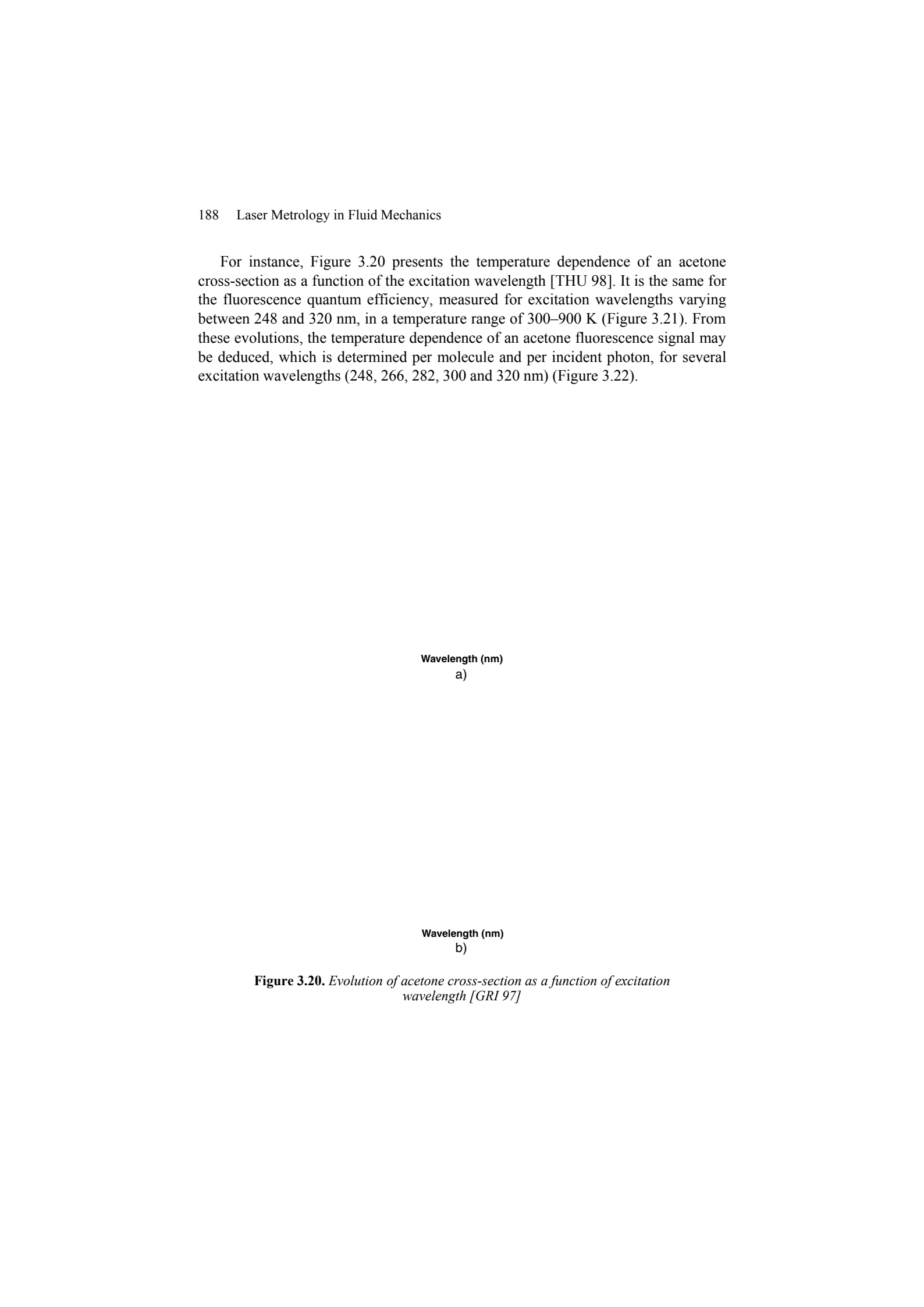

Figure 3.20. *Evolution of acetone cross-section as a function of excitation wavelength [GRI 97]*

Figure 3.21. *Evolution of acetone fluorescence quantum efficiency referred to its value at 296 K, with temperature for several excitation wavelengths [GRI 97]*

Figure 3.22. *Evolution of fluorescence signal (per molecule and per incident photon) as a function of temperature, referred to its value at 296 K, for different excitation wavelengths [GRI 97]*

It clearly appears that a variation of an acetone fluorescence signal with temperature depends upon the excitation wavelength. Fluorescence intensity per molecule and per incident photon decreases with temperature at λ_e = 248 nm, but it greatly increases at λ_e = 320 nm. On the contrary, the signal slowly evolves at λ_e = 282 nm in temperature range 300–600 K.

Figure 3.23. *Evolution of fluorescence signal per molar fraction unit and per incident photon, as a function of temperature, referred to its value at 296 K, for different excitation wavelengths [GRI 97]*

When the pressure and the acetone molar fraction are constant, evolutions of fluorescence signal per molar fraction unit and per incident photon are displayed in Figure 3.23; it shows that acetone excitation at 248 or 266 nm represents the case where fluorescence signal sensitivity with temperature is at its best inside a temperature range of 300–900 K. If the medium is reactive, compressible and turbulent, that is when the pressure, chemical composition and temperature vary with time and space, another measurement strategy must be used. This strategy consists in measuring ratio $R_{12} = I_f(\lambda_1)/I_f(\lambda_2)$ of the two fluorescence signals obtained at two different wavelengths:

$$R_{12} = \frac{I_f(\lambda_1)}{I_f(\lambda_2)} = K_{opt12} \frac{k_{\lambda_1}(\lambda_1, T)}{k_{\lambda_2}(\lambda_2, T)} \frac{\eta(\lambda_1, T)}{\eta(\lambda_2, T)} \quad [3.57]$$

K_{12} is a constant that characterizes optical properties of the measuring system. This measuring method is similar to that previously shown for simpler molecular tracers (equation [3.54]). The typical evolution of ratio R_{12} is shown on figure 3.24 for different excitation wavelength couples. An Acetone excitation by a wavelength couple at 248 and 320 nm, thus presents the best sensitivity in temperature between 300 and 1,000 K.

In order to illustrate these statements, some application results of fluorescence imagery (PLIF) on an acetone are now presented. These concern the study of a subsonic turbulent hot air jet diffusing into ambient air. Instantaneous and

quantitative measurements of temperature and concentration are achieved by PLIF with two wavelengths on acetone injected into air. The excitation laser sources used are an Excimer XeCl Laser, emitting at λ_e = 308 nm a laser pulse lasting 15 ns and delivering an energy of 200 mJ, and a frequency quadrupled Nd:YAG laser, emitting an energy of 100 mJ per pulse at λ_e = 266 nm with a repetition rate of 10 Hz. A delay between both pulses is fixed at 50 ns in order to temporally separate the collection of both acetone fluorescence emissions on two intensified ICCD cameras. Color filters set in front of camera lenses allow isolating fluorescence emitted by the acetone from other possible stray light emissions.

Figure 3.24. *Typical evolution of fluorescence signals ratio R_{12} as a function of temperature for different excitation couples of wavelengths λ_e [GRI 97]*

After data acquisition, each instantaneous image couple is transformed into a temperature and concentration image through image processing, including experimental data concerning evolutions of acetone fluorescence with temperature, calibrations of fluorescence signal (previously achieved in known thermodynamic conditions) and corrections of energy distribution inside the laser sheet (Figure 3.25). Turbulence effects acting on the main jet when it diffuses in air are thus visualized and quantified. A statistical exploitation of the temperature and concentration images gives access to information relative to turbulence (mean value, intensity, correlation terms between temperature and concentration, etc.); all these scalar quantities are required to improve turbulence modeling. This measuring technique may also be coupled with a planar velocity measurement technique PIV (Particle Image Velocimetry), in order to experimentally obtain fluctuation correlations of temperature/velocity and concentration/velocity [GRI 97, FUK 02].

Figure 3.25. *Instantaneous image of temperature and concentration in a hot air jet at 1000 K, seeded with a molar fraction of acetone in vapor phase of 2.5%. For a color version of this figure, see www.iste.co.uk/boutier/lasermetro.zip*

3.3.3.2. *Aromatics*

Aromatics are chemical species composed of several benzene nuclei arranged either linearly or angularly or as clusters. Among these species, mono-aromatics composed of one benzene nucleus (toluene, xylene, 1-2-4 trimethylbenzene, etc.) or bi-aromatics composed of two benzene nuclei (naphthalene) represent other fluorescent tracers allowing temperature and concentration measurements. Unlike ketones, these chemical species may be used for the quantity determination of real fuels used in aeronautics or automobiles (kerosene, gas-oil, etc.) because they are initially present in their chemical composition. This facilitates their use because it is not necessary to artificially inject fluorescent tracers into an analyzed fluid. As previously said, these molecules have numerous vibration states spread over several highly coupled electronic states (interactions between S_1 and T_1 electronic states), which makes their absorption spectrum very broad in frequency and easy to excite. Depending upon the number of benzene nuclei, absorption spectra of these products are spectrally shifted toward the UV domain, which simplifies their excitation. The fluorescence of aromatics set in UV-visible domain is also spectrally shifted toward the red depending upon the number of benzene nuclei. This spectroscopic property thus allows discriminating their fluorescence. For instance, Figure 3.26 shows spectral evolutions of 1-2-4 trimethylbenzene and naphthalene fluorescence. The fluorescence emissions of these two molecules are shifted by approximately 50 nm. These fluorescences evolve differently with temperature; fluorescence of 1-2-4 trimethylbenzene being greater than that of naphthalene. These evolutions are also observed for other mono-aromatics (toluene and xylene) and bi-aromatics (methylnaphtalene and bi-methylnaphtalene).

Figure 3.26. *Fluorescence evolution of a) 1-2-4 trymethylbenzene and b) naphtalene as a function of temperature at 0.1 MPa, diluted in nitrogen*

Unlike ketones, where the fluorescence signal mainly evolves with the temperature, the oxygen molar fraction plays a preponderant role in relaxation process (i.e. $k_0 \neq 0$), and thus on fluorescence's evolution. For instance, Figure 3.27 shows fluorescence evolutions of 1-2-4 trimethylbenzene and of naphthalene as a function of molar oxygen fraction at atmospheric pressure, in the temperature range of 300–640 K. For each species, we observe that the fluorescence signal varies inversely with $[O_2]$, as the Stern–Volmer law predicts [BIR 70]. As the fluorescence evolution of each species with oxygen concentration varies differently with temperature (Figure 3.27), fluorescence of these molecules is a function of both temperature and oxygen concentration.

Figure 3.27. *Fluorescence evolution of a) 1-2-4 trimethylbenzene and b) naphtalene as a function of an oxygen molar fraction at 0.1 MPa in the temperature range of 400–700 K. Curves represent expected dependency of fluorescence defined by the Stern–Volmer law [BIR 70]*

Joint use of these fluorescence properties allows simultaneously measuring the temperature and the local fuel air-ratio of a preheated flow. The measurement method consists in exciting with one single laser wavelength, two types of aromatics (one mono-aromatic and one bi-aromatic) naturally present (kerosene, gas-oil, etc.) or artificially seeded in a pure fuel, their fluorescence signals evolving differently with the temperature and oxygen concentration. Fluorescence emissions of both coupled tracers are processed, taking into account their dependency with the temperature and oxygen concentration (previously measured), so that the desired thermodynamic values are obtained by an iterative procedure. The same experimental approach may also use a mono-aromatic and a ketone.

An example of this experimental approach is obtained in a turbulent gaseous jet of a mixture 1-2-4 trimethylbenzene/naphtalene/N_2 diffusing in air and producing a mixing layer with the presence of a concentration and temperature gradients. The injection velocity of a gaseous jet into ambient air is a few meters per second. Both fluorescence images coming from excitation of the two aromatics at 266 nm are simultaneously acquired by two ICCD cameras equipped with color optical filters that allow isolating the two fluorescence emissions. Both images are thus processed using the fluorescence data of both aromatics previously acquired in an analysis cell at high temperature and high pressure. Figure 3.28 displays instantaneous measured fields of molar fractions of fuel, oxygen and mixing fraction at nozzle exit [BAR 05].

3.3.3.3. *Two-phase flows*

In several practical situations, fuel used in combustion chambers is not gaseous but liquid: petrol for internal combustion motors, gas-oil for diesel motors and kerosene for aeronautical combustion chambers. These fuels are usually injected as droplet sprays into a combustion chamber. They vaporize, probably with partial decomposition, and then only vapor escapes towards gaseous combustive, allowing their combustion.

Understanding of the different physical processes involved in fuel injection in a combustion chamber becomes essential to optimize injection systems. Fluorescence imaging is thus used as a diagnostic, providing a response to this need. The experimental results presented in this chapter come from fundamental studies concerning the evaporation of isolated fuel droplets and go towards final analysis of kerosene/air combustion at high pressure, achieved with a real aeronautical injection system.

Figure 3.28. *Instantaneous image of a) molar fraction of O_2, b) fuel and c) mixing fraction at nozzle exit. For a color version of this figure, see www.iste.co.uk/boutier/lasermetro.zip*

3.3.3.4. *Evaporation process of a pure fuel*

The evaporation and combustion of sprays are very complex to study and require the understanding of various processes such as spray formation, turbulence, chemical kinetics and different interactions between all these phenomena. In an industrial combustion chamber, all these phenomena are usually coupled, which makes the study particularly complex. For a better understanding of these different processes on combustion and to isolate their contribution, different simplified experiments are set up. Spray combustion has been largely studied during the last 30 years, experimentally [PUR 89, LI 93], or numerically [CHE 92, GAO 96] in burners at counter current. For spray evaporation or combustion, experiments are often based on a monodisperse stream of droplets (successive droplets equally spaced) either with a simple jet [VIR 00, LAV 02] or as a matrix of several parallel streams [SHA 02]. The state-of-the-art on this subject may be found in literature [ANN 92, UME 94]. This geometry has the advantage to produce a droplet jet repetitive with time and space, with injection frequency, droplet size and velocity, and well controlled distance parameters, allowing for study of the individual influence of these parameters on droplet evaporation.

An experiment using acetone fluorescence imagery had the purpose of quantifying pure fuel evaporation around a monodisperse stream of droplets, in order to study parameters such as droplet diameter, distance between droplets and ambient temperature on droplet evaporation. A stream of monodisperse droplets is formed by the disintegration of an acetone liquid jet using the Rayleigh principle. The liquid jet crosses a metallic cylinder submitted to mechanical vibrations imposed by two piezoelectric ceramics supplied by a generator delivering squared signals, with amplitude of 30 V and frequency adjustable between 0 and 40 KHz. A liquid jet passes through an aperture 100 μm in diameter in order to form monodisperse droplets of 10 m/s velocity, the diameter of which varies between 150 and 240 μm when frequency varies from 9 to 36 kHz. The acetone droplet stream is thus vertically injected into a heated enclosure, equipped with optical windows to allow the passage of the laser sheet into the visualization chamber in order to record fluorescence emitted by the acetone droplet stream. Figure 3.29 presents the measured distribution of acetone vapor around the droplet stream for two air temperatures. The concentration profiles of fuel in vapor phase are deduced from these images for different working regimes.

Figure 3.29. *Influence of air temperature on spatial distribution of acetone vapor around droplets.* F_{inj}*=12 kHz: a) T=298 K, b) T=338 K. For a color version of this figure, see www.iste.co.uk/boutier/lasermetro.zip*

Comparisons between experiments and numerical simulations have further showed limits of simplified numerical models for predicting vapor molar fraction profiles around droplets (Figure 3.30). Simulations finish being in agreement with experiments if the correction for the distance parameter is introduced and if ambient gas velocity is considered as depending upon the radial coordinate [ORA 05, CAS 07, MAQ 08].

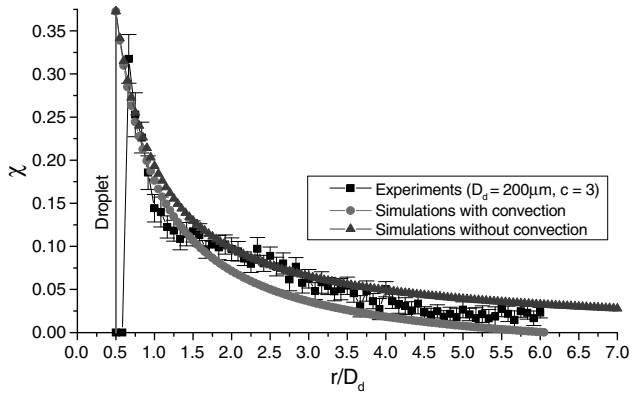

Figure 3.30. *Molar fraction radial profile of acetone vapor around droplets: comparison between experiments (F_{inj}=15 kHz, T_∞ = 355 K, c=3) and theory*

3.3.3.5. *Isolated droplet combustion*

A second application of PLIF concerns the combustion of isolated droplets. An experiment is carried out using a counter current CH_4/air burner, in which liquid acetone droplets are injected, using the monodisperse droplet generator discussed earlier. The experiment's results brought to evidence the different droplet combustion regimes (Figure 3.31) as they are theoretically described [MER 07]. Figure 3.31(a) presents a PLIF image on OH characterizing stationary droplet combustion. Three distinct zones are shown in the figure: a liquid droplet zone, a dark crown representing the fuel evaporation zone and the third zone – the localizing flame front. According to theoretical predictions, combustion is not produced at the droplet surface, but it starts at a distance of a few hundred of microns from the liquid phase. When a droplet has a velocity compared to the surrounding air, the flame spherical symmetry around the droplet is broken and the flame becomes elliptical (see Figures 3.31(b) to (d)). The reactive surface around the droplet is thus modified by a non-homogeneous distribution of fuel vapor around the droplet. Fuel vaporization will be more important upstream of the droplet (i.e. on the droplet side directly opposed to the main flow direction) than downstream, due to convective effects. When the droplet velocity relative to the surrounding flow becomes too high, local flame extinctions are visible. The flame is hung up at a certain distance from the droplet and extends in its wake. Flame structure is no more similar to a pure diffusion flame, with a zone of gas rich in fuel separated from a zone rich in oxidizer by a well-defined reactive zone. Figure 3.31(e) shows the case when a flame is extinguished at the stop point (upstream zone of droplet) and when a triple flame (partially premixed flame and diffusion flame) exists at the flame hanging point. Figure 3.31(e) finally presents the case of flame stabilization in a recirculation zone behind a droplet.

Figure 3.31. *Spatial distribution of OH radical around a droplet in combustion for various combustion regimes. a) envelope of stationary flame, b–d) envelop of a flame around a moving droplet, e) extinguished flame at stop point and f) flame hung in a droplet wake. For a color version of this figure, see www.iste.co.uk/boutier/lasermetro.zip*

The same experimental setup also allowed observing dynamic interaction between a flame front and a fuel droplet crossing it. Figure 3.32 shows flame front deformation when a droplet crosses it, but the droplet does not inflame. As the interaction between the droplet and the flame front starts, the droplet and fuel vapor zone situated upstream of the droplet begin wrinkling the front flame, without any notable perturbation of OH production. A local extinction of front flame, downstream of a droplet, further occurs due the droplet wake, which imposes a high local fuel-air ratio and a temperature decrease in this zone. The droplet, as well as the cloud of fuel vapor crossing the front flame, locally extinguishes the flame over the whole thickness of front flame due to induced mixing degree increase and to a local flame stretching provoked by a high droplet velocity. The droplet and its vapor cloud then propagate in the superior zone of the flame front. When a droplet exits from the flame front, the edges of the extinguished zone of the flame front propagate one toward the other, probably consuming the whole fuel vapor emitted downstream the droplet. A few moments later, the flame front, formed again in the inferior zone, undergoes a local deformation in its superior zone due to a strong interaction between the droplet wake and the flame front. The droplet displacement out of the flame front seems to suck up the front flame by a local fuel-air ratio increase downstream of the droplet. As the distance between the droplet and the flame front reaches one or two front flames thickness, the droplet/flame front interaction vanishes and the flame front recovers its initial position.

Figure 3.32. *Interaction of a fuel droplet not inflamed with a flame front. For a color version of this figure, see www.iste.co.uk/boutier/lasermetro.zip*

Similar works dealing with the interaction of an inflamed fuel droplet with a front flame have also been achieved; details are given in [MER 07].

3.3.3.6. *Evaporation of a spray*

The more complex case of spray evaporation has also been treated to qualify the way new injection systems work for aeronautical fuel, of either LPP (lean–premixed–prevaporized) or LP (lean–premixed). These injection systems allow increasing liquid fuel evaporation as well as the mixing of fuel vapor with oxidant. Unlike single phase flows where we could choose fluorescent tracers, tracers are now imposed by fuel composition, which is in this case kerosene, a multicomponent product. The fluorescent molecules probed are thus 1-2-4 trimethylbenzene, a majority mono-aromatic product and naphtalenes (naphtalene, 1-methylnaphtalene and 1,3 dimethylnaphtalene). Aromatics are excited at a 266 nm wavelength. Two ICCD cameras allow detecting fluorescence of all aromatics and of bi-aromatics. The processing of both images, which are simultaneously recorded, is thus achieved using calibration curves of fluorescence properties directly recorded on kerosene, and not on pure aromatics. Figure 3.33 shows the instantaneous and mean distribution of local fuel air-ratio at the LPP injection system exit. Experiments are achieved at atmospheric pressure, with an air intake temperature of 650 K and a global fuel air-ratio of 0.44 [ORA 06].

Figure 3.33. *Local fuel air-ratio distributions a) instantaneous and b) mean at the output of an aeronautical injection system for an air temperature of 650 K and a global fuel air-ratio $\Phi_0 = 0.44$. For a color version of this figure, see www.iste.co.uk/boutier/lasermetro.zip*

3.3.3.7. *Combustion of a spray*

To study air/kerosene combustion at high pressure, experiments are proven on a multipoint injection (TAPS) developed by SAFRAN in order to improve pollutant reduction at the combustion chamber exit [ORA 09]. This setup is equipped with two separated injection systems. The first one is used to make the pilot flame work; its purpose is to stabilize the flame in the combustion chamber. The second one, called the main system, injects the fuel in different points, equally spaced, around the pilot injection system. Depending on the motor working regime, the injection system works in a pressure range varying from 0.4 MPa (motor regime at slow running) to 3 MPa (motor regime stabilized for cruise flight at high altitude). PLIF is applied to completely characterize the injection system working with kerosene and in combustion. Figure 3.34 shows a picture of a test bench. An optical visualization box allows transmitting laser beams perpendicularly to the flow axis and collecting fluorescence signals across lateral windows.

These experiments allowed simultaneous study of the front flame structure and distribution of fuel vapor at injector exit. Two PLIF benches are coupled, which allow simultaneous quantity determination of OH radical and kerosene vapor. Two overlapping laser sheets are sent either on flow axis or perpendicularly to it (one at 266 nm and the other at 282.75 nm); fluorescence signals are collected from excited fluorescent species on three ICCD cameras (one for OH radical and two for kerosene). Excitation schemes of these species are identical to those described before. Figure 3.35 displays instantaneous and mean spatial distributions of OH, recorded for two pressure conditions: 0.45 and 1.65 MPa. A flame burst is observed on these images; the flame length depends upon fuel air ratio conditions. These measurements have been successfully achieved up to a maximal pressure of 2.2 MPa.

Figure 3.34. *Combustion chamber of M1 bench at ONERA Palaiseau*

Figure 3.35. *Radical OH distribution at multipoint injector exit: a), c) instantaneous images, b), d) mean images averaged on a sample of 100 images for two test conditions: T_{air}=470 K, P=0.45 MPa (Φ_{pil}=0.20, Φ_{princ}=0) and T_{air}=670 K, P=1.65 MPa (Φ_{pil}=0.036, Φ_{princ}=0.324). For a color version of this figure, see www.iste.co.uk/boutier/lasermetro.zip*

Figure 3.36 presents simultaneous distributions of kerosene and a OH radical when the combustion chamber pressure is fixed at 0.95 MPa. On both images, there is a very good correlation between kerosene disappearance and flame front production. These measurements allow validating PLIF use on kerosene in these high pressure conditions. All complementary information brought in addition to the flame structure contribute to a better understanding of the way the injection system works, because the zone where fuel is present at injector exit is well known.

Figure 3.36. *Instantaneous spatial distribution of kerosene and OH radical at multipoint injector exit. Test conditions:* T_{air} *= 590 K, P = 0.95 MPa (*Φ_{pil} *= 0.132,* Φ_{princ} *= 0.132). For a color version of this figure, see www.iste.co.uk/boutier/lasermetro.zip*

3.4. Laser-induced fluorescence in liquids

Results presented until now concerned application of LIF to gaseous fluorescent tracers. This technique is also used with liquid fluorescent tracers to determine the quantity of liquid phase in sprays, or in hydraulic flows, etc.

3.4.1. *Principles and modeling*

In condensed phases, as in the liquid phase, it is no more possible to solve the rotational and the vibrational tiny structure of the fluorescence spectrum. Energy bands are thus considered; they correspond to emission and absorption continuums. These energy bands may have a spectral width of about 100 nm. Therefore, an interaction term with the laser line, having a negligible width compared to the spectral width of an absorption band, may be integrated into spectroscopic constants, which will be noted along a generic manner $K_{opt}(\lambda)$.

A model with two energetic bands (denoted 1 and 2: 1 indicating fundamental state and 2 excited state) will be considered (Figure 3.37), with g_1 and g_2 being

degenerations of states 1 and 2, respectively. As fluorescence signal is expressed by equation [3.46], the molar absorption coefficient and the fluorescence quantum efficiency are both dependent on temperature. In a liquid phase, there is no notable dependency on pressure, except for extremely high pressure levels. The temperature dependency of the molar absorption coefficient k_λ mainly comes from a Boltzmann fraction $f(T)$. Total molecular population N is shared between energetic states 1 and 2, having respectively, energies E_1 and E_2 along the Boltzmann law.

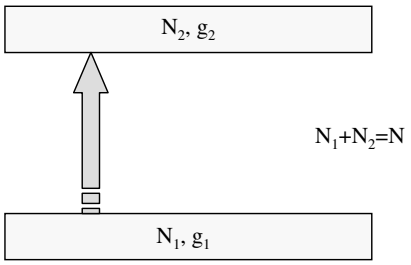

Figure 3.37. *Illustration of model with two energy levels*

Fraction $f(T)$ of molecules being in fundamental state is thus:

$$f(T) = \frac{N_1}{N} = \frac{g_1 e^{-E_1/kT}}{Q_v} \qquad [3.58]$$

where Q_v is the partition function defined in the case of a system with two energy levels by:

$$Q_v = g_1 e^{-\frac{E_1}{kT}} + g_2 e^{-\frac{E_2}{kT}} \qquad [3.59]$$

The following approximation can generally be admitted [HER 51]:

$$g_2 e^{-E_2/kT} >> g_1 e^{-E_1/kT} \qquad [3.60]$$

which leads to a simplified expression for $f(T)$:

$$f(t) = \frac{g_1}{g_2} e^{(E_2 - E_1)/kT} \qquad [3.61]$$

Collision deactivation rate (quenching) k_0 may be written as a function of a kinetic constant k_i and of the molecular concentration of species participating to collision deactivation, noted $[M_i]$:

$$k_Q = \sum_i k_i \left[M_i \right] \qquad [3.62]$$

Quenching constants k_{qi} depend on a medium temperature and may be expressed with the help of a Arrhenius type law [GLO 64]:

$$k_i = k_{0i} e^{-E_a/kT} \qquad [3.63]$$

k_{0i} is a constant and E_a is activation energy involved in the interaction of a fluorescent molecule with another molecule.

When ultra-minority fluorescent species in solution inside a mono-component solvent is concerned, [M] is considered as constant. Neglecting the spontaneous emission term compared to collision deactivation term, the fluorescence quantum yield η may be expressed as:

$$\eta \propto \frac{A_{21}}{k_0 e^{-E_a/kT}} \qquad [3.64]$$

This approximation covers a large validity domain, either in gaseous phase for pressures higher than 1,000 Pa or in condensed phase.

Using modeling adopted for absorption coefficient k_{λ_e} and for the fluorescence quantum efficiency η, expression of fluorescence spectrum in liquid phase is expressed as:

$$I_f(\lambda) = K_{\text{opt}}(\lambda) K_{\text{spec}}(\lambda) V_{\text{mes}} C I_0 e^{\beta(\lambda)/T} \qquad [3.65]$$

with $\beta(\lambda) = \dfrac{E_2 - E_1 + E_a}{kT}$. This parameter β (λ) takes into account spectrum deformation with temperature. This expression does not take into account the absorption of incident energy along the optical path, and neither the eventual reabsorption of fluorescence signal, because absorption and emission spectra may overlap partially.

The fluorescence signal is generally integrated on a sufficiently large spectral band [λ_1, λ_2]. Integration of spectral equation [3.35] leads to the following expression:

$$I_f = K_{\text{opt}} K_{\text{spec}} V_{\text{mes}} C I_0 \int_{\lambda_1}^{\lambda_2} e^{\beta(\lambda)/T} d\lambda = K_{\text{opt}} K_{\text{spec}} V_{\text{mes}} C I_0 e^{A/T^2 + B/T} \qquad [3.66]$$

where K_{opt} and K_{spec} are optical and spectroscopic constants specifically relative to the detection spectral band. A and B are two coefficients of sensitivity to temperature, relative to the chosen spectral band.

3.4.2. *Fluorescence reabsorption*

The problem of fluorescence reabsorption occurs when the chosen spectral detection band belongs to the absorption spectrum of fluorescent species. This problem may be constraining in a liquid phase due the molecular density of the medium, clearly higher than that in a gaseous phase.

From the spectral point of view, fluorescence reabsorption follows the Beer–Lambert law:

$$I_f(\lambda) = I_{f0}(\lambda) e^{-\varepsilon(\lambda)Cy} \qquad [3.67]$$

where $I_{f0}(\lambda)$ is florescence intensity emitted before reabsorption by the medium and $\varepsilon(\lambda)$ is the molar absorption coefficient at wavelength λ.

In the presence of reabsorption, equation [3.66] must be rewritten with an integration of wavelength dependency of $\varepsilon(\lambda)$:

$$I_f = K_{opt} K_{spec} V_{mes} C I_0 \int_{\lambda_1}^{\lambda_2} e^{\beta(\lambda)/T} e^{\varepsilon(\lambda)Cy} d\lambda \qquad [3.68]$$

In such a configuration, the crossed optical medium behaves as a spectral filter relative to fluorescence signal. This filtering effect is linked to the equivalent optical path $C.y$ crossed by the fluorescence signal, which is equivalent to make temperature sensitivity coefficients A and B of equation [3.66] dependent an the optical path. The separating terms relative to absorption and to temperature dependency, integrating optical path in temperature sensitivity coefficients, equation [3.68] is thus empirically expressed by:

$$I_f = K_{opt} K_{spec} V_{mes} C I_0 e^{-\left(kCy + \kappa C^2 y^2\right)} e^{\frac{A(Cy)}{T} + \frac{B(Cy)}{T^2}} \qquad [3.69]$$

Generally, A and B linearly evolve with optical path $C.y$ [LAV 04].

3.4.3. *Applications to concentration measurement*

Fluorescence intensity emitted at one point is proportional to concentration and presents a dependency with temperature. These properties may be used to measure

these parameters in liquid flows. For a concentration measurement, it is necessary to operate at constant temperature; measurement of a fluorescence intensity variation directly leads to a concentration variation of fluorescent species, if the incident laser intensity and probe volume are constant during the experiment. Use of a simple reference point allows an absolute concentration measurement, when a reabsorption on the optical path may be neglected. Concentration is thus expressed by:

$$\frac{I_f}{I_{\text{fref}}} = \frac{C}{C_{\text{ref}}} \qquad [3.70]$$

Yet, this measurement may be disturbed by the absorption of incident laser intensity in the medium seeded with fluorescent tracers. Intensity I_0 locally becomes I_{local} given by the Beer–Lambert law:

$$I_{\text{local}} = I_0 e^{-k_{\lambda e}\int_0^l C(x)\,dx} \qquad [3.71]$$

where l is the optical path of incident laser beam inside the absorbing medium and $k_{\lambda e}$ the molar absorption coefficient of incident radiation. Yet, for a weak equivalent optical path $\int_0^l C(x)\,dx$, this attenuation term remains negligible: it is the linear domain of fluorescence.

This attenuation effect is observed on Figure 3.38, where the fluorescence signal emitted by an organic dye (rhodamine B) in an aqueous solution has been measured with a constant optical path l, for increasing concentrations of fluorescent tracer. In the first limited zone, the fluorescence signal linearly increases with fluorescent tracer concentration; this increase further attenuates when extinction of incident radiation becomes important. In the curve-decreasing phase, dye concentration increase does not compensate incident beam attenuation, which thus becomes the dominant phenomenon.

This method is applied to the characterization of the mixing phenomenon in turbulent flow. For the study of turbulent transport of a passive scalar in a turbulent jet (Figure 3.39) [ANT 01], a measurement acquisition has been temporally achieved, which allowed extracting statistical parameters linked to turbulent transport of concentration. Therefore, mean and fluctuating values such as $\overline{C}$ and $\overline{c'^2}$ can be obtained (Figures 3.40 and 3.41).

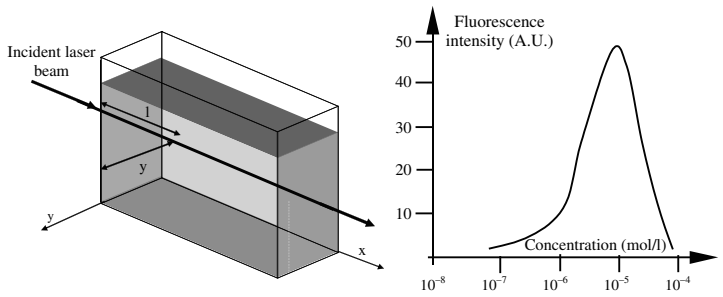

Figure 3.38. *Fluorescence signal evolution as a function of fluorescent tracer concentration (rhodamine B)*

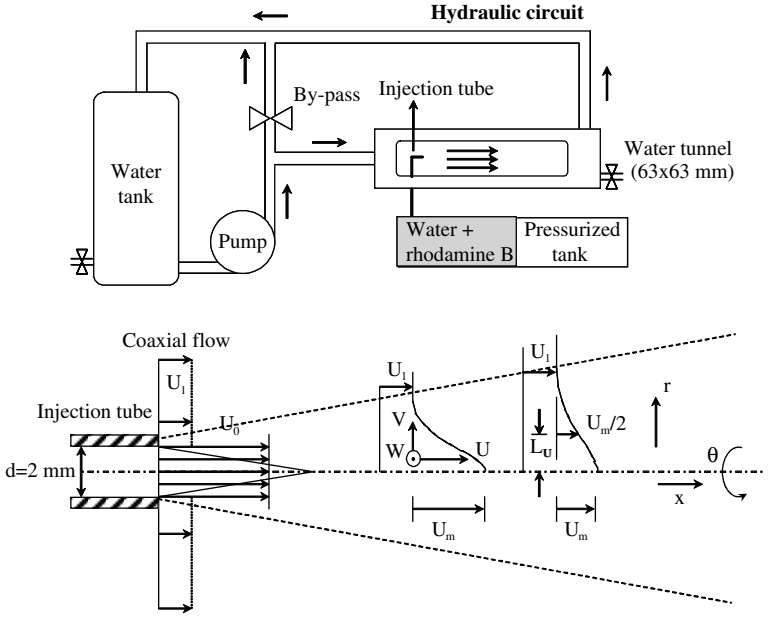

Figure 3.39. *Experimental setup scheme [ANT 01]: turbulent diffusion of a fluorescent dye in an axisymetric turbulent jet*

This method may be coupled with Laser Doppler Velocimetry (LDV); such an experimental setup is described in Figure 3.42. In addition to statistical values linked to velocity, concentration/velocity cross-correlations may be obtained, which characterize turbulent transport as $\overline{c'u'}$ and $\overline{c'v'}$ (Figures 3.43 and 3.44), or higher order correlations. To calculate these correlations, velocity and fluorescence signals

must be identically sampled (Figure 3.43) in order to get corresponding temporal inter–correlations:

$$\overline{v'c'} = \frac{1}{N}\sum_{i}^{N}(C_i - \overline{C})(V_i - \overline{V}) \qquad [3.72]$$

where C_i and V_i represent instantaneous samples of concentration and velocity.

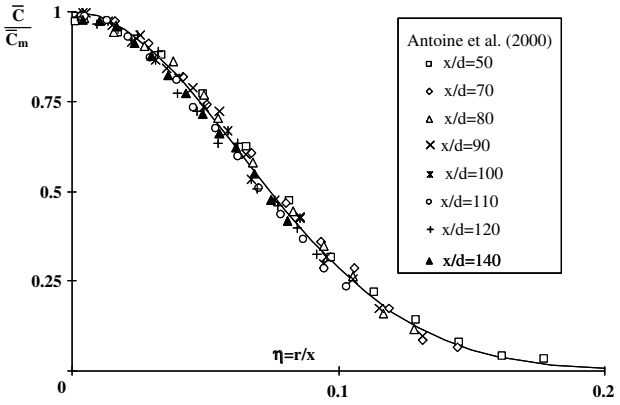

Figure 3.40. *Concentration radial profile in the jet [ANT 01]*

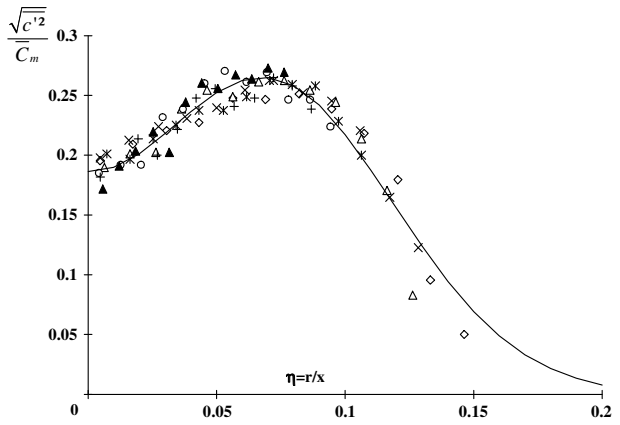

Figure 3.41. *Radial profile of R.M.S. (Root Mean Square) value of concentration fluctuations in the turbulent jet [ANT 01]*

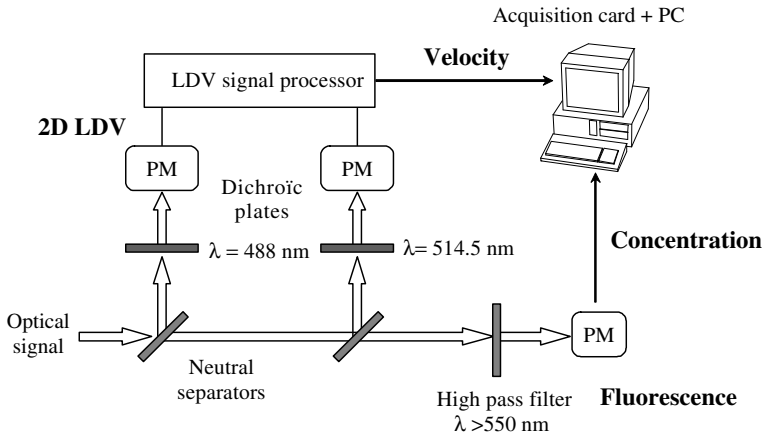

Figure 3.42. *Experimental setup to simultaneously measure velocity by LDV and tracer concentration by LIF*

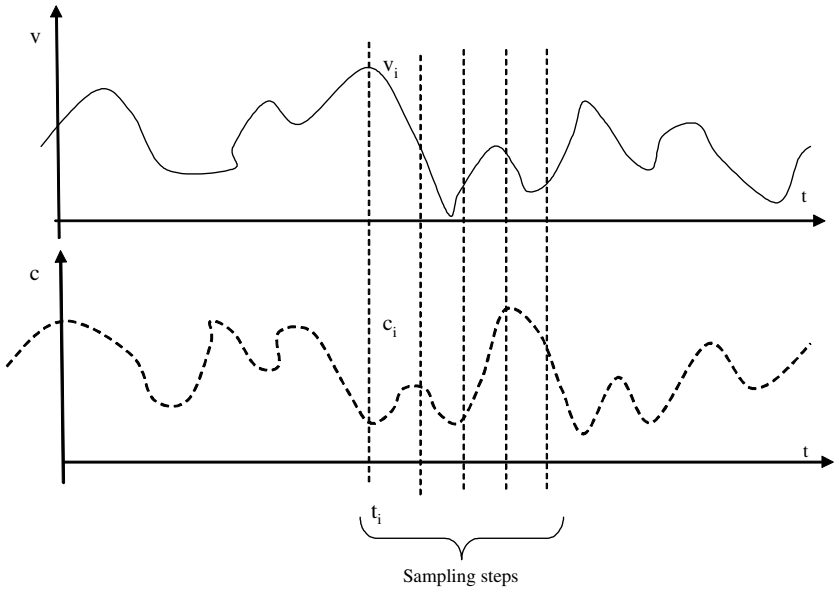

Figure 3.43. *Calculation principle of concentration/velocity intercorrelations by coupled use of LDV and LIF*

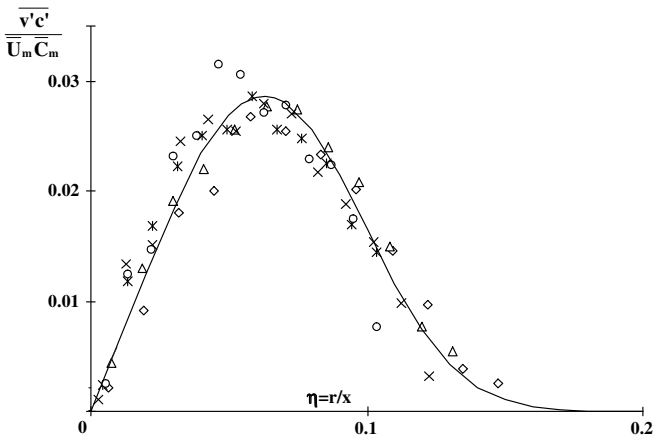

Figure 3.44. *Radial profile of turbulent scalar flux in the jet [ANT 01]*

3.4.4. *Application to temperature measurement*

3.4.4.1. *Method with one detection spectral band*

In order to measure temperature with the fluorescence collected in only one detection spectral band, it is necessary to operate with a constant concentration of a fluorescent tracer, also maintaining constant incident laser power and fluorescence collection volume. Moreover, the detection spectral band must be chosen such that fluorescence signal reabsorption by the medium is minimized. Therefore, the detection band is chosen (if possible) out of the absorption band of fluorescent tracer. Then A and B coefficients of equation [3.69] become independent of optical path $C.y$. If laser beam attenuation is not negligible, it becomes necessary to work with a constant optical path or a correction of this attenuation must be done using the Beer–Lambert law (equation [3.71]). In this case, use of a simple reference point where temperature T is known and where fluorescence intensity I_{f0} is measured allows deducing temperature with the relation issued from equation [3.65]:

$$\ln\left(\frac{I_f}{I_{f0}}\right) = A\left(\frac{1}{T} - \frac{1}{T_0}\right) + B\left(\frac{1}{T^2} - \frac{1}{T_0^2}\right) \qquad [3.73]$$

Coefficients A and B are previously determined by a calibration achieved inside an agitated cell, where temperature measured by a thermocouple is progressively increased. Agitation is necessary to ensure good temperature homogeneity inside the cell and to avoid a photo-bleaching of the fluorescent tracer, induced by extended exposure of the solution to laser radiation.

Use of equation [3.73] requires that fluorescence signal reabsorption is negligible. In contrast, a reference must be taken on the same optical path as the measurements. Figure 3.45 presents such a calibration result for rhodamine B in water solution at different concentrations [LEM 99]. Calibration independency to tracer concentration is thus observed.

Figure 3.45. *Variation of fluorescence intensity as a function of temperature and validation of temperature dependency law for different concentrations of tracer, rhodamine B [LEM 99]*

Furthermore, a fluorescence signal in the liquid phase presents a dependency more or less important to pH and to liquid composition, as a function of fluorescent tracer uses [WAL 97].

An application example of the method is given on a hot turbulent jet coflowing in a cold water stream. The jet is injected by a cylindrical nozzle, which is 2 mm in diameter, in a coaxial flow at low velocity. The jet water is previously heated and seeded with rhodamine B. The water of the coaxial flow is uniformly seeded with the same concentration of rhodamine B. This concentration is low enough to avoid the absorption phenomena on a laser beam optical path, as well as fluorescence reabsorption. The injection velocity is 4.5 m/s and injection temperature 43°C; parameters of coaxial flow are as follows: 0.6 m/s for velocity and 20°C for temperature (Figure 3.46).

The longitudinal decreasing of temperature is given in Figure 3.47. Temperature radial profiles are displayed on a normalized form in Figure 3.48. As in the previous example dealing with concentration, LIF may be coupled with LDV to determine the heat flux transferred by turbulence along two flow directions $\overline{u't'}$ and $\overline{v't'}$ (see Figure 3.49).

Figure 3.46. *Scheme of immerged hot turbulent jet [LEM 99]*

Figure 3.47. *Longitudinal decreasing of mean temperature in the hot jet and comparison with decreasing of mean longitudinal velocity (U_c and θ_c: velocity and temperature difference in the center, U_i and T_i: velocity and temperature at injection) [LEM 99]*

Figure 3.48. *Radial normalized profile of mean temperature in the hot jet (r_t is the radius of temperature radial profile at half-maximum) [LEM 99]*

$\overline{u't'}/\overline{U_c\theta_c}$ $\overline{v't'}/\overline{U_c\theta_c}$

Figure 3.49. *Turbulent flux $\overline{u't'}$ and $\overline{v't'}$ in the hot jet (r_u is the radius of velocity radial profile at mid-height) [LEM 99]*

Figure 3.50. *Radial profile of turbulent Prandtl number in the hot jet [LEM 99]*

Simultaneous measurement of Reynolds stresses by two-dimenmsional LDV allows determining the radial profile of turbulent Prandtl number (Figure 3.50).

3.4.4.2. *Method with two detection spectral bands*

Two-color LIF has mainly been developed to measure the evaporating droplet temperature. Only very short optical paths are considered, which allows neglecting

incident laser beam attenuation and fluorescence signal reabsorption. Nevertheless, in a droplet and in any fluid particle having a liquid/gas interface, probe volume is difficult to quantify and may vary as a function of the interface position relative to laser beams. Moreover, the laser energy distribution droplet depends on an interface form. In an evaporating droplet, the fluorescent tracer concentration is not constant; it increases uniformly. A measurement strategy based on fluorescence detection in two distinct spectral bands has thus been developed. This strategy rests on the strong dependence with the wavelength of the temperature sensitivity $\beta(\lambda)$ (equation [3.65]).

This property is illustrated for the case of sulforhodamine B in aqueous solution (Figure 3.51). Temperature sensitivity is weak around 540 nm and becomes important for wavelengths higher than 570 nm. Curve $\beta(\lambda)$ is highly dependent on the fluorescent tracer and on the solvent used. Such a curve is obtained by calculating the ratio of two fluorescence spectra, recorded at different temperatures.

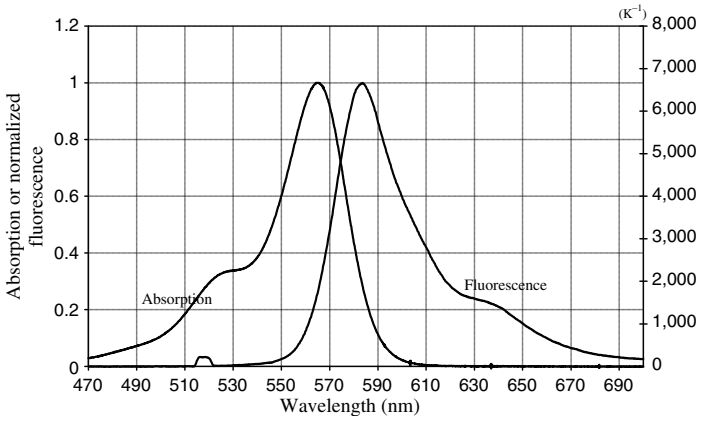

Figure 3.51. *Absorption and emission spectrum of sulforhodamine B in aqueous solution and temperature sensitivity curve*

In two-color LIF, fluorescence is simultaneously detected on two spectral bands, with very different temperature sensitivities. When neglecting any absorption-type, the signal on first band is expressed as (equation [3.66]):

$$I_{f1} = K_{\text{opt1}} K_{\text{spec1}} V_{\text{mes}} C I_0 e^{\frac{A_1}{T} + \frac{B_1}{T^2}} \qquad [3.74]$$

Similarly, a signal on second spectral band is expressed by:

$$I_{f2} = K_{\text{opt}2} K_{\text{spec}2} V_{\text{mes}} C I_0 e^{\frac{A_2}{T} + \frac{B_2}{T^2}} \quad [3.75]$$

Ratio R_{12} of the measured intensities on both spectral bands will thus be written as:

$$R_{12} = \frac{I_{f1}}{I_{f2}} = \frac{K_{\text{opt1}} K_{\text{spec1}}}{K_{\text{opt}2} K_{\text{spec}2}} e^{(A_1 - A_2)\frac{1}{T} + (B_1 - B_2)\frac{1}{T^2}} \quad [3.76]$$

This ratio is independent of the fluorescent tracer concentration, of incident laser energy and of the probe volume; it thus exclusively depends on temperature. Using a reference measurement where temperature T_0 is known and where the fluorescence ratio R_{120} may be measured, the temperature can be determined with the following relationship:

$$\ln\left(\frac{R_{12}}{R_{120}}\right) = (A_1 - A_2)\left(\frac{1}{T} - \frac{1}{T_0}\right) + (B_1 - B_2)\left(\frac{1}{T^2} - \frac{1}{T_0^2}\right) \quad [3.77]$$

Parameters $(A_1 - A_2)$ and $(B_1 - B_2)$ are obtained via a previous calibration, as it is done for fluorescence techniques using only one spectral band. The fluorescence ratio is totally independent of the incident laser beam attenuation. However, reabsorption of fluorescence by the medium remains a critical point, because it much more marked for the first spectral band than for the second. This phenomenon may strongly influence the fluorescence ratio if this reabsorption is not negligible. To perform the calibration, it is therefore required to work at constant and minimum optical path.

A calibration example of coefficients $(A_1 - A_2)$ and $(B_1 - B_2)$, achieved in an agitated tank at controlled temperature, is presented in the case of rhodamine B placed in a solution of ethanol (concentration 10^{-6} mol/l) (Figure 3.52). The following spectral bands are chosen:

– Band 1 : [525 nm; 535 nm]

– Band 2: [>590 nm]

A method with two spectral bands has been applied to temperature measurement of ethanol droplet in combustion. Droplets are produced by a piezo-ceramic injector, which allows producing a line of perfectly identical droplets at frequencies ranging from 5 to 30 kHz (Figure 3.53). Periodicity allows making means over a large number of droplets. The solution is stabilized in the basic medium [LAV 01a, LAV 01b] in order to prevent eventual pH variations due to droplet combustion. A diffusion laminar flame (Figure 3.53) is produced when droplet jet crosses a

heated resistance, brought to fuel inflammation temperature (actually ethanol). Then, droplet moves in the flame produced by combustion of previous droplets.

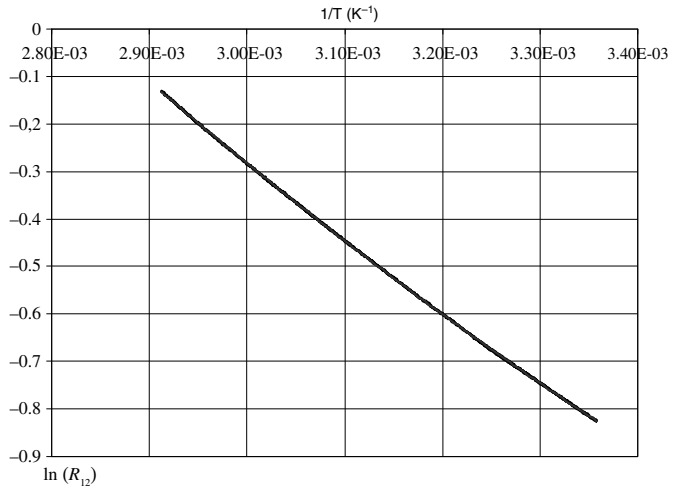

Figure 3.52. *Temperature calibration example (rhodamine B in aqueous solution)*

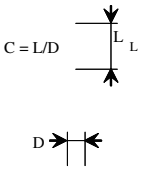

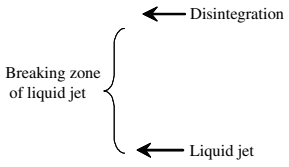

Figure 3.53. *Monodisperse droplet stream in combustion*

The setup of two-color LIF is shown in Figure 3.54. The laser excitation device is an LDV set-up, so the same volume droplet temperature and velocity are measured. The laser wavelength must also belong to the absorption spectrum of the fluorescent tracer, which is the case for a green line of ionized argon laser (514.5 nm) to excite rhodamine B in solution with ethanol. The signal is collected at a right angle by an achromatic doublet. It is previously filtered by a pass-band or high pass filter having a very high optical density (approximately 10^6) at the laser wavelength in order to eliminate the component of laser light scattered by droplets. Then the remaining signal is separated into two spectral bands using a set of dichroïc mirrors. Interferential filters allow adjusting spectral bands to the desired values. Optical signals are thus converted into an electric current by photomultipliers. All the data are acquired and processed by the software developed for this application. Temporal evolutions of the droplet temperature in the flame are presented in Figure 3.55 for various initial aero-thermal parameters: diameter D and adimensional spacing parameter C between droplets (ratio between space separating droplets and their diameter) [CAS 05].

The droplets initially undergo a heating phase, with the duration and slope strongly depending upon initial conditions (diameter and adimensional spacing). This first state is followed by an equilibrium state (characterized by a temperature $T_{\text{equilibrium}}$) where convective (and eventually radiative) flux responsible for heating are compensated by heat flux taken off by evaporation.

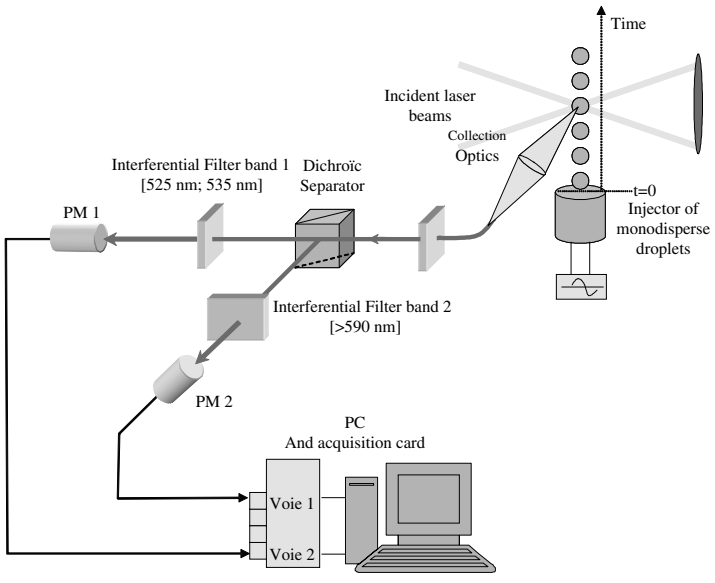

Figure 3.54. *Setup of two-color LIF applied to droplet temperature measurement*

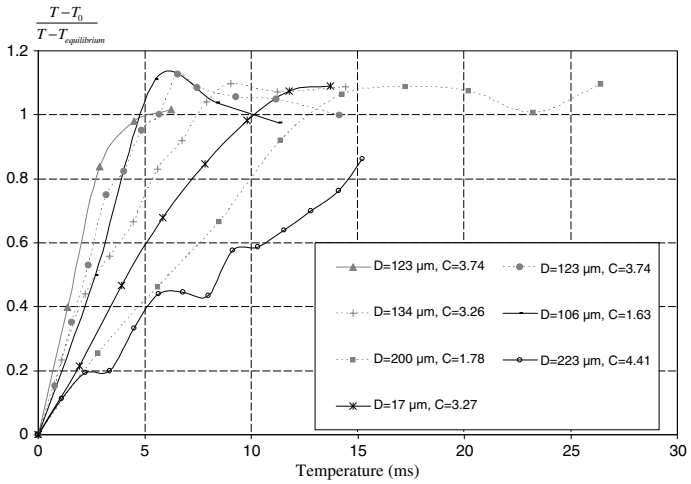

Figure 3.55. *Temperature measurement by two color LIF of ethanol droplets in combustion as a function of time after flame firing point (T_0, temperature of first measurement point)*

3.5. Bibliography

[ANN 92] ANNAMALAI K., RYAN W., "Interactive processes in gasification and combustion. I: liquid drop arrays and clouds", *Progress in Energy and Combustion Science*, vol. 18, pp. 221–295, 1992.

[ANT 01] ANTOINE Y., LEMOINE F., LEBOUCHÉ M., "Turbulent transport of a passive scalar in a round jet discharging into a co-flowing stream", *European Journal of Mechanics-B/Fluids,* vol. 20, pp. 275–301, 2001.

[BAR 05] BARANGER P., ORAIN M., GRISCH F., "Fluorescence spectroscopy of kerosene vapour: application to gas turbines", AIAA Paper 2005-828, *43rd AIAA Aerospace Sciences Meeting and Exhibit*, Reno, NV, 2005.

[BIR 70] BIRKS J.B., *Photophysics of Aromatic Molecules*, Wiley Interscience, New York, 1970.

[BRE 01] BRESSON A., BOUCHARDY P., MAGRE P., GRISCH F., "OH/acetone PLIF and CARS thermometry in a supersonic reactive layer, AIAA 2001-1759", *10th AIAA/NAL/NASDA/ ISAS International Space Planes and Hypersonic Systems and Technologies Conference*, Kyoto, Japan, 2001.

[BRE 03] BRESSON A., BROSSARD C., GICQUEL P., GRISCH F., "Simultaneous temperature, concentration, and velocity fields measurements in a turbulent heated jet using combined laser-induced fluorescence and PIV" in MERCER C.R., CHIANG F.P., SHEN G.X. (eds.), *Optical Diagnostics for Fluids, Solids, and Combustion II, Proceedings of SPIE's Volume 5191*, Society of Photo Optical, 2003.

[CAP 73] CAPELLE G.A., BROIDA H.P., "Lifetimes and quenching cross sections of $I_2(B^3P_{0u}^+)$", *Journal of Chemical Physics*, vol. 58, no. 10, pp. 4212–4222, 1973.

[CAS 05] CASTANET G., LEBOUCHÉ M., LEMOINE F., "Heat and mass transfer of combusting monodisperse droplets in linear stream", *International Journal of Heat and Mass Transfer*, vol. 48, pp. 3261–3275, 2005.

[CAS 07] CASTANET G., MACQUA C., ORAIN M., GRISCH F., LEMOINE F., "Investigation of heat and mass transfer between the two phases of an evaporating droplet stream using laser-induced fluorescence techniques: comparison with modelling", *International Journal of Heat and Mass Transfer*, vol. 50, pp. 3670–3683, 2007.

[CHE 92] CHEN N.H., ROGG B., BRAY K.N.C., "Modelling laminar two-phase counterflow flames with detailed chemistry and transport", *24th International Symposium on Combustion*, pp. 1513–1521, 1992.

[FUK 02] FUKUSHIMA C., AANEN L., WESTERWEEL J., in ADRIAN R.J., DURAO D.J., (eds), "Investigation of the mixing process in an axisymmetric turbulent jet using PIV and LIF" in ADRIAN R.J., DURAO D.F.G., DURST F., HEITOR M.V., MAEDA M., WHITELAW J.H. (eds), *Laser Techniques for Fluid Mechanics*, Springer-Verlag, Berlin, Chapter IV, 339–356, 2002.

[GAO 96] GAO L.P., D'ANGELO Y., SILVERMAN A., GOMEZ A., SMOOKE M.D., "Quantitative comparison of detailed numerical computations and experiments in counterflow spray diffusion flames", *26th International Symposium on Combustion*, pp. 1739–1746, 1996.

[GLO 64] GLOWACKI J., "Further investigations into fluorescence quenching of the dyes by neutral salts", *Acta Physica Polonica*, vol. 15, pp. 767–780, 1964.

[GRI 97] GRISCH F., THURBER M.C., HANSON R.K., "Mesure de température par fluorescence induite par laser sur la molécule d'acétone", *Revue Scientifique et Technique de Défense*, vol. 4, pp. 51–60, 1997.

[HAR 93] HARTFIELD R.J., HOLLO S.D., MCDANIEL J.C., "Planar measurement technique for compressible flows using laser-induced iodine fluorescence", *AIAA Journal*, vol. 31, no. 3, pp. 483–490, 1993.

[HER 51] HERZBERG G., *Spectra of Diatomic Molecules*, 2nd ed., D Van Nostrand Company, 1951.

[HIL 90] HILLER B., HANSON R.K., "Properties of iodine molecule relevant to laser-induced fluorescence experiments in gas flows", *Experiments in Fluids*, vol. 10, pp. 1–11, 1990.

[KOH 94] KOHSE-HOÏNGHAUS K., "Laser techniques for the quantitative detection of reactive intermediates in combustion systems", *Progress in Energy and Combustion Science*, vol. 20, p. 203, 1994.

[LAV 01a] LAVIEILLE P., LEMOINE F., LEBOUCHÉ M., LAVERGNE G., "Mesure de la température de gouttelettes en combustion par fluorescence induite par laser à deux couleurs: résultats préliminaires et perspectives", *Comptes Rendus de l'Académie des Sciences t.329*, Série IIb, pp. 557–564, 2001.

[LAV 01b] LAVIEILLE P., LEMOINE F., LEBOUCHÉ M., LAVERGNE G., "Evaporating and combusting droplet temperature measurement using two colors laser-induced fluorescence", *Experiments in Fluids*, vol. 31, pp. 45–55, 2001.

[LAV 02] LAVIEILLE P., LEMOINE F., LEBOUCHÉ M., "Investigations on temperature of evaporating droplets in linear stream using two-color laser-induced-fluorescence", *Combustion Science and Technology*, vol. 174, pp. 117–142, 2002.

[LAV 04] LAVIEILLE P., DELCONTE A., BLONDEL D., LEBOUCHÉ M., LEMOINE F., "Non-intrusive temperature measurements using three-color laser–induced fluorescence", *Experiments in Fluids*, vol. 36, pp. 706–716, 2004.

[LEM 95] LEMOINE F., LEPORCQ B., "An efficient optical pressure measurement in compressible flows by laser-induced iodine fluorescence", *Experiments in Fluids*, vol. 19, pp. 150–158, 1995.

[LEM 99] LEMOINE F., ANTOINE Y., WOLFF M., LEBOUCHÉ M., "Simultaneous temperature and 2D velocity measurements in a turbulent heated jet using combined laser-induced fluorescence and LDA", *Experiments in Fluids*, vol. 28, pp. 315–323, 1999.

[LI 93] LI S.C., LIBBY P.A., WILLIAMS F.A., "Spray structure in counterflowing streams with and without a flame", *Combustion and Flame*, vol. 94, pp. 161–177, 1993.

[LOZ 92] LOZANO A., YIP B., HANSON R.K., "Acetone: a tracer for concentration measurements in gaseous flows by planar laser-induced fluorescence", *Experiments in Fluids,* vol. 13, pp. 369–376, 1992.

[MAQ 08] MAQUA C., CASTANET G., GRISCH F., LEMOINE F., KRISTYADI T., SAZHIN S.S., "Monodisperse droplet heating and evaporation: experimental study and modelling", *International Journal of Heat and Mass Transfer*, vol. 51, no. 15–16, pp. 3932–3945, 2008.

[MCD 83] MCDANIEL J.C., "Non-Intrusive pressure measurements with laser-induced fluorescence", *AIAA 18th Thermophysics Conference*, Montreal, Canada, 1983.

[MER 07] MERCIER X., ORAIN M., GRISCH F., "Experiments on droplet combustion in strained counterflow diffusion flames using planar laser–induced fluorescence", *Applied Physics B*, vol. 88, pp. 151–160, 2007.

[MIL 94] MILLER M.F., ISLAND T.C., SEITZMANN J.M., BOWMAN C.T., MUNGAL M.G., HANSON R.K., "An experimental investigation of supersonic reacting mixing layer", AIAA 94-0823, *32nd Aerospace Sciences Meeting*, Reno, NV, 1994.

[ORA 05] ORAIN M., MERCIER X., GRISCH F., "PLIF imaging of fuel vapour distribution around a monodisperse stream of acetone droplets, comparison with modelling", *Combustion Science and Technology*, vol. 177, no. 2, pp. 1–30, 2005.

[ORA 06] ORAIN M., VERDIER H., GRISCH F., "Equivalence ratio measurements in kerosene–fuelled LPP injectors using planar laser–induced fluorescence", paper 27.4, *13th International Symposium on Applications of Laser Techniques to Fluid Mechanics*, Lisbon University Ed., Portugal, 26–29 June 2006.

[ORA 09] ORAIN M., GRISCH F., JOURDANNEAU E., ROSSOW B., GUIN C., TRÉTOUT T., "Simultaneous measurements of equivalence ratio and flame structure in multipoint injectors using PLIF", *Comptes Rendus Mécanique*, vol. 337, pp. 373–384, 2009.

[PUR 89] PURI I.K., LIBBY P.A., "Droplet behavior in counterflowing streams", *Combustion Science and Technology*, vol. 66, pp. 267–292, 1989.

[SHA 02] SHAW B.D., DWYER H.A., WEI J.B., "Studies on combustion of single and double streams of methanol and methanol/dodecanol droplets", *Combustion Science and Technology*, vol. 174, pp. 29–50, 2002.

[THU 98] THURBER M.C., GRISCH F., KIRBY B.J., VOTSMEIER M., HANSON R.K., "Measurements and modelling of acetone laser-induced fluorescence with implications for temperature-imaging diagnostics", *Applied Optics*, vol. 37, no. 21, pp. 4963–4978, 1998.

[UME 94] UMEMURA A., "Interactive Droplet vaporization and combustion: approach from asymptotics", *Progress in Energy and Combustion Science*, vol. 20, pp. 325–372, 1994.

[VAL 04] VALEUR B., *Invitation à la fluorescence moléculaire*, De Boeck, Brussels, 2004.

[VIR 00] VIREPINTE J.F., BISCOS Y., LAVERGNE G., MAGRE P., COLIN G., "A Rectilinear droplet stream in combustion: Droplet and gas phase properties", *Combustion Science and Techonology*, vol. 150, pp. 143–159, 2000.

[WAL 97] WALKER D.A., "A fluorescence technique for measurement of concentration in mixing liquids", *Journal of Physics E: Scientific Instruments*, vol. 20, pp. 217–224, 1997.

Chapter 4

Diode Laser Absorption Spectroscopy Techniques

4.1. High spectral resolution absorption spectroscopy in fluid mechanics

Absorption spectroscopy of a beam from a diode laser was developed around 1970 by using a lead salt diode laser (PbSe, [HIL 76, ROS 88]) emitting infrared radiation for combustion studies [ROS 88, HIL 76], then around 1990 to probe free flow in various hypersonic wind tunnels [ARR 94, MOH 95] dedicated to the study of phenomena occurring in atmospheric re-entry. These test facilities run high enthalpy flows, such as the arc facilities F4 of ONERA at Le Fauga-Mauzac [MOH 98] and SIMOUN of Astrium [MOH 00] and the HEG shock tube of DLR at Gottingen [BEC 97]. But this technique may also be applied at lower enthalpy as in the S4 cold wind-tunnel of Modane-Avrieux at ONERA [MOH 99].

The technique consists of characterizing the absorption of a laser beam crossing a flow with the wavelength of the laser being rapidly and finely tuned around one or several molecular or atomic absorption lines. Velocity and translation temperature as well as the concentration of some species may be deduced from the spectral analysis of absorption lines acquired at high spectral resolution. Measurements are achieved on heteronuclei species (such as CO, NO or H_2O), which are pollutants found as traces or which are results of real gas effects, either in air flows simulating Earth re-entry, or in CO_2 flows in the case of Mars re-entry. The most intense molecular absorption strengths for these species, corresponding to their fundamental lines, are located in the mid-infrared (between 3 and 7 μm). This spectral zone is well covered by a lead salt diode lasers (Figure 4.1).

Chapter written by Ajmal MOHAMED.

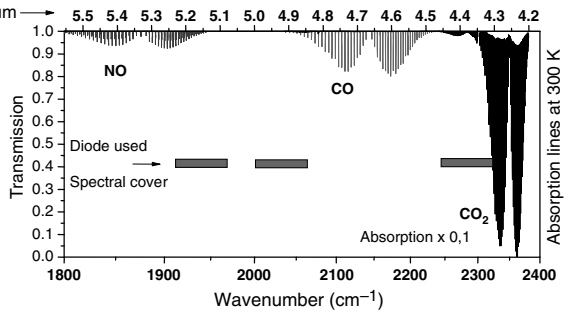

Figure 4.1. *Absorption spectra of some molecules studied in aerodynamics and emission extent of used diodes during technique tests in wind tunnels mentioned in the text*

Lead salt diode lasers emit lines with a relatively narrow spectral width (approximately a few megahertz or 10^{-3} cm^{-1}); they may be finely tuned (with a spectral resolution close to 10^{-4} cm^{-1}) around the absorption lines of molecules having typically 10^{-1} cm^{-1} width at atmospheric pressure (combustion) or 10^{-2} cm^{-1} width at pressure lower than 10 mbar (in the case of hypersonic flows studied). Other types of lasers also exist that offer similar or greater spectral widths. This high spectral resolution thus allows us to directly observe line spectral broadening, due to temperature and/or pressure, without being disturbed by spectral width of laser emission or by the emission-detection apparatus function. The temperature measurement is thus obtained via the Doppler line profile (this profile is dominant in low-pressure conditions, lower than 1,000 Pa generally found in hypersonic flows). At high enthalpy, free stream velocity is obtained by measuring the Doppler shift induced into absorption lines when the beam crosses the flow with an angle not perpendicular to the flow axis. This Doppler shift is approximately 10^{-2} cm^{-1} for wavelengths of 5 μm (2,000 cm^{-1}) at velocities of approximately 1,000 m/s. This velocity measurement is crucial because it allows us to evaluate enthalpy via the simple relationship $H = 1/2\ mV^2$ where V is velocity in m/s. Species density is also deduced from the integrated intensity of absorption lines. Only one absorption line is enough to determine a specie density for a gas at Boltzmann equilibrium; otherwise several lines are required to give, instead of a density, the population distribution on several energy levels of the atomic or molecular specie.

In order to illustrate the possible measurements with this technique, Figure 4.2 presents a spectrum with an absorption line of NO obtained in a hypersonic flow (the conditions are indicated on the figure). The spectrum contains the band that is Doppler shifted as well as the line at rest coming from molecules at zero velocity which are present outside the flow. The line profile is very symmetric indicating that the transition layer where velocity varies from zero to its maximum value is not very thick and that the angular dispersion of velocity vectors is also very low.

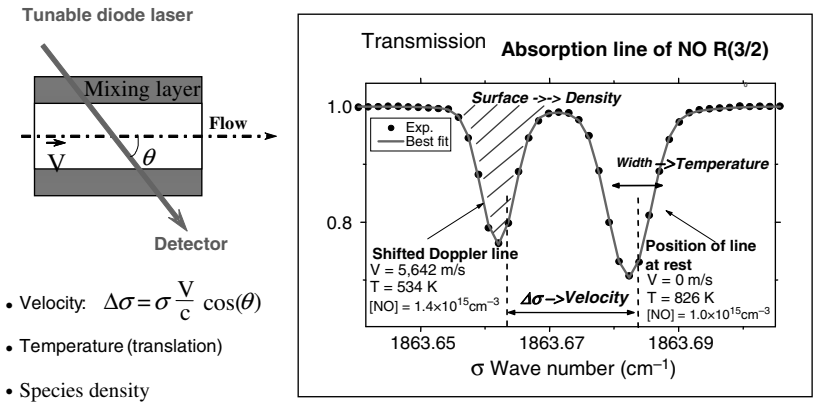

Figure 4.2. *Illustration of possible measurements on an absorption line of NO with a Doppler shift contribution, obtained in a hypersonic flow*

This technique provides velocity values with approximately 5% uncertainty; temperature and density are obtained with uncertainties of approximately 10%.

These measurements may be achieved at a 10 kHz data acquisition rate, determined by the bandwidths of the optical detection and of the diode laser current controller. This repetition rate is fundamental to efficiently probe high enthalpy flows that often have very shortrun durations (approximately 200 ms for an arcjet facility like the ONERA F4 wind tunnel and a few milliseconds for a shock tube like the DLR HEG), and with aerodynamic conditions evolving rapidly at about 1% per ms. A lead-salt diode laser emits infrared radiation at a high repetition rate, but they present two drawbacks: they are not powerful enough and they work at low temperature. Cumbersome cryogenic means (cryostat using helium or liquid nitrogen) are required for laser emission. Such cooling devices must also be implemented for the appropriate infrared optical detectors.

Instruments based on non-cryogenic components make use of diode lasers emitting in the visible or the near infrared, but they are limited to detecting species such as H_2O or atoms such as rubidium or potassium that must be seeded into the flow [BEC 97]. Due to recent developments in laser technology, new infrared sources have appeared on the market such as quantum cascade lasers (QCL) [KOS 02], interband cascade lasers [BEW 08, SAL 06] and optical parametric oscillators (OPO) [DÉS 04]. These new sources allow more elaborate compact instruments. Multipass methods or methods using resonant optical cavities (CRDS, ICOS, etc.) [BER 00] to enhance detection sensibility may also be implemented with visible diode lasers, working close to ambient temperature on weak absorption lines in the visible domain.

4.2. Recap on molecular absorption

In a homogeneous medium, intensity attenuation $I(\sigma)$ of a laser beam at wave number σ is described by the Beer–Lambert law:

$$I(\sigma) = I_0(\sigma) e^{-S_r \cdot f(\sigma,\sigma_r) \cdot N \cdot L} \quad [4.1]$$

where $I_0(\sigma)$ is the initial intensity, N the density of absorbing species, L is the length over which the laser beam undergoes absorptions and S_r the absorption force of an absorption line (indexed r) and centered at wave number σ_r.

The exponential part factor, in expression [4.1], is often called optical thickness or absorption coefficient τ:

$$\tau = NLS_r(T) \cdot f_r(T, p) \quad [4.2]$$

In a homogeneous medium separable into layers "c" containing several species "k", each one having several absorption lines "r", the previous expressions remain valid after adding all these contributions:

$$\tau = \sum_{k,c,r} N_{k,c} \cdot L_c \cdot S_{k,r}(T_c) \cdot f_{krV}(\sigma - \sigma_{k,r}, P_c, T_c) \quad [4.3]$$

If the medium cannot be separated into layers, but has spatial profiles $P(L)$, $T(L)$ and $N_k(L)$, along the beam path, the optical thickness is expressed by:

$$\tau = \int_L N_k(L) \cdot S_{k,r}(T(L)) \cdot f_{krV}(\sigma - \sigma_{k,r}, P(L), T(L)) dL \quad [4.4]$$

All further expressions given in the text will be established for a homogeneous medium with an optical thickness defined by [4.2]; they can be generalized afterward to non-homogeneous media owing to expressions [4.3] and [4.4].

4.2.1. *Line profile*

The function $f(\sigma,\sigma_x)$ represents the spectral intensity distribution or line profile of a normalized absorption line; it takes into account all broadening sources around the central wave number σ_r. There is no instrumental broadening in this high resolution measurement technique. Tine profile $f(\sigma,\sigma_x)$ is only determined by the molecular and thermodynamic parameters of the gas medium. It is mostly a Voigt

profile that results from the convolution of a Doppler profile f_D with a Lorentz profile f_L. The Doppler profile describes the broadening due to molecular thermal motion at kinetic temperature T:

$$f_D(\sigma-\sigma_r,T)=\frac{1}{\sqrt{\pi}\,\alpha_{rD}(T)}\cdot e^{-(\sigma-\sigma_r/\alpha_{rD}(T))^2} \quad [4.5]$$

The half width at half maximum of absorption intensity is expressed in cm^{-1} by:

$$\alpha_{rD}(T)=\sqrt{\ln(2)}\frac{\sigma_r}{c}\sqrt{\frac{2k_BT}{m_{\text{molecule}}}}=3.58\times10^{-7}s_r\sqrt{\frac{T}{M}} \quad [4.6]$$

where k_B is the Boltzmann constant and M the molar mass.

The Lorentz profile represents broadening due to collisions; it depends on pressure P and kinetic temperature T of the medium:

$$f_L(\sigma-\sigma_r,P,T)=\frac{1}{\pi\alpha_{rL}(P,T)}\cdot\frac{1}{1+((\sigma-\sigma_r)^2/\alpha_{rL}^2(P,T))} \quad [4.7]$$

The half width half maximum of the absorption intensity is expressed in cm^{-1} by:

$$\alpha_{rL}(P,T)=\alpha_{rL}^0(P_0,T_0)\frac{P}{P_0}\left[\frac{T_0}{T}\right]^{\text{ylor}} \quad [4.8]$$

Coefficients $\alpha_{rL}^0(P_0,T_0)$ and ylor are obtained either by quantum mechanics calculations or by experiment. For current applications, the value of ylor is 1.5 and $\alpha_{rL}^0(P_0,T_0)$ is provided by the HITRAN database [ROT 09], where the pressure P_0 is chosen equal to 1 bar and the temperature T_0 is equal to 296 K.

Practically, the Voigt profile is reduced to a Doppler profile at a low pressure less than 10 mbar, which is the current situation found in hypersonic flows simulating atmospheric re-entry in the upper atmosphere. In ambient temperature and pressure conditions, this Voigt profile is dominated by broadening due to collisions: it is very close to a Lorentz profile. It must also be noted that, at pressures around 100 mbar, collisions bring spectral narrowing in a line profile: it is the Dicke effect due to collisions with velocity modification [DIC 53]. In some cases, this second-order effect may bring a significant deviation to the traditional Voigt profile and therefore a significant error in measurements from an isolated line profile. In such cases, a Galatry profile [GAL 61] must be used. Other effects exist: natural

broadening, the dependency of relaxation rates to molecular velocities, narrowing at very high pressure, etc. They can also modify significantly the Voigt profile; these cases will not be considered here, an excellent description of these phenomena is given in [NAG 98].

In a flow of velocity V, the wave number of a line center σ_x will be shifted by the Doppler effect toward the value $\sigma_x - \Delta\sigma_x$ such as:

$$\Delta\sigma_x = \sigma_x \frac{v}{c}\cos(\theta)$$

where θ is the angle between the laser beam and the flow axis and c light velocity. In addition to velocity measurement via this Doppler shift, study of this shifted line shape allows inferring the temperature, pressure and the density inside the flow layer moving at velocity V.

4.2.2. *Line strength*

In a medium at thermodynamic equilibrium at temperature T, the expression of line strength S_r is given by:

$$S_r(T) = S_r(T_0) \cdot \frac{Q_r(T_0)}{Q_r(T)} \cdot \frac{1 - \mathrm{e}^{-hc\frac{\sigma_r}{k_B T}}}{1 - \mathrm{e}^{-hc\frac{\sigma_r}{k_B T_0}}} \cdot e^{-\frac{E_r}{k_B}\left(\frac{1}{T} - \frac{1}{T_0}\right)} \qquad [4.9]$$

where:

$S_r(T_0)$: the force experimentally determined, or by calculation, at reference temperature $T_0 = 296$ K of HITRAN database [ROT 09];

$Q_r(T)$: population distribution on molecule levels (partition function);

c: the light velocity in m/s;

h: the Planck constant in J.s;

k_B: the Boltzman constant in $\mathrm{J.K^{-1}}$;

E_r: the energy of the lowest level of transition at wave number σ_x.

$S_r(T_0)$ is experimentally determined or calculated at $T_0 = 296$ K [ROT 09]. $Q_r(T)$ is the partition function, E_r is the molecular transition at low energy absorbtion at wave number σ_r.

4.3. Absorption spectroscopy bench

The elements forming a bench of a diode laser absorption spectroscopy are presented in Figure 4.3. The diode laser is placed inside a cryostat of liquid nitrogen. Its temperature is finely controlled by an electric current that passes through a heating coil supporting the diode. Laser emission is obtained by making another electric current pass through the diode, and the spectral sweep is obtained by a fine intensity tuning of this current. Compact modules are now commercially available to provide these currents with a low noise, as well as all regulation functions of temperature and currents. QCL [KOS 02] working in a continuous mode may also be installed in such a cryostat. An off-axis parabolic mirror is placed at the cryostat output in order to collimate the beam to have a diameter of approximately 15 mm. The diode laser may be multimode, which implies using an optical grating in order to select only one mode at a time. A calibrated monochromator is more advantageous because it also provides a coarse spectral determination of emission wavelength of the diode laser.

Two parts of the beam are picked up via separating plates; they are sent into a Fabry–Pérot and a cell filled with the species to be detected. These channels are necessary for intensity and wavelength calibration of the laser emission. All these elements can be gathered on an optical bench 1.5 m long and 0.8 m wide.

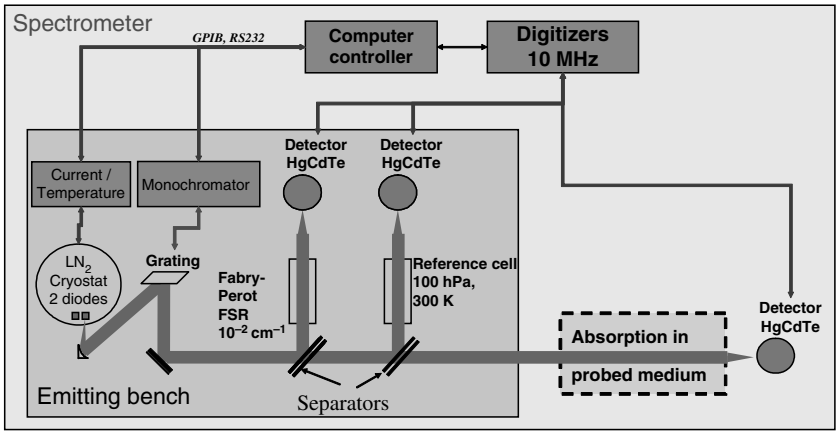

Figure 4.3. Principle of diode laser absorption spectroscopy bench

Figure 4.4 represents set of spectra acquired with such a bench operating a diode laser probing CO at wavelengths close to 2,055.6 cm^{-1} in order to perform velocity measurements. Such spectra are obtained simultaneously within 1 ms, with a repetition rate of 1 kHz.

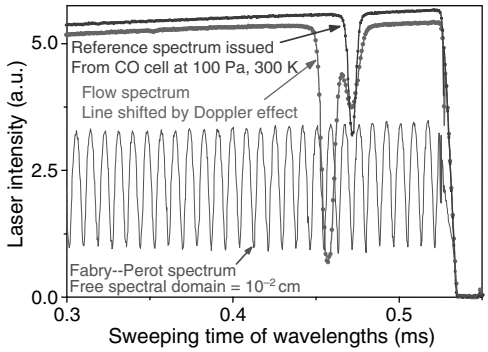

Figure 4.4. *Raw spectra obtained by a diode laser absorption spectroscopy bench on CO*

4.3.1. *Emitting optics*

A diode laser is a junction of two semiconductors, such as a classical electroluminescent diode/diode. There are three characteristic zones: a confinement layer of n type, an active zone and a confinement layer of p type. Confinement layers allow optimizing the use of the current inside a diode and improving its efficiency. The active zone is formed by a wave guide surrounding the laser emission location; it is made of a massive or quantum material (well, box or wire). When this diode is directly polarized, a large current is allowed to pass, which populates the conduction band and thus may achieve population inversion. In practice, an intermediate layer having a superior optical index, plays the guide role in a fiber. Extremities are split and provide perfectly plane faces that play the role of semi-reflecting mirrors, which creates the resonant cavity. A diopter between a semiconductor (an index of approximately 3.5) and air (an index of one) thus presents a reflection coefficient of 30%. This coefficient may be decreased on both sides when an anti-reflecting coating is deposited in order to obtain a more important output power. Depending upon the application domain, either a focusing lens for pointers or readers, or a temperature/current servo control and a preliminary fiber for applications in telecommunications and spectroscopy is added. In this last case, the optoelectronic chip is mounted on a radiator, then on a butterfly Peltier module. A superior contact is connected to the current source by a bonding process.

The luminous emission is based on the electroluminescence phenomenon, which includes a photon emission by recombination of a electron-hole pair and population of the conduction band by current injection. The emission wavelength is provided by the application of the principle of energy conversion: the photon wavelength will be approximately equal to the forbidden material bandwidth (Figure 4.5). Another principle of physics, which you cannot get away from, is momentum conservation when recombining or absorbing; it directs which materials at a direct gap must be

used: the minimum of the conduction band is vertically aligned with the maximum of the valence band in the momentum space. GaAs possesses this property and has been the first one successfully used. It is called a binary component III–V because Ga belongs to column III and As to column V of the periodic table of elements. With a width of the forbidden band 1.424 eV, a wavelength of 870 nm is generated.

Figure 4.5. *Stimulated emission principle in a semiconductor*

As with any laser, the region where gain is created is surrounded by an optical cavity in order to constitute a laser. Amongst the simpler form of a diode laser, an optical wave guide is formed on a crystal surface in such a way that light is confined along a relatively narrow line. Both crystal extremities are split in order to form parallel and perfectly smooth sides, which constitute a Fabry–Pérot resonator. Photons emitted in wave guide mode propagate along this guide-wave and are reflected several times on its extremities before they are emitted. When a luminous wave crosses a cavity, it is amplified by stimulated emission, but light is also lost by absorption and by uncomplete reflexions on faces of cavity extremities. Finally, if there is more amplification than losses, the diode begins to emit a laser beam.

Some important properties of diode lasers are determined by the geometry of the optical cavity. Along a vertical direction, light is generally confined into a very tiny layer; the structure supports only one optical mode along the direction perpendicular to the layers. Along the lateral direction, if the wave guide is big compared to the emitted wavelength, the wave guide may admit multiple lateral optical modes: the laser is said to be multimode. Multimode lasers are convenient for applications requiring a high degree of power, but a small beam, limited by diffraction, is not available. This type of laser is used for printing or pumping other types of lasers.

In applications requiring use of a small focused beam, the wave guide must be narrow (same order of magnitude as wavelength). Therefore, only one lateral mode is created and a diffraction limited beam is emitted. Theses devices with only one spatial mode are used for optical storage, laser pointers and optical fibers. Nevertheless, these lasers may emit multiple longitudinal modes, which allow emitting simultaneously, laser beams at different wavelengths.

The emitted wavelength is a function of the forbidden band of the semiconductor and of the optical cavity modes. The maximum gain is generally obtained for photons having energy slightly higher than forbidden band energy; modes that are nearer gain peak will emit a more powerful beam. If, a diode laser is piloted powerfully enough, additional lateral modes may also emit. Some visible diodes work at one wavelength, but this wavelength is unstable and moves due to temperature and current fluctuations.

The beam rapidly diverges after leaving the component (due to diffraction), typically 30° vertically and 10° laterally. A lens must be used to form a collimated beam, such as the one produced by a laser pointer. If a circular beam is desired, cylindrical lenses and other optics are used. For lasers having only one spatial mode, when using symmetric lenses, the collimated beam has finally an elliptical shape, due to the differences in vertical and lateral divergences (this phenomenon is easily seen on a laser pointer).

A diode laser made in PbSe material [HEC 99] has been commercialized for more than 20 years and has become essential for gas analysis, with a high sensitivity and a great selectivity in the mid-infrared. Their emission covers wavelengths ranging from 3 μm to more than 20 μm; they are thus well adapted for probing many interesting species for aerodynamics and pollution, as Figure 4.6 shows. Their geometry is provided in Figure 4.7. Continuous emission is observed above 80 K and pulsed emission above 200 K.

The tuning range of PbSe diode lasers [INF] covers several hundred wavenumbers. Temperature and current are used for emission wavelength tuning; usually, temperature is fixed at a constant value and the diode is controlled by a current, either directly, or via different modulation types at frequencies that may vary from a few hertz to a few gigahertz.

Figure 4.8 shows the injection current as a function of an emitted wavelength at constant temperature. The tuning range of one diode mode is approximately 0.5 to 1 cm^{-1} (it may reach 5 cm^{-1}).

Figure 4.6. *Positions of lines emitted by diode lasers PbSe*

Figure 4.7. *Geometry of PbSe diode lasers*

Figure 4.8. *Behavior of spectral emission of a diode laser for several currents*

4.3.2. *Optical detection*

4.3.2.1. *Optical detectors*

The diode laser sources usually employed have a low power less than 1 mW. Mostly, after splitting of the initial beam into several beams for calibration needs and other transformations (spectral filtering, multiple reflexions on mirrors, etc.), the power reaching a detector is rather in the order of 100 μW. For visible or near infrared measurements, uncooled detectors based on silicon (InGaAs, GaP or Ge) are sensitive enough. Beyond 2 μm, infrared detectors must be cooled by Peltier effect (InAs, PbS, PbSe, etc.) for the range 2–3 μm, and cooled by liquid nitrogen (HgCdTe, PbSe, etc.) for the range higher than 3 μm. Figure 4.9 shows the sensitivity D_l^* of some infrared detectors as a function of wavelength and of working temperature [CHA 10].

Other properties, such as bandwidth or linearity, must be considered for optical detectors: a vast bibliography is available on this subject [WOL 07]. Depending upon application and detection method, the most appropriate specifications must be chosen to amplify and condition the electric output signal. Two methods are generally used: direct detection (when absorption is higher than a few percents) or detection with a frequency or amplitude modulation. For direct detection of transient phenomena in hypersonic or of turbulence in combustion, a bandwidth in the order of 1 MHz is required, but for atmospheric probing 1 Hz is sufficient.

Figure 4.9. *Characteristics of infrared detectors (source: Hamamatsu Technical note SD-12, 2010)*

4.3.2.2. *Signal acquisition*

4.3.2.2.1. Direct detection

The direct detection method consists of digitizing the signal issued from a photodetector, while the diode current along a linear ramp is varying: the wavelength is thus continuously and finely swept over a spectral range containing the desired absorption lines.

Owing to the use of very quick digitizers, having a wide dynamic range and a high storage capacity, three can be simultaneously digitized, at a 60-MHz frequency with a 12-bit dynamics, continuous over several seconds. The 12-bit dynamics feature means that the photodetector signal intensity can be sampled by steps of 1/4096. In current applications, taking into account the usual noise level that represents approximately two bits, detectable absorption is approximately 1/10 bit, that is 1/1024, which leads to an uncertainty of 0.1%.

4.3.2.2.2. Amplitude or wavelength modulation

This technique is used when absorption is very weak. A high frequency modulation ($\omega_m = 2\pi f_m$) is superimposed to the current ramp sent to the diode (Figure 4.10). Therefore, both emission wave number $\sigma(t)$ and laser intensity $I_0(t)$ are modulated:

$$\sigma(t) = \sigma_s + a \cdot \cos(\omega_m t)$$
$$I_0(t) = I_{0s} + i_0 \cdot \cos(\omega_m t + \theta)$$

where σ_s and I_{0s} are parameters without modulation, a and i_0 the modulation amplitudes and θ the modulation phase.

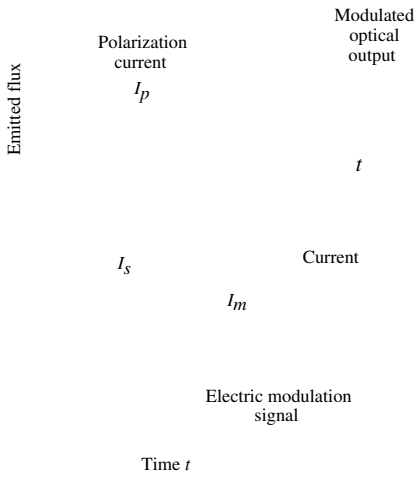

Figure 4.10. *Frequency modulation superimposed on the current ramp*

The absorption coefficient in the laser beam intensity expression after passage across the medium will also be modified by this modulation:

$$\tau(\sigma) = \tau(\sigma_s + a \cdot \cos(\omega_m t))$$

which may be written as a Fourier series:

$$\tau(\sigma_s + a \cdot \cos(\omega_m t)) = \sum [H_n(\sigma_s, a) \cdot \cos(n\omega_m t)]$$

where H_n is the harmonic function of nth order that may be written as follows:

$$H_0 = \frac{1}{2\pi} \int_{-\pi}^{\pi} \tau(\sigma_s + a \cos(\omega_m t)) d\omega_m t$$
$$H_n = \frac{1}{\pi} \int_{-\pi}^{\pi} \tau(\sigma_s + a \cos(\omega_m t) \cos(n\omega_m t)) d\omega_m t$$

The components I_n of the intensity corresponding to these functions are represented in Figure 4.11.

Figure 4.11. *Harmonic components of detected intensity*

Each component $n\omega_m$ may be individually obtained by analyzing the total intensity with a synchronized detection amplifier on frequency $n\omega_m$. The most often used component is $2\omega_m$ (or $2f$ in the frequency domain) because it is the only one that displays a symmetric peak relative to the absorption line center, as shown in Figure 4.11.

Detection at 2f allows observing absorptions with 10^{-6} order of magnitude; nevertheless, as the line shape is altered, it is not now possible to extract the temperature or pressure. Only velocity and concentration measurements remain possible.

4.3.3. *Spectra processing*

Researched parameters (concentration, velocity and temperature) are obtained by inverting normalized and calibrated spectra. Before undertaking an inversion, the shaping of raw spectra is achieved in several steps: cutting out, normalization and calibration. Cutting out consists of extracting on the one hand the useful part of the spectra comprising absorption lines and, one the other hand, the zone close to optical zero, that is when there is no laser emission; extraction of this last zone is necessary to normalize results.

4.3.3.1. *Intensity calibration*

The global shape of spectra without absorption, called the envelope, results from the diode laser emission mode and from the apparatus function of the optical setup. The division of an absorption spectrum by its envelope allows normalization; value

1 corresponds to a zero absorption and value 0 to 100% absorption. If during successive sweeps, the emission of the diode laser is very stable and reproducible, then the spectrum of the measurement channel acquired activation of medium to be characterized, may be used as an envelope.

During a measurement series, diode laser power fluctuates and induces variations of a mode envelope. An additional channel may be used to calibrate this envelope at each diode laser sweep; nevertheless, this channel does not directly provide the envelope for the measurement channel because slight differences always occur. In order to palliate these differences, a correction function is previously determined: this is the ratio of the calibration channel over the measurement channel before activation of the medium to be characterized. Normalization is operated by dividing the measurement channel by the calibration channel, and multiplication by this correction function. When absorption lines are isolated, only the method measurement channel may be used to extract an envelope, which is extrapolated from portions that do not contain absorption lines. This last method is the most commonly used in low-pressure flows where lines have Doppler profiles with a small extent at aisle level.

4.3.3.2. *Spectral calibration*

Normalized and cut out spectra must be calibrated along wave numbers. This is achieved by using spectra issued from Fabry–Pérot and a cell containing a reference gas. The first one provides a relative spectral calibration, via interference fringes the spectral spacing of which is known. The absolute reference in a wave number is obtained by the position of the absorption lines of the gas present in the tank cell. This type of calibration allows for the breaking free from the nonlinearity of acquisition and of the diode sweep ramp. Calibration is often presented as an n degree polynomial, associating each point i to the processed spectrum, the wave number $\sigma(i) = \sigma_0 + \sigma_1.i + \sigma_2.i^2 + ..\sigma_n.i^n$.

4.3.3.3. *Spectra inversion*

When calibration in wavelength and intensity is achieved using the calibration channel, the useful part of each calibrated spectrum is compared to a spectrum simulated by means of an iterative smoothing process based on the least squares method: this allows for the determining of velocity, kinetic temperature and concentration of absorbing species. Simulated spectrum is elaborated from the classical absorption law of Beer–Lambert (equation [4.1]).

4.3.3.3.1. General description of the method for spectra inversion

Comparison of an experimental spectrum to a calculated spectrum may be written under a vector form as:

$$\vec{\mathrm{I}}_e = \vec{\mathrm{I}}_s(\vec{\mathrm{P}}) + \vec{\mathrm{E}}$$

where:

$\vec{I}_e$: column vector containing intensities $I_{e\,i}$ of each discrete point of experimental spectrum;

$\vec{I}_s$: vector of calculated intensities using an appropriate absorption model;

$\vec{P}$: model parameters (for instance T, P, V, etc.);

$\vec{E}$: errors between simulated and experimental intensities.

Statistical properties of experimental data are expressed as a variance matrix $\vec{\vec{\Sigma}}$ for the intensity vector of experimental points $\vec{I}_e$. As obtaining such an intensity vector $\vec{I}$ is governed by a probability law, the variance matrix is expressed by:

$$\vec{\vec{\Sigma}} = \int \left(\vec{I}_e - \vec{I}_e^0\right)\left(\vec{I}_e - \vec{I}_e^0\right) P(\vec{I}) d\vec{I}$$

or in component terms:

$$\Sigma_{ij} = \int \left(I_{ei} - I_{ei}^0\right)\left(I_{ej} - I_{ej}^0\right) P(I) dI$$

In the case where noise is not correlated between experimental points, this matrix is reduced to diagonal terms equal to ε_i^2, where ε_i is intensity measurement error on the *i* spectrum point.

4.3.3.3.2. Least squares method

Least squares method [ARM 92, SCH 92, TAU 88] consists of minimizing the mean square deviation Z_0 expressed as:

$$Z_0 = {}^t\vec{E}\vec{\vec{W}}\vec{E}$$

where $\vec{\vec{W}} = \vec{\vec{\Sigma}}^{-1}$ is matrix of weights of measured intensities.

If a series of initial values is taken for parameters $\vec{P}_0$, using Taylor development $\vec{I}_e$ may be written as:

$$\vec{I}_e = \vec{I}_s(\vec{P}_0) + \frac{\partial\, \vec{I}_s(\vec{P}_0)}{\partial \vec{P}}(\vec{P} - \vec{P}_0) + \vec{E}$$

Term $(\partial\, \vec{\mathrm{I}}_s(\vec{\mathrm{P}}_0))/\partial\vec{\mathrm{P}}$ is called Jacobian matrix, Jacobian $\vec{\vec{\mathrm{J}}}$.

Starting from an initial ensemble of parameters $\vec{\mathrm{P}}_0$, the ensemble of parameters $\vec{\mathrm{P}}_1$ that minimizes errors $\vec{\mathrm{E}}$ is the solution of the following equation:

$$(\vec{\mathrm{P}}_1 - \vec{\mathrm{P}}_0) = ({}^t\vec{\vec{\mathrm{J}}}\vec{\vec{\mathrm{W}}}\vec{\vec{\mathrm{J}}})^{-1}\ {}^t\vec{\vec{\mathrm{J}}}\vec{\vec{\mathrm{W}}}(\vec{\mathrm{I}}_e - \vec{\mathrm{I}}_s)$$

But ensemble $\vec{\mathrm{P}}_1$ is not necessarily the ensemble for the exact solution, even if it is closer than ensemble $\vec{\mathrm{P}}_0$. In order to go to the closest of the exact solution, an iteration process is undertaken: if $\vec{\mathrm{P}}_1$ is now considered as $\vec{\mathrm{P}}_0$, the previous equation can be solved in order to obtain a new ensemble of $\vec{\mathrm{P}}_1$ much closer to the exact solution. This process is repeated until difference $\vec{\mathrm{P}}_1 - \vec{\mathrm{P}}_0$ cannot be further reduced, or is under a value fixed in such a way that an acceptable solution is obtained with a realistic number of iterations.

In order to accelerate convergence and to limit instability risks, a damped form is used for the previous equation:

$$(\vec{\mathrm{P}}_1 - \vec{\mathrm{P}}_0) = ({}^t\vec{\vec{\mathrm{J}}}\vec{\vec{\mathrm{W}}}\vec{\vec{\mathrm{J}}} + \lambda\vec{\vec{D}})^{-1}\ {}^t\vec{\vec{J}}\vec{\vec{W}}(\vec{I}_e - \vec{I}_s) \text{ where } \vec{\vec{D}} = diag\,({}^tJWJ)$$

where λ is a damping weight generally taken equal to Z_0 (standard deviation between observed and calculated spectra), which tends toward a very small value when the system converges toward a solution.

For the Jacobian matrix, the following derivatives are necessary:

$$\frac{\partial \mathrm{I}}{\partial N_{\mathrm{k}l}} = -\mathrm{I}\sum_r \int_l \left(\mathrm{S}_{\mathrm{kr}l}\mathrm{f}_{\mathrm{kr}l}\right)\mathrm{d}l$$

$$\frac{\partial\, \mathrm{I}}{\partial\, \mathrm{P}_l} = -\mathrm{I}\sum_{\mathrm{kr}} \int_l \left(\mathrm{N}_{\mathrm{k}l}\mathrm{S}_{\mathrm{kr}l}\frac{\partial\, \mathrm{f}_{\mathrm{kr}l}}{\partial\, \mathrm{P}_l}\right)\mathrm{d}l$$

$$\frac{\partial\, \mathrm{I}}{\partial\, \mathrm{T}_l} = -\mathrm{I}\sum_{\mathrm{kr}} \int_l \mathrm{N}_{\mathrm{k}l}\left(\mathrm{f}_{\mathrm{kr}l}\frac{\partial\, \mathrm{S}_{\mathrm{kr}l}}{\partial\, \mathrm{T}_l} + \mathrm{S}_{\mathrm{kr}l}\frac{\partial\, \mathrm{f}_{\mathrm{kr}l}}{\partial\, \mathrm{T}_l}\right)\mathrm{d}l$$

$$\frac{\partial \mathrm{I}}{\partial \sigma_{\mathrm{kr}l}} = -\mathrm{I}\sum_{\mathrm{kr}}\int_{l} \mathrm{N}_{\mathrm{k}l}\left(\mathrm{f}_{\mathrm{kr}l}\frac{\partial \mathrm{S}_{\mathrm{kr}l}}{\partial \sigma_{\mathrm{kr}l}} + \mathrm{S}_{\mathrm{kr}l}\frac{\partial \mathrm{f}_{\mathrm{kr}l}}{\partial \sigma_{\mathrm{kr}l}}\right)\mathrm{d}l$$

$$\frac{\partial \mathrm{I}}{\partial \mathrm{V}_l} = \sum_{\mathrm{kr}}\frac{\partial \mathrm{I}}{\partial \sigma_{\mathrm{kr}l}}\frac{\partial \sigma_{\mathrm{kr}l}}{\partial \mathrm{V}_l} = \sum_{\mathrm{kr}}\frac{\partial \mathrm{I}}{\partial \sigma_{\mathrm{kr}l}} a_l \sigma_{\mathrm{kr}}$$

$$= -I \cdot a_l \cdot \sum_{\mathrm{kr}} \sigma_{\mathrm{kr}} N_{\mathrm{kr}}\left(\mathrm{S}_{\mathrm{kr}l}\frac{\partial \mathrm{f}_{\mathrm{kr}l}}{\partial \sigma_{\mathrm{kr}l}} + \mathrm{f}_{\mathrm{kr}l}\frac{\partial S_{\mathrm{kr}l}}{\partial \sigma_{\mathrm{kr}l}}\right)$$

Starting from line strength expression [4.9], and using kb = hc/k_B,

$$\mathrm{S}_{\mathrm{kr}l}(\mathrm{T}_l) = \mathrm{S}_{\mathrm{kr}l}(\mathrm{T}_0)\cdot\frac{\mathrm{Q}_{\mathrm{kr}l}(\mathrm{T}_0)}{\mathrm{Q}_{\mathrm{kr}l}(\mathrm{T}_l)}\cdot\frac{1-\mathrm{e}^{-\frac{\mathrm{kb}.\sigma_{\mathrm{kr}l}}{\mathrm{T}_l}}}{1-\mathrm{e}^{-\frac{\mathrm{kb}.\sigma_{\mathrm{kr}l}}{\mathrm{T}_0}}}\cdot\mathrm{e}^{-\mathrm{kb}.\mathrm{E}_{\mathrm{kr}}\cdot\left(\frac{1}{\mathrm{T}_l}-\frac{1}{\mathrm{T}_0}\right)}$$

Then, it comes:

$$\frac{\partial S_{\mathrm{kr}l}}{\partial \sigma_{\mathrm{kr}l}} = S_{\mathrm{kr}l}.\mathrm{kb}\left(\frac{\mathrm{e}^{-(\mathrm{kb}.\sigma_{\mathrm{kr}l}/\mathrm{T}_l)}}{\mathrm{T}_l\left(1-\mathrm{e}^{-(\mathrm{kb}.\sigma_{\mathrm{kr}l})/\mathrm{T}_l}\right)} - \frac{\mathrm{e}^{-(\mathrm{kb}.\sigma_{\mathrm{kr}l}/\mathrm{T}_0)}}{\mathrm{T}_0\left(1-\mathrm{e}^{-(\mathrm{kb}.\sigma_{\mathrm{kr}l}/\mathrm{T}_0)}\right)}\right)$$

In order to calculate the derivative with respect to temperature, the partition function must be first developed, using the following approximation:

$$\mathrm{Q}(\mathrm{T}) \approx \underbrace{\left(\sum_{\Lambda}\mathrm{g}_{\Lambda}.\mathrm{e}^{-\frac{\mathrm{E}_{\Lambda}}{\mathrm{k}_{\mathrm{B}}\mathrm{T}_{\Lambda}}}\right)}_{\text{Electronic}} \times \underbrace{\left(\sum_{\mathrm{v}}\mathrm{g}_{\Lambda}.\mathrm{e}^{-\frac{\mathrm{E}_{\mathrm{v}}}{\mathrm{k}_{\mathrm{B}}\mathrm{T}_{\mathrm{v}}}}\right)}_{\text{Vibration}} \times \underbrace{\left(\sum_{N}\mathrm{g}_{N}.\mathrm{e}^{-\frac{\mathrm{E}_{N}}{\mathrm{k}_{\mathrm{B}}\mathrm{T}_{N}}}\right)}_{\text{Rotation}}$$

$$\approx \left(\mathrm{C}_{\Lambda}\right) \times \left(\mathrm{C}_{\mathrm{v}}\prod_{\mathrm{v}}\left(1-\mathrm{e}^{-\frac{\mathrm{E}_{\mathrm{v}}}{\mathrm{k}_{\mathrm{B}}\mathrm{T}_{\mathrm{v}}}}\right)^{-\mathrm{g}_{\mathrm{v}}}\right) \times \left(\mathrm{C}_{\mathrm{N}}\mathrm{T}^{\gamma}\right)$$

Normalization coefficients C_Λ, C_V and C_N are not important because only ratio $Q(T)/Q(T_0 = 296\ K)$ is required. Values of E_v, g_v and γ are taken from the database from [ROT 09].

At equilibrium, $T_v = T_r = T$, the derivative with respect to temperature is:

$$\frac{\partial Q}{\partial T} = \frac{Q}{T}\left(\gamma + \frac{1}{T}\sum_v \left[g_v.\sigma_v.kb.\frac{e^{-\frac{kb.\sigma_v}{T}}}{T\left(1-e^{-\frac{kb.\sigma_v}{T}}\right)}\right]\right)$$

Absorption force may thus be derived relative to temperature:

$$\frac{\partial S_{krl}}{\partial T_l} = S_{krl}\left(-\frac{\partial Q/\partial T_l}{Q} + \frac{kbE_{kr}}{T_l^2} - \frac{kb.\sigma_{krl}}{T_l^2}\frac{e^{-\frac{kb.\sigma_{krl}}{T_l}}}{T_l\left(1-e^{-\frac{kb.\sigma_{krl}}{T_l}}\right)}\right)$$

Using dimensional variables:

$$x = \frac{\sigma - \sigma_{krl}}{\alpha_D(T)} \text{ and } y = \frac{\alpha_L(P,T)}{\alpha_D(T)}$$

the line profile may be expressed using the Voigt function $K(x,y)$:

$$f_{krl} = f(x,y) = \frac{1}{\alpha_D\sqrt{\pi}}K(x,y)$$

$$K(x,y) = \frac{y}{\pi}\int_{-\infty}^{+\infty}\frac{e^{-t^2}}{(x-t)^2 - y^2}dt$$

It is easier to calculate a Voigt function in complex space because it is simply the real part of complex error function $w(z)$:

$$w(z) = e^{-z^2}\left(1 + \frac{2i}{\pi}\int_0^z e^{-t^2}dt\right)$$

$$K(x,y) = \mathrm{Re}(w(z)) \; ; \; z = x + iy \; ; \; \mathrm{y} > 0$$

To calculate this error function, a Hui approximation [HUI 78] is used at 6th order:

$$w(z) = \frac{\sum_{m=0}^{6} a_m (y - ix)^m}{\sum_{n=0}^{7} b_n (y - ix)^n} \; ; \; b_7 = 1$$

where a_m and b_n are coefficients given in [HUI 78]. Calculation time is longer than for other approximation types [ARM 67, DRA 76, MOH 96], but accuracy is better (error less than 10^{-6}) and valid for any x and y.

Use of error function presents another advantage for calculations: the derivatives from the Voigt function required to build the Jacobian matrix can be calculated starting from simple mathematical expressions:

$$K'_x = \frac{\partial K(x,y)}{\partial x} = -2\,\mathrm{Re}(zw(z)) = 2\left[y\,\mathrm{Im}(w) - x\,\mathrm{Re}(w)\right]$$

$$K'_y = \frac{\partial K(x,y)}{\partial y} = 2\,\mathrm{Im}(zw(z)) - \frac{2}{\sqrt{\pi}} = 2\left[x\,\mathrm{Im}(w) + y\,\mathrm{Re}(w) - \frac{1}{\sqrt{\pi}}\right]$$

For pressure and temperature:

$$\frac{\partial \mathrm{f}}{\partial \mathrm{T}} = -\frac{1}{2\mathrm{T}} \frac{1}{\alpha_\mathrm{D}\sqrt{\pi}} \left[K + xK'_x + 2y\left(\mathrm{ylor} + \frac{1}{2}\right)K'_y\right]$$

$$\frac{\partial \mathrm{f}}{\partial \mathrm{P}} = \frac{y}{\mathrm{P}} \frac{1}{\alpha_\mathrm{D}\sqrt{\pi}} K'_y$$

For wave number σ, $\dfrac{\partial \mathrm{f}}{\partial \sigma} = +\dfrac{1}{\alpha_\mathrm{D}^2\sqrt{\pi}} K'_x$.

For position of line center $\sigma_{\mathrm{kr}l}$, $\dfrac{\partial \mathrm{f}}{\partial \sigma_{\mathrm{kr}l}} = -\dfrac{1}{\alpha_\mathrm{D}^2\sqrt{\pi}} K'_x$.

4.3.3.3.3. Derivatives for Jacobian matrix

Two notations simplify expressions:

$$\bar{S} = \frac{S_{krl} N_{kl}}{\alpha_D \sqrt{\pi}} \quad \text{and} \quad \overline{dS_T} = \frac{N_{kl}}{\alpha_D \sqrt{\pi}} \frac{\partial S_{krl}}{\partial T}$$

Then, final expressions are obtained for derivatives that are implemented in calculation procedures:

$$\frac{\partial I}{\partial N_{kl}} = -I \sum_r \int_l \left(\frac{S_{krl}}{\alpha_D \sqrt{\pi}} \cdot K \right) dl$$

$$\frac{\partial I}{\partial P_l} = -I \sum_{kr} \int_l \left(\frac{\bar{S}}{P_l} \cdot y \cdot K'_y \right) dl$$

$$\frac{\partial I}{\partial T_l} = -I \sum_{kr} \int_l \left(\overline{dS_T} \cdot K - \frac{\bar{S}}{2T} \left(K + xK'_x + 2y(\text{ylor} + \frac{1}{2}) K'_y \right) \right) dl$$

$$\frac{\partial I}{\partial \sigma} = -I \sum_{kr} \int_l \left(\frac{S.K'_x}{\alpha_D} \right) dl - \frac{1}{I_0(\sigma)} \frac{\partial I_o(\sigma)}{\partial \sigma}$$

$$\frac{\partial I}{\partial V_l} = -I \sum_{kr} \int_l \sigma_{kr}.a_l.\bar{S} \left[-\frac{K'_x}{\alpha_D} + K.kb \left(\frac{e^{-\frac{kb.\sigma_{krl}}{T}}}{T\left(1-e^{-\frac{kb.\sigma_{krl}}{T}}\right)} - \frac{e^{-\frac{kb.\sigma_{krl}}{T_0}}}{T_0\left(1-e^{-\frac{kb.\sigma_{krl}}{T_0}}\right)} \right) \right] dl$$

These formulas are implemented in most of the spectra inversion software [MOH 96]. Uncertainties linked to inversion code are due to diagonal elements of matrix ${}^t JWJ$:

$$\text{error on } x_j = \sqrt{\frac{Z}{N-M} \left({}^t\vec{J}\vec{\vec{W}}\vec{J} \right)^{-1}} \quad \text{where } Z = \vec{E}\vec{\vec{W}}\vec{E} \text{ and N-M >> 1.}$$

In case of low noise, these uncertainties are very low and often less than 1%. Global measurement uncertainties are higher due to other error sources:

– systematic experimental errors, as for instance angle measurement between diode laser beam and flow axis;

– spectrum calibration errors (in wavelength and intensity), coming from noisy data or from oscillations of emission envelope;

– least mean square smoothing adjustment errors: for a given convergence criterion, there is not necessarily a unique value ensemble.

4.4. Applications in hypersonic

In aerodynamics, hypersonic domain corresponds to velocities higher than Mach 5. Hypersonic flow regime [AND 89] is reached when molecular dissociation reactions exist inside the gas flow: this flow may be so hot locally that plasma is created. Gas can no more be considered as a perfect gas. Usual flow properties are often modified (boundary layer, turbulence).

Hypersonic flows are found in atmospheric re-entry conditions, typically for the Earth from an altitude of 100 km (Figure 4.12).

Figure 4.12. *Examples of atmospheric re-entry trajectory, indicating high velocities and Mach numbers*

At a high Mach number, viscous effects lead to transformation of an important part of kinetic energy into internal energy, which involves a high temperature increase in the flow. As pressure gradient perpendicular to the flow is quasi-null in

the boundary layer, this temperature increase coincides with a density decrease: boundary layer thickens and may often join the tiny shock layer. High temperatures are the cause of chemical features out of equilibrium, as molecule dissociation or ionization, which creates important radiative and convective fluxes. All these effects highly depend upon velocity and on vehicle type, but they are very different from those usually found for planes flying in subsonic regime.

Ground test facilities have recently been subject to a high renewal of interest [LU 02] to dispose of high enthalpy flows, allowing us to try to understand complex phenomena involved with these very high velocity flows. Flow is generated from a gas highly compressed in a chamber and which is then strongly expanded after passing across a nozzle throat (Figure 4.13).

Figure 4.13. *Iso-enthalpy expansion principle*

4.4.1. *F4 characteristics*

The F4 wind tunnel [FRA 94] has mainly been designed to study viscous interaction effects and real gas effects with chemical kinetic, associated with high enthalpy hypersonic flows. The F4 is an arc driven blowdown facility. This calling results from the gas (air or nitrogen) heating process with a brief electric arc, which lasts a few tens of milliseconds in a closed chamber (generating chamber); this chamber is previously filled at ambient temperature at a pressure up to 20 bar which rises to several hundred bars after heating. This procedure is the opposite to a plasma generator, called long duration arc, which allows achieving quasi-continuous wind tunnels (i.e. working during several seconds and even up to several tens of minutes) where stagnation pressure is limited to a few tens of bars.

The electric arc is obtained from a pulse generator, formed by an inertia wheel, an alternator, and excitation and rectification apparatus. When the alternator is functioning as a motor, it allows launching the 15-ton wheel at 6,000 t/mn. During arc formation, which lasts approximately 20 ms, a part of kinetic wheel energy is recovered (up to 15 MJ or a power up to 160 MW). The blowdown flow is triggered after arc extinction and lasts approximately 20–400 ms. Gas is expanded into a

nozzle to have a velocity depending on initial enthalpy H_i (theoretically 5,600 m/s for $H_i \approx 20$), flows as a free jet around a model and finishes in a vacuum tank of 35 m^3. Flow establishment is only possible if initial pressure remains lower than 10 Pa in this vacuum tank. Blowdown triggering takes place after ejection of a plug installed at the nozzle throat. This Teflon plug is manufactured in order to glide across the throat when pressure and enthalpy conditions are reached inside the generator chamber. In order to avoid untimely starting, this plug is maintained by a pyrotechnic valve. The explosive charge weakens the plug and opens the valve at wanted moment after arc extinction.

In spite of high generating pressures (P_i = 500 bar), chemical and vibrational freezing rapidly occurs, approximately 25 cm downstream the nozzle throat. For lower enthalpies, as blowdowns achieved with pure nitrogen, flow is quasi-totally recombined in the throat region; only vibrational non-equilibrium remains.

Difficulties	Consequences
Brief flow duration	A few milliseconds for shock tubes and a few hundred milliseconds for arc facilities; only a few measurement points are possible with pulsed laser sources working at a few tens of hertz
Transient flows	Aerodynamic conditions rapidly change, with characteristic times of approximately 1 ms; only instantaneous values are often obtained, which prevents performing averaging of measurements that could improve a signal-to-noise ratio
Long preparation times	Optimization of an instrument during a blowdown run is impossible; several runs are required to gain expertise on an instrument
Important straylight level	Sophisticated spectral filtering techniques are necessary; a very narrow interferential filter also reduces the useful signal, which is not very intense. Stray light must be acquired in order to subtract it from data obtained when a large band is observed (rotation lines of a molecular band)
Low pressure and low density	Laser techniques perform analysis of a signal that is proportional to molecule number; low pressure or low density means a weak signal to noise ratio
High temperature	Energies are distributed over a great number of levels, which reduces the population on each excited level, thus a weaker signal-to-noise ratio
Out of equilibrium species	Effect is identical to the previous one, but with more unknowns concerning the manner population is distributed over the various energy levels, which makes data interpretation more sensitive

The F4 offers a very harsh environment to implement in situ measuring techniques. The following table summarizes the main difficulties, also found in other high enthalpy facilities (shock tube, plasmatron, etc.).

4.4.2. *Setup installed at F4*

The laser beam issued from an emitting bench crosses the gaseous medium to be studied with the use of appropriate mirrors, before measuring its intensity by a photodetector located on the opposite side of the test section (Figure 4.14). The laser emitting bench and detection system are set outside the vacuum chamber. The laser beam enters this vacuum chamber through a CaF_2 window and crosses the flow along a direction making a minimal angle with the flow axis, in order to create the largest possible Doppler shift for measuring velocities.

Figure 4.14. *Diode laser spectrometer setting in hypersonic wind-tunnel F4*

4.4.3. *Results obtained at F4 and HEG*

A simple model with two layers is generally used in high enthalpy facilities. One layer corresponds to the flow core, with a constant velocity V leading to Doppler shifted lines in the absorption spectrum. The second layer contains all gases located outside the central flow (their velocity is considered as null) presenting absorption lines as for a static gas and referred to as lines at rest position.

Examples of profiles obtained by computational fluid dynamics (CFD) calculations are shown on Figure 4.15 (three dotted line curves). These curves are presented as those seen by a laser beam crossing a flow at an angle relative to the flow axis: flow dispersion is exaggerated here, which explains the lack of symmetry relative to the flow axis. Profiles of the two-layers model are represented by black curves.

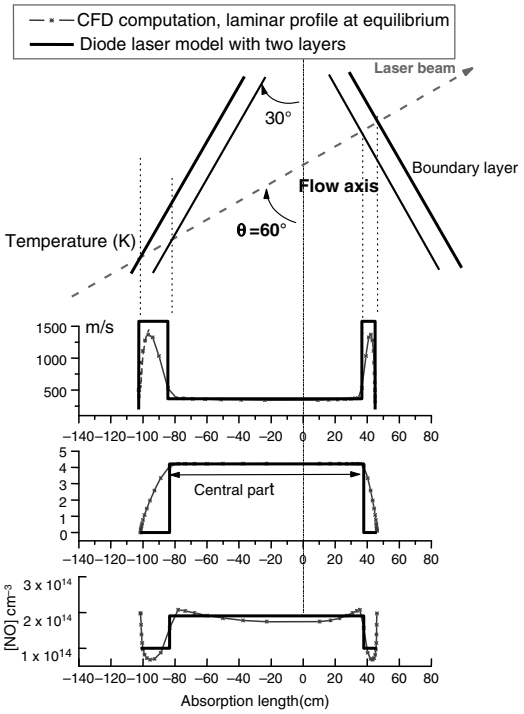

Figure 4.15. *CFD calculations for the two layers model*

Absorption spectra have been simulated using the profiles depicted in Figure 4.15 for the CFD model and the corresponding two-layers model. Figure 4.16 shows spectra obtained for a single and a doublet absorption lines for the NO molecule. Spectra issued from both models are quasi-identical; spectrum part containing line at

rest is very weak, which indicates that the boundary layer contributes not much to absorption (its thickness is rather thin and it contains a very low number of molecules).

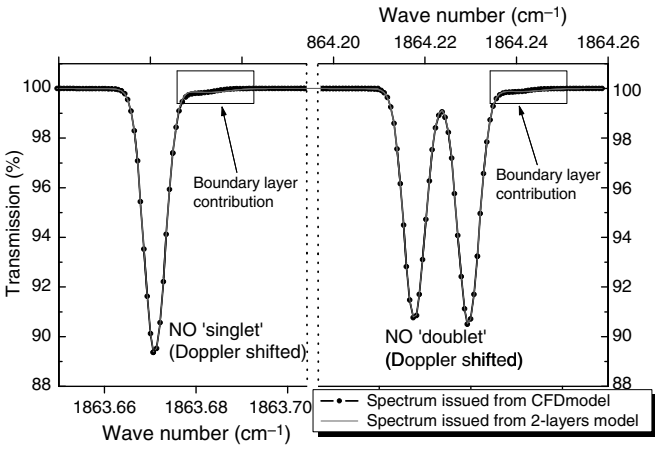

Figure 4.16. *Comparison between spectra issued from CFD profile and from two layers model (lines are shifted by the Doppler effect)*

Figure 4.17 shows a series of spectra acquired at different moments during a run; when comparing them with simulated spectra, velocity, temperature and density of NO are deduced. Figure 4.17(b) shows their temporal variations during a run: values are compared to two series of fluid mechanics numerical calculations making two assumptions [SAG 98a, SAG 98b], the one with conditions of thermodynamic equilibrium (vibration temperature is assumed to be equal to kinetic temperature) and the other with frozen conditions (vibration temperature keeps a higher value than kinetic temperature: vibration temperature remains frozen at the value it had before fluid expansion from the nozzle throat).

4.5. Other applications of diode laser absorption spectroscopy

4.5.1. *Combustion applications*

Diode laser absorption spectroscopy has been initially developed for combustion research [HIL 76, HAN 77, FAR 08, FAR 09, CHA 09, BEH 08]. Spectral region beyond 2 μm remains interesting to detect many major or minor species issued from combustion (COx, NOx, CH4, etc.). High temperatures encountered also provide more lines in the near infrared between 1 and 2 μm (Figure 4.18), which allows using non-cryogenic diode lasers, issued from developments undertaken in telecommunications. Works have also been done in the ultraviolet domain [PET 99].

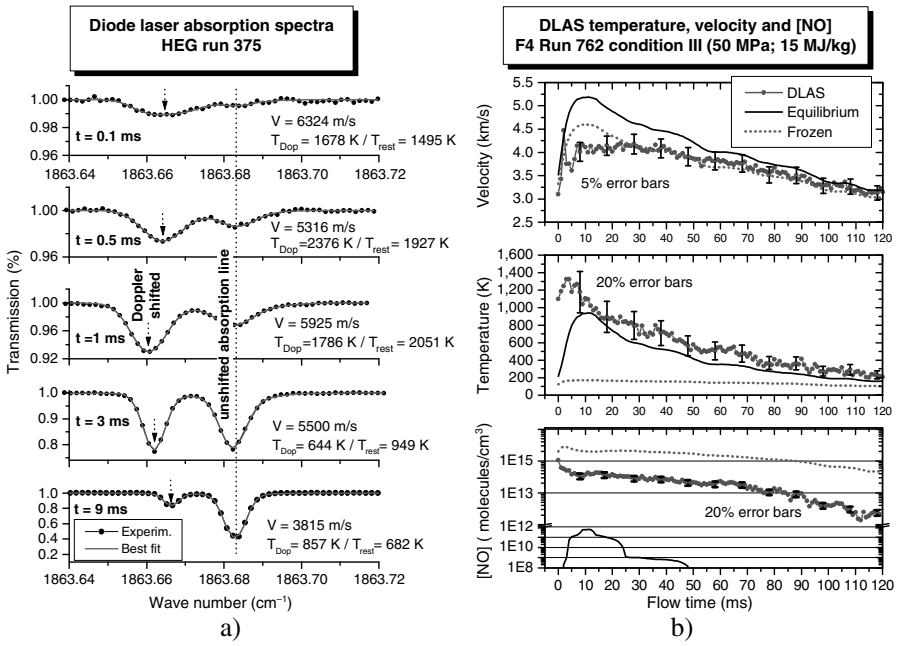

Figure 4.17. *Measurement results of diode laser absorption spectrometry in hypersonic facilities. a) Evolution of NO (R3/2) absorption [BEC 97] during a run at HEG shock tube of DLR at Göttingen, which allows deducing velocity, temperature and NO density; b) temporal evolution of velocity, temperature and concentration of NO deduced from spectra acquired at F4 [MOH 98, MOH 00]*

Figure 4.18. *Absorption line strengths in near infrared for H_2O, CO_2 and CO at 1,500 K*

a)

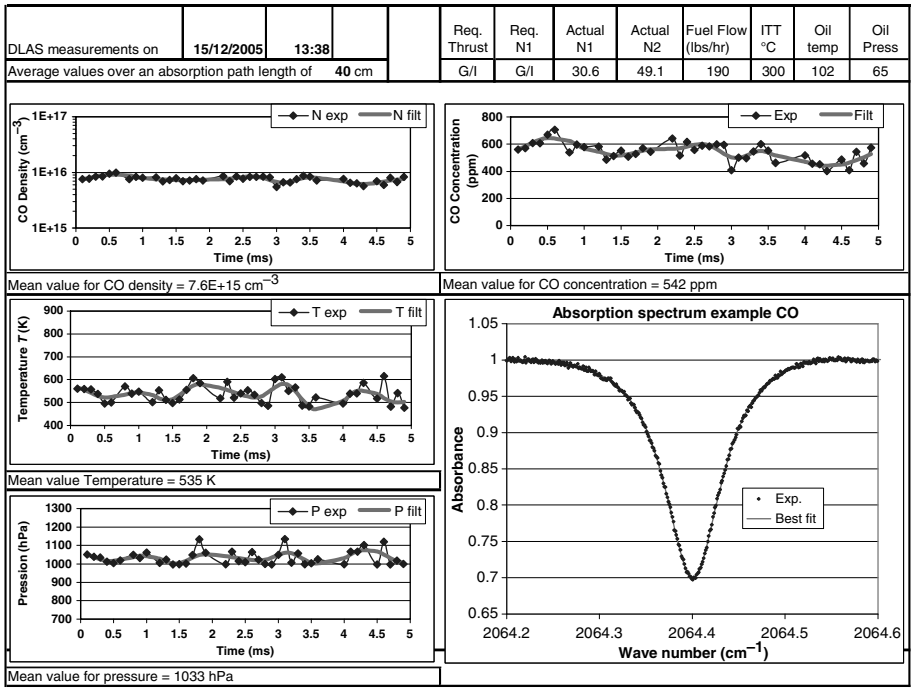

b)

Figure 4.19. *Measurements by diode laser absorption spectroscopy in the gas emission at jet engine exit of a research plane Cessna Citation II at the Amsterdam Schiphol airport. a) Setup on a research site in the airport; b) measurement examples*

This technique has also been used many times to characterize emissions of car [MCC 05] and of airplane motors in operation, in order to try to evaluate efficiency of combustion and of pollutant norms.

For instance, probing of CO and H_2O has been done at the jet engine exit of a research plane, a Cessna Citation II at Amsterdam Schiphol airport [JEN 06]. Spectrometer has been installed in a lorry located at approximately 4 m away from the measuring zone (Figure 4.19(a)): vertical line probing CO and H_2O was located 80 cm downstream of the nozzle exit. Measurements acquired at a 10-kHz rate during 6 ms are shown in Figure 4.19(b), the engine working at 30% of its maximal regime [JEN 06]. Other measurements on these same species are cited in [BER 99], [HER 06] and [HER 04].

These experiments have shown that infrared diode laser spectroscopy allowed for achieving rapid measurements with a good spatial resolution on species issued from combustion. Nevertheless, apparatus must become more robust if, in the long term, it has to replace present intrusive probes that achieve gas analyses.

4.5.2. *Applications to atmospheric probing*

Diode laser spectroscopy in the infrared is also widely used in atmospheric probing of chemical components present as traces on a large altitude range, from ground to the stratosphere, and using any type of bearing vehicle (ground vehicle, jet, stratospheric balloon). For instance, SPIRALE experiment (Spectroscopie Infra-Rouge par Absorption de Lasers Embarqués, which means “infrared absorption spectroscopy using in-flight lasers” [MOR 05]) is initially based on use of six simultaneous diode lasers and is dedicated to in situ measurement of chemical components present as traces in high atmosphere and stratosphere, up to an altitude of 35 km. Absorption of laser beams emitting in the mid infrared takes place in a Herriott cell freely open at air, between two mirrors separated by 3.5 m: the optical path is very long (up to 544 m). Flights have been achieved at different latitudes: Kiruna (Sweden, 67.5°N), Aire-sur-l'Adour (France, 43.4°N), Gap (France, 44.3°N), Teresina (Brazil, 5.08°S). Concentration vertical profiles of a dozen of species – O_3, CH_4, CO, CO_2, N_2O, HNO_3, NO_2, NO, HCl, HOCl, H_2O_2, COF_2 – are measured with a high vertical resolution (a few meters), a great sensitivity (mixing ratios > 10 pptv) and a high accuracy. Besides validation objectives, these measurements contribute to a better knowledge of the dynamics and the chemistry of the high troposphere and of the low equatorial stratosphere, the key region of atmosphere for stratospheric ozone formation, injection of water vapor, pollutants and aerosols, and for circulation at a global scale. Experiments in the low stratosphere have also been performed onboard specialized airplanes [POD 93, TOC 02].

4.6. Other devices for diode laser absorption spectroscopy

4.6.1. *Multipass spectrometry*

Cavities with multiple passages, called multipass cells, have the purpose of increasing interaction length between laser beam and medium to be probed, radiation being confined between two mirrors. Resonant optical cavities (Cavity Ring Down Spectroscopy – CRDS [OKE 88]) are different from non-resonant multipass cells (Herriott cells). The high mechanical sensitivity of a CRDS system has been pointed out when used in wind tunnel with short duration runs [DEB 05]. In fact, conditions found in F4 (vibrations, pressure) do not allow maintaining an optical cavity under these drastic resonance requirements during a run. The setup must be either more rigid, or miniaturized for better robustness. To increase detection sensitivity, multipass cells of Herriot type have been developed, because they are *a priori* less sensitive to mechanical vibrations.

These multipass cells are formed by two mirrors set facing one another, where a hole placed on each one, respectively, allows injecting and extracting radiation after a desired number N of passages (Figure 4.20).

Figure 4.20. *Principle scheme of a non-resonant multipass cell*

The application of matrix optics allows tracing trajectories followed by the laser beam when it propagates across the whole optical system. In any plane of space located inside the cell, laser impacts printed on the mirrors during multiple round trips can be predicted, and thus trajectories that have impacts on mirrors outside the holes to be perforated are found. For the F4 facility, the cylinder has a diameter of 60 cm and a cavity 1.2 m long has been achieved where light does 31 passages before extraction (Figure 4.21). Experimentally, when adjusting the mirrors (slight misalignment), a trajectory with 46 passages can be obtained with the same conditions.

Results obtained during a first measurement campaign attempting to measure molecular oxygen showed that this 46-passage system was not sensitive enough. When looking at laser impacts simulated for a system of spherical mirrors, the number of passages across the cavity is limited by the mirror size (trajectories of impacts on mirrors are elliptic in general). As early as 1963, Herriot showed that under some conditions of beam injection, circular trajectories may be formed for these impacts on mirrors. Theoretically, with mirrors of 50.8 mm diameter, 140 passages may be considered, before beams spatially overlap on themselves (Figure 4.22).

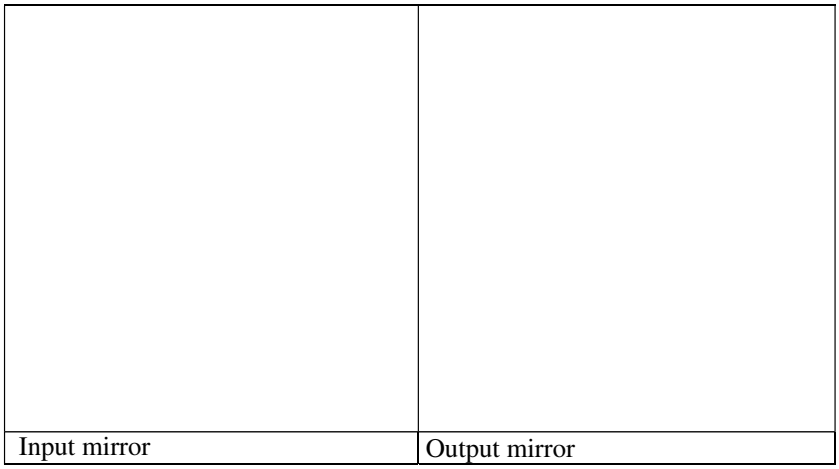

Figure 4.21. *Visualization of impacts on mirror faces. In red are presented the holes to be perforated in order to allow input and output of laser beam*

With circular systems called “re-entrant” (Figure 4.23), only one hole is used (red impact on input mirror) for mirror set, this hole having both the roles of injection and extraction. In spite of a scheme less convenient to extract beam transmitted by a cavity (as injection and extraction are done through the same hole, it is less easy to detect absorption signal), the “re-entering” system appears more efficient because it allows having several configurations with only one set of mirrors. Re-entrant cavity rules allow several cavity lengths (until (N-1)) for 2N passages; depending upon application, it is also possible to make variations in the number of passages for a given cavity length (within a few centimeter range). Experimentally, it appears that impact size decreases with the reflexion order. The last impacts are less spatially scattered than the first ones, as they transport less energy. The re-entrant order of a cavity may be increased without extracting a beam that is close to the injection/extraction hole.

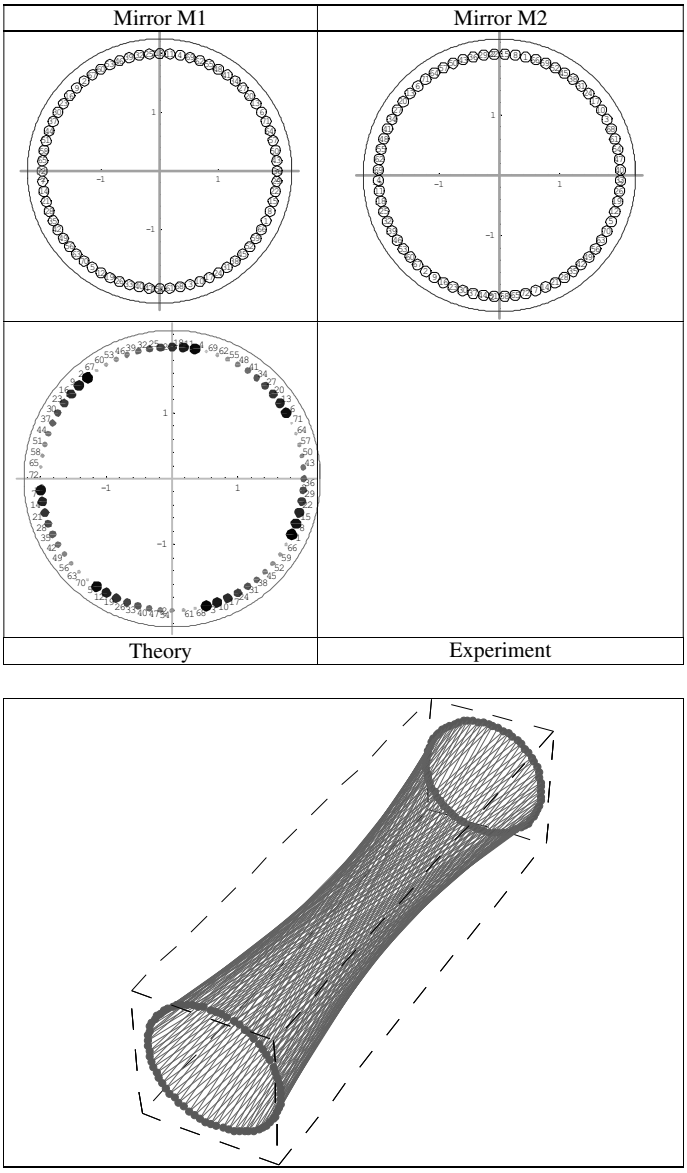

Figure 4.22. *System of 140 passages across a 121.6 cm cavity (mirrors of 50.8 mm diameter). The second line of images compares theory and experiment. Progressively, impact intensity and beam size decrease. Bottom image spatially visualizes beam trajectories*

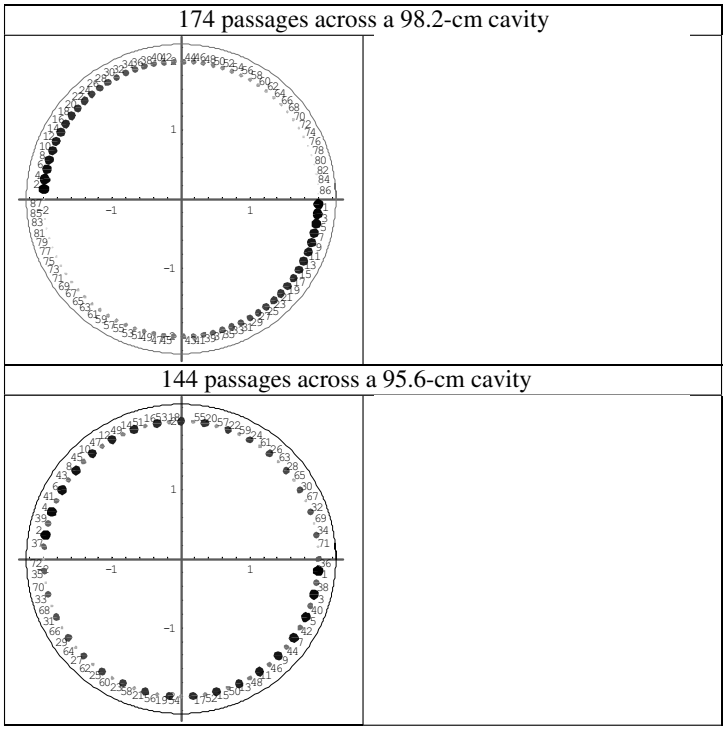

Figure 4.23. *The re-entrant system is easily adjustable. With a hole in the input mirror (place of injection and extraction), different cavities may be imagined depending upon applications (number of passages or cavity size)*

4.6.2. *Spectrometry in a resonant cavity*

This option is called cavity ring down spectroscopy (CRDS): it allows deducing species concentrations from losses occurring in an optical cavity at high fineness [DEB 05, ROM 97, HE 01, HE 04, SAL 06, VAL 10]. The ringdown cavity is created by setting two high reflecting mirrors (R > 99.99%) around the medium to be probed. The laser source is coupled to the cavity in such a way that it results in a quick increase of intensity of light trapped inside. After a sudden break of laser injection, the stored light propagates making round trips inside the cavity, but at each passage loses a small part of its intensity by transmission through the mirrors. Transmitted intensity $I(t)$ exponentially decreases from initial intensity I_0 according to equation:

$$I(t) = I_0 \exp\left(-t / \tau\right) \qquad [4.10]$$

where τ is the characteristic cavity damping time. Loss rate is given by:

$$\frac{1}{c\tau} = \frac{1-R+A}{L} + \alpha \qquad [4.11]$$

where c is light speed, L cavity length, R mirror reflexion coefficient, A losses by diffraction on mirrors and α absorption coefficient of medium. A profile drawing of losses by absorption as a function of laser frequency provides the CRDS spectrum. As the profile of absorption losses is directly proportional to the absorption line profile of chosen species, concentration of this species is thus deduced, as well as its temperature and its velocity in a gaseous flow. CRDS has been initially developed with pulsed lasers [ROM 97], but works also with continuous lasers [HE 04]. The basic principle of a CRDS setup working with a continuous laser is represented in Figure 4.24.

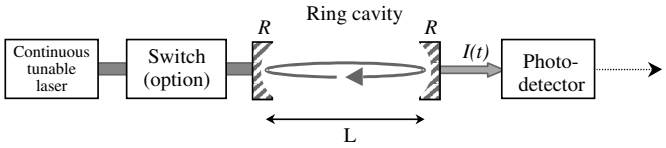

Figure 4.24. *Scheme of a ring setup that produces an exponential decay of transmitted light at the end of laser coupling. An acousto-optic or electro-optic switch is used to stop injection by a continuous laser source and prevent any other light entrance. τ_0 and τ are, respectively, characteristic time of empty cavity and of cavity filled with a gas sample*

Compared to traditional absorption methods with one or several passages, CRDS has the advantage of an effective absorption path that is very long (several kilometers); moreover, it is not sensitive to intensity fluctuations of the source. Therefore, its very high sensitivity has already been employed in many domains. Nevertheless, measuring times using a classical scheme are very long (a few seconds and up to several minutes) because the laser line and the optical shutter must be well positioned in order to obtain a clear exponential decrease inside the cavity.

Improvement in measurement acquisition velocity is therefore needed in order to accurately probe transient flows generated in hypersonic blowdown wind tunnels, with run duration lasting a few hundreds of milliseconds and initial conditions varying a few percents each millisecond. Another difficulty resides in the fact that the very low pressure level in these facilities (a few millibars) leads to absorption lines having a width ten times narrower than those found at atmospheric pressure (in combustion for instance).

With a conventional CRDS setup, rapid laser beam extinction can be obtained, without any need for a quick optical shutter: it is sufficient to use a quick sweep of either the cavity length at a fixed laser emission frequency [SAL 06], or the laser frequency relative to cavity fixed modes [VAL 10]. In both cases, energy rapidly increases inside cavity as soon as the resonance condition between laser frequency and one cavity mode is met; the exponential decay of transmitted light is observed as soon as laser frequency and cavity mode are no more resonant. The result signal is of much lower intensity than with the use of an optical shutter. In order to get an adequate signal-to-noise ratio, averaging processes must be employed which re-increase slightly acquisition time but which still remains in the ms regime. A setup made of a laser having a rapid sweep, coupled to an avalanche photodiode of low noise level, allowed reducing acquisition time to 2 ms, with an acquisition rate of 250 Hz [HE 01].

When laser frequency is swept on a static cavity of length L, the maximal frequency resolution that may be obtained corresponds to the free spectral range (FSR), which is $FSR_{\text{static}} = 1/2nL$ in cm^{-1} (with a refraction index n assumed to be equal to 1). Therefore, with cavity length of 50 cm, separation between modes is 0.01 cm^{-1}, that is 0.3 GHz. This resolution is not sufficient to probe low-pressure flows simulating high altitude re-entry phenomena because the absorption line width is approximately 0.05 cm^{-1}. The two following CRDS setups may be implemented to improve spectral resolution.

4.6.2.1. *Spectral resolution improvement by simultaneous tuning of laser and cavity*

In order to increase the number of recorded events in a given time or spectral interval, frequencies of resonance modes inside cavity (V_{mode}) must sweep along a synchronous manner in the opposite direction to laser mode sweeping (V_λ). This allows increasing the number of events where frequencies between laser and cavity are coupled; the resultant free spectral interval is smaller than the FSR of a static cavity (see Figure 4.25). Figure 4.26 shows an experimental result obtained on O_2 line at high, then low, pressure.

Spectral resolution improvement is deduced from the expression of the dynamic FSR for a cavity with moving mirrors (moving cavity) [HE 01]:

$$\text{FSR}_{\text{dynamic}} = \frac{1}{2L - 2\lambda(V_L / V_\lambda)} \qquad [4.12]$$

where V_λ and V_L are linear sweeps for, respectively, laser wavelength and cavity length tuning. Velocity for a cavity resonance mode is expressed by $V_{\text{mode}} = -\lambda V_L/L$ and must have an opposite sign to V_λ in order to improve spectral resolution.

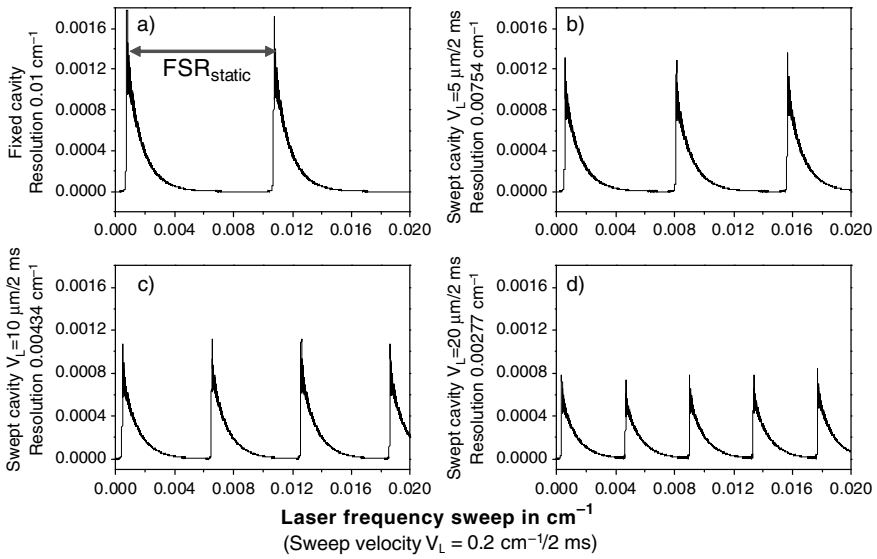

Figure 4.25. *Increased event number in a ring cavity when cavity length and laser frequency are simultaneously swept (0.4 cm^{-1} within 2 ms)*

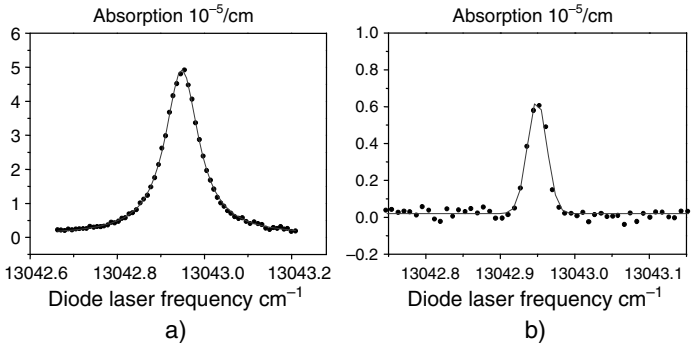

Figure 4.26. *Absorption spectrum of O_2 in air during a laser sweep at 280 Hz and a 5-µm cavity synchronous modulation (a) at atmospheric pressure: Lorentz profile of 0.095 cm^{-1} and (b) at 20 mbar: Gaussian profile of 0.025 cm^{-1}*

Figure 4.27(a) shows the influence of sweep velocity of cavity length V_L when other parameters keep fixed values (λ = 0.766 µm, L = 0.5 m, V_λ = 0.2 cm^{-1}/ms) [HE 01]. Figure 4.27(b) shows that resolution improvement increases with shorter cavities, which is favorable to miniaturize CRDS systems.

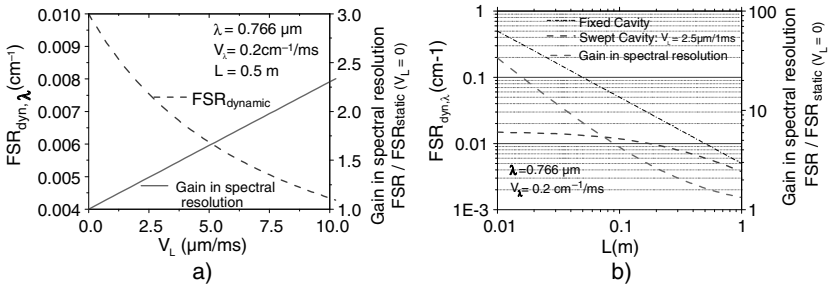

Figure 4.27. *Influence of free spectral range and improvement of spectral resolution as a function of cavity sweep velocity. a) Influence of velocity for cavity length tuning; b) influence of cavity length*

4.6.2.2. *Spectral resolution improvement when using transverse modes*

Another way to improve spectral resolution is to make use of a cavity transverse mode structure. Use of other modes may induce noisy absorption profiles because on the one hand modes may overlap and, on the other hand, each transverse mode has a distinct decay coefficient. In fact, each mode presents a different spatial figure of superposition with mirror surfaces, which do not have a very homogeneous reflection factor. These problems may be overcome by an off-axis injection (Figure 4.28). With an appropriate cavity length choice (called "magic" length), the continuous comb of TEM_{mn} cavity structure modes encountered by a plane wave is converted into a structure of modes which are fractionnally degenerated. For the "magic" length, there is a finite number N of degenerated mode families included inside a cavity free spectral interval $FSR_{on\text{-}axis}$. This N factor also defines the number of passages inside the cavity before the beam spatial superposition really induces to $FSR_{off\text{-}axis} = FSR_{on\text{-}axis}/N$, which leads to increase of the spectral sampling by a factor N. It may also be considered that cavity length is stretched by a factor N. There is no superposition between individual transverse modes and the same mirror surfaces are seen by all groups of degenerated modes; that avoids any fluctuation from mode to mode and thus allows obtaining smooth absorption profiles.

In off-axis injection (for a discrete phase value), the light beam is superposed to itself after N passages inside cavity, the apparent FSR is divided by N. As a resonance leads to one point on absorption profile, spectral resolution is therefore improved by a factor N.

4.7. Perspectives and conclusion on diode laser absorption spectroscopy

Diode laser absorption spectroscopy is nowadays a powerful tool to characterize gaseous media in various domains as aerodynamics, combustion or atmospheric

probing. This chapter has mainly described the methodology applied to high enthalpy hypersonic flow studies, because they are often very difficult to characterize. This technique is currently used and serves as a reference for velocity measurement. Nevertheless, this technique may still be largely improved; the most important points are described below.

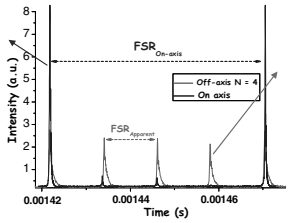

a) b)

Figure 4.28. *a) Off-axis injection principle (below is shown its on-axis spectral equivalence); b) comparison between on-axis injection along TEM_{00} mode (excitation of first transverse modes is seen on the figure) and off-axis in cavity with N = 3 and K = 1 (for same cavity size)*

4.7.1. *Laser source: use of non-cryogenic diodes*

One major advantage of diode laser absorption spectroscopy is that use of cryogenic diode lasers allows probing interesting species in the mid infrared (where their lines are the most intense) such as CO, NO, CO_2, etc. Owing to recent technological improvements, new non-cryogenic diodes, which are easier to use, are available in the range 2–3 μm [VAL 10] and will allow setting up miniature devices, as well as using several diodes for simultaneously probing different species. Different research laboratories around the world have begun using these new diodes [FAR 09, CHA 09, BEH 08, KAL 09, WEH 97]. Other types of laser sources also begin to appear that may be used in absorption spectroscopy benches (OPO, ICL, etc. [KOS 02, BEW 08, SAL 06, DÉS 04]).

4.7.2. *Spatial resolution: use of probe in flow*

One main drawback of absorption spectroscopy is the lack of spatial resolution, because measurement is integrated over the laser beam part crossing medium to be characterized. A lidar with differential absorption (DIAL) may be used: spatial resolution is obtained via the lidar temporal resolution. If this method is well suited for atmospheric probing, where a spatial resolution of approximately 100 m and up to 1 km is searched, it is presently difficult to adapt it to wind tunnels or combustion

facilities with a typical size of approximately 1 m, which requires a spatial resolution of approximately 1 cm. Difficulties come from the weak scattered lidar signal (especially at low density) and from the need for picosecond (and even femtosecond) lasers and detectors. However, recent technological advances suggest that the DIAL method can be applied to combustion studies [PAL 01].

Another way to improve spatial resolution consists of setting in the medium an optical probe linked to the emitting and receiving benches (placed away from the medium) by optical fibers. This optical probe is composed of two hollow metallic tubes allowing propagation in free space of a laser beam part. The tube extremities in front of the flow are chamfered in order to minimize disturbances due to shock waves. The velocity measurements by Doppler shift require implementation of mirrors so that the laser beam crosses the flow at an angle θ relative to the flow axis. Works relating to these experiments are shown in Figures 4.29 and 4.30 [VAL 10, WEH 97, PAL 01].

Figure 4.29. *Example of optical probe achieved with metallic tubes containing mirrors and other optical components*

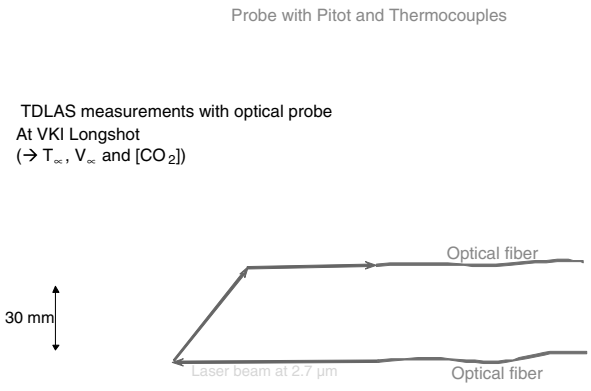

Figure 4.30. *Example of an optical probe in a CO_2 flow at Mach 15*

This type of probe clearly presents the risk of disturbing the flow; it also generates shock waves which can disturb measurements. Nevertheless, as the concept has demonstrated, miniaturization has to be optimized to diminish these disturbances, while maintaining good detection sensitivity. Use of this technique in hostile environments, such as high thermal flux flows or combustion, remains to be demonstrated.

4.7.3. *Use of frequency combs*

Femtosecond optical frquency combs [YE 05] are actually bringing a revolution in optical metrology. John L. Hall and Theodor W. Hänsch are researchers who initiated these works; they received the Nobel Prize for Physics in 2005. Such combs, produced in majority until now by femtosecond lasers, consist of very narrow laser lines (a few tens of femtoseconds), which are very stable, emitted at a 100-MHz rate and cover a very wide spectral domain.

These two last properties open new perspectives in spectroscopy, especially for the two following aspects:

– measurement rapidity (acquisition time less than 1 ms, going down until a few tens of nanoseconds and at a rate exceeding 1 kHz);

– wide spectral band (several hundreds of millimeters are covered), which will allow detecting simultaneously a great number of molecular species, as well as complete rotation–vibration bands for the study of gases in thermochemical non-equilibrium (plasma, high enthalpy gas, etc.).

This new method will thus have an important impact on the development of new optical diagnostic means to study flows (aerodynamics, combustion, pollutant measurements for environment).

4.8. Bibliography

[AND 89] ANDERSON J.D., Jr., *Hypersonic and High Temperature Gas Dynamics*, McGraw Hill Inc., New York, NY, 1989.

[ARM 67] ARMSTRONG B.H., "Spectrum line profiles: the Voigt function", *Journal of Quantitative Spectroscopy and Radiative Transfer*, vol. 7, no. 1, pp. 61–88, 1967.

[ARM 92] ARMANTE R., Inversion by solar occultation spectra recorded in the infrared, Thesis, University of Paris VI, 1992.

[ARR 94] ARROYO M.P., LANGLOIS S., HANSON R.K., "Diode laser absorption technique for simultaneous measurements of multiple gas dynamic parameters in high speed flows containing water vapor", *Applied Optics*, vol. 33, no. 15, pp. 3296–3307, 1994.

[BEC 97] BECK W.H., TRINKS O., WOLLENHAUPT M., MOHAMED A.K., NIEDERBAÜMER C., ANDRESEN P., KISHIMOTO T., BITO H., "Probing of the reservoir, free stream and shock layers in HEG using spectroscopic techniques", Paper 1350, *21st International Symposium on Shock Waves*, Great Keppel Island, Australia, 20–25 July 1997.

[BEH 08] BEHRENDT T., HASSA C., MOHAMED A.K., FALÉNI J.P., "In situ measurement and validation of gaseous species concentrations of a gas turbine model combustor by tunable diode laser absorption spectroscopy (TDLAS)", Paper GT2008-51258, *Proceedings of ASME Turbo Expo 2008*, Berlin, Germany, 9–13 June 2008.

[BER 00] BERDEN G., PEETERS R., MEIJER G., "Cavity ring-down spectroscopy: experimental schemes and applications", *International Reviews in Physical Chemistry*, vol. 19, no. 4, pp. 565–607, 2000.

[BER 99] BERKOFF T.A., WORMHOUDT J., MIAKE-LYE R.C., "Measurement of SO_2 and SO_3 using a tunable diode laser system, environmental monitoring and remediation technologies", *SPIE Conference*, Boston, vol. 3534, pp. 686–693, 1999.

[BEW 08] BEWLEY W.W., CANEDY C.L., KIM C., KIM M., NOLDE J.A., LARRABEE D.C., LINDLE J.R., VURGAFTMAN I., MEYER J.R., "Mid-infrared interband cascade lasers operating CW at thermoelectric-cooler temperatures", *Conference on Lasers and Electro-Optics/Quantum Electronics and Laser Science Conference and Photonic Applications Systems Technologies*, OSA Technical Digest (CD), Paper CTuZ3, Optical Society of America, 2008.

[CHA 09] CHAO X., JEFFRIES J.B., HANSON R.K., "Absorption sensor for CO in combustion gases using 2.3 μm tunable diode lasers", *Measurement Science and Technology*, vol. 20, no. 11, 2009.

[CHA 10] CHARACTERISTICS AND USE OF INFRARED DETECTORS, Hamamatsu Technical Note SD-12, 2010.

[DEB 05] DEBECKER I., MOHAMED A.K., ROMANINI D., "High speed cavity ringdown spectroscopy with increased spectral resolution by simultaneous laser and cavity tuning", *Optics Express*, vol. 13, no. 8, pp. 2906–2915, 2005.

[DÉS 04] DÉSORMEAUX A., LEFEBVRE M., ROSENCHER E., HUIGNARD J.P., "Mid-infrared high-resolution absorption spectroscopy by use of a semimonolithic entangled-cavity optical parametric oscillator", *Optical Letters*, vol. 29, pp. 2887–2889, 2004.

[DIC 53] DICKE R.H., "The effect of collisions upon the Doppler width of spectral lines", *Physical Review*, vol. 89, pp. 472–473, 1953.

[DRA 76] DRAYSON S.R., "Rapid computation of the Voigt profile", *Journal of Quantitative Spectroscopy and Radiative Transfer*, vol. 16, no. 7, pp. 611–614, 1976.

[FAR 08] FAROOQ A., JEFFRIES J.B., HANSON R.K., "CO_2 concentration and temperature sensor for combustion gases using diode-laser absorption near 2.7 μm", *Applied Physics B*, vol. 90, pp. 619–628, 2008.

[FAR 09] FAROOQ A., JEFFRIES J.B., HANSON R.K., "Measurements of CO_2 concentration and temperature at high pressures using 1*f*-normalized wavelength modulation spectroscopy with second harmonic detection near 2.7 μm", *Applied Optics*, vol. 48, no. 35, pp. 6740–6753, 2009.

[FRA 94] FRANÇOIS G., LEDY J.P., MASSON A., "ONERA high enthalpy wind-tunnel F4", *82nd Meeting of the Supersonic Tunnel Association*, Wright Patterson AFB, OH, 16–18 October 1994.

[GAL 61] GALATRY L., "Simultaneous effect of Doppler and foreign gas broadening on spectral lines", *Physical Review*, vol. 122, no. 4, pp. 1218–1223, 1961.

[HAN 77] HANSON R.K., KUNTZ P.A., KRUGER C.H., "High-resolution spectroscopy of combustion gases using a tunable IR diode laser", *Applied Optics*, vol. 16, pp. 2045–2048, 1977.

[HE 01] HE Y., ORR B.J., "Optical heterodyne signal generation and detection in cavity ringdown spectroscopy based on a rapidly swept cavity", *Chemical Physics Letters*, vol. 335, pp. 215–220, 2001.

[HE 04] HE Y., ORR B.J., "Rapid measurement of cavity ringdown absorption spectra with a swept-frequency laser", *Applied Physics B*, vol. 79, pp. 941–945, 2004.

[HEC 99] HECHT J., *The Laser Guidebook*, 2nd ed., McGraw-Hill Professional, New York, 1999.

[HER 04] HERNDON S.C., SHORTER J.H., ZAHNISER M.S., NELSON D.D., Jr., JAYNE J., BROWN R.C., MIAKE-LYE R.C., WAITZ I., SILVA P., LANNI T., DEMERJIAN K., KOLB C.E., "NO and NO_2 emission ratios measured from in-use commercial aircraft during taxi and takeoff", *Environmental Science and Technology*, vol. 38, no. 22, pp. 6078–6084, 2004.

[HER 06] HERNDON S.C., ROGERS T., DUNLEA E.J., JAYNE J.T., MIAKE-LYE R.C., KNIGHTON B., "Hydrocarbon emissions from in-use commercial aircraft during airport operations", *Environmental Science and Technology*, vol. 40, no. 14, pp. 4406–4413, 2006.

[HIL 76] HILL J.C., MONTGOMERY G.P., "Diode lasers for gas analysis", *Applied Optics*, vol. 15, no. 3, pp. 748–755, 1976.

[HUI 78] HUI A.K., ARMSTRONG B.H., WRAY A.A., "Rapid computation of the Voigt and complex error functions", *Journal of Quantitative Spectroscopy and Radiative Transfer*, vol. 19, no. 5, pp. 509–516, 1978.

[INF] INFRARED DIODE LASERS, Lead Salt Technology, LASER COMPONENTS technical note.

[JEN 06] JENTINK H.W., VEERMAN H.P.J., MOHAMED A.K., GEISER P., Spectroscopic measurements of aircraft exhaust gas, MENELAS Report D 12, National Aerospace Laboratory NLR Report NLR-CR-2006-100, 2006.

[KAL 09] KALDVEE B., EHN A., BOOD J., ALDÉN M., "Development of a picosecond lidar system for large-scale combustion diagnostics", *Applied Optics*, vol. 48, no. 4, pp. B65–B72, 2009.

[KOS 02] KOSTEREV A.A., TITTEL F.K., "Chemical sensors based on quantum cascade lasers", *IEEE Journal of Quantum Electronics*, vol. 38, no. 6, pp. 582–591, 2002.

[LU 02] LU F.K., MARREN D.E. (eds), *Advanced Hypersonic Test Facilities*, American Institute of Aeronautics and Astronautics Inc., 2002.

[MCC 05] MCCULLOCH M.T., LANGFORD N., DUXBURY G., "Real-time trace-level detection of carbon dioxide and ethylene in car exhaust gases", *Applied Optics*, vol. 44, pp. 2887–2894, 2005.

[MOH 95] MOHAMED A.K., ROSIER B., HENRY D., LOUVET Y., VARGHESE P.L., Tunable diode laser measurements on nitric oxide in a hypersonic wind tunnel, AIAA Paper 95-0428, 1995.

[MOH 96] MOHAMED A.K., MSTP Phase 2 Progress Report, infrared diode laser absorption spectroscopy in wind tunnels, I-Experimental Setup, II-Data Reduction Procedures (ESA -HT-TN-E34-701&702&703-ONER), ONERA Technical Report nos. 8 and 9 /7301 PY, 1996.

[MOH 98] MOHAMED A.K., ROSIER B., SAGNIER P., HENRY D., LOUVET Y., BIZE D., "Application of infrared diode laser absorption spectroscopy to the F4 high enthalpy wind tunnel", *Aerospace Science and Technology*, vol. 2, no. 4, pp. 241–250, 1998.

[MOH 99] MOHAMED A.K., HENRY D., FALÉNI J.P., SAGNIER P., MASSON A., BECK W., "Infrared diode laser absorption spectroscopy measurements in the S4MA, F4 and HEG hypersonic flows", *International Symposium on Atmospheric Re-entry Vehicles and Systems*, Arcachon, France, 16–18 March 1999.

[MOH 00] MOHAMED A.K., VÉRANT J.L., SOUTADÉ J., VIGUIER P., VAN OOTEGEM B., TRAN P., "Mid-infrared diode laser absorption spectroscopy measurements in CO-CO_2 hypersonic flows of F4 and SIMOUN", *6th European Symposium on Aerothermodynamics for Space Vehicles*, Versailles, France, 3–5 November 2000.

[MOR 05] MOREAU G., ROBERT C., CATOIRE V., CHARTIER V.M., CAMY-PEYRET C., HURET N., PIRRE M., POMATHIOD L., CHALUMEAU G., "SPIRALE: a multispecies in situ balloon borne instrument with six tunable diode laser spectrometers", *Applied Optics*, vol. 44, pp. 5972–5989, 2005.

[NAG 98] NAGALI V., Diode laser study of high-pressure water-vapor spectroscopy, PhD Dissertation, Stanford University, Stanford, CA, 1998.

[OKE 88] O'KEEFE A., DEACON D.A., "Cavity ringdown optical spectrometer for absorption measurements using pulsed laser sources", *Review of Scientific Instruments*, vol. 59, pp. 2544–2551, 1988.

[PAL 01] PALMA P., BECK W., Diode-laser absorption spectroscopy of rubidium in hypersonic flows, DLR Report No. DLR-IB 223-01 A13, p. 86, 2001.

[PET 99] PETERSON K.A., OH D.B., "High-sensitivity detection of CH radicals in flames by use of a diode laser-based near-ultraviolet light source", *Optical Letters*, vol. 24, pp. 667–669, 1999.

[POD 93] PODOLSKE J., LOEWENSTEIN M., "Airborne tunable diode laser spectrometer for trace-gas measurement in the lower stratosphere", *Applied Optics*, vol. 32, no. 27, pp. 5324–5333, 1993.

[ROM 97] ROMANINI D., KACHANOV A.A., SADEGHI N., STOECKEL F., "CW cavity ring down spectroscopy", *Chemical Physics Letters*, vol. 264, pp. 316–322, 1997.

[ROS 88] ROSIER B., HENRY D., COPALLE A., "Carbon monoxide concentrations and temperature measurements in a low pressure CH4-O2-NH3 flame", *Applied Optics*, vol. 27, no. 2, pp. 360–364, 1988.

[ROT 09] ROTHMAN L.S., GORDON I.E., BARBE A., BENNER D., BERNATH P.F., BIRK M., BOUDON V., BROWN L.R., CAMPARGUE A., CHAMPION J.P., CHANCE K., COUDERT L.H., DANA V., DEVI V.M., FALLY S., FLAUD J.M., GAMACHE R.R., GOLDMAN A., JACQUEMART D., Kleiner I., "The HITRAN 2008 molecular spectroscopic database", *Journal of Quantitative Spectroscopy and Radiative Transfer*, vol. 110, no. 9–10, pp. 533–572, 2009.

[SAG 98a] SAGNIER P., VÉRANT J.L., "Flow characterization in the ONERA F4 high enthalpy wind tunnel", *AIAA Journal*, vol. 36, no. 4, pp. 522–531, 1998.

[SAG 98b] SAGNIER P., VÉRANT J.L., "On the validation of high enthalpy wind tunnel simulations", *Aerospace Science and Technology*, vol. 2, no. 7, pp. 425–437, 1998.

[SAL 06] SALHI A., BARAT D., ROMANINI D., ROUILLARD Y., OUVRARD A., WERNER R., SEUFERT J., KOETH J., VICET A., GARNACHE A., "Single-frequency Sb-based distributed-feedback lasers emitting at 2.3 μm above room temperature for application in tunable diode laser absorption spectroscopy", *Applied Optics*, vol. 45, pp. 4957–4965, 2006.

[SCH 92] SCHREIER F., "The Voigt and complex error function: a comparison of computational methods", *Journal of Quantitative Spectroscopy and Radiative Transfer*, vol. 48, no. 5/6, pp. 743–762, 1992.

[TAU 88] TAUPIN D., *Probabilities, Data Reduction and Error Analysis in the Physical Sciences*, Chapter VI, Les Editions de Physique, Les Ulis, France, 1988.

[TOC 02] TOCI G., MAZZINGHI P., MIELKE B., STEFANUTTI L., "An airborne diode laser spectrometer for the simultaneous measurement of H_2O and HNO_3 content of stratospheric cirrus clouds", *Optics and Lasers in Engineering*, vol. 37, pp. 459–480, 2002.

[VAL 10] VALLON R., MOHAMED A.K., SOUTADÉ J., PARIS S., MEYERS J., "Hypersonic flows probing with a compact absorption spectrometer monitoring CO_2 at 2.7 μm", *48th AIAA Aerospace Sciences Meeting*, AIAA Paper 2010-304, 4–7 January 2010.

[WEH 97] WEHE S.D., BAER D.S, HANSON R.K., "Tunable diode-laser absorption measurements of temperature, velocity, and H_2O in hypervelocity flows", *33rd AIAA/ ASME/SAE/ASEE Joint Propulsion Conference and Exhibit*, AIAA Paper 97-3267, Seattle, 6–9 July 1997.

[WOL 07] WOLFE W.L., ZISSIS G.J., The Infrared Handbook, Infrared Information and Analysis Centre, Environmental Research Institute of Michigan, for the Office of Naval Research, Department of the Navy, 2007.

[YE 05] YE J., CUNDIFF S.T., *Femtosecond Optical Frequency Comb: Principle, Operation and Applications*, Springer, New York, NY, 2005.

Chapter 5

Nonlinear Optical Sources and Techniques for Optical Diagnostic

5.1. Introduction to nonlinear optics

Nonlinear optics was developed just after the laser was invented. Indeed, the laser was the first source delivering light with a degree of spatial and temporal coherence that was high enough to reach a lighting level capable of modifying optical properties of illuminated medium. Hence, the second harmonic generation was the first experiment in nonlinear optics (frequency doubling): it was achieved by Franken [FRA 61], less than one year after Maiman invented the ruby laser.

Nonlinear effects appear as soon as the electrical field of an externally applied radiation cannot be considered as a small perturbation of the internal atomic field so the medium optical response is deeply modified by the presence of external optical fields. Under such conditions, the response of an illuminated medium deviates from a linear function of light intensity, so that it becomes necessary to take into account perturbations of the medium induced by the applied optical fields. Interpretation of phenomena observed in this illumination regime cannot simply be done by separately considering light propagation and optical properties of the illuminated medium, as is usually done in linear optics. From a mathematical point of view, a nonlinear contribution $\vec{P}_{NL}(\vec{r},t)$ has to be introduced into the medium optical polarization:

$$\vec{P}(\vec{r},t)=\vec{P}_{L}(\vec{r},t)+\vec{P}_{NL}(\vec{r},t) \qquad [5.1]$$

Chapter written by Michel LEFEBVRE.

where $\vec{P}_L(\vec{r},t)$ is the usual linear polarization generated by the different optical fields applied at position $\vec{r}$ and at time *t*. Introducing the nonlinear polarization in Maxwell's equations leads us to take into account the coupling between the light and the medium through the wave equation. Assuming a lossless non-magnetic medium, we get:

$$\Delta\vec{E}(\vec{r},t) - \varepsilon_0\mu_0 \frac{\partial^2 \vec{E}(\vec{r},t)}{\partial t^2} = \mu_0 \frac{\partial^2 \vec{P}(\vec{r},t)}{\partial t^2} \qquad [5.2]$$

where $\vec{E}(\vec{r},t)$ is the total electrical field that accounts for all the radiations applied to the medium, ε_0 and μ_0 are respectively the electric and magnetic permittivity in free space. In equation [5.2], the left hand is related to the propagation of optical fields in vacuum, whereas the right hand represents for the response of the medium through the total polarization. Given that polarization is directly connected to the displacement of electronic charges induced by electrical fields, the second derivative of $\vec{P}(\vec{r},t)$ in [5.2] is related to the acceleration motion of the electronic charges that appears in the wave equation as a source term of radiation (Larmor's law). Therefore, the presence of quadratic terms $\left(P_{NL}(\vec{r},t) \propto \vec{E}\vec{E}\right)$ or higher order terms in the polarization leads to the generation of radiation at new frequencies (second harmonic or other frequency values) that are not pre-existing in the input frequencies: this is the first illustration of the nonlinear response of the medium.

A comprehensive study of various effects in nonlinear optics needs to detail the nonlinear part of the polarization so as to find the solutions of the wave equation; these two complementary aspects have to be considered in nonlinear optics. Basically, the determination of the nonlinear polarization requires us to take into account the quantum nature of the interaction between the applied fields and the material system; however, a semi-classical approach taking into account only the quantum properties of the material is usually relevant providing that the intensity of the external fields is high enough so as to be considered as classical variables. We will see further in this chapter that simple mechanical models can be used to specify the physical meaning of the nonlinear response of the illuminated medium.

5.2. Main processes in nonlinear optics

The main nonlinear optical processes are commonly classified according to the successive orders of interaction between the electrical field and the material system. Indeed, the total polarization is expanded in increasing orders of the electric field:

$$\vec{P}(\vec{r},t) = \varepsilon_0 \chi^{(1)} \vec{E} + \varepsilon_0 \chi^{(2)} \vec{E}\vec{E} + \varepsilon_0 \chi^{(3)} \vec{E}\vec{E}\vec{E} + \ldots \quad [5.3]$$

where $\chi^{(i)}$ is the *i*th order susceptibility term, which is a $i + 1$ rank tensor, from a general point of view. The linear contribution of the polarization is related to the first order of development, while higher order terms account for the second, third, etc., nonlinear contributions according to the successive order of powers of the applied field(s).

Before focusing our discussion on second- and third-order nonlinear contributions, let us remember the physical processes involved in the linear susceptibility $\chi^{(1)}$ because such processes play an important role in: (1) the conditions of propagation of all the connected fields and (2) the efficiency of nonlinear processes.

5.2.1. *Propagation effects*

From a general point of view, the linear susceptibility $\chi^{(1)}$ accounts for the propagation of optical fields through anisotropic media. For non-absorbing media, the second-order tensor $\chi^{(1)}$ is written as a 3 × 3 symmetric matrix containing only real components. This matrix is made diagonal in a Cartesian frame $(\vec{X}, \vec{Y}, \vec{Z})$, where directions *X, Y* and *Z* are known as the main axes:

$$\chi^{(1)} = \begin{bmatrix} \chi^{(1)}_{XX} & 0 & 0 \\ 0 & \chi^{(1)}_{YY} & 0 \\ 0 & 0 & \chi^{(1)}_{ZZ} \end{bmatrix} \quad [5.4]$$

Depending on whether the diagonal matrix contains two or three different elements, we will respectively distinguish uniaxial ($\chi^{(1)}_{XX} = \chi^{(1)}_{YY} \neq \chi^{(1)}_{ZZ}$) or biaxial ($\chi^{(1)}_{XX} \neq \chi^{(1)}_{YY} \neq \chi^{(1)}_{ZZ}$) media. Uniaxial media features one particular direction called the optical axis, along which optical field propagation does not vary with polarization direction, as is the case for an isotropic medium. On the other hand, two optical axes have to be considered for biaxial media as a consequence of a lower degree of symmetry.

Conditions of wave propagation are obtained from equation [5.2] where only the linear part of polarization has to be considered. Finding solutions of this equation is commonly achieved by taking a Fourier development, assuming plane waves as particular solutions in the first order of development. Such particular solutions are

a function of harmonics terms that can be written in complex notation as $\exp i\left(\vec{k}.\vec{r}-\omega t\right)$, where $\vec{k}$ and ω are respectively the wave vector and the angular frequency of the plane wave, with:

$$\left|\vec{k}(\omega)\right| = n(\omega)\,\omega / c \qquad [5.5]$$

$n(\omega)$ is the refraction index seen by the wave propagating in $\vec{k}$ direction and c is the light velocity. In the case of an anisotropic medium, we have to consider the tensor of the refraction indexes, which relies on the linear susceptibility tensor, according to:

$$n^2(\omega) = 1 + \chi^{(1)}(\omega) \qquad [5.6]$$

where the explicit dependence of the susceptibility is written, versus the angular frequency in order to introduce the optical medium dispersion. According to expression [5.6], the tensor of the refraction indexes can also be expressed as a diagonal matrix in the $(\vec{X}, \vec{Y}, \vec{Z})$ Cartesian frame. For a uniaxial medium, the two identical elements on the diagonal are called the ordinary optical index whereas the third element is related to the extraordinary index.

Looking for plane wave solutions in equation [5.2] leads to the Fresnel equation [BLO 77] that gives the dependence of the refraction index versus the propagation direction of the plane wave; using the Euler angles (θ, ϕ) ((θ, ϕ) angles are defined with respect to (z, x) axes, in Cartesian coordinates), we obtain:

$$\frac{\sin^2\theta\cos^2\phi}{\frac{1}{n^2}-\frac{1}{n_{XX}^2}} + \frac{\sin^2\theta\sin^2\phi}{\frac{1}{n^2}-\frac{1}{n_{YY}^2}} + \frac{\cos^2\theta}{\frac{1}{n^2}-\frac{1}{n_{ZZ}^2}} = 0 \qquad [5.7]$$

where $n_{ii}^2 = 1 + \chi_{ii}^{(1)}$. Given that equation [5.7] admits two solutions $n_{+,-}(\theta,\phi)$, it appears that two plane waves can propagate through an anisotropic medium. These two waves are linearly polarized along orthogonal directions with different phase velocities according to $V_{\Phi\,+,-} = n_{+,-}/c$ where the refraction index $n_{+,-}(\theta,\phi)$ depends on the polarization direction. We will see further that the phase velocity mismatch between both waves plays an important role in the conversion efficiency of nonlinear processes.

In addition to the phase velocity mismatch, the group velocity can play an important role in the conversion efficiency of nonlinear processes. In dispersive media, the influence of the group velocity is pointed out by developing the wave vector modulus around the central frequency ω_0 of the considered wave:

$$\left|\vec{k}(\omega)\right| = k(\omega_0) + \left(\frac{\partial k}{\partial \omega}\right)_{\omega_0}(\omega-\omega_0) + \frac{1}{2}\left(\frac{\partial^2 k}{\partial \omega^2}\right)_{\omega_0}(\omega-\omega_0)^2 + \ldots \qquad [5.8]$$

where the group velocity is given by $1/V_G = \left(\partial k/\partial\omega\right)_{\omega_0}$ whereas the second derivative $\left(\partial^2 k/\partial\omega^2\right)_{\omega_0}$ stands for the group velocity dispersion around the central frequency ω_0. At this stage, let us simply note that mixing waves with different group velocities can lead to a reduction of the time overlap between interacting waves, and thus to a lower efficiency of the nonlinear wave mixing process.

Besides the phase and group velocity dispersions, the propagation of the electromagnetic field energy (beam direction) has also to be considered in order to determine the efficiency of nonlinear processes. Indeed, for an anisotropic medium, the propagation of light energy is generally not aligned with the wave vector direction. For illustration, Figure 5.1 shows the orientation of the components of the electromagnetic field within an isotropic or anisotropic medium as well as the direction of the linear part of the displacement field $\vec{D} = \varepsilon_0\left[1+\chi^{(1)}\right]\vec{E}$. In the first case, the displacement and field vectors are colinear whereas in the second case their directions are separated by an angle ρ, called the walk-off angle; thus, for an anisotropic medium, it is seen that the electromagnetic field energy, given by the Pointing's vector $\vec{S} = \vec{E}\times\vec{B}/\mu_0$, where $\vec{B}$ is the magnetic induction, does not propagate along the wave vector $\vec{k}$. This kind of propagation, which has to be considered in birefringent media, can be detrimental for nonlinear wave mixing processes given that the beam separation leads to a lower efficiency.

In general, the propagation effects discussed above have to be taken into account in anisotropic media. Conveniently, here we consider single crystal materials for which efficient nonlinear processes can be performed; such single crystals will be referred to below as nonlinear crystals. In crystal physics, the group theory is used to classify all crystals in terms of 32 classes of symmetry; from these, we can extract three optical classes: they are named isotropic, uniaxial and biaxial. Let us note that the main axes $(\vec{X},\vec{Y},\vec{Z})$ and the crystallographic axes $\left(\vec{a},\vec{b},\vec{c}\right)$ are generally

different; furthermore, the crystallographic frame is not necessarily orthogonal. The isotropic crystals belong to the cubic crystal system, with $\left(\chi_{XX}^{(1)} = \chi_{YY}^{(1)} = \chi_{ZZ}^{(1)}\right)$.

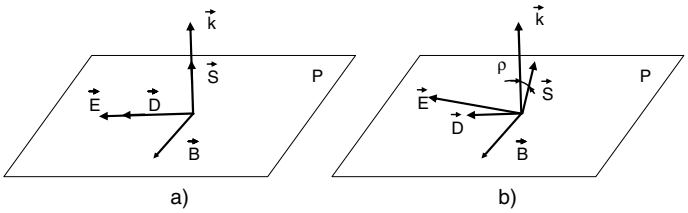

Figure 5.1. *Propagation of an electromagnetic field through an a) isotropic and b) anisotropic medium*

In conclusion, propagation effects play an important role in nonlinear optics; there may also be a combination of two functionalities, that is laser and nonlinear conversion, within the same material by doping the crystal with trivalent-rare-earth ions (Nd^{3+}, Er^{3+}, Gd^{3+}, Yb^{3+}, etc.). Under such conditions, we have to consider the presence of absorption and emission bands in the nonlinear crystal; consequently, the elements of the $\chi^{(1)}$ tensor become complex quantities, with potentially real and complex parts, showing a different spatial symmetry.

5.2.2. *Second- and third-order nonlinearities*

Equations [5.2] and [5.3] are appropriate to introduce the existence of new components in the nonlinear medium response producing waves at frequencies that are not existing in the applied radiation. However, such a mathematical treatment does not provide an explanation about the physical process that is involved in the generation of these new frequencies. For that, we need to express in detail all the terms $\chi^{(i)}$ involved in the expansion of the susceptibility; in general, such a calculation leads to rather heavy developments. Indeed, for a single crystal, we have to compute the tensor elements $\chi^{(i)}$ for $i \geq 2$ along the directions of polarization of the input field(s). For a gas, these elements have to be determined by taking into account the different contributions of the molecules due to their random orientation. Fortunately, from considerations of symmetry, the number of elements that have to be computed can be noticeably reduced. Indeed, we can demonstrate that second-order nonlinearities can only take place in a non-center-symmetric media, whereas third-order nonlinearities can be produced whatever the symmetry properties of the medium, especially in gases (being invariant by inversion symmetry) for which second-order processes are not possible.

To clarify the physical processes involved in second- or third-order nonlinearities, a simple approach based on the Lorentz's model can be used to describe the atom-field coupling in a dielectric medium; the Drude's model can be used for light interaction with free electrons in a conductive material. The Lorentz model assimilates the atom to an harmonic oscillator in which the external electron is linked to the nucleus by a restoring force $\vec{F}$ that is proportional to its displacement (x) relative to its equilibrium position:

$$\vec{F} = -\text{grad}U(x) \text{ with } U(x) = \frac{1}{2} m\omega_0^2 x^2 \quad [5.9]$$

$U(x)$ is the harmonic potential due to the restoring force between the nucleus and the electron of mass m, $\omega_0 = \sqrt{e/m}$ where e is an electron charge. Dynamic equation resolution shows that the electron oscillates at a resonant frequency $\omega_0/2\pi$ around its equilibrium position.

When an external oscillating field at angular frequency ω is applied, different situations must be considered depending upon field intensity. If the intensity is weak compared to the atom's internal field, the electron oscillates around its equilibrium position at the frequency ω of the applied field: $x = x_0 \exp i\omega t$, where x_0 depends on field intensity and on frequency deviation from resonance $(\omega - \omega_0)$. It is the usual case when the regime is linear: the medium polarization, given by $P_L(t) = -\text{Nex}(t)$, oscillates at the external field frequency (N is the atom number contributing to medium polarization). When applied field intensity is no more negligible relative to the internal field, an electron strongly goes away from its equilibrium position, in such a way that the restoring force is no longer proportional to the electron displacement. The movement is then anharmonic and may be described considering an-harmonicity corrective terms inside the $U(x)$ electron–nucleus interaction potential. Expressions [5.10] and [5.11] provide corresponding potentials, assuming a medium that respectively is non-center-symmetric or center-symmetric [BOY 92].

$$U(x) = \frac{1}{2} m\omega_0^2 x^2 + \frac{1}{3} m\alpha x^3 \quad [5.10]$$

$$U(x) = \frac{1}{2} m\omega_0^2 x^2 + \frac{1}{3} m\beta x^4 \quad [5.11]$$

Constants α and β are introduced in order to comply with the $U(x)$ potential deformation relative to harmonic potential. Figure 5.2 illustrates potential curve deformation along medium symmetry properties.

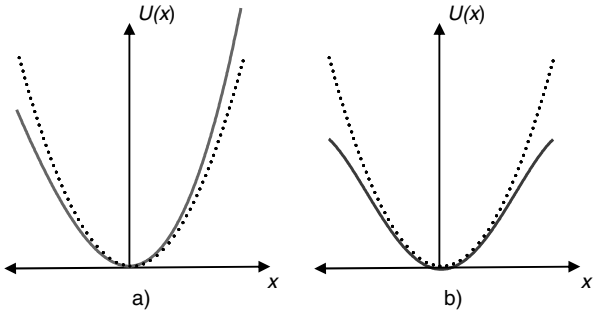

Figure 5.2. *Harmonic potential deformation: a) non-center-symmetric medium, b) center-symmetric medium; parabola (dotted line) represents harmonic potential*

To know the medium response to an external field of frequency ω, as before, the equation of dynamics must be solved, taking into account the $U(x)$ potential curves provided above. A general solution does not exist for any shape or intensity of the applied field; it is the reason why a process is undertaken using a resolution with perturbations, a function of various applied field orders. It is shown that:

– in case (a) of Figure 5.2, x electron displacement around its equilibrium position contains terms oscillating at the external field frequency 2ω. In this case, medium polarization contains nonlinear terms at frequency 2ω, which induce production of radiation at frequency 2ω, along wave equation [5.2];

– in case (b) of Figure 5.2, x electron displacement around its equilibrium position contains terms oscillating at the external field frequency 3ω. In this case, medium polarization contains nonlinear terms at frequency 3ω, which induce production of radiation at frequency 3ω, along wave equation [5.2].

Extending this procedure, it is possible to demonstrate that radiations may be obtained having frequencies corresponding to the sum or the difference of incident field frequencies, when this incident field is composed of several frequencies.

The previous analysis, based on the Lorentz's model, shows that order 2 or 3 nonlinearities may be attributed to the anharmonic response of N independent atoms submitted to the action of a high-intensity laser field. When the lighted medium cannot be considered a collection of independent atoms, other physical processes may contribute to the nonlinear response. Therefore, in the case of a nonlinear crystal where atoms are linked together by a crystalline field to form a 3D lattice of coupled harmonic oscillators, characterized by collective vibration modes (phonons), medium polarization is modulated at the ω_v frequency of these collective vibrations. The nonlinear response will then include new waves, frequency shifted from primary radiation by a quantity equal to the frequency of these collective

vibrations (Brillouin scattering). In the case of a molecular gas, new radiations may be produced due to the polarization modulation by vibrational or rotational nuclei movements of each molecule (Raman scattering). In addition to vibrational or rotational movements, molecules may also be oriented (especially in the case of highly anisotropic molecules) or move in a field gradient (electrostriction effect), which will induce a modification of optical medium index, at the origin of optical nonlinearities. Table 5.1 illustrates the main nonlinear effects, distinguishing first and second orders; some of these effects will be studied in more detail later in this chapter.

Order	Physical process	Nonlinear term
2	Sum and difference frequencies	$\chi^{(2)}(\omega_1+\omega_2;\ \omega_1,\ \omega_2)$
	Optical rectification	$\chi^{(2)}(0;\ \omega,-\omega)$
	Parametric generation	$\chi^{(2)}(\omega_1-\omega_2;\ \omega_1,\ \omega_2)$
	Pockels effect	$\chi^{(2)}(\omega;\omega,\ 0)$
3	Third harmonic generation	$\chi^{(3)}(3\omega;\ \omega,\ \omega,\ \omega)$
	Four-wave mixing	$\chi^{(3)}(\omega_1+\omega_2\pm\omega_3;\ \omega_1,\ \omega_2,\pm\omega_3)$
	Optical Kerr effect, auto-focusing	$\chi^{(3)}(\omega;\ \omega,\ \omega,-\omega)$
	Two-photon absorption	$Im\ \chi^{(3)}(\omega;\ \omega,-\omega,\ \omega)$
	Raman, Brillouin scattering	$\chi^{(3)}(\omega\pm\omega_v;\ \omega,-\omega,\omega\pm\omega_v)$

Table 5.1. *List of main nonlinear processes (second and third order); the left value inside each bracket stands for the frequency produced by the nonlinear interaction*

Parametric processes, introduced in Table 5.1, have been initially proposed in order to explain the oscillating movement of a pendulum submitted to periodic modifications of one of its parameters. Parametric processes are characterized by the fact that they directly couple optical fields together without transferring energy toward the medium supporting these processes. Conversely, processes that go with an energy transfer toward the crossed medium (absorption, Raman or Brillouin scattering, stimulated amplification, etc.) are considered non-parametric.

In conclusion regarding these second- and third-order nonlinearities, it must be noticed that the development into successive orders of equation [5.3] assumes that the nonlinear effects created by optical fields appear as perturbations of the linear response of the lighting medium: in fact, mathematically, the development of [5.3] is that of a convergent series. There may be cases where this convergence is not ensured: it is particularly true for resonant processes of saturated absorption. Only a non-perturbation quantum treatment is relevant for explaining the medium nonlinear behavior.

5.2.3. *Phase matching notion*

As seen in the previous section, the medium polarization is obtained by taking into account the response of a collection of N molecules or atoms, and not by considering the individual response of an atom or molecule. In order that this collective response is maximal, fields emitted by the different particles must be added in phase. This coherent addition of individual fields is obtained when a condition of phase matching is satisfied: this means that the relative phase between the different waves must be maintained during propagation through the medium in order to, on the one hand, ensure a constructive interference between waves and, on the other hand, maintain the energy transfer direction between waves. The efficiency of frequency conversion processes (doubling, tripling, etc.) can be high only if the phase matching condition is satisfied. This condition is expressed as a function of wave vectors $\vec{k}_i$ of the various radiations coupled by nonlinear interaction and it is interpreted as a momentum conservation, when considering photon exchange. Dependency upon wave vectors is naturally linked to the propagation conditions of the different radiations (see section 5.2.1). For instance, for the frequency doubling process ($\omega \rightarrow 2\omega$), schematized in Figure 5.3, the phase matching condition is written as:

$$\Delta\vec{k} = \vec{k}(2\omega) - 2\vec{k}(\omega) = 0 \qquad [5.12]$$

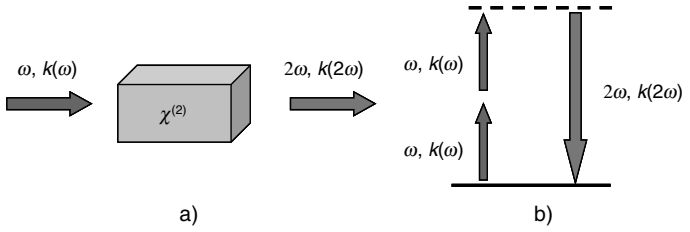

Figure 5.3. *a) Principle of frequency doubling and b) representation as a photon exchange*

In collinear geometry, equation [5.12] becomes $n(2\omega) = n(\omega)$, a condition that is impossible to satisfy in a normally dispersive medium characterized by $n(2\omega) > n(\omega)$. Yet, different approaches have been developed in order to overcome this limitation. Among the approaches, two are well mastered and spread: phase matching by birefringence and quasi-phase matching (see Figure 5.4).

The birefringence phase matching takes advantage from propagation conditions within anisotropic media. As recalled in section 5.2.1, two orthogonally polarized waves may propagate with two different indices noted $n_{+,-}(\theta,\phi)$. Thus, a couple of

indices n_+ and n_- may be found so that, for some values of θ and φ angles, the phase matching condition is verified, leading for instance to $n_-(2\omega) = n_+(\omega)$. As the doubling process is a mixing process involving three waves, where photon production at 2ω requires two incident photons at frequency ω (see Figure 5.3(b)), it results that two types of phase matching are accessible:

– phase matching of type I where the two incident waves at frequency ω have the same polarization, whereas the 2ω wave is orthogonally polarized;

– phase matching of type II that mixes two incident orthogonally polarized waves, whereas the 2ω wave is produced along the one or the other of the incident polarizations.

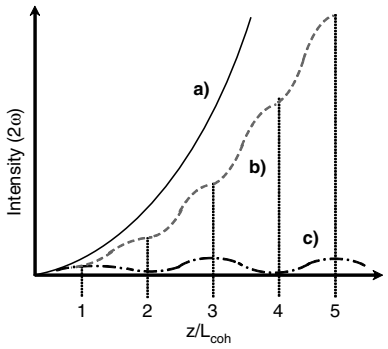

Figure 5.4. *Evolution of doubled signal intensity along phase matching type: a) by birefringence, b) by quasi-phase matching, c) out-of-phase matching. The same nonlinear coefficient has been considered in the three cases, while, in practice, the quasi-phase matching gives access to the highest nonlinear coefficients, leading to the highest conversion efficiency*

Numerous nonlinear crystals are available that allow satisfying phase matching by birefringence of type I or II: this technique is thus widely used. Yet, birefringence phase matching presents limitations if the walk-off angle ρ for double refraction becomes important enough so that beam overlapping is insufficient. Angles θ and φ that allow obtaining phase matching are generally not those which lead to the highest values of nonlinear coefficients of tensor $\chi^{(2)}$, limiting the efficiency of the nonlinear process.

The quasi-phase matching is a technique that periodically introduces a phase shift π between waves in order to compensate the phase mismatch that is progressively established when radiations propagate through the nonlinear crystal. This technique is applied to nonlinear media, either anisotropic or not. Moreover, quasi-phase matching allows choosing propagation conditions that, on one hand,

present the highest nonlinear coefficients and, on the other hand, ensure an optimal overlapping of beams due to the absence of a walk off refraction effect. Basically, a phase shift π is periodically introduced as soon as the radiation has traveled a distance equal to one coherence length L_{coh}; for frequency doubling, L_{coh} is defined by:

$$L_{coh} = \frac{\pi c}{2\omega\left(n(2\omega) - n(\omega)\right)} \qquad [5.13]$$

This technique is particularly well established for ferroelectric crystals (lithium niobate, lithium tantalate, etc.) for which the phase shift π is obtained by periodically poling the orientation of ferroelectric domains. Practically, this periodic poling is obtained by setting the crystal between two electrodes and by applying an electrical field higher than the coercive electrical field, in order to move the relative arrangement of ions that create the material ferroelectricity. Periodicity is obtained by using a periodic electrode because of photolithography. This technique allows the easy adjustment of the reversal period and, thus, the working spectral domain of the nonlinear crystal. Figure 5.5 illustrates application of quasi-phase matching technique for a lithium niobate crystal.

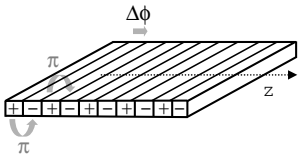

Figure 5.5. *a) Quasi-phase matching illustration b) and picture of a crystal having a dozen of reversal periods*

5.3. Nonlinear sources for optical metrology

The achievement of the first laser sources has been the starting point of various works, having led numerous research teams toward different ways in order to master in the best way, properties of coherent light produced by stimulated emission. This research area is still very active with various objectives: the extension of spectral cover, the production of ultra-short light pulses, increasing illumination level, etc. For optical metrology, producing a radiation, with frequency tunability over a wide range, appears as a major challenge for setting up techniques such as absorption, fluorescence and Raman scattering: in fact, they all require tuning the source frequency on a given transition of the analyzed medium. Infrared sources, and more especially those working inside transmission bands of the atmosphere

(1.9–2.1 μm, 3–5 μm or 8–12 μm), are particularly suitable because they allow detecting most of chemical species that present intense absorption transitions in these wavelength ranges.

Although today various laser materials are available, which allow producing a large number of wavelengths, frequency emitted by a laser is intrinsically not very tunable because it is imposed by the energy gap between the energy levels at the origin of the laser emission. Today, the most widely used tunable lasers are vibronic lasers (vibronic is a contraction of vibrational and electronic, which is used to recall that, for this type of laser, the electronic transition is broadened by phonons): Ti^{3+}:Al_2O_3, Cr^{3+}:$BeAl_2O_4$, Cr^{3+}:$LiSrAlF_6$, Cr^{2+}:ZnSe), dye lasers and quantum well or cascade lasers.

Through processes of frequency conversion, nonlinear optics appears as a very interesting approach to overcome the tuning limitation of lasers. Nonlinear techniques with a frequency shift of the input radiation (doubling as well as stimulated Raman) allow producing new discrete wavelengths starting from one primary laser while parametric generation allows reaching a very wide spectral tuning starting from a primary laser at a fixed frequency.

5.3.1. *Sum frequency generation and frequency doubling*

Frequency doubling, already introduced in section 5.2.3, is a particular case of sum-frequency generation, which is a nonlinear second-order process where two primary radiations of frequencies ω_1 and ω_2 are mixed inside a nonlinear crystal in order to obtain the sum-frequency ($\omega_3 = \omega_1 + \omega_2$). Assuming a collinear plane waves model, optical field E_j is given by:

$$E_j(z,t) = \frac{1}{2} A_j(z,t) \exp i(\omega_j t - k_j z) + cc \qquad [5.14]$$

Let us consider the potential $U(x)$ of a non-center-symmetric medium in the Lorentz's model (section 5.2.2) and assume that intensity of applied fields remains relatively low; then, the dynamic equation of the anharmonic oscillator can be solved and it can be demonstrated that, at the second order of development, the nonlinear susceptibility component, related to sum-frequency, is expressed as a function of linear susceptibility by [BOY 92, BLO 77]:

$$\chi^{(2)}(\omega_3;\omega_1,\omega_2) = \frac{\alpha m \varepsilon_0^2}{2N^2 e^3} \chi^{(1)}(\omega_3)\chi^{(1)}(\omega_1)\chi^{(1)}(\omega_2) \qquad [5.15]$$

where $\chi^{(1)}\left(\omega_j\right)$ is a complex quantity defined by:

$$\chi^{(1)}\left(\omega_j\right)=\frac{Ne^2}{m\varepsilon_0\left(\omega_0^2-\omega_j^2+2i\gamma\omega\right)} \qquad [5.16]$$

γ is the oscillator damping constant. For optical frequencies far from the resonance ($\omega_j >> \omega_0$), expressions [5.15] and [5.16] simply become:

$$\chi^{(1)}\left(\omega_j\right)=Ne^2/m\varepsilon_0\omega_0^2 \quad \text{and then} \quad \chi^{(2)}\left(\omega_3;\,\omega_1,\,\omega_2\right)=N\alpha e^3/2m\varepsilon_0\omega_0^6 \qquad [5.17]$$

Radiation intensity at ω_3 frequency is obtained by introducing the expression of the second-order nonlinear susceptibility into wave equation [5.2]. In a linear regime of low conversion rate $\left(\partial A_1/\partial z=\partial A_2/\partial z=0\right)$, solving the wave equation leads to:

$$I_3(L)=\frac{\omega_3^2\left|\chi_{\text{eff}}^{(2)}\right|^2L^2}{2\varepsilon_0c^3n_1n_2n_3}I_1I_2\frac{\sin^2\left(\Delta kL/2\right)}{\left(\Delta kL/2\right)^2} \quad \text{where} \quad I_j=\frac{n_j\varepsilon_0c}{2}A_jA_j^* \qquad [5.18]$$

Δk is the phase mismatch, n_j is refraction index at frequency ω_j, $\chi_{\text{eff}}^{(2)}$ is the component of tensor $\chi^{(2)}\left(\omega_3;\,\omega_1,\,\omega_2\right)$ for the directions of polarization and propagation (θ and φ) of the three radiations through the nonlinear crystal. Usually, a contracted notation d_{ij} of elements *i, j* of $\chi^{(2)}_{\text{eff}}$ is defined; depending upon authors, it comes: $d_{ij}=\chi^{(2)}_{\text{eff}}/2$ or $d_{ij}=\varepsilon_0\chi^{(2)}_{\text{eff}}$.

Equation [5.18] shows that the intensity of the radiation produced at sum-frequency increases in a quadratic manner with the interaction length L on a spectral width imposed by phase mismatch ΔkL.

Depending if the sum of frequencies ω_1 and ω_2 is achieved according to an exact phase matching by birefringence or a quasi-phase matching, it respectively comes:

$$\Delta k=k_3-\left(k_1+k_2\right) \text{ or } \Delta k=k_3-\left(k_1+k_2\right)+\frac{2\pi}{\Lambda_c} \qquad [5.19]$$

Practically, frequency doubling is the most widely used nonlinear process. Indeed, it allows obtaining a visible beam (532 nm) from a Nd:YAG laser at 1.06 µm. In the nanosecond regime, the doubling efficiency reaches 40–50% in most commercial systems, if the primary laser beam has a good spectral quality and is well polarized. In the continuous-wave regime, a high intensity level has to be

achieved in order to reach good conversion efficiency. It may be obtained by putting the nonlinear crystal inside the laser cavity: it is called intracavity doubling.

The crystal may also be set inside an external passive cavity whose frequency resonance is tuned on the fundamental frequency. For instance, Figure 5.6 represents such an arrangement for frequency doubling a fibered laser emitting at 1.56 µm. A ring cavity is generally chosen in order to be able to adjust the size of pump beam within the crystal that is heated in order to avoid photorefractive effects; in the chosen example, the lithium niobate crystal is used in quasi-phase matching (PPLN).

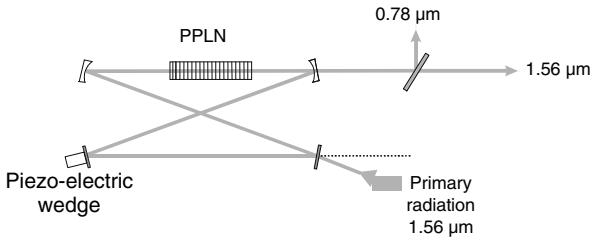

Figure 5.6. *Scheme of doubling setup inside a cavity*

5.3.2. *Raman converters*

Raman generators and lasers allow simply and efficiently producing discrete wavelengths in the visible and near infrared domains, starting from a primary radiation at shorter wavelength. This frequency conversion is based on stimulated Raman scattering that is a third-order nonlinear process.

As mentioned in section 5.2.2, collective vibrations of atoms or molecules of an illuminated medium may be at the origin of a nonlinear response. Raman conversion may be described as a physical process in which medium vibrations are considered a collection of harmonic oscillators: it uses this type of nonlinearity. Under the action of an optical field, external electrons are forced to oscillate at the applied field frequency, whereas nuclei, due to their inertia, cannot follow optical oscillation and are thus only actuated by collective vibration. Forced oscillation of electrons induces an electronic polarizibility which, due to the slower vibration movement of nuclei (adiabatic approximation), may be expanded as follows:

$$\alpha(R) = \alpha_0 + \left(\frac{\partial \alpha}{\partial R}\right)_{R_0} Q + \frac{1}{2}\left(\frac{\partial^2 \alpha}{\partial R^2}\right)_{R_0} Q^2 + \ldots \qquad [5.20]$$

where $\alpha(R)$ is the electronic polarizibility tensor, $Q = (R - R_0)$ is the normal coordinate of vibration, R_0 is the nuclei distance for equilibrium position. The medium polarization is thus given by $\vec{P}(\vec{r},t) = N\bar{\alpha}\vec{E}(\vec{r},t)$ where $\bar{\alpha}$ is the polarizibility tensor component linked to polarization directions of $\vec{E}$ and $\vec{P}$ fields, which is averaged over all orientations of N molecules contributing to the polarization.

In the harmonic oscillator approximation, Q has an oscillating movement at the Raman frequency ω_R. This vibration movement modulates the electronic polarizibility at ω_R frequency; the medium polarization thus comprises frequency components $\omega_L \pm \omega_R$ where ω_L is the optical field frequency. These modulations of the electronic polarization act as source terms in wave equation [5.2]; they then produce new radiations at frequencies ($\omega_{St} = \omega_L - \omega_R$) and ($\omega_{AS} = \omega_L + \omega_R$) called Stokes and anti-Stokes waves, respectively.

When the optical field is weak, Stokes and anti-Stokes waves are spontaneously produced in all space directions (spontaneous Raman scattering process). On the other hand, if a dense medium is illuminated (high pressure gas, liquid or solid) by a laser radiation of high intensity, Stokes and anti-Stokes waves are emitted colinearly relative to laser beam, according to a stimulated Raman scattering process. The stimulated process takes place when the mixing of laser radiation with the Stokes and anti-Stokes waves coherently drives a collective vibration of medium molecules. In such conditions, it can be shown that the Stokes wave is amplified during its propagation, whereas the anti-Stokes wave is attenuated. This behavior difference is related to the energy distribution established between the Raman medium and the various radiations when they propagate (see Figure 5.7):

– The production of a Stokes wave from laser radiation is accompanied by an energy transfer toward medium, with a Raman vibration that is reinforced; in its turn, Raman vibration acts as a source term for the Stokes wave.

– The production of an anti-Stokes wave from the laser radiation requires an additional energy, which is provided at the detriment of Raman vibration; this leads to a necessary attenuation of the anti-Stokes wave.

Nevertheless, in some specific geometric conditions, there may be a phase matching for a four-wave mixing process where the intensity of the anti-Stokes wave is progressively increasing with interaction. This type of process is detailed in section 5.4.

During its amplification, the Stokes radiation may itself be used as a pump for producing a new Stokes wave: it is thus called Stokes 2. Following a similar

approach to that introduced for the sum-frequency process, we may obtain, in the case of plane waves and in low conversion regime, the expression of nonlinear susceptibility at the Stokes wave frequency [BOY 92, ECK 88]:

$$\chi_{\text{eff}}^{(3)}(\omega_{St}) = \frac{N\Delta_{ab}}{8M} \frac{\overline{\left(\frac{\partial\alpha}{\partial R}\right)_{ab}}^{2}}{\omega_R^2 - (\omega_L - \omega_{St})^2 + 2i\gamma_{ab}(\omega_L - \omega_{St})} \qquad [5.21]$$

where Δ_{ab} is a quantum parameter that has been introduced in order to take into account the probability difference of occupation between a and b levels of Raman transition; first derivative of polarizibility is averaged over all the molecular orientations. M represents the molecules reduced mass and γ_{ab} is the oscillator damping constant, which is linked to the Raman line width in a collision regime by $\Delta\omega_R = 2\gamma_{ab}$.

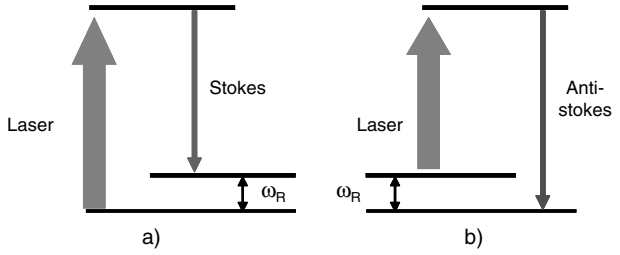

Figure 5.7. *Process scheme of a) Stokes or b) anti-Stokes scattering*

In the stationary regime (laser pulse duration >> $1/\gamma_{ab}$), intensity of the Stokes wave (I_{St}) exponentially increases according to expression [5.22]:

$$I_{St}(z) = I_{St}(0)\exp(gI_L z) \text{ with } g = \frac{2\omega_{St}\,\text{Im}\left[\chi_{\text{eff}}^{(3)}(\omega_{St})\right]}{n_{St}n_L\varepsilon_0 c^2} \qquad [5.22]$$

where I_L is laser intensity, n_L and n_{St} are refraction indices at the laser and Stokes frequencies.

For a given Raman transition, expressions [5.21] and [5.22] show that a high Raman gain is obtained if the Raman line width is narrow. Conversion rates higher than 50% may be reached, especially in picosecond regime inside crystals.

Nevertheless, the quality of the beam produced by stimulated Raman may be altered by cascade processes, especially in the case of the presence of a four-wave mixing process.

For the purpose of illustration, in Table 5.2 are indicated values of some frequency shifts that can be obtained in the most used Raman media. Conversion in gases may reach more important shifts compared to values obtained in solids, for which Raman shifts are ranging between 700 and 1,000 cm^{-1}.

Raman medium		Raman shift (cm^{-1})
Gas	H_2	4,155
	CH_4	2,916
	D_2	2,991
	N_2	2,327
Crystal	$Ba(NO_3)^2$	1,047
	$BaWO_4$	925
	$KGdWO_4$	767
		901

Table 5.2. *Raman frequencies for some media that are the most used*

The Raman medium may be set inside an optical cavity to achieve a Raman laser. Let us note that the use of an optical cavity allows improving beam quality; however, conversion rates obtained in this way are generally weaker than in single-pass geometry at one or two passages: in fact, the cavity selects an oscillation direction and thus spatially filters the Raman emission. Different configurations are possible depending if a Raman laser is placed outside or inside the cavity of primary laser (see Figure 5.8).

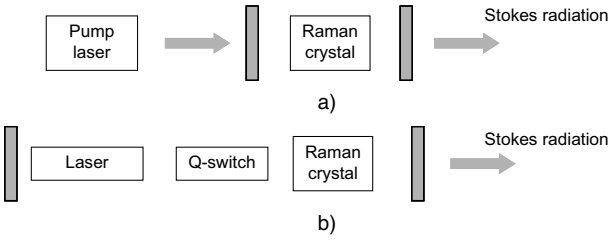

Figure 5.8. *Configurations for Raman laser: a) outside the cavity, b) inside the cavity*

The intracavity arrangement allows taking benefit of the high intensity of pump radiation; however, it assumes that the resonator dynamics must be taken into

account in the presence of two thermal lenses (laser medium and Raman medium). The intracavity setup is generally chosen to work at high rate (several kHz) where energy per pulse remains limited, the mean power being around 1 W.

5.3.3. *Optical parametric generators and oscillators*

Parametric generation is a second-order nonlinear process, where a primary laser radiation, called pump, is converted inside a non-center-symmetric crystal into two new coherent radiations called signal and idler (see Figure 5.9).

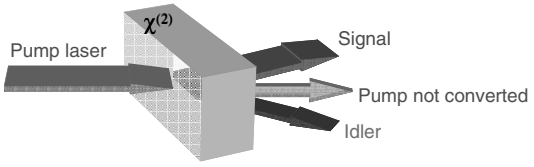

Figure 5.9. *Principle of parametric generation process*

This process of frequency conversion verifies the law of energy conservation expressed by:

$$\omega_p = \omega_s + \omega_i \text{ , or in an equivalent manner } \omega_p / 2 - \omega_i = \omega_s - \omega_p / 2 \qquad [5.23]$$

where ω_p, ω_s and ω_i are pump, signal and idler frequencies, with $\omega_s > \omega_i$ by convention.

The physical mechanism at the origin of parametric conversion is difference-frequency generation: the mixing of the pump and idler fields forces the nonlinear medium polarization to oscillate at difference-frequency ω_s and ω_i; in other words, mixing of pump and signal fields forces oscillation at the difference-frequency $(\omega_p - \omega_s)$. From equation [5.2], these oscillations of nonlinear polarization at frequencies $(\omega_p - \omega_i)$ and $(\omega_p - \omega_s)$ are at the origin of the emission of signal and idler waves at frequencies ω_s and ω_i, knowing that energy conservation law imposes that $\omega_s = \omega_p - \omega_i$ and $\omega_i = \omega_p - \omega_s$.

The propagation equations of the three waves are obtained by identifying in [5.2] polarization terms oscillating at frequencies $(\omega_p - \omega_i)$ and $(\omega_p - \omega_s)$ with fields oscillating at frequencies ω_s and ω_i. In a model of plane waves slowly varying, propagating along z, the following system of coupled equations is obtained [BOY 92, BLO 77]:

$$\begin{aligned}
&\frac{\partial A_p}{\partial z}+\frac{1}{V_{G,p}}\frac{\partial A_p}{\partial t}=\frac{i\omega_p}{2cn_p}\chi_{\text{eff}}^{(2)}A_sA_i\exp-i\Delta kz\\
&\frac{\partial A_s}{\partial z}+\frac{1}{V_{G,s}}\frac{\partial A_s}{\partial t}=\frac{i\omega_p}{2cn_s}\chi_{\text{eff}}^{(2)}A_pA_i^*\exp-i\Delta kz\\
&\frac{\partial A_i}{\partial z}+\frac{1}{V_{G,i}}\frac{\partial A_i}{\partial t}=\frac{i\omega_p}{2cn_i}\chi_{\text{eff}}^{(2)}A_pA_s^*\exp-i\Delta kz
\end{aligned} \qquad [5.24]$$

where Δk is the phase mismatch, n_i is the refraction index at wave frequency i, $V_{G,I}$ is group velocity of wave i; system [5.24] does not take into account higher order terms that are associated with group velocity dispersion. Depending if we consider a three-wave interaction under an exact birefringence phase matching or a quasi-phase matching, it will respectively come:

$$\Delta k=k_p-\left(k_s+k_i\right)\ \text{ or }\ \Delta k=k_p-\left(k_s+k_i\right)+\frac{2\pi}{\Lambda_i} \qquad [5.25]$$

Initially, the parametric conversion process is established by mixing pump photons with quantum fluctuations of the electromagnetic field at frequencies ω_s and ω_i. Progressively, in parametric conversion, the energy of the pump laser is transferred toward the signal and idler radiations. This energy redistribution between fields reinforces polarization oscillations at frequencies ($\omega_p - \omega_i$) and ($\omega_p - \omega_s$), which depend on a proportional manner of fields $A_pA_i^*$ and $A_pA_s^*$ (see equations of system [5.24]). Consequently, the efficiency process progressively increases with wave propagation inside the crystal: it is thus more parametric amplification than parametric conversion. The crystal then behaves as an amplifying medium at frequencies ω_s and ω_i.

The gain "small signal" Γ defined by considering constant pump intensity $\left(\partial I_p/\partial z=0\right)$ is given, at exact phase matching $\left(\Delta k=0\right)$ by:

$$\Gamma^2=\frac{\omega_s\omega_i\left|\chi^{(2)}\right|^2}{2n_pn_sn_i\varepsilon_0c^3}I_p\ \text{ avec }\ I_p=\frac{n_p\varepsilon_0c}{2}A_pA_p^* \qquad [5.26]$$

Resolution of equations of system [5.24] in stationary regime shows that amplification of the signal wave is given by:

$$\frac{Is(L)}{Is(0)}=\cosh^2\left(\Gamma L\right) \qquad [5.27]$$

Inside the limit of weak gain $(\Gamma L << 1)$, it becomes:

$$\frac{Is(L)}{Is(0)} \approx 1 + (\Gamma L)^2 \qquad [5.28]$$

While at high gain $(\Gamma L >> 1)$

$$\frac{Is(L)}{Is(0)} \approx (1/4)\ \exp(2\Gamma L) \qquad [5.29]$$

Conversely to the stimulated amplification process that is at the origin of laser emission, frequencies of signal and idler radiations are not imposed by the energy difference between the levels of the amplifying medium, as Figure 5.10 shows. The parametric amplification is, in fact, a non-resonant process in which energy distribution between photons ω_s and ω_c is fixed by phase matching condition.

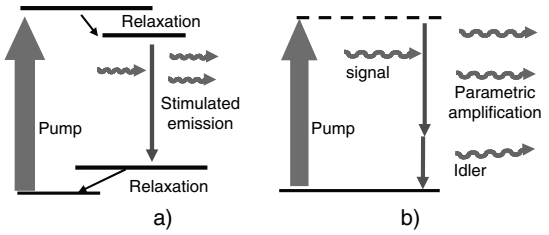

Figure 5.10. *Amplification schemes of a a) laser medium with four levels and b) parametric medium*

Acting on the phase matching condition allows the frequency tuning of delivered radiation. A widely tunable radiation source is thus available: it is a major advantage of parametric optical sources. For instance, in the case of an exact phase matching in type I, Figure 5.11 shows the range of signal and idler wavelengths that can be obtained by adjusting the angular orientation of a lithium niobate crystal with a primary beam at 1.06 μm delivered by a Nd:YAG laser.

In the case of a ferroelectric material such as lithium niobate, a three-wave mixing may also be obtained in a quasi-phase matching configuration. Practically, several domain inversions may be achieved with the same crystal in order to produce various couples of signal and idler wavelengths. For each inversion domain, converted wavelengths can be continuously tuned by adjusting the crystal temperature. Figure 5.12 shows accessible working ranges with a lithium niobate crystal including five inversion domains.

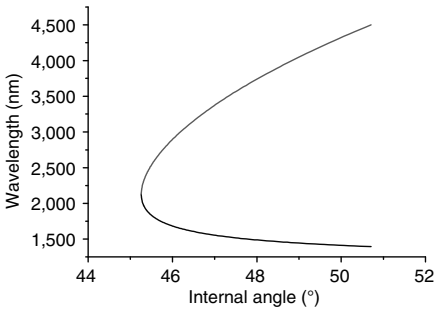

Figure 5.11. *Type I phase matching for lithium niobate crystal pumped by a Nd; YAG laser; red and black parts of the curve are respectively for signal and idler wavelengths. For a color version of the figure see www.iste.co.uk/boutier/lasermetro.zip*

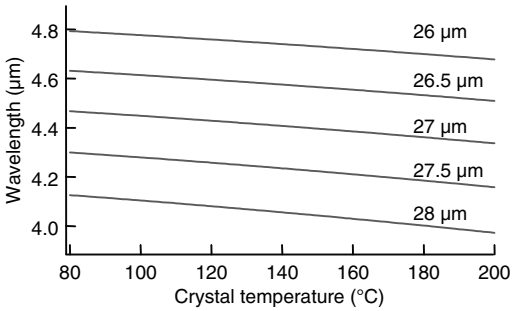

Figure 5.12. *Accessible wavelengths in quasi-phase matching with a lithium niobate crystal having five gratings, the reversal periods of which being indicated on the figure; pump wavelength is set at 1.06 µm*

Given that parametric conversion is a "gain process", optical parametric oscillators (OPOs) can be achieved by setting a nonlinear crystal inside an optical cavity. Such a nonlinear crystal inserted inside an optical cavity pumped by an external laser forms an OPO. While close to a laser oscillator, an OPO exhibits very specific geometries as three radiations are coupled in the parametric amplification process. Then, three main categories of OPO are distinguished depending upon the number of radiations that are forced to oscillate within the OPO cavity:

– Singly resonant OPO: It is basic configuration where only one wave (signal or idler) oscillates inside cavity.

– Doubly resonant OPO: The optical cavity ensures oscillation of two waves, the signal and the idler. This configuration offers the advantage of a particularly low oscillation threshold, which allows considering the achievement of a very compact OPO sources.

– Triply resonant OPO: The cavity must be resonant for three radiations. This geometry is mainly used for a continuous operation, in which the available pump power can be limited.

Figure 5.13 represents the scheme of a singly resonant OPO. There is the pump laser as well as the OPO cavity containing the nonlinear crystal. To obtain a tunable infrared radiation around 4 µm from a Nd:YAG pump laser at 1.06 µm, the specifications of cavity mirrors are defined in such a way that the signal wave is resonant around 1.5 µm.

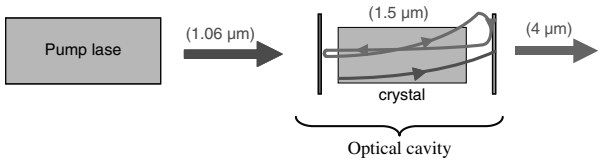

Figure 5.13. *Principle scheme of a simple resonant OPO*

Depending upon application, various geometries may be envisioned to achieve an OPO belonging to one of the three categories introduced before. Hybrid configurations may also be considered where oscillation alternatively takes place on the signal wave and idler wave. For an optical diagnostic, it is important to have a tunable source emitting a narrow line width, so that the emitted source frequency can be tuned in resonance with a specific transition of the medium to be probed. It is the reason why different architectures have been proposed to produce a narrow line width of an OPO.

According to previous approaches developed for dye lasers, two methods have been mainly investigated:

Optical injection: By seeding inside the OPO cavity with a single frequency radiation produced, for instance, by a laser diode, the parametric conversion may be forced on the injected radiation. This method has been validated many times; however, it presents major drawbacks: complexity, limited tuning range (it is limited by the tunability of the injection source and not by OPO itself), low side-mode suppression ratio, especially out of exact phase matching or when working several times above the threshold.

Using of spectrally selective cavity: Instead of simply using an OPO cavity composed of two mirrors, one mirror is replaced by a grating (Littrow) or a Fabry-Perot étalon is inserted inside the cavity in order to select one longitudinal mode. These different approaches have the drawback of increasing cavity losses yielding a higher oscillation threshold; it results in making use of high power lasers, thus is cumbersome. Moreover, in these working conditions, the damage resistance of optical components may become a limitation.

In addition to these spectral refinement techniques issued from laser technology, there is another approach, which is very specific to parametric conversion process, that has been developed: it is based on using a doubly resonant OPO architecture with separated cavities. Basically, the idea is to use a resonator composed of two cavities, the lengths of which are independently adjustable. Mirror coatings are chosen so that one of the cavities oscillates at idler wavelength, whereas the other one oscillates at the signal wavelength. Figure 5.14 provides a scheme of the doubly resonant OPO with separated cavities.

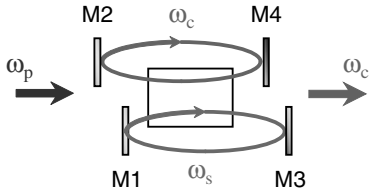

Figure 5.14. *Principle scheme of the doubly resonant OPO with separated cavities*

The different output frequencies that can be emitted by such an architecture must simultaneously satisfy the following three conditions:

– for the signal, to be resonant with one or several longitudinal modes of cavity M1–M3;

– for the idler, to be resonant with one or several longitudinal modes of cavity M2–M4;

– the sum of signal and idler frequencies must be equal to the pump frequency, in order to satisfy conservation energy law given in [5.23].

Given that position of longitudinal modes in each cavity is directly imposed by cavity length, it is always possible to adjust each length so that the three conditions are satisfied (which is not the case for doubly resonant OPO using a common cavity for the signal and idler radiations). Moreover, if the cavity lengths are chosen slightly different (typically 10%), a parametric radiation with a high spectral purity may be produced (longitudinal mode operation). It is called Vernier spectral filtering. In these conditions, inside the parametric gain curve, only one couple of signal and idler frequencies may exist capable of satisfying the stated conditions. Figure 5.15 illustrates such a mode of operation using the frequency diagram of Giordmaine and Miller, where the direction axes of signal and idler frequencies are oriented in opposite directions, in order to satisfy the energy conversion condition [KEL 66], whatever the signal and idler frequencies.

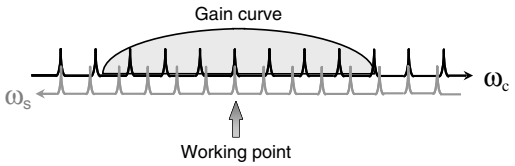

Figure 5.15. *Determination of point of operation for a doubly resonant OPO with separated cavities, using the Giormain and Miller representation*

Figure 5.16 represents a doubly resonant architecture where both signal and idler cavities are embedded in order to optimize the source compactness at its best. In this geometry, the signal and idler waves respectively oscillate between mirrors M1–M3 and M2–M4. Mirrors M2 and M3 have been directly deposited on the exit faces of the nonlinear crystal, in order to reduce the resonator dimensions, and thus benefit of all available space between external mirrors [DRA 02].

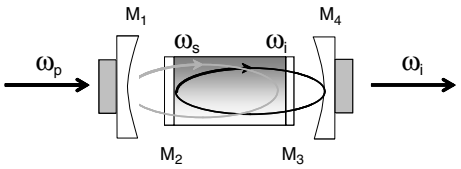

Figure 5.16. *Principle scheme of doubly resonant OPO with two embedded cavities*

This architecture, achieved in such a way, offers at the same time a narrow line width as well a wide tuning range. Its potential capabilities for chemicals analysis are illustrated in Figure 5.17, which shows photoacoustic spectra of N_2O and methane (CH_4) obtained with a 10 cm absorption cell.

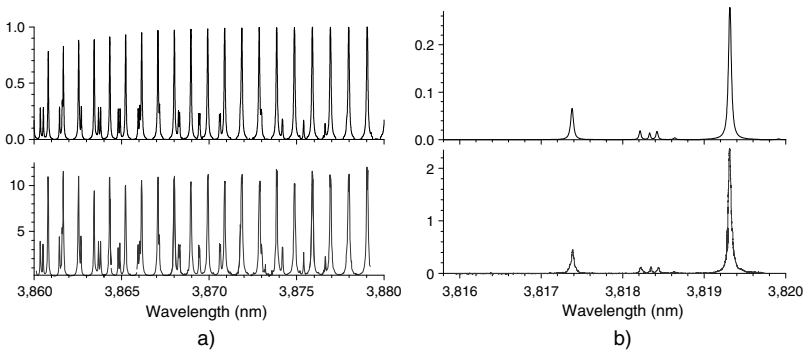

Figure 5.17. *Photoacoustic spectra of a) N_2O and b) CH_4 for a 100 mbar pressure obtained with an OPO with embedded cavities, operating in nanosecond regime; lower curves: experimental spectra; upper curves: spectra simulated from Hitran database*

5.4. Nonlinear techniques for optical diagnostic

As seen in section 5.2.2, the nonlinear response of a gas can only result from a third-order contribution, which assumes an interaction involving three incident optical fields. When the polarization created by the product of these three fields vary with time, the gas medium is able to emit a new radiation, the characteristics of which depend of the thermodynamic conditions of the studied medium; hence, the analysis of this new radiation allows achieving optical diagnostic. The main feature of these techniques involving four waves in total is that the produced signal is collimated and similar to a laser beam. This is the reason why four-wave mixing techniques are also called coherent techniques. The signal beam may thus be reflected by using a set of mirrors to be detected at a large distance from the medium where it has been created. This essential characteristic makes four-wave mixing approaches very attractive for reactive media studies (especially in combustion facilities) where it is of prime necessity to suppress radiations emitted by probed medium. Moreover, the signal is only produced in a volume where incident laser beams overlap. Four-wave mixing techniques thus allow achieving local measurements.

5.4.1. *Introduction to four-wave mixing techniques*

The most widely used four-wave mixing techniques for flow diagnostics are the degenerated mixing called degenerate four-wave mixing (DFWM) [FIS 83] and the coherent anti-Stokes Raman scattering (CARS) [ECK 88]. In DFWM, the four implied fields in mixing process have the same frequency. The signal beam resulting from the nonlinear response is particularly intense when field frequency is in resonance with a gas absorption transition: diagram Figure 5.18(a) illustrates such a situation in the case of one-photon resonance. Situations may also be found where resonance is obtained by a two-photon process (see Figure 5.18(b)). Frequency adjustment nearby molecular resonances makes the DFWM technique very sensitive. This is why DFWM is mainly used to detect minority compounds (radicals or traces). However, only molecular species having a permanent dipolar moment can efficiently be probed through the field coupling in the neighborhood of an absorption mechanism sustained in DFWM. Therefore, this technique is not applicable to diatomic and homonuclear molecules (nitrogen, oxygen, etc.), which do not have a permanent dipolar moment, due to the symmetric repartition of the electronic cloud around nuclei. For these majority species, coherent Raman scattering is the recourse; this is briefly introduced hereafter.

In its basic version, the CARS technique requires two pulse lasers at frequencies ω_L and ω_{St}, called pump and Stokes. The signal beam is produced at the anti-Stokes frequency ω_{AS}, such as $\omega_{AS} = \omega_L - \omega_{St}$.

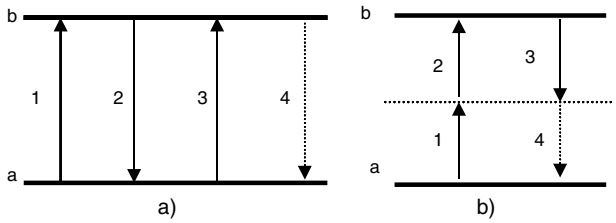

Figure 5.18. *Energy levels diagrams for a degenerate four-wave mixing a) one-photon resonance; b) two-photon resonance; 1, 2 and 3 are exciting radiations, 4 is for the signal*

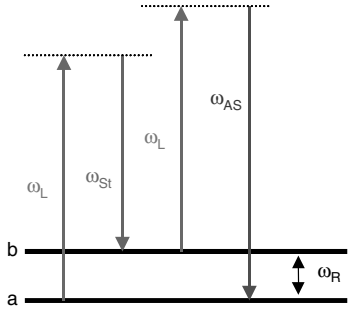

Figure 5.19. *Interaction diagram in CARS*

Figure 5.19 illustrates the coupling of various involved radiations with two molecular levels (vibration and rotation). The anti-Stokes signal production results from Raman scattering of the pump beam on the molecules of gas, the movement (vibration or rotation) of which is forced in phase by the combined action of both photons at frequencies ω_L and ω_{St}. Therefore, as Figure 5.19 shows, the pump beam acts both to force Raman coherence and to probe this coherence. The anti-Stokes beam intensity is obtained by following the same proceeding as it has been done for stimulated Raman scattering. It comes out:

$$I_{AS}(L) = \frac{\omega_{AS}^2 \left|\chi_{\text{eff}}^{(3)}(\omega_{AS})\right|^2 L^2}{\varepsilon_0^2 c^4 n_L^2 n_{St} n_{AS}} I_L^2 I_{St} \frac{\sin^2(\Delta kL/2)}{(\Delta kL/2)^2} \qquad [5.30]$$

where $\Delta k = k_{AS} - (2k_L - k_{St})$ is the phase mismatch expressed in colinear geometry, $\chi_{\text{eff}}^{(3)}(\omega_{AS})$ is given by expression [5.20] where ω_{st} is replaced by ω_{AS}, which leads to $\chi_{\text{eff}}^{(3)}(\omega_{AS}) = \chi_{\text{eff}}^{(3)}(\omega_{St})^*$. From expressions [5.20] and [5.29], it is deduced that

$I_{AS}(L)$ will be optimal if frequency difference between the pump and Stokes photons is in resonance with a Raman transition: $\omega_L - \omega_{St} = \omega_{AS}$.

While stimulated Raman gain depends on imaginary part of $\chi^{(3)}_{\text{eff}}(\omega_{St})$, the expression [5.30] shows that the anti-Stokes wave intensity is a function of the modulus of third-order nonlinear susceptibility. This dependency leads to interference between the responses connected to the real and the imaginary parts of $\chi^{(3)}_{\text{eff}}(\omega_{AS})$,which appears as a dissymmetry of anti-Stokes lines.

Either in DFWM or CARS, the signal beam resulting from the nonlinear interaction will be intense and detectable only if fields re-emitted by the various atoms or molecules add in phase ($\Delta k = 0$). In the case of CARS, the phase matching condition is:

$$\vec{k}_{AS} = \vec{k}_L + \vec{k}'_L - \vec{k}_{St} \qquad [5.31]$$

where $\vec{k}_L$, $\vec{k}'_L$, $\vec{k}_{St}$ and $\vec{k}_{AS}$, respectively are pump, Stokes and anti-Stokes wave vectors. This relationship is immediately extended to the DFWM process, considering that $\vec{k}_{AS}$ is a wave vector of a signal beam, $\vec{k}_L$ and $\vec{k}'_L$ are wave vectors of pump beams, whereas $\vec{k}_{St}$ is the wave vector of probe beam. In DFWM, all these wave vectors have the same module. Figure 5.20 illustrates a non-collinear disposal of beams, which allows satisfying phase matching condition in CARS as well in DFWM. According to geometrical arrangement of Figure 5.20, called "boxcars", the signal beam can only be produced in overlapping zone of the beams, so that four-wave mixing techniques allow achieving local measurements with a spatial resolution that is in the same order of what is achieved in laser velocimetry. The signal beam being emitted in a direction different from the exciting beams, a spatial filter can be used to separate the signal from the laser beams.

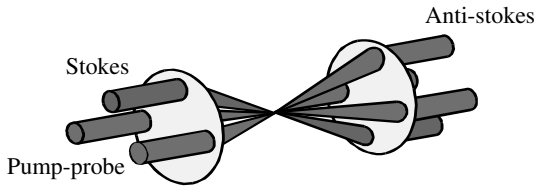

Figure 5.20. *Beam arrangement in the "boxcars" geometry*

5.4.2. *Temperature and concentration measurements in four-wave mixing*

To measure the temperature and species concentrations, the main approaches are based on the spectral analysis of the signal beam, in DFWM as well as in CARS. The signal temporal analysis of four-wave mixing also allows obtaining temperature and concentration.

The equation of linear susceptibility $\chi_{\text{eff}}^{(3)}(\omega_{AS})$ has been previously established for a Raman frequency between two levels a and b. However, molecules have numerous rovibrational levels that make that expression $\chi_{\text{eff}}^{(3)}(\omega_{AS})$ has to be developed into a sum of terms corresponding to the different resonances of analyzed molecular species; $\chi_{\text{eff}}^{(3)}(\omega_{AS})$ can thus be expressed as:

$$\chi_{\text{eff}}^{(3)}(\omega_{AS}) \propto N\left[\sum_{a,b} \Delta_{ab} \frac{\overline{\left(\frac{\partial\alpha}{\partial R}\right)_{ab}}^{2}}{\omega_{ab}^{2}-\left(\omega_{L}-\omega_{AS}\right)^{2}+2i\gamma_{ab}\left(\omega_{L}-\omega_{AS}\right)}+\chi_{NR}^{(3)}\right] \qquad [5.32]$$

where the summation is done on levels of the probed molecule, limiting it to Raman active transitions, which are obtained by the selection laws established for spontaneous Raman; $\chi_{NR}^{(3)}$ is the non-resonant contribution associated with the real part of susceptibility.

By recording the nonlinear response as a function of the frequency of the exciting lasers, we obtain a series of intensity maxima: each one is related to a different resonance ω_{ab} of the probed species. These resonance peaks are called a DFWM or a CARS spectrum of the probed species, depending on considered process. Since the coefficients of occupation probability of Δ_{ab} levels depend on the temperature of the probed medium according to Boltzmann's law (in the case of a medium at thermal equilibrium), the relative intensity of the various peaks forming the spectrum depends on the medium temperature. The analysis of the shape of the spectrum allows us to obtain the medium temperature. Concentration measurements can be deduced from the absolute intensity of the spectrum, but a preliminary calibration of the experimental response is required.

Depending on the application, various approaches have been developed to measure temperature and concentration. The most widely used ones are:

– Scanning spectroscopy, where the various Raman resonances of the analyzed medium are sequentially probed, changing step-by-step Stokes laser frequency. This approach needs lasers with a narrow spectral width (a few hundredths of cm^{-1}, typically), which ensures a great selectivity as well a high enough sensitivity for allowing diagnostic of low pressure gases. Nevertheless, the recording time of one spectrum generally takes several minutes, which is redhibitory for study of turbulent flows. It is why only stationary or transient (but reproducible) process may be analyzed by scanning spectroscopy.

– Multiplex spectroscopy, where the Stokes radiation is produced over a wide spectral range (several tens cm^{-1}) in order to simultaneously probe several resonances of the species to be analyzed. In these conditions, at each laser pulse, a spectrum may be obtained, from which temperature and concentration can be deduced. This approach has mainly been used in CARS for thermometry in non-stationary media.

Figure 5.21 shows a CARS spectrum obtained with this multiplex approach. Rotational structures and two successive vibrational bands are clearly distinguished. The shape analysis of each vibrational band leads to the rotational temperature while the relative intensity of two vibrational bands provides the vibrational temperature. In addition, the concentration of the probed species can be deduced from the absolute intensity of the spectrum.

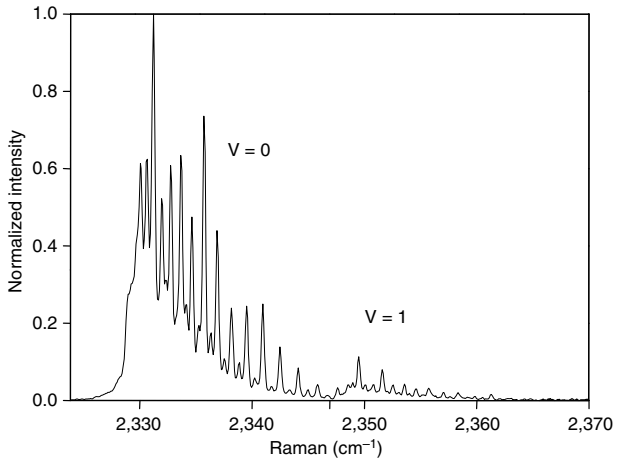

Figure 5.21. *Multiplex CARS spectrum of nitrogen recorded in air at 1,750 K; the two first vibrational bands are distinguished: they are made of rotational resonances (of Q branch)*

5.4.3. *Velocity measurements in four-wave mixing*

In four-wave mixing, velocity measurement techniques can be introduced using the dynamic grating approach [RIB 00]. Let us consider the two-beam crossing geometry of Figure 5.22. Both pump beams (ω_L, $\vec{k}_L$) and (ω_L, $\vec{k}'_L$) being spatially coherent, they interfere in order to form an intensity grating in the crossing zone. Figure 5.22 illustrates such a grating obtained with a nanosecond frequency doubled Nd:YAG laser.

Figure 5.22. *Illustration of intensity grating created by pump beams; the distance between two bright fringes is typically about 10 μm*

In CARS process, Raman coherence is created by mixing the pump and Stokes beams. Taking into account the intensity grating issued from the two pump beams, it is seen that the nonlinear mixing (thus the creation of Raman coherence) will be only efficient in intensity maxima, that is in bright fringes of the pump grating. Consequently, the spatial distribution of the Raman coherence will be the image of the intensity grating produced by the pump beams: so, there is creation of a coherence grating. This grating is said to be a dynamic grating because its intensity evolves with time. By analyzing the temporal behavior of such a coherence grating, created in a moving gas, has led to the demonstration of the feasibility of local and instantaneous velocity measurements [EIC 86] without any particle seeding.

The method used consists of lighting the studied medium by means of a long pump pulse, synchronized with a short Stokes pulse (see Figure 5.23). The frequencies of long and short pulses are chosen in resonance with a Raman transition of medium. Two steps may be distinguished:

– During short pulse, the simultaneous application of two fields forces the oscillation of Raman coherence at frequency $\omega_L - \omega_{St}$: it is the excitation phase or the coherence formation step.

– After stopping the short pulse, the Raman coherence freely oscillates at frequency ω_R: its temporal evolution is continuously probed by the long pulse.

With such an excitation diagram, the shape of the anti-Stokes response is asymmetric: the intensity increases during excitation step, then we observe a decay of the anti-Stokes signal during the free oscillation of the Raman coherence. If the experiment is performed in a gas at rest, the temporal decreasing is monotonous. At atmospheric pressure (collision regime), the damping time is about a few tens of picoseconds, whereas at low pressure (Doppler regime), it depends on gas temperature. Therefore, the measurement of decrease in time allows the determination of the gas temperature.

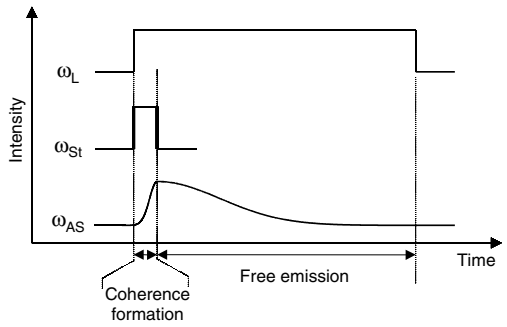

Figure 5.23. *Excitation time diagram with two pulses and evolution of anti-Stokes signal*

To simultaneously produce a long pulse (30 ns) and a short tunable pulse (1 ns), the setup of Figure 5.24 has been developed. The long pulse is produced from an injected Nd:YAG laser, then frequency is doubled. The insertion of an acoustic cell at 80 MHz allows extending the potential use range of this technique toward low velocities. The short pulse is produced by slicing out a 1 ns pulse within the long pulse. After amplification and frequency doubling, the short pulse at 532 nm is used to pump an optical parametric amplifier, while the non-doubled short pulse is summed with the tunable pulse available at the output of parametric amplifier. Let us note that the parametric oscillator is pumped from a small part of the long pulse at 532 nm, in order to ensure a good beam quality and a narrow line width. At the output of the parametric chain, a short 1 mJ pulse is available, which is tunable between 534 and 540 nm to excite pure rotational Raman lines.

If the experiment is performed in a low pressure gas with a high velocity (supersonic flow), a beating of the anti-Stokes response is observed: the higher the velocity, the higher is the frequency beating (see Figure 5.25). This beating signal results from the spatial interference between coherence and pump gratings. Indeed in a moving gas, the coherence grating moves with the gas velocity and so, it spatially interferes with the pump grating that does not move in time. Then, during free decay of the Raman coherence, the anti-Stokes response is modulated because

the coherence grating is moving through the stationary pump grating, which plays the role of reading the grating of the Raman coherence. The flow velocity can be extracted from the beating frequency. In fact, it can be shown that this frequency is proportional to the velocity component orthogonal to the beam direction.

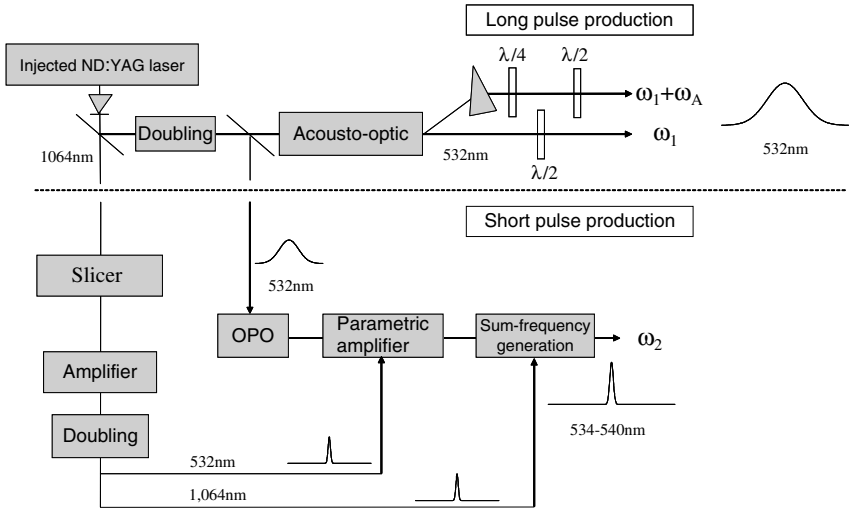

Figure 5.24. *Scheme of optical bench that allows synchronously producing a long pulse and a tunable short pulse. Let us note the introduction of a photoacoustic cell in the long pulse part for low velocity measurement. Picture on the right illustrates the parametric source*

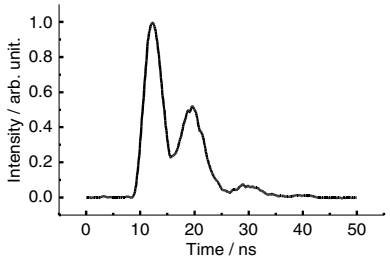

Figure 5.25. *Example of beating obtained in Mach 10 flow; crossing angle between the pump beams is 2.2; laser beams cross the jet perpendicularly to its axis*

This previous approach allows undertaking velocity, temperature and concentration measurements in hypersonic flows at low pressure. Figure 5.26 shows the evolution of these different parameters across a bow shock in front of a cylinder, placed in a Mach 10 flow. The shock formation is revealed by:

– a gas rotation temperature increasing from 50 to 1,100 K, this last value corresponding to stagnation temperature;

– a density increasing in a ratio ≈ 6;

– a velocity reduction from 1,500 to 200 ms^{-1}.

These variations are localized over a distance of about 0.5 mm providing an estimation of the shock thickness. Let us note that the velocity profile appears shifted relative to temperature and concentration profiles: this difference is explained by the fact that velocity measurement has been achieved by probing a low rotational level (J = 4) corresponding to a class of cool molecules having a few collisions when crossing the shock. These results illustrate the strong lack of equilibrium between rotation and translation motions in the shock thickness.

Figure 5.26. *Temperature, density and velocity measurements along the stagnation line and across a bow shock in front of a cylinder. Mach 10 flow is running from left to right. The shock visualization is obtained by a) electron beam fluorescence technique, b) CARS measurements*

In conclusion, for this part, the time domain CARS technique allows measuring two velocity components (parallel and perpendicular to the axis of dynamic grating in Figure 5.22). It is mainly applied to the main molecular species (N_2, O_2 or CO_2),

but may also be used for temperature and velocity measurements of oxygen atoms especially produced in high enthalpy facilities, in high dissociation conditions. This technique may be transposed to a DFWM to characterize other less abundant gaseous species. However, employment of Raman coherence gratings is no more appropriate at high pressure (in collision regime) or when the velocity is low (subsonic flow), because the anti-Stokes signal beating cannot be observed due to the fast damping of the signal. Other kinds of dynamic gratings, with a persistence time remaining high, even at high pressure, may be considered.

Until now, thermal and electrostrictive gratings have been essentially used. The approach followed is similar to the one presented for CARS: a short (nanosecond) pulse creates the grating while the evolution of the so-formed grating is probed by means of a continuous laser, which often is an argon laser.

Creation of a thermal grating, which is related to an absorption mechanism, is associated with degenerate four-wave mixing. However, production of electrostrictive gratings, which does not rely on any absorption mechanism, may be efficient during an experiment of four-wave mixing of Raman type. Without providing too many details about physical processes of thermal and electrostriction grating formation, let us simply indicate that:

– for thermal gratings, the radiation absorption induces a local heating gas that is accompanied by an index variation, similar to intensity grating. Therefore, there is creation of an index grating that allows diffracting probe radiation delivered by a continuous laser;

– for electrostrictive gratings, index grating creation is related to a molecule migration toward intense field zones (bright fringes of pump grating).

Let us note that, in both cases, acoustic waves are produced, which propagate perpendicularly to the mean laser beam direction. Scattering of a probe beam by these acoustic waves gives rise to a coherent Brillouin signal.

5.5. Bibliography

[BLO 77] BLOEMBERGEN N., *Nonlinear Optics*, W.A. Benjamin, Inc., New York, 1977.

[BOY 92] BOYD R.W., *Nonlinear Optics,* Academic Press, Inc., Boston, MA, 1992.

[DRA 02] DRAG C., DESORMEAUX A., LEFEBVRE M., ROSENCHER E., "Entangled-cavity optical parametric oscillator for mid-infrared pulsed single-longitudinal-mode operation", *Optics Letters*, vol. 27, pp. 1238–1240, 2002.

[ECK 88] ECKBRETH A.C., *Laser Diagnostics for Combustion Temperature Species*, Abacus, Cambridge, MA, 1988.

[EIC 86] EICHLER H.J., GUNTER P., POHL D.W., *Laser-Induced Dynamic Gratings*, Springer, Berlin, 1986.

[FIS 83] FISCHER R.A., *Optical Phase Conjugation*, Academic Press, London, 1983.

[FRA 61] FRANKEN P.A., HILL A.E., PETERS C.W., "Generation of optical harmonics", *Physical Review Letters*, vol. 7, pp. 118–119, 1961.

[KEL 66] KELLEY P., LAX B., TANNENWALD P.E., *Physics of Quantum Electronics*, McGraw-Hill, New York, NY, 1966.

[RIB 00] RIBET I., SCHERRER B., BOUCHARDY P., POT TH., TARAN J.-P., LEFEBVRE M., "Supersonic flow diagnostics by single-shot time-domain coherent anti-Stokes Raman scattering", *Journal of Raman Spectroscopy*, vol. 31, pp. 689–696, 2000.

Chapter 6

Laser Safety

6.1. Generalities on laser safety

A symbol of a new technology already widely introduced in fluid mechanics laboratories, optical techniques, used for aerodynamics of flows and tracking of molecules, largely use laser sources (laser stands for Light Amplification by Stimulated Emission of Radiation). From concept to installation, their implementation obliges the user to integrate safety for people and the environment, facing dangers that are linked to them. It is thus necessary to make experimenters aware of the risks from lasers, in order to implement individual and collective means of protection, integrating orders of instruction and human behavior.

A luminous source generally radiates in all directions; therefore, the more distant the object from the source is, the weaker the received energy. Conversely, light generated by a laser is concentrated and collimated as soon as it is emitted, so that when the laser beam hits an object, all its energy is concentrated into a minuscule impact point.

The purpose of this chapter is to make users of laser techniques in fluid mechanics sensitive to the real risks associated with laser employment, in order to optimize prevention and protection of individuals and their environment. Radiation produced by lasers may be dangerous for eyes and skin. It may also present electrical, chemical and biological risks by the emanation of toxic gases (producing cancer), as well as fire or flood. To evaluate each of them, the users must:

– know the different types and classification of the lasers used inside the laboratory;

Chapter written by Jean-Michel MOST.

– master their applications; know the dangers, the precautions to be taken, the regulations linked to their use (internal regulations and standards, as well as the European guidelines on laser safety). The objective of this chapter is not the recalling of official safety standards of the apparatus containing a laser (standards NF EN 60825-1/x are available in libraries or on the Web), but making users sensitive to precautions to be taken when using these lasers;

– be able to evaluate specific risks as well as risks associated to use, analyze and organize safety in a laser zone;

– know how to select and operate necessary actions on protection, of individual and collective levels;

– determine the process for education of exposed people.

6.2. Laser type and classification

Table 6.1 sums up characteristics of the main lasers used in fluid mechanics. These lasers are used either to create a fringe pattern or a light sheet. These lasers not only allow us to perform flow visualizations, velocity measurements and particle size determinations (LDV, PIV, Phase Doppler Analyzer, tomography) using Mie scattering of particle tracers, but also temperature and concentration measurements (emission spectroscopy, PLIF, CARS, fluorescence, incandescence, etc.) using molecular scattering. The lasers used are either continuous (He–Ne, argon, krypton, dye laser, semiconductor laser, diode laser, CO_2) or pulsed (Ruby, Nd:YAG). Pulse laser rates are generally low (about 10 Hz up to 1 kHz); they reach approximately 10 kHz for copper vapor lasers.

For an analysis of laser risk, first the user must be informed about the main characteristics of the laser he/she has to deal with:

– type: gas, solid, liquid or semiconductor (diode laser);

– wavelength (adaptation to the phenomenon to be characterized or to the detector);

– power (continuous laser) or energy (pulse laser);

– beam diameter and divergence;

– pulse type: triggered (Q-switch) or free running (flash rate).

A classification of the various lasers as a function of the potential risk they present (type, power or energy, wavelength, associated optics) is presented in Table 6.2. If lasers of classes 1 and 2 are *a priori* without any danger, particularly without any biological risk to man, lasers of classes higher than three must be used with many precautions. Currently these lasers of class 3 are mainly used for

measurements in fluid mechanics. The biological risk increases with beam power or energy and is more pronounced if the emission takes place in the visible domain, the near ultraviolet (UV) and infrared (IR) where attenuation for tissues is less.

Active material	Wavelength (nm)	Regime: continuous or pulsed	Pulse rate	Energy or power
Gas				
Excimer	193–351	Pulse	1–400 Hz	100 mJ to a few J
	248, 308			
Metallic vapor	511 and 578	Pulse	10 kHz	5–20 W
	Au 628			
He-Ne	632	Continuous	–	0.1–50 mW
Argon	488–515	Continuous	–	0.1–20 W
Krypton	647–976			
CO	5,300	Continuous	–	1–20 W
CO_2	10,600	Pulse	10 kHz	100 J
		Continuous	–	1–100 W
Solid				
YAG-Erbium	2,930	Pulse	A few Hz	10 J·cm^{-2}
YAG doubled	532	Pulse	1–50 Hz	
		Continuous		1–120 W
Ruby	694	Pulse	A few Hz	10–50 mJ
Diode laser	850	Pulse		A few Watt
		Continuous		
Nd:YAG	1,064	Pulse	1–50 Hz	1–60 W
doubled	532	Continuous		
Titanium Sapphire	700–1,070	Pulse	1–50 kHz	A few mJ
Double	350–535	Continuous		1 W
YAG-Holmium	2,100	Pulse	1–5 Hz	0.5–100 J·cm^{-2}
Liquid				
Dye lasers	320–1,200	Pulse		A few W
		Continuous		

Table 6.1. *Various types of lasers*

Class 1	No danger
Class 1M	302.5 nm < wavelength < 4,000 nm
	Low power; laser does not present any known biological risk in conditions of reasonable use, but take care if beam is used with optics.
Class 2	400.5 nm < wavelength < 700 nm (visible domain)
	No danger in conditions of reasonable use, but take care if beam is used with optics. The reflex of the eyelid beating protects, but the eye must not be intentionally kept in the beam axis.
Class 2M	400.5 nm < wavelength < 700 nm (visible)
	Do not intentionally keep eye in beam axis; do not look directly at laser beam with an optical instrument.
Class 3R	302.5 nm < wavelength < 10^6 nm
	Direct vision of laser beam is potentially dangerous.
Class 3B	Direct vision of laser beam is dangerous.
	Risk to skin injuries.
	Diffused reflexion without danger if distance between cornea and screen is higher than 13 cm and if time of exposure is less than 10 s.
Class 4	Dangerous exposition of eye and skin for direct or scattered beams

Table 6.2. *Classes of lasers*

6.3. Laser risks: nature and effects

Risks linked to lasers are multiple; the most important are risks to health risks (biological risks). Others affect materials.

6.3.1. *Biological risks*

Biological risks are evaluated as a function of the maximal authorized exposure (MAE), defined by the maximum level to which an eye may be exposed without suffering immediate or long-term damage. This value, measured at cornea level, is determined as a function of wavelength, duration and exposure conditions (criteria defined by standards serve as a reference) for direct beams, specular or diffused reflexions. Reflexions produced by reflecting objects present the same risk as direct radiations, because they are not only insidious but they also may contain up to 90% of incidental initial energy. Optical fibers, which carry laser light, may also be assimilated to a laser source and present equivalent risks. Figure 6.1 shows

the surface power density (W/cm² or J/cm² depending on the regime), which will be received at the retinal level as a function of the retina image. The nominal distance of ocular risk (NDOR) corresponds to the distance from which, in ideal conditions, illumination or energetic exposure falls under appropriate MAE. The relations of geometric optics allow us to evaluate this NDOR: computation must be done again if optical fibers or observation optics is used.

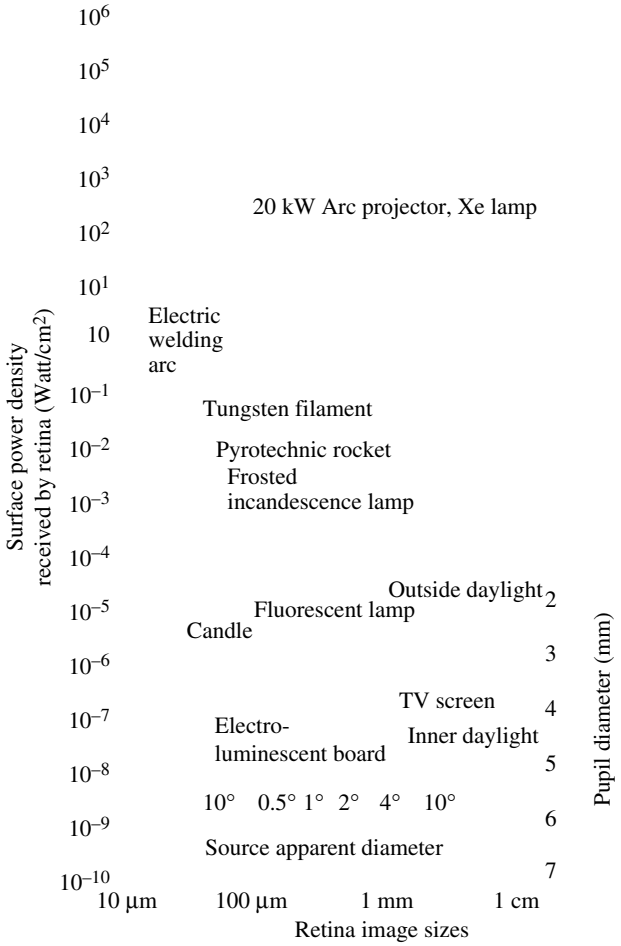

Figure 6.1. *Maximal emission allowed*

Lasers used in fluid mechanics practically always expose the eye beyond MAE: they are thus potentially dangerous.

Injuries to eye or on the skin not only depend upon wavelength, power or energy carried by the beam, but also on the exposure distribution with time (continuous or pulse exposure, duration and rate of pulses).

6.3.1.1. *Thermal and photochemical effects*

Thermal effects (specifically of IR and visible domains), when controlled, are widely used for some medical treatments; they serve to increase temperature from 10 to 20°C, which induces protein alteration and cell death. For higher temperatures, tissues withdraw through water evaporation, the ultimate state being tissue volatilization. Photochemical effects (UV and visible) excite molecules; absorbed energy induces chemical reactions. Out of control, these effects provoke photochemical burnings and a premature ageing; they may induce perforations and cuts in skin tissue, leading to cancers. It is thus necessary to prevent these effects when employing a laser in a laboratory.

6.3.1.2. *Mechanical effects*

Intense laser beam concentration on a small surface, under action of an electrical field and absorption of several photons by an atom, induces ionization, acceleration and multiplication of electrons until a mini plasma is formed: this is the laser shock. A shock wave sometimes goes with this plasma relaxation, which may occur at the origin of cell displacement. These effects are observed with very short pulses, less than 100 ns. The damaged biological tissues mainly concern the eye, but it can also affect skin.

6.3.1.3. *Electromagnetic effects*

The electrical field inside a laser beam may reach values of about 10^{12} V/m. A powerful beam may induce bond breakings and modify the conductivity and dielectric tissue constant.

6.3.2. *Risks to the eye*

The eye presents a spherical shape about 25 mm in diameter (Figure 6.2). From front to rear, it is composed of: cornea, aqueous humor, iris, crystalline lens, vitreous body and the retina. Cornea, 0.4–0.7 mm thick, sticks to conjunctiva.

Laser risks are linked to energy absorption or transmission inside the eye. If the beam wavelength sets in the UV or furthest IR, the majority of the radiation is absorbed by the ocular tissue (Figure 6.3); a burn to these ocular tissue follows, but

the retina normally remains protected. Conversely, radiations emitted in the visible and in the IR spectra are slowly absorbed by transparent media and induce the most dangerous injuries to the back of the eye, being focused on the retina. If beam energy reaches the peripheral retina, burning affects retinal rods (thus lateral vision); if the central macula region is burnt, visual losses become irreversible. Finally, if energy is focused on the fovea, eyesight is quasi-lost: therefore, it is of a real danger.

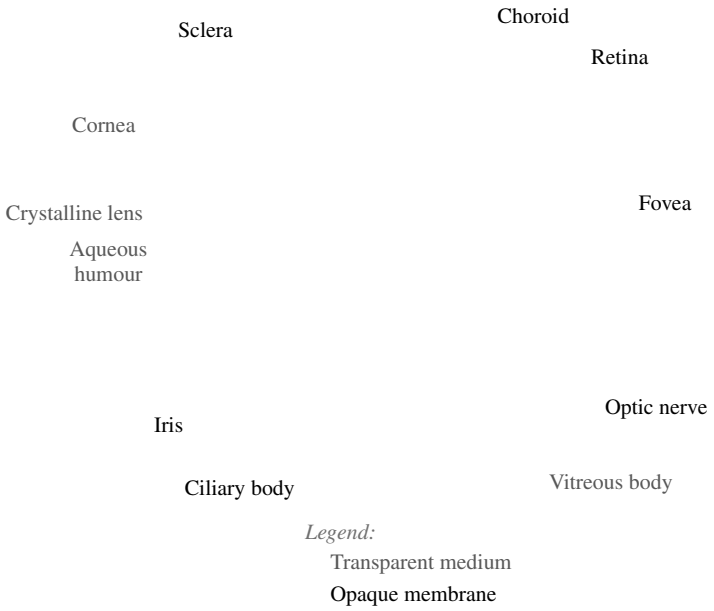

Figure 6.2. *Eye scheme*

Considerable risks may be induced by UV radiation due to flash lamps or discharge tubes of continuous lasers. Visible and near IR radiations emitted by flash lamps, pump sources and radiation coming back from targets may have enough luminance to create a potential danger.

In dark ambiance, pupil dilatation to 7 mm increases the risk. In fact, eye aperture increases energetic illumination between cornea and retina, which may reach 2×10^5 W/cm^2 (effect of magnifying glass). In these conditions, a few mJ or mW pulses may do damage to the retina. Moreover, working in the dark also increases risk to stumbling or to falling on objects, thus to exposing the eye to a

beam in an inopportune manner. A beam emitting in the visible induces the eyelid reflex (eyelids are closed within 0.25 s), which limits burn seriousness; but for an IR or UV beam, this, reflex does not take place.

Figure 6.3. *Absorption and transmission variation in ocular medium*

6.3.3. *Risks to the skin*

The skin is less sensitive than the eye, and serious injury is generally more limited due to the immediate reaction of the exposed person. The effects are mainly thermal and the surface wound is generally small. However, in some conditions, the skin appears more vulnerable than the eye which is protected by specific ocular means. The horny layer of the epidermis constitutes an efficient filter against UV and remote IR radiations. Wavelengths of very near IR are the most penetrating ones; in the visible, red is more penetrating than blue. Three degrees of burning are observed according to the delivered energy and penetration. The most penetrating rays are A in IR, A in UV and the visible spectrum; the most aggressive rays for the skin are UV B, UV C, IR B and IR C because the skin surface presents a high absorption for these radiations. Burns are classified by three degrees of seventy:

– in the first degree, erythema is characterized by the redness of the (skin pigmentation and the vascular aspect similar to an ordinary sunburn); the burn remains limited to the epidermis,

– in the second degree, blisters which are due to a detachment of the horny skin layer,

– in the third degree, a skin scab is observed. It is formed by gray or dark stains, dry and insensitive to touch, covering the whole skin thickness.

Table 6.3 summarizes the main illnesses due to burn effects on the eye and the skin by a luminous beam.

Wavelength	Effects on eye	Effects on skin
Ultraviolet C (200–280 nm)	Photokeratitis	Erythema (sunburn)
Ultraviolet B (280–315 nm)	Cataract (loss of crystalline lens transparency)	Speeding up of skin ageing process. Increase in pigmentation
Ultraviolet A (315–400 nm)	Photochemical cataract	Pigment tanning
Visible (400–780 nm)	Photochemical and thermal retinal injuries	Photosensitive reactions
Infrared A (780–1,400 nm)	Cataract, retinal burn	Skin burn
Infrared B (1,400–3,000 nm)	Aqueous inflammation, cataract	Skin burn
Infrared C (3,200–10^6 nm)	Burn limited to front cornea epithelium	Skin burn

Table 6.3. *Main diseases caused by the effects of laser radiation on the ocular media*

6.3.4. *Risks to hearing*

Hearing risks, which must be prevented, are mainly due to high voltage breakdown.

6.3.5. *Other biological risks*

6.3.5.1. *Chemical risks*

Dye lasers make use of toxic and powdery carcinogenic products; solvents are also toxic and must be handled with care (gloves, ventilated enclosures, used dye storage). Some lasers use toxic gases (excimer lasers: XeCl, ArF, KrF) or emit ozone. Risks are thus present and the precautions to be taken must be known.

6.3.5.2. *Electric risks*

Nearly all lasers make use of voltages higher than 1 kV; pulse lasers are particularly dangerous due to the energy accumulated in batteries and capacitors. Unless they are suitably protected, some components such as electronic tubes, working with an anode voltage higher than 5 kV may emit X-rays. We must be very careful when intervening on a laser tube, after removal of the safety casing.

6.3.5.3. *Fire risks*

A continuous laser, with a power higher than 0.5 W, may provoke inflammation of materials such as wood, tissues or plastics; the beam must thus be confined and a

beam must be eventually provided in order to discharge waste emitted power (graphite block, for instance). Static electricity and risks of explosion due to laser barrels or excitation flashes must be also taken into account.

6.3.5.4. *Flood risks*

Even for medium powers or energies, laser tubes are often cooled by water circulation (closed or open circuit). In the case of a circuit rupture, a safety procedure stops the electric tube power supply, which protects the tube; conversely, water may pour out and provoke a flood, which may induce electrical short circuits.

6.4. Protections

6.4.1. *Accident prevention*

The main reasons for accidents result from either a technical problem (disfunctional apparatus, electrocution with high voltage, etc.) or an insufficient protection (bad or even no ocular protection), or a bad use (handling incident, lack of precaution during an alignment process). Nd:YAG and argon ion lasers (currently used in fluid mechanics laboratories) present the highest rates of accident, 29 and 20%, respectively, with 12% of skin injuries and 68% of ocular injuries. The most common reasons for 90% of accidents are human or occasional in origin:

– eye exposure during alignment or adjustments;

– wearing no ocular protection (disposal not used or not appropriate);

– insufficient precautions taken during handling of high-voltage parts (electric shocks, burns);

– badly used laser.

The remaining 10% of accidents have a technical origin (beam badly confined, laser dysfunction).

6.4.2. *Collective protection*

This protection is the first one to be set-up and to be integrated as soon as the experimental system is conceived. The laser zone is the location where a laser beam may be emitted (laser, optical fibers); it must be conceived and equipped with signposting and protection. At the entrance door, a warning poster indicates the highest class of lasers present in the room. For laboratories where classes 3B and 4

lasers are present, a luminous panel as well as an emergency stop switch must be installed. Offices must be conceived in the context of safety:

– the laser zone must be closed by curtains or fire-proof absorbing screens;

– wall facings must have mat colors and should be non-reflecting;

– lighting must be minimal in order to limit pupil dilation;

– accesses and openings must not be along the beam axis, or they must be well protected from the laser beam;

– the laser beam must be at a height different from the experimenters eye (sitting or standing);

– any source of possible accidental reflexion must be eliminated (metallic objects with polished surfaces, furniture, mirrors, window panes, liquid surface, etc.);

– possibilities of impact on flammable materials must be eliminated.

A luminous panel must attract attention draw risks: it is generally red to the flashing and indicates that the laser is working.

6.4.2.1. *Labels*

Pictograms, provided by laser manufactures or available on the the Web, must be posted up inside and outside the laser office. All lasers and laser systems must have a signposting providing details about maximum output power, the wavelength – indicating if they work continuously or in pulse mode, with duration and pulse rate. It is important that billposting is permanent, readable and clearly visible during laser working and service operations. Moreover, it must be possible to read panels without entering the radiation zone.

6.4.2.2. *Important points for safety regulations*

– Use of a distant locking switch.

– A key to command the laser, which should be deactivated after use.

– Beam stop or subduing disposal.

– Implementation of an safety instructions panel.

– Protect the path of laser beam and the specular reflexions.

– Strict employment of ocular protection (appropriate protection spectacles NF EN 208).

– wearing of protective clothing.

– Laser safety training.

– Medical monitoring.

Be careful to not make these uses and requirements too restrictive, which could lead to set safety systems out of service by user!

6.4.3. *Individual protection*

In any case, implementation of collective protection does not exempt you from individual protection, and in the same way individual protection cannot substitute for collective protection. Individual protection mainly focuses on the wearing of protective glasses, which reduces harm from laser beam power or energy, in order that ocular exposure becomes less than MAE at considered wavelength. This indispensible wearing of protective glasses that the collective protection warrants appears partial or impossible to implement (during adjustment phase, for instance).

To be efficient, glasses must imperatively be adapted to laser characteristics, that is its power or its energy, its emission of continuous or pulsed wavelengths. Three important parameters of safety glasses are written on the frame or the lens (Figure 6.4).

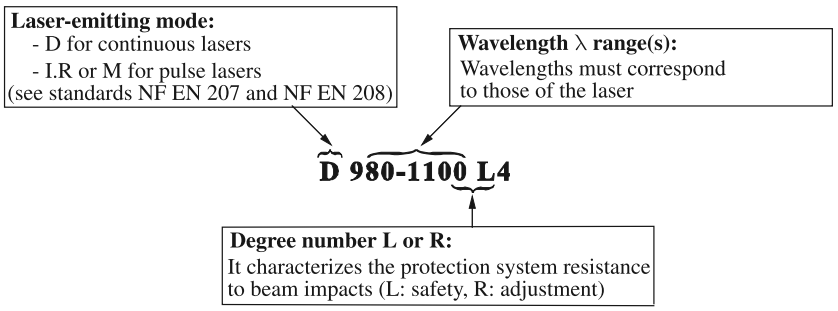

Figure 6.4. *Indications mentioned on laser protection spectacles*

Some manufacturers add optical density D or DO: it depends on the power of the laser or energy. When choosing glasses, visibility, transparency, weight, comfort, mechanical resistance and frame envelopment must not be ignored; the wearing of prescription glasses must also be taken into account.

Whatever quality of glasses used, it is strictly forbidden to intentionally look at a laser beam along its axis.

6.5. Safety advice

Before entering the laboratory, the risk level to exposure must be verified for yourself and visitors. Inside the laboratory, where there are lasers, all working staff must be informed of the risks and of the preventive measures to be taken. Laser operators must have followed safety training. This training must be renewed every three years.

Moreover, in order to optimize safety in laboratories, instructions must be respected. Therefore, anybody who enters or works in a laser laboratory must:

– wear protective glasses adapted to the laser's characteristics;

– wear a cotton overall; clothes with wide sleeves must not be worn because they may catch optical instruments;

– remove any visible reflecting object (watch, jewellery, pen, ring, belt buckle, cloth with metallic zip, etc.). If rings cannot be removed, a non-reflective adhesive masking-tape should cover the ring;

– take care of visitors;

– observe preventive measures for electrical apparatus;

– handle dyes and solvents according to their safety rules;

– establish and maintain a program that allows you to control dangers relative to laser use (sensitivity to laser safety).

If possible, it is recommended:

– to use a class 1 or 2 laser to achieve optical alignments;

– to attenuate the beam from maximum (filters, diaphragms, etc.) every time maximal emission is not necessary (biological and thermal risks for humans, mechanical and thermal risks for optical fibers, lenses and mirrors). Laser beam alignment may vary with laser power and modify its optical path; therefore, only the final adjustment must be done at power use, doubling employment precautions;

– fire a pulse laser only after being sure that nobody is placed in a dangerous position;

– never deliberately direct the beam toward a person or his/her eyes;

– never deliberately keep an eye in the beam axis;

– every time an optical instrument must be moved, ensure that the beam is blocked and that the element serving to block the beam is correctly fixed;

– when using a UV laser, wear a visor and gloves, in addition to protective glasses and overall;

– ensure that the number of people present is reduced to a minimum when using a laser;

– in the case of a laser accident, consult the details set out at the laboratory entrance;

– perform medical monitoring, with eyes being examined every five years.

Most of these instructions come from common sense, but it is necessary to remember to strictly respect them and to protect visitors and colleagues.

When a laser accident occurs, call for assistance and specify the part of the body that is injured and identify the laser. It is necessary to rapidly act in order to bring efficient and appropriate help to the victim. The emergency process must be posted up at each laboratory entrance, and provide steps to follow during intervention. When the eye is injured, close eyes and press one or several sterile compresses on both eyes in order to avoid contact with light, treat for light shock, place the victim on the floor, resting the body, while maintaining the head higher and wait for the ambulance.

6.6. Human behavior

Human behavior is unpredictable; it induces most of the accidents. Habit, rushing, and discomfort due to wearing glasses during adjustments, concentration on measurements and the experiment, or on visitors, more than on laser beams and reduced attention increases error and accident risks. Therefore, keep calm, concentrate and always be aware of risk.

Conclusion

Measurement setups providing images in flow field have been largely developed for velocity measurements as well as for temperature and concentration measurements (see "Laser Velocimetry for Fluid Mechanics", by the same authors), due to the commercial availability of more and more performing CCD cameras. Therefore, experimenters have a global vision of the phenomena of interest, but very often as instantaneous snapshots and with a relatively low data acquisition rate. Ongoing technological developments to laser sources and detectors will progressively allow increasing data acquisition rates in order to satisfy the requirements of turbulent phenomena analysis.

To better manage flow physics, the simultaneous measurement of two (or more) parameters is under development and leads to experiments of greater complexity, but also enables a greater understanding of the physical phenomena involved. The huge quantity of information collected has led to sophisticated and continuously evolving data postprocessing.

As the measurement principles are now well established, experiments unceasingly improve owing to the technological evolution of laser sources (delivered power, compact disposals, narrow lines emitted, impulsion rate, line tuning, etc.), detectors (sensitivity, matrix field, data rate for CCDs, etc.), electronic means and computing devices.

Software for data processing provides quasi-real-time curves or maps of measured quantities, but the experimenter must verify whether displayed data are pertinent, taking into account measurement uncertainties and must maintain a permanent dialog with those involved with theory and modeling in fluid mechanics.

Conclusion written by Alain BOUTIER.

Nomenclature

a: local sound velocity

a: particle radius, index designing an absorption term

c: light speed ($c = 3 \times 10^8$ m/s)

c_D: aerodynamic lag coefficient

d_0: grating step

e: electron charge (1.6×10^{-19} J)

e: index for extinction

f: signal light frequency received by a detector

f_0: laser beam emission frequency in vacuum ($T_0 = f_0^{-1}$ is period of line emitted in vacuum); $f_0 \approx 6 \times 10^{14}$ Hz

f_p: light frequency received by particle

f_d: fringe movement frequency due to use of Bragg cells

f_D: signal frequency due to interferences received on a detector

$f(t)$: signal (velocity); $f(t) = \frac{1}{2\pi} \int_{-\infty}^{+\infty} \hat{f}(\omega') e^{i\omega' t} d\omega'$

$\hat{f}(\omega)$: Fourier Transform (FT) of $f(t)$: $\hat{f}(\omega) = \int_{-\infty}^{+\infty} f(t) e^{-i\omega t} dt$

$\hat{f}^*$: conjugate of $\hat{f}$

h: Planck constant (6.63×10^{-34} J·s)

i: fringe spacing

i: index for incident

k: Stokes coefficient

$\vec{k}$: wave vector

k_m: imaginary part of particle or medium refraction index

$\tilde{m}$: particle complex index

m_1, m_2, m: real indices of medium, of particle in air and in medium $\left(m = m_1 / m_2\right)$

n: medium index where measurement is achieved (n ≈ 1 in air, n = 1.33 in water)

$n(D)$: size distribution in number, normalized

p: diffusion order: diffraction and reflexion (p = 0), simple refraction (p = 1), refraction after one (p = 2) or two (p = 3) internal reflection

$p(\tau)$: probability density

$\hat{p}(\omega)$: characteristic function

$\vec{r}_1$: unitary vector in the direction of a laser beam of index 1

$\vec{r}_d$: unitary vector along observation direction (toward detector)

$\vec{r}$: coordinate vector

s: index for scattering

t: time

u_d: fringe movement velocity

u_i, v_i, w_i: three components of instantaneous velocity vector in an orthogonal frame

$\overline{u'^2}, \overline{v'^2}, \overline{w'^2}$: second-order velocity moments (root mean square values)

$\overline{u'v'}, \overline{u'w'}, \overline{v'w'}$: crossed correlations

$\mathrm{var}\left[f(t)\right] = < f(t)^2 >$: variance of f

x: particle size parameter $\left(x = \pi D / \lambda\right)$

$\left(x, y, z\right)$: coordinates in a Cartesian frame

ACF: auto correlation function

CARS: coherent anti-Stokes Raman scattering

C_e, C_a, C_s: extinction, absorption and scattering cross sections

C_N, C_V: medium concentration in particle number and volume

D_{1/e^2}: laser beam diameter at emitting optics level

D, D_v: spherical particle diameter, of a same volume sphere

D_i: detector i

DSP: power spectral density

DFWM: degenerate four-wave mixing

DLS: diffusion light scattering

DWS: diffusing wave spectroscopy

$\vec{E}$: electric field vector

F: emitting optics focal length

F_A: flatness factor

$F(t)$: sampled signal

$\hat{F}(\omega)$: Fourier transform of $F(t)$

G: photomultiplier gain PM ($\approx 10^6$)

$G(t)$: rebuilt signal (staircase)

$\hat{G}(\omega)$: Fourier transform of $G(t)$

$\vec{H}$: magnetic field vector

I: anode electric current

I, I_0: local and initial wave intensities

K: absorption of particle or medium $\left(K = 4\pi k_m / \lambda\right)$

K_n: Knudsen number ($K_n = L/D$)

L_p: molecule mean free path

L: distance traveled by beam inside medium

LIF: laser-induced fluorescence

LII: laser-induced incandescence

M: probe volume

M_∞: Mach number $\{M_\infty = (\,|\, V_f - V_p \,|\,)/a\}$

MEB: sweeping electronic microscopy

N: particle number, or particle number per unit volume

OEM: electromagnetic wave

OPO: optical parametric oscillator

$\vec{P}$: Poynting vector

P_L: laser beam power in Watts

PM: abbreviation for photomultiplier

PCS: photon correlation spectroscopy

PDI, PDA: phase Doppler interferometry, anemometry

PDPA: Phase Doppler Particle Analyzer

Q_e, Q_a, Q_s: extinction, absorption and scattering coefficients

QELS: quasi elastic light scattering

R: photomultiplier response

R_e: particle Reynolds number

S: electric signal delivered by a quadratic receiver

S_D: skewness factor

S_v: probe volume transverse section area

SNR: signal-to-noise ratio

S_i: scattering amplitude function: perpendicular polarization state $(i = 1, \text{ or } \perp)$ and parallel polarization state ($i = 2$, or $\parallel$)

$S_F(\omega)$: $F(t)$ spectrum

$S_f(\omega)$: $f(t)$ spectrum

$S_G(\omega)$: $G(t)$ spectrum

$(S_G(\omega))_c$: corrected spectrum

LMT: Lorenz–Mie Theory

T: transmission rate of wave or beam

T_p: time constant

$\vec{V}$: instantaneous and local velocity vector

V_d: fringe movement velocity

α: polarizability

δ: distance separating incident parallel beams on emitting lens

ε_0: vacuum permittivity

η: PM quantum efficiency PM (0.1)

θ: angle between laser beams crossing in probe volume M

θ: scattering angle

λ: laser beam wavelength in a medium of index n

λ_0: laser beam wavelength in vacuum

λ_t: Taylor temporal microscale

μ_0: vacuum permeability

ν: frequency ($\nu = \dfrac{\omega}{2\pi}$)

$\nu(D)$: normalized volume size distribution

φ: probe volume diameter

ψ: elevation angle

σ: particle scattering cross-section

τ: time interval between two successive samplings

χ: electric susceptibility

$\chi^{(i)}$: term of electric nonlinear susceptibility of order i

ψ: angle between incident beam and order r + 1 diffracted beam in a grating or a Bragg cell

ω: wave pulsation

ω': grating angular rotating velocity

ω_0: emitting line pulsation ($\omega_0 = 2\pi c/\lambda_0$)

ω_0: radius, beam waist

Δf: bandwidth of signal processor electronics

Δs: optical path difference introduced between two arms of an interferometer

$\Delta\phi$: wave, ray, signal phase shift

Λ: photon mean free path

Λ_t: integral time scale

Φ: angle off-axis

ϕ: phase, azimuthal angle

Ω: solid angle of scattered flux collecting optics

$< >$ or $\overline{( )}$: ensemble mean

List of Authors

Séverine BARBOSA
University of Aix-Marseille
France

Alain BOUTIER
ONERA
Palaiseau
France

Frédéric GRISCH
INSA
Rouen
France

Michel LEFEBVRE
ONERA
Palaiseau
France

Fabrice LEMOINE
University of Lorranine
Vandoeuvre-lès-Nancy
France

Ajmal MOHAMED
ONERA
Palaiseau
France

Jean-Michel MOST
CNRS
Laboratoire P'
Poitiers
France

Fabrice ONOFRI
CNRS
IUSTI
Marseille
France

Index